Institute of Astronomy & Clare Hall
University of Cambridge
June 2021

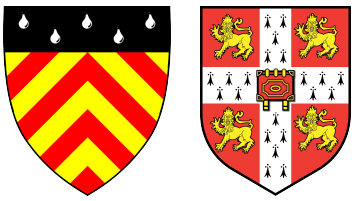

OUTFLOW PROPERTIES OF LUMINOUS QUASARS

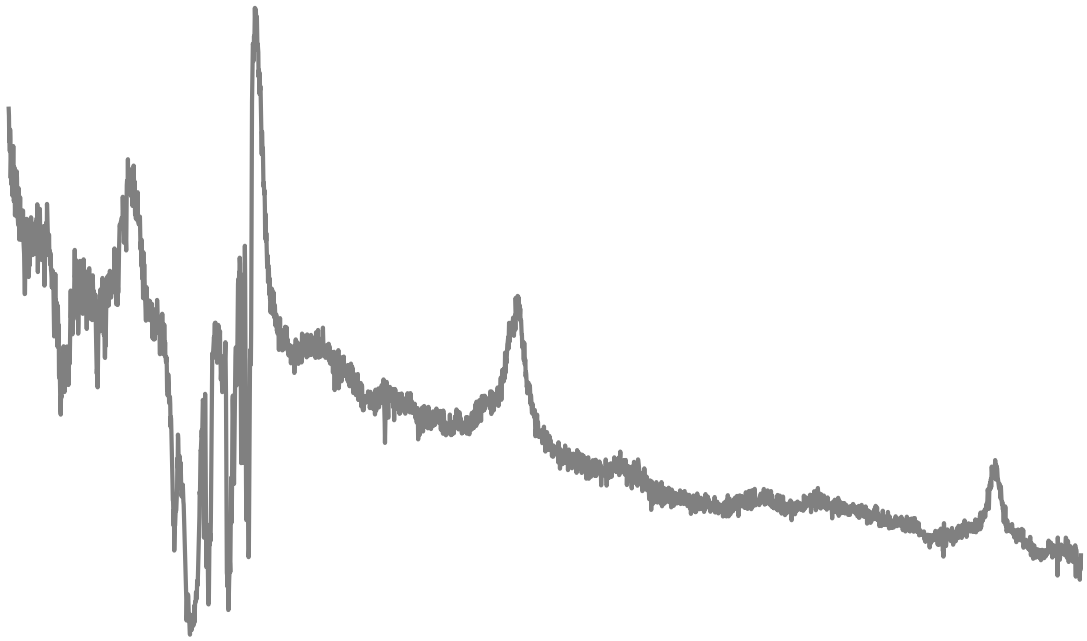

AMY LYNNE RANKINE
under the supervision of
PAUL C. HEWETT & MANDA BANERJI

This thesis is submitted for the degree of Doctor of Philosophy.

To Mum, Dad & Sarah
who constantly remind me that I've got this
and call me a nugget when I forget.

Declaration

This thesis is the result of my own work and includes nothing which is the outcome of work done in collaboration except as declared in the preface and specified in the text. It is not substantially the same as any work that has already been submitted before for any degree or other qualification. The use of 'we' instead of 'I' throughout various parts of this thesis merely reflects a stylistic choice. This thesis does not exceed the prescribed word limit for the Degree Committee for the Faculty of Physics & Chemistry.

Most of the work presented in this thesis has been published in the articles listed below. At the beginning of each chapter, I state explicitly what work has been contributed by the co-authors of these articles.

- Chapters 2 & 3:
  A. L. Rankine, P. C. Hewett, M. Banerji, G. T. Richards
  BAL and non-BAL quasars: continuum, emission, and absorption properties establish a common parent sample
  MNRAS, Volume 492, Issue 3, March 2020, Pages 4553–4575

- Chapter 5:
  A. L. Rankine, J. H. Matthews, P. C. Hewett, M. Banerji, L. K. Morabito, G. T. Richards
  LOFAR-detected quasars in C IV emission space: implications for winds, jets and star formation
  MNRAS, 502, Issue 3, April 2021, Pages 4154–4169

Outflow properties of luminous quasars

Amy Rankine

Quasars, powered by accretion onto the super-massive black holes at their galaxies' centres, are capable of ejecting highly energetic outflows of gas, which can suppress star formation in the host galaxy, thereby impacting its evolution. Quasar-driven outflows are widely invoked in galaxy formation models in order to reproduce the observed properties of massive galaxies. However, there are still fundamental open questions regarding the origins of these outflows, and their relationship to accretion processes. This thesis covers a series of multi-wavelength studies of the outflow properties of quasars at redshifts $1.5 < z < 3.5$ from the Sloan Digital Sky Survey. In particular, I focus on the C IV emission space which is often used to infer the strength of quasar winds via the C IV blueshift. A major aim of this thesis is to constrain the outflow properties of quasars by combining studies of emission lines, broad and narrow absorption lines.

After an introduction to quasars and their outflows, I describe my use of independent component analysis (ICA) for reconstructing the quasar spectra. With the reconstructions, I define a sample of broad absorption line (BAL) quasars, named for the presence of broad absorption lines in their spectra.

I subsequently explore the outflow properties, evident both in absorption and emission, of the high-ionisation BAL and non-BAL quasars, revealing strong systematic correlations between the emission and absorption properties. I also demonstrate that (high-ionisation) BALs and non-BALs likely represent different views of the same underlying quasar population by revealing similarities in the luminosities and emission-line outflow properties between the BAL and non-BAL quasar populations.

I investigate the prevalence of associated and outflowing narrow C IV absorption lines (NALs) in quasars across the C IV emission space. I find that the velocity of the outflowing NALs increases with C IV emission-line outflow velocity in BAL and non-BAL quasars alike. I use this result to further argue that BAL and non-BAL quasars arise from the same parent population. The velocity of line-locked systems, which are evidence for radiation line-driving, is also shown to increase as the C IV blueshift increases in BAL and non-BAL quasars which indicates the importance of radiation line-driving for driving outflows in both quasar populations.

Finally, I present an investigation of the low-frequency radio and ultraviolet properties. I find quasars with similar ultraviolet properties but differing radio properties suggesting, perhaps, that the radio and ultraviolet emission is tracing activity occurring on different time-scales. Additionally, opposing trends are observed between the radio-detection and radio-loud fractions as functions of C IV blueshift which alludes to multiple processes contributing to the radio emission. I explore the plausibility of winds, compact jets, and star formation as sources of the radio-quiet emission, ruling out none.

Acknowledgments

I have to start by saying a massive thank you to Paul Hewett and Manda Banerji for their enthusiastic supervision. Their scientific, career, and general life advice have made every step of the last four years and the first step of the next three much easier. Without fail, our weekly meetings always ended with me feeling more motivated, more confident, and much happier.

Thank you also to my co-authors, Gordon Richards, James Matthews, and Leah Morabito. Without their guidance my papers would not yet be submitted. To my examiners, Katherine Blundell and Richard McMahon, for taking the time to read and think critically about my thesis. Matthew, thank you for the science chats on the stairs in Oxford Road and then for the walks during the last year. I'm glad we got to collaborate during our PhDs.

Ultimately, my PhD research was enabled by funding from STFC, and the astronomical observations of the SDSS and LOFAR. I am also grateful for all of the helpful discussions with Bob Carswell, Amy Kimball, Norm Murray and Vivienne Wild. I also need to thank Debbie Peterson for a great deal of hard work in making the PhD programme run smoothly.

I had the pleasure of staying in Clare Hall during my first year with Dimitra, Kostas, Marc, and Yash. Dinner together in College was a lovely way to round off each day (I could always rely on Kostas to be there at 6pm) and their all-round support and joy set me up for a good first year. Thank you also to all of Clare Hall choir and especially Ben for keeping me in touch with College and for giving me an excuse to sing.

Laura, Aoife, Anjali, Chiara, and Antonia, thank you for all the laughs and memories and for generally being an encouraging bunch. Our regular Zooms reminded me that there was life outside of my flat. Laura Moran pointed out that the Cambridge PhD applications weren't in fact closed and so I mean it quite literally when I say that I wouldn't be where I am today without her. Despite being all the way away in Exeter (and dealing with her own PhD) she has been one of my main supporters (my back-up woah girl). Amy Brown, thank you for always believing in me and sending me all of the questions about space. I'm extremely glad that Sophie found me on that first day at the STFC Summer School. I can't truly express how fantastic it has been to have a friend who I can trust with the smallest of things (wording emails), to the biggest of things (post-PhD choices). It's been really nice to have someone there through all of it, and as my perennial Greenwich lunch partner. I will miss Sophie and I look forward to the time when we can collaborate.

Thank you to Mum, Dad, Sarah, Lynne, Eddie, and all of my grandparents for their constant love. They have always believed in me and I am incredibly lucky to have them.

I have no doubt that Aneesh made the whole PhD process much easier and the postdoc applications much less stressful, not least because of the technical support with LaTeX and Python, and all of the proofreading. Whatever I write here does not do Aneesh justice but I will say that his silliness, warmth, and love have kept me light and my heart happy.

Contents

List of Figures

List of Tables

List of Abbreviations

AGN	Active Galactic Nucleus/Nuclei
(B/N)AL	(Broad/Narrow) Absorption Line
(Hi/Lo)BAL	(High/Low)-ionisation Broad Absorption Line
BC	Bolometric Correction
(B/N)LR	(Broad/Narrow) Line Region
BOSS	Baryon Oscillation Spectroscopic Survey
DR	Data Release
(H/L)ERG	(High/Low)-Excitation Radio Galaxy
EW	Equivalent Width
FeLoBAL	Low-ionisation BAL with strong Fe II and Fe III absorption
FIRC	Far-Infrared Radio Correlation
FIRST	Faint Images of the Radio Sky at Twenty-Centimetres
FR	Fanaroff & Riley
(A/B)I	Absorption/Balnicity Index
ΛCDM	Lambda cold dark matter
LDR1	LOFAR Data Release 1
LLS	Largest Linear Size
LOFAR	Low-Frequency Array
LoTSS	LOFAR Two-metre Sky Survey
MAD	Median Absolute Deviation
MC	Monte Carlo
MFICA	Mean-Field Independent Component Analysis
NMF	Non-Negative Matrix Factorisation
PCA	Principal Component Analysis
RLF	Radio-Loud Fraction
SDSS	Sloan Digitial Sky Survey
SED	Spectral Energy Distribution
SFR	Star-Formation Rate
S/N	Signal-to-Noise ratio
(E)UV	(Extreme) Ultraviolet

Chapter 1

Introduction

1.1 Active galactic nuclei and quasars

It is believed that at the centre of every massive galaxy, there is a super-massive black hole (SMBH) and that it has spent some time over the course of its lifetime, rapidly accreting material from the inner regions of the galaxy such that it emits vasts amount of energy (Lynden-Bell, 1969). Basic arguments involving the galaxy luminosity function tracing the black hole accretion rate provide estimates of 10^7–10^9 yr for the total period over which the galactic nuclei are expected to be in this active galactic nucleus (AGN) phase (Soltan, 1982; Yu & Tremaine, 2002; Marconi *et al.*, 2004). However, shorter timescales for individual active phases of order 10^5 yr have also been postulated based on models whereby the AGN 'flickers' on and off (Schawinski *et al.*, 2015).

AGN are fundamental to galaxy evolution. Twenty years ago galaxy evolution studies were transformed by the unexpected observational discovery that the mass of the SMBH is correlated with the galactic velocity dispersion (Magorrian *et al.*, 1998; Ferrarese & Merritt, 2000; Gebhardt *et al.*, 2000). Additionally, the correlation between the star formation rate and black hole accretion rate over cosmic time (e.g., Aird *et al.*, 2010) implies that galaxy growth and black hole growth are linked.

One of the many illustrations that exist in the literature of the AGN phenomenon is presented in Fig. 1.1. All models have in common the SMBH surrounded by an accretion disc which emits in the ultraviolet (UV) and is often considered to be geometrically thin and optically thick (Shakura & Sunyaev, 1973). The broad UV and optical emission lines found in a population of AGN spectra give rise to the notion of the broad line region (BLR), originally proposed as consisting of discrete clumps or clouds of gas (Antonucci, 1993). The exact structure of the BLR is still uncertain but the presence of emission lines of a range of ionisation potentials in spectra and their differing response times to changes in the UV continuum (from reverberation-mapping studies and using light travel-time arguments; Li *et al.*, 2017) suggest that the BLR is stratified and covers a range of distances from light-

days to light-months (Grier *et al.*, 2019). Farther out from the black hole, on kiloparsec or galaxy scales, is the narrow line region (NLR) from which the narrow optical/UV emission lines originate. Other components of the basic AGN model include a dusty torus (termed 'circumnuclear region' in Fig. 1.1 due to the uncertainty surrounding the exact structure of this optically thick component) which must exist at radii at least as large as the dust sublimation radius. Recent studies have garnered support for this highly-obscuring structure being formed by a failed wind (Wada, 2012; Izumi *et al.*, 2018). The origin, structure, and driving mechanism of the wind itself, most notably observed via the blueshifted absorption present in UV spectra (e.g., Turnshek, 1988; Weymann *et al.*, 1991; Murray *et al.*, 1995), are unclear. The various observational signatures of winds are discussed later and are the main subject of this thesis.

AGN emit across the electromagnetic spectrum and populations of AGN have been identified at X-ray, UV, infrared, and radio wavelengths. In fact, AGN were first discovered at radio wavelengths via emission from highly energetic, collimated radio jets (Schmidt, 1963). Now, however, only ∼0.4 per cent of the luminous AGN in the Sloan Digital Sky Survey (SDSS) are posited as having extended jets (Ivezić *et al.*, 2002). The mechanisms for turning a jet on are not known but black hole spin is likely a key factor (Blandford & Znajek, 1977).

Figure 1.1 provides just one illustration of the AGN phenomenon and it has been chosen here for providing a clear representation of the many components of an AGN. The covering fraction of each feature and the launch radius and angle of any wind (or jet) vary between models. Additionally, these parameters are expected to vary with fundamental properties of the AGN including accretion rate and black hole mass, but also with orientation which makes AGN all the more challenging to unravel.

High-luminosity AGN are referred to as quasars and are the focus of this thesis. They typically have bolometric luminosities $\gtrsim 10^{45}$ erg s^{-1} and black hole masses of 10^8–10^{10} M$_\odot$. They represent the most radiatively-efficient phase of SMBH growth. The quasar sample used throughout this thesis is a subset of the quasar catalogue compiled from the fourteenth data release of the Sloan Digital Sky Survey (Pâris *et al.*, 2018). Objects are classed as quasars in the catalogue if they have $M_i[z = 2] < -20.5$ and at least one emission line with Full Width at Half Maximum (FWHM) > 500 km s^{-1}.

1.2 Feedback

The difference in physical scales, coupled with the correlation between the masses of the black hole and galaxy, implies the existence of some 'feedback' mechanism linking the growth of the black hole to the growth of the galaxy (Kormendy & Ho, 2013).

Energetically, feedback is feasible: a typical central black hole of mass 10^8 M$_\odot$ solar

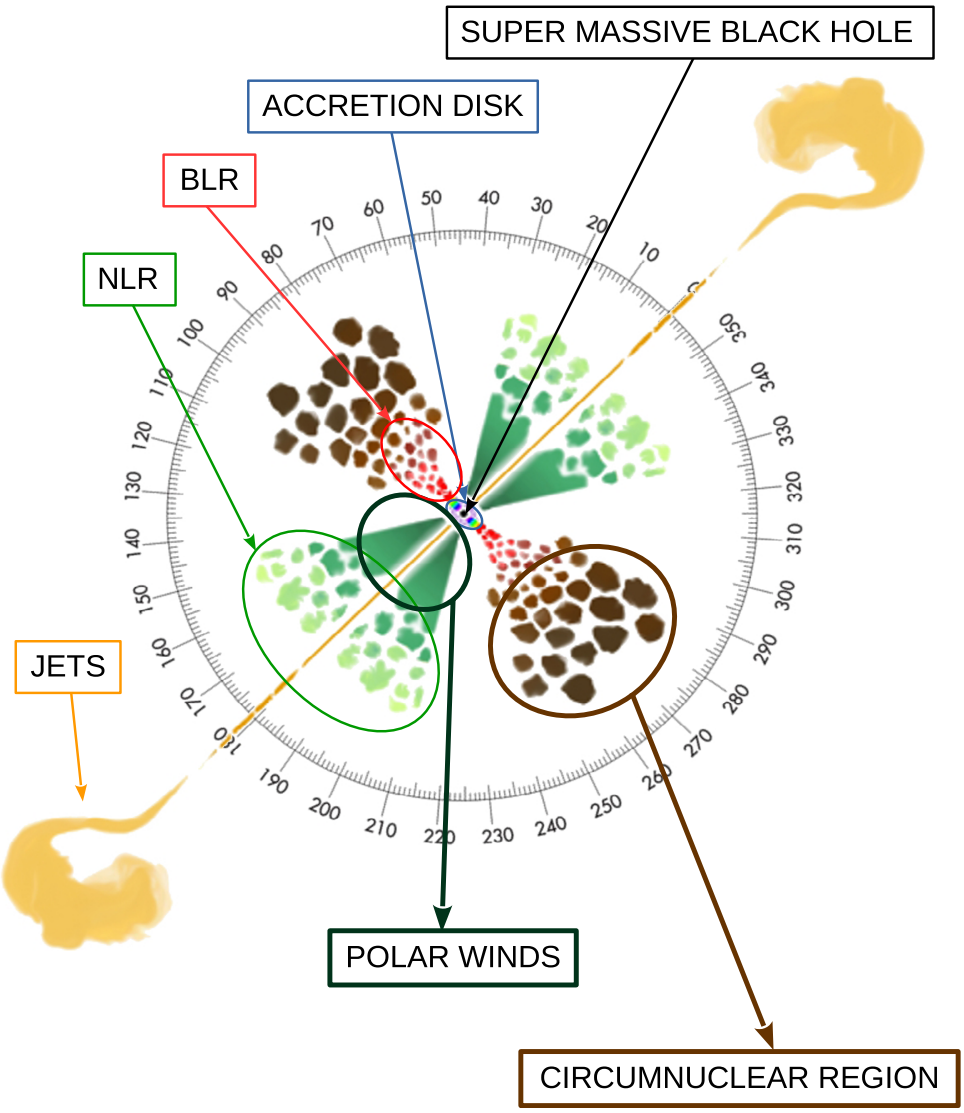

Figure 1.1: Unscaled illustration of the AGN phenomenon taken from Rojas Lobos *et al.* (2018, fig. 1) who adapted the original by Marin (2016, fig. 1). Credit: Rojas Lobos *et al.*, A&A, 611, A39, 2018, reproduced with permission © ESO.

masses, accreting material, releases 10^{61} erg in the form of radiation and kinetic energy during its growth, assuming an efficiency of 10 per cent. The released energy is 100 times the gravitational binding energy of a 10^{11} $M_\odot$ galaxy, thus only one per cent of the energy released during the accretion process is required to influence the evolution of the galaxy. The timescales involved with AGN activity are uncertain and estimates range from 10^4 years for individual AGN phases (Schawinski *et al.*, 2015) to 10^9 years for total activity (e.g., Marconi *et al.*, 2004).

Moreover, cosmological simulations now routinely invoke AGN feedback, albeit often in the form of sub-grid physics, in order to reproduce the observed galaxy mass function (Somerville & Davé, 2015; Vogelsberger *et al.*, 2020). Specifically, simulations of ΛCDM-based models with no prescription for AGN feedback overestimate the number density of high mass galaxies. Feedback mechanisms such as fast winds with large angular scales

which can blow the cold gas from the galaxy, or collimated radio jets injecting energy to heat up the gas, could reduce the star formation rates in the galaxies (Fabian, 2012; Heckman & Best, 2014), thus reducing the number density of galaxies at the high mass end of the mass function.

There are two general modes of feedback that are expected to occur during different black hole states. 'Quasar' mode becomes important at high Eddington ratios ($\gtrsim 10^{-2}$). In this mode feedback occurs via winds that are driven from the disc by radiation pressure from the radiatively-efficient disc, sweeping away gas in the galaxy that would otherwise have formed stars. The winds are believed to originate from the accretion disc; however, it is unclear how far they extend with estimates ranging from parsec to kilo-parsec scales. At low Eddington rates ($\lesssim 10^{-3}$), the 'radio' mode kicks in, whereby relativistic jets, which can extend well beyond the edge of the host galaxy, deposit kinetic energy into the host galaxy and prevent cooling of the gas. However, the situation is not simple given there exist many sub-Eddington AGN without jets and others with high accretion rates *and* jets (e.g., Willott *et al.*, 1999).

1.2.1 Signatures of feedback in the UV

Quasar winds can be detected in the rest-frame UV spectra of quasars at $1 \lesssim z \lesssim 4$ – the epoch of black hole activity – with optical spectrographs such as those of the SDSS. Fundamental questions remain about the key aspects of the physics of winds and how they relate to the properties of the black hole, such as its mass and accretion rate.

Disc winds (Murray *et al.*, 1995; Elvis, 2000; Proga *et al.*, 2000; Proga, 2003) are one of the main sets of models explaining quasar winds. From a thin accretion disc, a wind emerges as a result of radiation pressure from the disc's UV emission (see fig. 1 of Murray *et al.*, 1995). Some models invoke shielding of the wind (Murray *et al.*, 1995; Proga *et al.*, 2000) or perhaps disc geometry (Leighly, 2004; Luo *et al.*, 2015) to explain the high velocities that the gas can reach without being over-ionised by the central source. Radiation line-driving by ultraviolet photons has been considered as an acceleration mechanism of the wind (e.g., Giustini & Proga, 2019). However, acceleration by magnetohydrodynamics has also been considered (Blandford & Payne, 1982) and it is probable that a combination of acceleration mechanisms is responsible for the observed winds.

There exist multiple signatures of accretion disc winds in the ultraviolet/optical spectra of quasars: blueshifted broad emission lines (BELs), broad absorption lines (BALs), and narrow absorption lines (NALs). Each signature has been studied in isolation and this thesis documents the first attempt to combine them in order to make progress towards a holistic understanding of quasar outflows.

Blueshifted emission lines

The C IV λ1549 emission line is often blueshifted with respect to the systemic redshift of the quasar. Excess emission in the blue wing of the emission line produces the skewed C IV profiles that are ubiquitous in quasar spectra. Disc winds may explain the blueshifted emission by means of the outflowing material emitting C IV photons. The optically-thick disc in the mid-plane can account for the lack of excess emission in the red wing of the line which would be associated with the wind flowing away from the observer on the other side of the disc (e.g., Gaskell, 1982; Sulentic *et al.*, 2000; Leighly, 2004; Richards *et al.*, 2002b, 2011).

Broad absorption lines

One of the major obstacles in studying quasar winds as evidenced by the C IV blueshift is the presence of broad (and narrow) absorption at the spectral location of the C IV emission line. By definition, the broad absorption lines have FWHM > 2000 km s^{-1}. Chapter 2 describes the technique we employ to overcome the difficulty via the reconstruction of the quasar spectra, including the intrinsic unabsorbed C IV emission.

Broad absorption lines observed in the UV spectra of quasars are long established as providing evidence for the presence of high-velocity outflows among a substantial fraction of the quasar population (Weymann *et al.*, 1991; Hewett & Foltz, 2003; Allen *et al.*, 2011). Of the intrinsic (extinction-corrected) ≃40 per cent of luminous, optically-selected quasars classed as BAL-quasars (Dai *et al.*, 2008; Allen *et al.*, 2011) the majority, so called 'Hi-BALs', show absorption of highly-ionised species such as C IV λ1549, Si IV λ1397, N V λ1240 and O VI λ1034. LoBAL-quasars also show absorption from low-ionisation species (e.g., Al III λ1857 and Mg II λ2800), while FeLoBALs are quasars which additionally display Fe II and Fe III absorption over extended wavelength intervals. The broad, blueshifted absorption is believed to result from the presence of outflowing gas along the direct line-of-sight and observations typically detect gas travelling at velocities of many thousands of km s^{-1}. Evidence for the presence of infalling or rapidly rotating material from broad absorption lines is rare due to the small number of redshifted BALs that have been observed and it is not yet clear why this is the case (Hall *et al.*, 2013).

The location of the outflowing gas is uncertain and establishing their radial distance from the ionising source would go some way to ascertaining their impact on the host galaxy. Without spatially resolving the wind, time-resolved spectroscopy can be used to constrain its location. With multi-epoch spectroscopy BAL variability has been observed on rest-frame timescales of ≤5 years with some objects transitioning from BAL quasars to non-BAL quasars (Filiz Ak *et al.*, 2012, 2013; Sameer *et al.*, 2019) and vice versa (Rogerson *et al.*, 2018). Such transformations may arise due to changes in the ionising state of the outflowing gas or result from wind motion transverse to the line-of-sight (e.g., Gibson *et al.*, 2010; Sameer

et al., 2019). With such arguments in mind, the gas responsible for the BALs has been estimated to be on pc scales (Capellupo *et al.*, 2013), but also up to at least 500 pc (Arav *et al.*, 2018), and even kpc scales (Dunn *et al.*, 2010; Xu *et al.*, 2019).

There are generally two types of model postulated to explain the presence of BALs in only a fraction of quasar spectra. The first being that all quasars have the gas responsible for the BALs but that the gas has a ∼20 per cent covering fraction. The second theory would have all quasars being BAL quasars at an early stage of the fuelling-cycle for the quasar before much of the gas is expelled during a phase of strong winds.

Discriminating between the different models would make for encouraging progress on the question of the structure and prevalence of disc winds and the nature of feedback. In Chapter 3 I describe an investigation into the similarities and differences between high-ionisation BAL and non-BAL quasars, making use of the C IV emission space, in an effort to address this question.

Narrow absorption lines

Narrow absorption lines (NALs) are, as their name suggests, much narrower ($\lesssim 200\,\mathrm{km\,s^{-1}}$) than the broad absorption introduced above and can be broadly divided into three main populations based on their velocity with respect to the systemic quasar redshift. NALs at velocities $\gtrsim 15\,000\,\mathrm{km\,s^{-1}}$ are mostly associated with intervening galaxies close to the line-of-sight, and are unrelated to the quasar; however, some of these extreme-velocity NALs are potentially tracing fast outflows (Hamann *et al.*, 2011; Chen *et al.*, 2021). For velocities in the range 3000–15 000 km s^{-1}, a significant fraction of NALs result from outflowing systems associated with the quasar (Nestor *et al.*, 2008; Wild *et al.*, 2008), while NALs with velocities $\lesssim 3000\,\mathrm{km\,s^{-1}}$ are called associated absorption lines (AALs) and are generally believed to originate in the quasar environment (Weymann *et al.*, 1979; Wild *et al.*, 2008).

Much can be learnt about the outflow properties from the NALs. Performing population studies of NALs of various ionic species – e.g., the high-ionisation C IV, N V, O VI lines, and the low-ionisation Mg II and Lyα lines – can reveal information about the ionisation state of the gas. The ionisation parameter is defined as

$$U = \frac{Q(\mathrm{H})}{4\pi r^2 c\, n_{\mathrm{H}}}, \tag{1.1}$$

where Q(H) is the total luminosity of ionising photons, n_{H} the hydrogen number density, and r the distance between the ionising photon source and the 'cloud' of gas. Photoionisation modelling (with e.g., CLOUDY; Ferland *et al.*, 2017) of the line ratios has been used to infer the velocity structure of the wind. Bowler *et al.* (2014) found that the ionisation parameter decreased as NAL velocity increased. The observation is consistent with the

discrete structures (responsible for the NALs) in an accelerating outflow whereby the ionising flux decreases as distance increases (see also Perrotta *et al.*, 2018, for a similar analysis but with a smaller sample size).

While outflowing NALs populate the 3000–15 000 km s^{-1} velocity range, intervening systems, unrelated to the quasar, are also present. However, one observational signal that provides unambiguous evidence for an origin in outflows, and particularly radiatively line-driven outflows, is line-locked systems. Line-locking can occur when an outflowing cloud of gas moving along our line-of-sight is shielded from the ionising source, which is responsible for the gas' acceleration, by a second cloud also moving along our line-of-sight at a velocity relative to the shielded cloud corresponding to the velocity by which two absorption lines are separated. The shielded cloud experiences a reduction in the line flux of the species responsible for the line-driving causing the gas to slow and the velocities of the two clouds become synchronised (Scargle, 1973; Strittmatter *et al.*, 1973; Burbidge & Burbidge, 1975). In Chapter 4, we investigate C IV NALs, line-locked and otherwise, in the context of the C IV emission outflow signature.

1.2.2 Signatures of feedback in the radio

Since the discovery of AGN it has been known that the rapidly spinning black holes are capable of launching powerful highly-collimated jets that can reach well beyond the extent of the host galaxy. It is thought that jets become important at low accretion rates when disc winds are weakest; however, quantitative observational evidence for this is lacking. AGN jets are often identified and studied through their radio emission. Approximately 5 per cent of quasars are classed as 'radio-loud' although the fraction evolves with redshift and luminosity (Jiang *et al.*, 2007; Kratzer & Richards, 2015). The origin of the radio-emission in radio-loud quasars is dominated by the large lobes that are produced by powerful jets and such radio sources can be categorised based on their morphology.

The origin of the radio emission in the much more abundant radio-quiet quasars is less well understood. Quasars that are detected in large radio surveys such as the Faint Images of the Radio Sky at Twenty-Centimetres (FIRST) survey (Becker *et al.*, 1995) are typically radio-loud. It is only in recent years with more sensitive surveys such as the Low-Frequency Array (LOFAR; van Haarlem & et al., 2013) that the properties of radio emission in the radio-quiet population have been studied in detail. Winds are capable of producing radio emission (Stocke *et al.*, 1992; Zakamska & Greene, 2014); however, compact and/or weak jets are also contenders for contributing significantly to the radio-quiet emission (e.g., Sadler *et al.*, 2014) with evidence for relativistic beaming in some systems (e.g., Blundell *et al.*, 2003). However, the relative importance of these sources in producing the observed radio emission is still unclear (Panessa *et al.*, 2019) and knowing how they relate to accretion processes would be significant progress in understanding the lifecycle of quasars. In Chapter 5

we explore the possible contributions of these phenomena to the radio-quiet emission and consider the relationship between the UV and radio properties.

1.2.3 Feedback signatures at other wavelengths

This thesis focuses on the UV (and radio) signatures of feedback. However, winds are multi-phase in nature and the cool molecular gas outflows tracing galaxy-scale winds can be studied in $z \sim 2$ quasars with sub-mm telescopes such as ALMA (Veilleux *et al.*, 2020), and ultra-fast outflows have been studied via X-ray absorption (e.g., Chartas *et al.*, 2002). Additionally, blueshifted [O III] λ5007 in the rest-frame optical spectra of $z \sim 2$ objects has been observed with near-infrared instruments such as VLT-SINFONI and Gemini-GNIRS (Coatman *et al.*, 2019; Temple *et al.*, 2019). [O III] is tracing ionised outflows on kpc scales thought to be coincident with the NLR. Coatman *et al.* (2019) found correlations between the C IV blueshift and the [O III] kinematics suggesting the outflows traced by these lines are linked over an extended range of scales. Correlations between BAL properties and [O III]-emission properties have also been found by Xu *et al.* (2020).

1.3 Unification

The original AGN unification schemes of Scheuer (1987), Antonucci (1993), and Urry & Padovani (1995) considered the AGN phenomenon to result from different, but unchanging, components with the observational signature depending solely on orientation on the sky and the presence or absence of a jet. Type-1 AGN are viewed from an angle such that the BLR is visible, thus broad emission lines observed. Type-2 AGN, on the other hand, have an orientation edge-on to the accretion disc with a dusty torus obscuring the BLR and instead have only narrow emission lines in their spectra which are thought to be produced at much greater radii from the black hole.

More recently, time dependence and even evolution have been invoked to unify all AGN. Giustini & Proga (2019) provide an updated view on AGN unification and their fig. 5 (reproduced here in Fig. 1.2) includes different black hole masses, Eddington ratios, and orientation to explain the diverse observations that exist. The authors implement different disc structures and outflow processes as the Eddington ratio and black hole mass evolve.

The Eddington ratio drives the structure of the accretion disc and the subsequent accretion flow. At low Eddington ratios ($\sim 10^{-4}$) the inner accretion disc is hot, geometrically thick and radiatively inefficient. Jet feedback is important in this regime and it is only as the Eddington ratio increases that the disc becomes radiatively efficient and thin, and the jet weakens. In this moderate Eddington-ratio regime ($\sim 10^{-2}$), the black hole mass dictates the strength of the line-driven winds. The larger the black hole mass, the cooler the disc

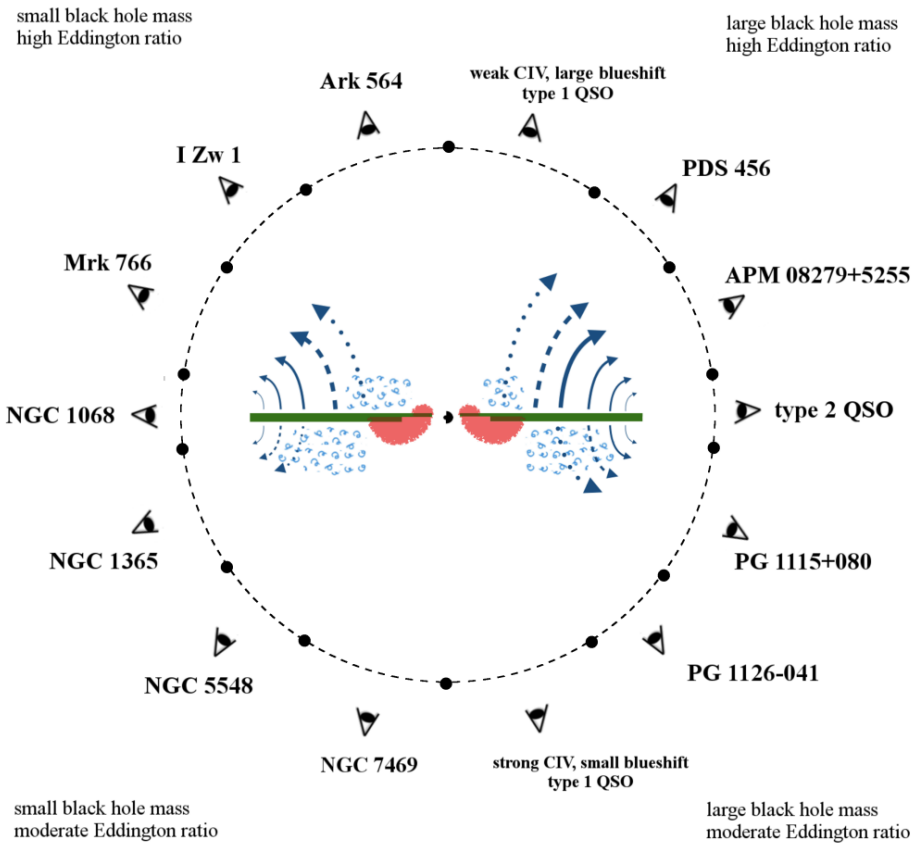

Figure 1.2: Sketch of the inner accretion disc and outflow region for all four combinations of a small ($\ll 10^8\,M_\odot$) or large ($\gtrsim 10^8\,M_\odot$) black hole mass, and moderate ($\simeq 10^{-3}$–10^{-1}) or high ($\gtrsim 0.25$) Eddington ratio from Giustini & Proga (2019), fig. 5. At high Eddington ratios, the cold, optically thick accretion disc (green disc) extends closer to the black hole compared to at moderate Eddington ratios, and the hot, optically thin accretion flow (red blob) is smaller. Radiatively-driven winds – persistent (solid blue arrows) and transient (dashed) – are launched from smaller radii but only large-radius streamlines escape whilst the close-in streamlines fail (blue swirls). At moderate Eddington ratios, much more of the wind fails, and smaller black holes have less persistent winds. In this model, quasars viewed directly along the winds are likely to have BALs, including the examples listed around the right-hand side. Credit: Guistini & Proga, A&A, 630, A94, 2019, reproduced with permission © ESO.

(following Shakura & Sunyaev, 1973), and the greater the ratio of optical/UV flux to far-UV / soft X-ray flux. A successful line-driven wind can only be launched if the UV flux is strong enough to exert enough radiation pressure on the gas and if the X-ray flux is weak enough so as to not over-ionise the gas; therefore disc winds will be strongest in the high black hole mass quasars. The UV/X-ray flux ratio will increase along the radial axis of the disc, and as such, the launch radius of the winds will also depend on the Eddington ratio and black hole mass.

In the model of Giustini & Proga (2019), orientation also plays a part in the ability to detect the wind via BALs, but the importance of orientation changes as a function of Eddington ratio and black hole mass. The line-of-sight required to intersect the wind will change as the shape and launch radius of the wind changes.

Accretion is expected to be regulated and so while the purpose here is not to explain physically how this regulation may occur, it is clear from Fig. 1.2 that however the accretion rate and Eddington ratio may vary, these changes would result in changes in the observed UV and X-ray continua, broad UV and optical emission lines, and absorption features.

1.4 Thesis structure

This thesis consists of various large statistical studies investigating multiple observational diagnostics of outflows in quasars across a range of spatial (and temporal) scales. A multi-wavelength approach is necessary in order to gain a holistic understanding of how quasars can influence their host galaxies.

The structure of the thesis is as follows. Chapter 2 includes a breakdown of the spectrum reconstruction technique which utilises Independent Component Analysis (ICA). In doing so, we are able to use information from elsewhere in the spectra to inform the shape of the – often absorbed – C IV emission line profile. The base sample of quasars from SDSS in the redshift range $1.5 < z < 3.5$ is also described and the BAL quasar sample defined.

The spectrum reconstructions thus allow us to investigate the kinematics of the C IV emission profiles of the BAL and non-BAL quasars in a consistent manner in Chapter 3. Additionally, we have investigated correlations between the C IV blueshift and BAL trough parameters including trough velocities and depth.

Chapter 4 describes an investigation into the relationship between the C IV blueshift and the outflows traced by C IV NALs. We also explore any potential differences between the NALs found inside BAL troughs and those outside.

In Chapter 5 we attempt to tie the low-frequency radio emission as observed by the Low Frequency Array (LOFAR) to physical processes including jets, star formation and winds. Again, we use the diagnostic power of the C IV emission space to explore the connection between jets and winds.

Finally, in Chapter 6 I provide some concluding remarks and suggest a few possible directions for future investigations.

Throughout the thesis, vacuum wavelengths are employed and we adopt a ΛCDM cosmology with $h_0 = 0.71$, $\Omega_m = 0.27$ and $\Omega_\Lambda = 0.73$ when calculating quantities such as quasar luminosities.

Chapter 2

Spectrum Reconstructions

Summary

Using a sample of ≃144 000 quasars from the Sloan Digital Sky Survey data release 14 (DR14) we define the population of high-ionisation BAL and non-BAL quasars with redshifts $1.6 \lesssim z \leq 3.5$ and luminosities $45.3 < \log_{10}(L_{\rm bol}/{\rm erg\,s}) < 46.6$. Key to the investigation is a continuum and emission-line reconstruction scheme, based on mean-field independent component analysis, that allows the intrinsic C IV emission and continuum to be recovered. We compare our classifications of BAL and non-BAL quasars to those from the SDSS DR14 catalogue and find that differences are most apparent when absorption is present at low velocities relative to the systemic redshift of the quasar. We attribute the differences in classification to our updated and improved redshift estimates which are based on a separate ICA analysis. The reconstructions presented here form the foundations of the investigations in the subsequent chapters.

This Chapter is based on Section 2 of the article:

A. L. Rankine, P. C. Hewett, M. Banerji, G. T. Richards

BAL and non-BAL quasars: continuum, emission and absorption properties establish a common parent sample

MNRAS, Volume 492, Issue 3, March 2020, Pages 4553–4575

P. C. Hewett calculated the quasar redshifts detailed in Section 2.3, generated the ICA components (Section 2.4.2), and morphed the spectra (Section 2.4.1).

2.1 Introduction

Large spectroscopic surveys such as the SDSS (York *et al.*, 2000) have the capacity for statistical studies of quasars; the latest data release (DR16; Lyke *et al.*, 2020) contains ∼750 000 quasars. Prior to SDSS, the Palomar Bright Quasar Survey (BQS; Schmidt & Green, 1983) consisted of 114 optical spectra mostly from the Palomar-Green catalogue (Green *et al.*, 1986). With this now seemingly small catalogue, Boroson & Green (1992) conducted a principal component analysis (PCA) to unravel correlations between various measured optical properties of the low-redshift quasars, namely the Hβ, [O III] λ5007, He II λ4686, and Fe II emission lines.

Later came the optically-selected Large Bright Quasar Survey (LBQS; Hewett *et al.*, 1995). Francis *et al.* (1992) applied a principal component analysis directly to the spectra in order to examine correlations between individual component weights and various emission line strengths at UV wavelengths, from Lyα through to Al III.

At $z \sim 2$, the rest-frame UV is observable with the optical spectrographs of SDSS, providing access to radiation from the accretion disc, the broad-line region, and any winds at the peak epoch of black hole activity. The modest S/N of the spectra and the large sample sizes mean that significant time and energy must first be invested in the methods of extracting useful information from the spectra. Additionally, the presence of extensive absorption due to outflowing gas along the line-of-sight in the spectra of a significant population of quasars of interest further complicates the task. We review the task of recovering the unabsorbed ultraviolet SEDs of BAL quasars and the approach taken to perform the investigation here.

Performing a statistical analysis of quasar UV spectra to produce a small number of 'components', linear combinations of which are capable of reproducing individual quasar SEDs, is long established (Francis *et al.*, 1992; Yip *et al.*, 2004). Application of the component reconstruction techniques has proved successful in the context of BAL quasars, where it is necessary to reconstruct the unabsorbed SED at wavelengths affected by the presence of BAL troughs. The non-negative matrix factorisation (NMF)-based analysis of the SDSS DR6 spectra (Allen *et al.*, 2011) resulted in very effective reconstructions, albeit over a restricted range in wavelength given their focus on primarily the C IV λ1549 emission line and the BAL/non-BAL classification. Implementations involving principal component analysis (PCA) now form key elements of the redshift determination for quasars and the identification of BALs in recent large-scale surveys, particularly the SDSS (Pâris *et al.*, 2017; Abolfathi *et al.*, 2018; Pâris *et al.*, 2018).

From previous work (Allen *et al.*, 2011), it is clear that the accuracy of any component-based reconstructions of quasar spectra needs to be high in order to parameterise differences in the emission-line SEDs such as the He II λ1640 properties, particularly for spectra with extensive wavelength ranges affected by BAL troughs. In order to undertake such a quantitative investigation of the underlying UV SEDs of high-ionisation BAL quasars and

non-BAL quasars using the large quasar spectra samples available from the SDSS (Pâris *et al.*, 2018) we have revisited the question of how to obtain high-accuracy reconstructions of individual BAL and non-BAL spectra that possess extensive ranges in SED properties.

The structure of the Chapter is as follows. A brief description of the task of reconstructing quasar spectra is provided in Section 2.2. The selection of the quasar sample is described in Section 2.3 before the specific recipe for the spectral reconstructions is presented in Section 2.4. The question of the definition of the sample of quasars that possess 'broad-absorption' is the topic of Section 2.5, where both the classic definition, involving the balnicity-index (BI) from Weymann *et al.* (1991), and the more extensive absorption-index (AI) from Hall *et al.* (2002), are employed.

2.2 The problem at hand: reconstructing quasar spectra

The PCA, NMF and mean-field independent component analysis (MFICA) (see below) approaches all involve reconstructions based on linear combinations of derived components. There is, however, a significant variation in the form of quasar UV SEDs due to multiplicative changes as a function of wavelength; the effect of extinction due to dust along the line-of-sight is a familiar example. Such intra-population non-linear variations are not optimally characterised via PCA/NMF/MFICA analyses and we have therefore applied an empirical large-wavelength scale correction to the overall shape of the quasar spectra prior to deriving components and generating reconstructions of individual spectra. Essentially, the individual spectra are given the same overall shape and we term the process 'morphing' throughout the Chapter. The application of the large-scale multiplicative shape-morphing has the advantage of reducing the number of components required to produce a reconstruction of specified accuracy. A full description of the procedure is given in Section 2.4.

To generate the components that allow spectrum reconstructions we have used MFICA decompositions (Højen-Sørensen *et al.*, 2002; Opper & Winther, 2005; Allen *et al.*, 2013). For a specified number of components, the MFICA works as well or better than any decomposition scheme currently used for astronomical spectra (Allen & Hewett, in preparation). As a result, relatively few components are required to produce reconstructions, making reconstructions of only partially complete spectra (as required for the BAL quasars) more stable.

The question of reconstruction reliability and stability for spectra with extensive missing regions, such as the underlying emission spectra for BAL quasars with troughs extending over a significant range in velocity, is key and discussed in some detail by Allen *et al.* (2011). In our analysis we are able to place priors on the component weights when reconstructing wavelength regions affected by BALs (particularly the C IV λ1549 emission and wavelength regions to the blue) using the properties of the individual quasar spectra unaffected by BAL troughs. In more detail, our novel scheme uses priors on the MFICA

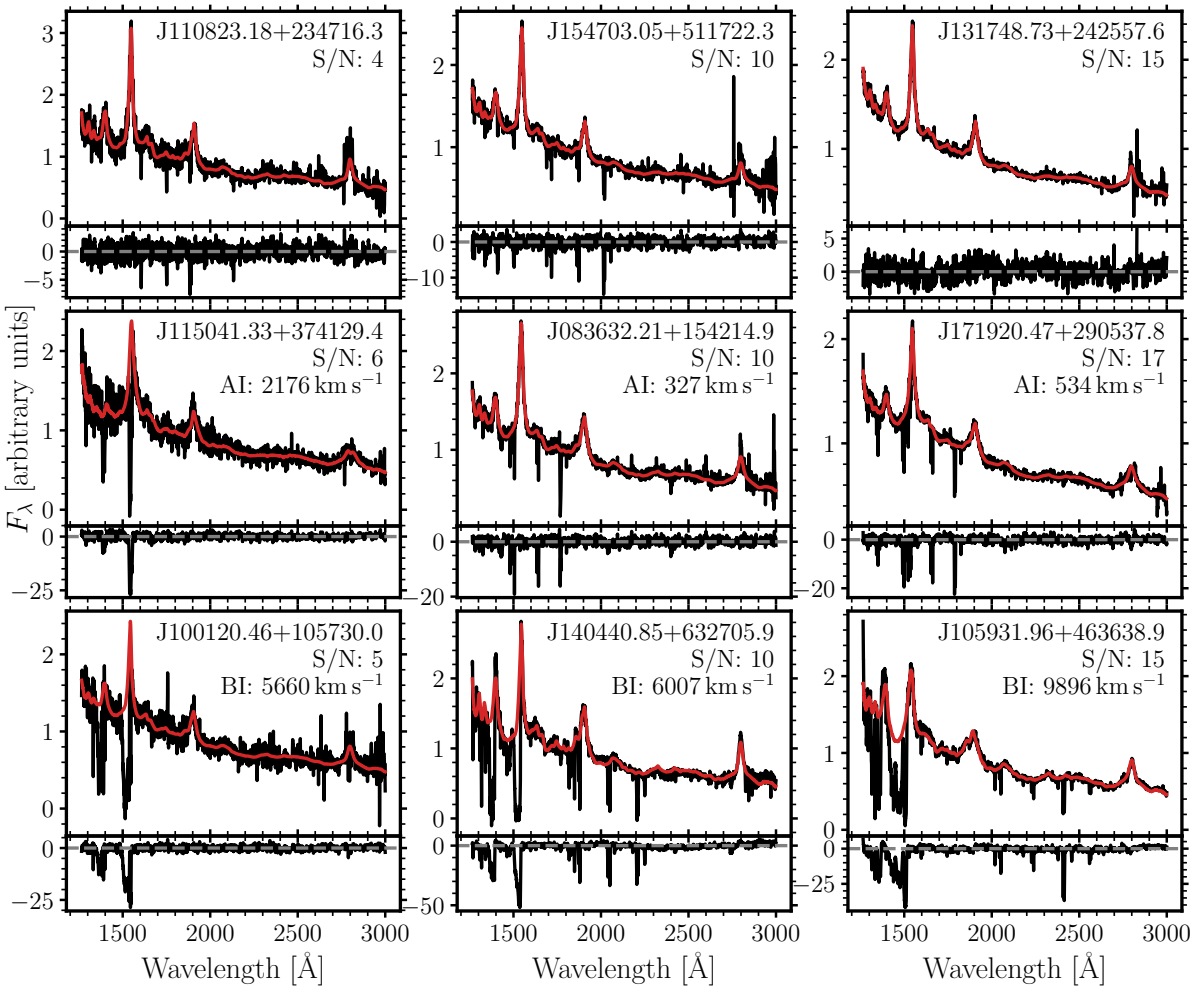

Figure 2.1: Example spectra (black; smoothed with the variance-weighted five-pixel scheme) and reconstructions (red) showing the quality of the reconstructions across the full range of spectrum S/N. Also plotted, are the residuals (spectrum − reconstruction) divided by the spectrum noise at each pixel. Non-BAL quasars are plotted in the top row and classically-defined BAL quasars are in the bottom row. The middle row contains spectra with absorption too narrow to have positive balnicity index (BI) but with positive absorption index (AI). The spectrum S/N increases from left to right.

component-weights based on the properties of the C III] λ1908-Si III] λ1892-Al III λ1857 complex, which are closely related to the morphology of the emission in the 1200–1600 Å range as evident in fig. 11 of Richards *et al.* (2011).

Using the MFICA-component scheme, we have the ability to reconstruct 95 per cent of (non-) BAL quasar spectra to an accuracy[1] of 93 (94) per cent over wavelength ranges 1265–3000 Å. The procedure is described in detail in Section 2.4 but we provide a few example reconstructions in Fig. 2.1 to show the quality of the reconstructions achieved.

[1] Defined as the fraction of the (spectrum − reconstruction) residuals within 2σ where σ is the spectrum noise at each pixel.

2.3 Quasar sample

The quasar sample is based on the catalogue compiled from the fourteenth data release of the Sloan Digital Sky Survey (SDSS DR14Q; Pâris *et al.*, 2018), which contains ≃526 000 quasars. The Baryon Oscillation Spectroscopic Survey (BOSS) involved observations of galaxies as well as quasars to allow an investigation of the intervening Lyman-α forest absorption. Unlike the initial SDSS survey, which resulted in the Schneider *et al.* (2010) quasar catalogue drawn from the SDSS DR7, determination of a quantitative selection-function for quasars as a function of SED, redshift and magnitude was not attempted for the BOSS survey. As a consequence, completeness information for quasars (Richards *et al.*, 2002a) and BAL-quasars (Allen *et al.*, 2011) is not available. The situation is compounded by the fainter magnitude limit to which SDSS DR14 extends and the significant fraction of quasar spectra with very low signal-to-noise ratio (S/N).

Fortunately, for the comparative investigation presented here, it is not necessary to determine the detection probability $P_{qso}(\mathrm{SED},m,z)$ but only to ensure that the probabilities for BAL and non-BAL quasars are similar. The detectability of BAL-troughs decreases significantly as the spectrum continuum S/N decreases (Allen *et al.*, 2011). Only the most extreme BAL-quasars are, therefore, identifiable in the DR14 quasars that possess low continuum S/N. As the intention is to investigate the relationship between BAL-quasar absorption properties and their underlying emission-line properties, a minimum spectrum S/N-threshold for inclusion of quasars is adopted.

The majority of spectra included in the sample possess an average S/N≥5.0 threshold, per SDSS-spectrum pixel, over the rest-frame wavelength interval 1600–2900 Å (when Mg II λ2800 is present in the spectrum) or 1600–2000 Å (at higher redshifts).[2] Figure 2.2 plots the fraction of BAL and non-BAL quasars as a function of average S/N. As expected, the fraction of BAL quasars decreases at low-S/N.

The classification of quasars as HiBALs or non-BALs is based on the C IV $\lambda\lambda$1548,1551 emission line and the 25 000 km s^{-1} region blueward of the line (Section 2.5). Minimum redshifts of $z = 1.56$ for quasars with SDSS-III spectra (minimum $\lambda_{obs} \simeq 3600$ Å) and $z = 1.67$ for quasars that possess only spectra from DR7 (minimum $\lambda_{obs} \simeq 3800$ Å) are therefore adopted. The number of quasars with redshifts $z > 3.5$ whose spectra satisfy the S/N-threshold is small and a maximum redshift of $z = 3.5$ is also imposed. The sample of quasars satisfying the redshift-interval constraints and the spectrum S/N-threshold numbers ≃144 000. Our sample contains only the default spectra listed in DR14Q of quasars for which duplicate observations exist.

The estimation of systemic redshifts for quasars in the SDSS data releases has improved

[2] For ≃6 per cent of the sample the S/N≥5.0 threshold applies to more restricted wavelength intervals that include the low-ionisation Mg II and C III]-emission complex but none of the conclusions of the thesis depend on the inclusion/exclusion of the small percentage of such spectra.

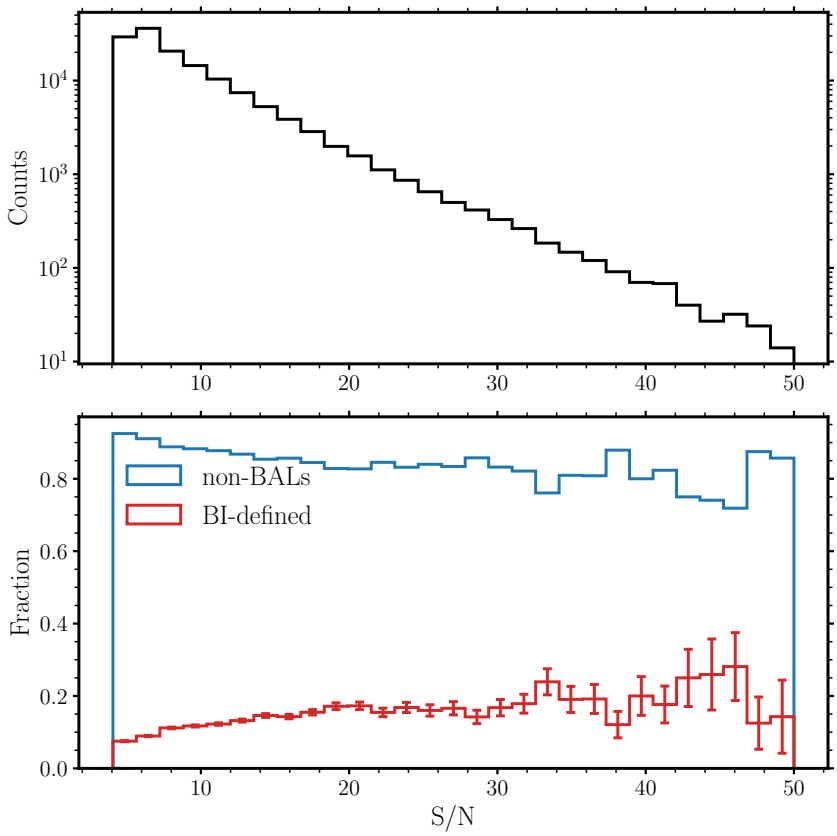

Figure 2.2: Top: Distribution of average S/N for our quasar sample. Bottom: fraction of BAL and non-BAL quasars as a function of S/N with Poisson errors on the BAL fraction. At each S/N bin, the fraction of BALs and non-BALs adds to unity. Note the drop in BAL quasars at low-S/N is due to the difficulty in detecting troughs in noisy spectra.

significantly since DR7 (Schneider *et al.*, 2010) and the reanalysis of Hewett & Wild (2010). Extensive discussion of the effectiveness of the improved schemes is contained in Pâris *et al.* (2017, 2018) and the implications for clustering investigations are reviewed by Zarrouk *et al.* (2018). Notwithstanding the improvements, our own investigations demonstrate that substantial advances in the accuracy of systemic redshift estimates can be made relative to those included in Pâris *et al.* (2018).

Here, quasar redshifts are calculated using spectrum reconstructions based on a separate mean-field independent component analysis scheme (Allen *et al.*, 2013) with the redshift as a free parameter. The reconstructions are deliberately confined to the 1600–3000 Å region, *thereby excluding the C IV emission line*. The stability of the rest-frame wavelengths of the low-ionisation emission lines including O I λ1304+Si II λ1307, C II λ1335, Al III λ1857, Si III] λ1892, C III] λ1908 and Mg II λ2800, independent of the large range of ultraviolet SEDs, including high-ionisation emission-line blueshifts, is used to verify the effectiveness of the redshift determinations. In terms of the quasar rest-frame velocity differences, in excess of 35 000 quasars show a shift of $>$500 km s^{-1} between the DR14 and our new redshifts, with $\simeq$9800 quasars possessing shifts of $>$1000 km s^{-1}. While the use of the new redshifts has an impact on the effectiveness of the spectral reconstructions and which objects are classified

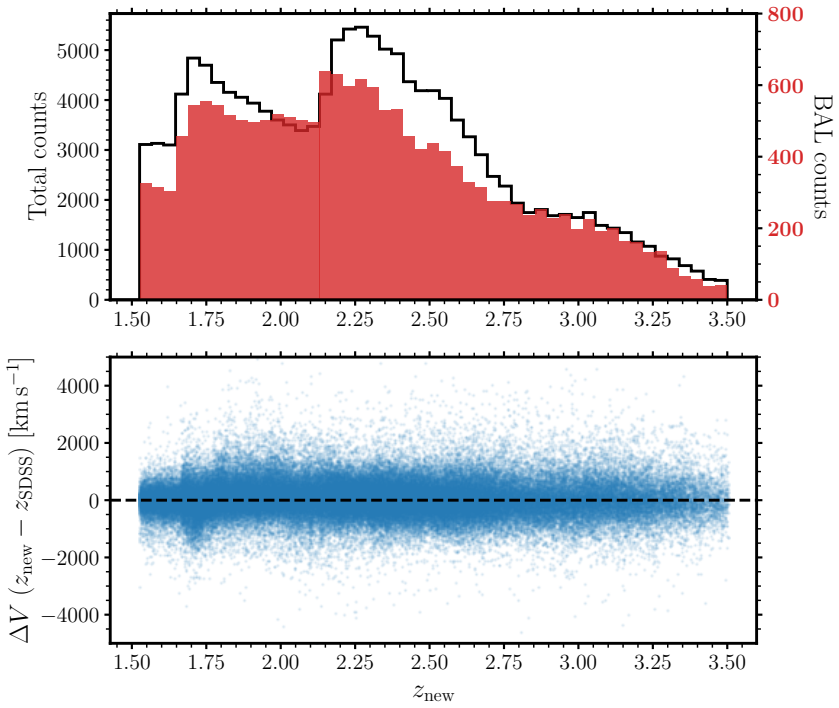

Figure 2.3: Comparison of DR14Q redshifts, $z_{\rm SDSS}$, with our new redshifts, $z_{\rm new}$. Top: distribution of corrected redshifts of all quasars in our base sample (black; left-hand axis) and the sub-sample of classically-defined BAL quasars (red; right-hand axis; see Section 2.5). Bottom: difference between $z_{\rm new}$ and $z_{\rm SDSS}$, as a velocity in the rest-frame, as a function of $z_{\rm new}$.

as BAL-quasars (details of which are presented in Section 2.5), none of the statistical results presented in Section 3.2 change if the DR14 redshifts are employed.

The redshift distribution of the base 143 664-quasar sample to be analysed is presented in Fig. 2.3 along with a comparison of the SDSS DR14 redshifts with our new values. The redshift distribution of our whole sample reflects that of SDSS DR14Q (see fig. 5 of Pâris *et al.*, 2018). The distribution of BAL and non-BAL quasars as a function of redshift differ (top panel) and Allen *et al.* (2011) performed a careful examination of the dependence on BAL quasar detection as a function of redshift. The SDSS quasar sample is not complete and selection is based on the photometric properties of the quasar targets as well as some selection of FIRST sources. The BAL quasar colours as a function of redshift will differ from those of the non-BAL quasars due to the presence of significant absorption and so their selection will also differ. Additionally, BAL quasars exhibiting more dust reddening than non-BAL quasars (e.g., Reichard *et al.*, 2003; Allen *et al.*, 2011) could result in a lower BAL than non-BAL quasar detection rate at a given redshift due to preferentially losing higher $E(B-V)$ sources as redshift increases.

The first stage in the analysis is to generate reconstructions for each of the quasar spectra as described in the next section.

2.4 Quasar spectra reconstructions

The rest-frame wavelength range selected for the investigation is 1260–3000 Å. The long-wavelength limit ensures the inclusion of the Mg II λ2800 emission line for quasars with redshifts up to $z \simeq 2.4$ in the DR14 spectra. The short-wavelength limit allows BAL troughs associated with the O IV+Si IV emission at 1400 Å to be included as well as emission due to the low-ionisation species O I λ1304+Si II λ1307 and C II λ1335. The strong BAL absorption associated with the N V λ1242 emission and Lyman-α emission are in principle also of interest. The presence of absorption from the Lyman-α forest, however, complicates the problem of reconstructing the intrinsic quasar SEDs, particularly where the aim is to utilise only a small number of components to achieve the reconstructions.

The spectral resolution of the data used in this thesis is ≈2000 and the velocity resolution ∼150 km s^{-1} which is appropriate for the investigations presented throughout: we are considering C IV emission blueshifts spanning ∼5000 km s^{-1}, BAL absorption features with widths > 450 km s^{-1}, and NAL FWHM > 160 km s^{-1}.

2.4.1 Quasar spectrum shape standardisation: 'morphing'

Unlike the original SDSS DR7 quasar spectra the observational constraints relating to the placement of the fibres for the BOSS DR14 observations mean that differential atmospheric refraction has an effect on the spectrophotometry, most significantly at blue wavelengths. In detail, one of the primary goals of BOSS was to observe the Lyα forest in $z = 2$ quasars such that increased S/N at blue wavelengths was prioritised over other wavelength ranges and achieved by centering the target's fibre at 4000 Å. The spectrophotometric standard stars were however centred at 5400 Å. The offset from the fibre's position due to refraction is greater for blue wavelengths compared to red wavelengths and the offsets between quasar target and standard stars are the primary cause of errors in the quasar spectrophotometry. An extensive discussion of the effect and a scheme for performing post-reduction corrections to the spectrophotometry is presented in Margala *et al.* (2016).

The differential atmospheric refraction effects give rise to ±10 per cent multiplicative variations in the spectrophotometry. Variations in the amount of dust extinction affecting the ultraviolet continuum and emission-line fluxes from quasar to quasar also produce 'intrinsic' multiplicative differences in the large-scale shape of the observed spectra. As heralded in Section 2.1 the presence of such wavelength-dependent multiplicative changes complicates any scheme whereby spectra are reconstructed using linear-combinations of fixed 'components'. The first stage in the spectrum reconstruction procedure is therefore to ensure that all the individual quasar spectra possess the same overall shape. This morphing process is effective at removing the effect of dust; however, SDSS is biased against even moderately red quasars and so the morphing is not required to correct extreme reddening.

The reference SED used in the spectrum-shape morphing is a model quasar spectrum as described in Maddox *et al.* (2012). By construction the model reproduces the ultraviolet SED of luminous, unreddeded quasars and a mean spectrum from the SDSS DR7 quasar catalogue would work equally well.

The shape-morphing proceeds as follows. Eight MFICA components (Section 2.4.2), to allow spectrum reconstructions, are generated using ≃4000 spectra[3] of non-BAL quasars with a range of spectrum shapes which have *not* been shape-morphed. Individual spectrum reconstructions are then calculated using the masking procedure (to exclude wavelengths affected by both broad and narrow absorption features) described in Section 2.4.3 for *all* spectra. The scheme thus allows spectra with high-equivalent width BAL troughs to be shape-morphed while ensuring that all spectra are processed in the same way. The resulting reconstructions capture the overall large-scale shape of the spectra. The continuum in the reference model and each individual reconstruction is then interpolated across the locations of the strongest emission lines. The ratio of the reconstruction continuum and reference model is calculated and median filtered using a 601-pixel (≃250 Å) window. The original spectrum is then multiplied by the resulting smooth function (see top two rows of Fig. 2.4 for examples of the morphing procedure). Approximately 76 per cent of spectra are modified by factors of less than ±10 per cent over the full wavelength range. Should it be required, the individual spectra and the reconstructions can be straightforwardly 'unmorphed'.

2.4.2 MFICA-component generation

Samples of morphed spectra are used to calculate the components to be employed in the definitive spectrum reconstructions. First, bad pixels identified in the SDSS reduction pipeline are masked along with strong sky lines (e.g., the 5578 Å [O I] emission) in the blue. Narrow absorption features are also masked by applying a 61-pixel median filter to define a pseudo-continuum and masking the pixels where the spectrum lies below this pseudo-continuum by at least 3σ, where σ is the spectrum noise. Three pixels blueward and redward of each such pixel are also masked.

The MFICA-components are calculated (see Allen *et al.*, 2013) using a sample of ≃4000 quasar spectra with complete coverage of the 1260–3000 Å wavelength range[4] and without

[3] MFICA components generated using different samples of ≳1000 spectra, selected to span the dynamic range in properties of interest (e.g. emission-line equivalent width), are extremely similar. The small-scale, pixel-to-pixel, 'noise' in the components does, however, reduce as the number of spectra employed is increased. The DR14-quasar sample is large and all components generated for the investigation are calculated using ≃4000 spectra, with S/N≥8 per pixel and very few masked/bad pixels. The components, and therefore the conclusions, would not change significantly if different, appropriately chosen, samples of 4000 spectra were used.

[4] The quasar spectra have redshifts in the interval $z \simeq 2.0-2.3$.

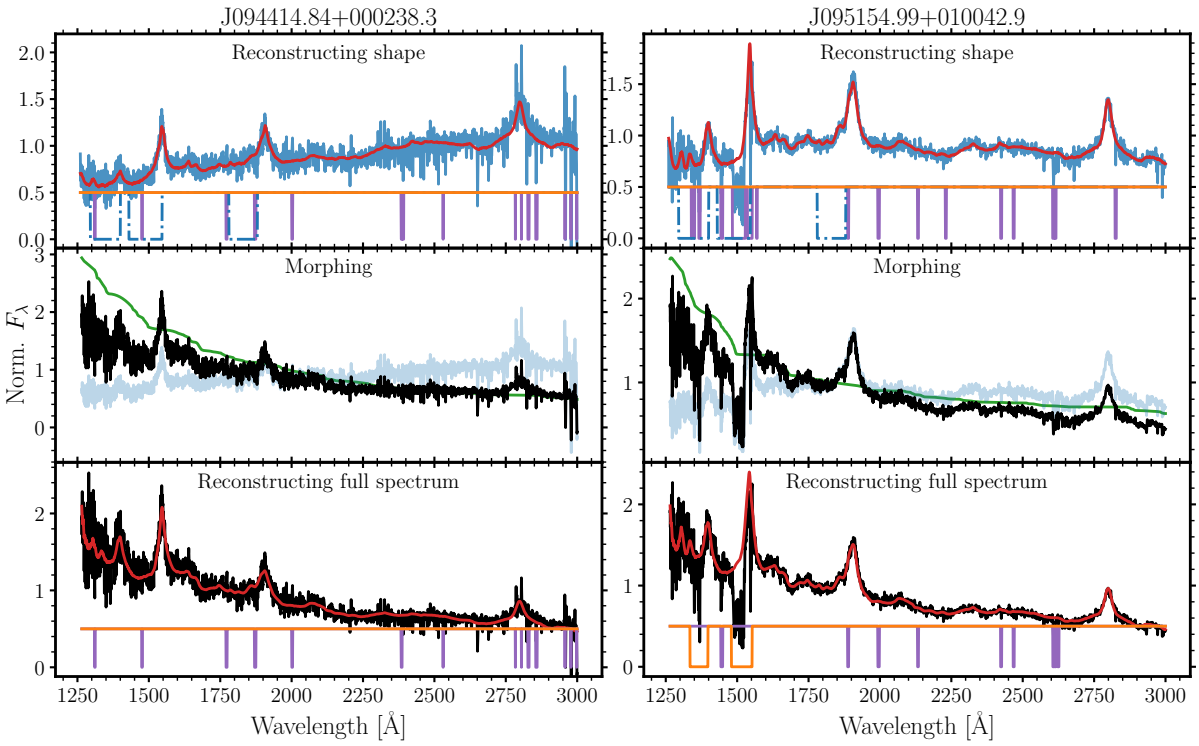

Figure 2.4: A non-BAL quasar spectrum (left) and BAL quasar spectrum (right) illustrating, from top to bottom, the main stages in the MFICA-reconstruction procedure. The two quasar spectra both show significant differences in shape compared to the majority of the quasar population. The original spectra in the top panels (blue) are reconstructed using the BAL-masking routine and the MFICA-components that account for large-scale spectrum shape information. The initial BAL mask (dotted blue) and the iteratively-produced final BAL mask (solid orange) are also shown, along with the narrow absorption-line mask in purple. From the reconstructions in the top panels (red), the morph arrays are produced (green, middle panel; see text for details). The original spectra are multiplied by the morph arrays to produce the black spectra in the middle panels which now have the same overall spectral shape as the master quasar-template spectrum. The morphed-spectra are then fitted with MFICA-derived components to reconstruct the 1260–3000 Å wavelength interval. The morphed spectra (black), component reconstructions (red) and final BAL- and narrow-absorption-mask (orange and purple respectively) are shown in the bottom panels. It is from such reconstructions that all emission-line and continuum-derived parameters are calculated.

any BAL-troughs. Linear combinations of the resulting 10-components reproduce ≃99 per cent of the non-BAL quasars, with (spectrum-reconstruction)/reconstruction, the average fractional error, less than 2 per cent. Systematic deviations are greatest for quasars with the most extreme C IV emission equivalent widths. For the purpose here, the form of the MFICA-components is not important, the goal is simply to reproduce the quasar SEDs accurately. Two further sets of components were therefore generated using ≃2000 spectra with C IV EW >40 Å (7 components[5]) and ≃2000 more with C IV EW < 20 Å (10 components) specifically to allow more accurate reconstructions of spectra with extreme emission-line properties. Each quasar with weak or strong C IV EW – measured from an initial reconstruc-

[5]The number of components required is fewer than that for the initial set because of the reduced dynamic range in SED-properties.

tion using the standard set of components – is fitted with the corresponding extreme-C IV components and from the standard and the extreme reconstructions, the best is chosen based on a χ^2 measurement.

2.4.3 Fitting the whole quasar sample

The routine for fitting the MFICA components utilises the Python package LMFIT (Newville *et al.*, 2014) for non-linear least squares minimisation using the Levenberg-Marquardt algorithm with priors (L-BFGS-B). The priors adopted for the component weights are based on the strong correlation between the morphology of the C III]-complex and that of the C IV line (see Appendix A for details). Reconstruction of the intrinsic C IV emission when much of it has been absorbed or masked is greatly improved by the use of the priors on the component weights (see discussion below). Figure 2.4 illustrates the full fitting procedure.

In addition to the shape morphing and masking of the narrow absorption lines (NALs), in order to successfully fit BAL quasars with the MFICA components, it is crucial that the wavelength regions of the spectra that are affected by BAL troughs are masked. For HiBALs, these are regions blueward of 1400 Å for Si IV+O IV and 1549 Å for C IV. Troughs differ greatly in velocity width and position (up to thousands of km s^{-1}) across BAL quasar spectra and to avoid masking more or less of each spectrum than necessary an optimal mask for each spectrum was defined in a similar manner to Allen *et al.* (2011). The routine also takes into account absorption redward of the BAL regions presented above resulting from errors in redshift. The steps applied to the morphed spectra, with flux F_λ and noise σ, are as follows:

1. The initial mask covers regions of the spectra just blueward of the peak of the emission lines where troughs are likely to appear: 1295–1400 Å for Si IV+O IV, 1430–1546 Å for C IV and 1780–1880 Å for Al III.

2. The components are then fitted to the unmasked parts of the spectrum.

3. A new mask is created by considering every pixel in turn. For pixel *cpix*, if the majority of the pixels in [*cpix*−30,*cpix*+30] have (reconstruction − spectrum F_λ) $> N\sigma$ then pixel *cpix* is masked. Initially, $N = 2$.

4. Once the pixels have been identified, an extra 10 pixels (∼4 Å at 1549 Å) are masked blueward and redward of each of the masked regions.

5. The BAL troughs associated with the Si IV+O IV λ1400 emission are weaker than those associated with C IV λ1549. For much of the quasar redshift range the troughs lie at wavelengths where the spectrum S/N is lower and the masking algorithm is not always fully effective. To ensure absorption associated with Si IV+O IV is masked effectively, the masked region from C IV in velocity-space is applied to the Si IV region, in addition to pixels masked in the iterative process.

Steps 2 through 4 are repeated until the mask converges, normally after two or three iterations. When there is no mask convergence after 10 iterations, the process is started from scratch at step 1 with $N = N + 0.25$ up to $N = 4$, at which point the spectrum is flagged as not having converged.

In order to quantify our ability to accurately reconstruct the BAL quasar spectra we performed tests using 7000 non-BAL spectra covering the full observed-range in C IV emission properties. In detail, we masked portions of the non-BAL quasar spectra across wavelength ranges where BAL troughs appear in the BAL quasar spectra matched in C IV emission properties and S/N and then reconstruct the spectra. To quantify the differences between the spectra and the reconstructions we measure the cumulative difference in the C IV line between 1400 and 1600 Å as a fraction of the C IV EW as measured from the spectrum:

$$f(\mathrm{EW}) = \frac{1}{\mathrm{EW}} \sum \frac{(\mathrm{spectrum} - \mathrm{reconstruction})}{\mathrm{continuum}} \Delta\lambda. \tag{2.1}$$

When fitted without masking, 97 per cent of the 7000 non-BAL quasar spectra had $f(\mathrm{EW}) < 10$ per cent and a median $f(\mathrm{EW})$ of only 2 per cent. The investigation confirmed the importance of employing priors on the component weights (see Appendix A). Unsurprisingly, when the reconstructions are relatively poorly constrained, due to extended masked regions or low spectrum S/N, the use of priors for the component weights is essential. $f(\mathrm{EW})$ is anti-correlated with S/N but only rises to a median of 6 per cent for $\mathrm{S/N} \simeq 5$.

When the spectra were masked to simulate BAL quasars but the priors were not implemented, only 78 per cent of the sample had $f(\mathrm{EW}) < 10$ per cent even though the median $f(\mathrm{EW})$ increased to only 4 per cent. Upon employing the priors to fit the masked non-BAL quasar spectra, the percentage of spectra with $f(\mathrm{EW}) < 10$ per cent increased to 85 per cent and maintained a low median $f(\mathrm{EW})$ of 4 per cent. Statistically, the average gain of using the priors appears small for the sample as a whole. However, for the relatively small fraction of spectra with extended masks (corresponding to quasars with large BI values) the reconstructions improve significantly. For the actual BAL-spectra, in the iterative process of fitting the components and defining the mask, the component weight priors prevents a bias towards narrower BAL masks and the presence of 'dips' in the reconstructions where the troughs are present.

The use of priors derived from the properties of the C III]-complex emission is predicated on the assumption that the relationship between the C IV emission properties and the C III]-complex emission is the same for both BAL and non-BAL quasar populations. While, by definition, it is not possible to test the assumption directly for individual BAL-quasars it is possible to perform a powerful test for the BAL-population as a whole. The results, presented in Appendix B, demonstrate that the assumption regarding the similarities of emission-line properties for the BAL and non-BAL quasar populations is true to very high accuracy.

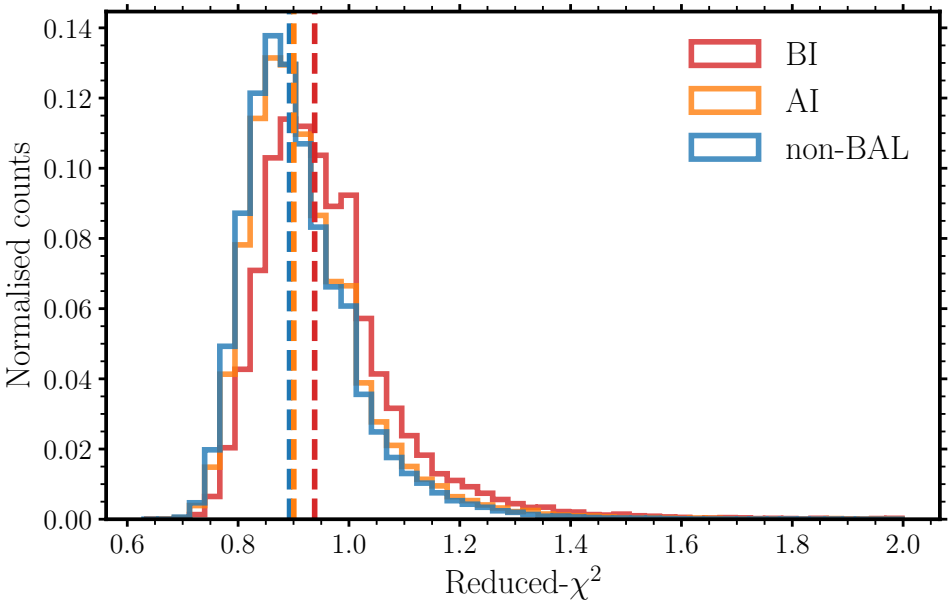

Figure 2.5: Reduced-χ^2 distributions for the non-BAL (blue), AI (orange) and BI quasars (red). See Section 2.5 for a description of the various BAL definitions. The vertical dashed lines mark the median values for each sub-sample.

Visual inspection of the sparsely occupied regions at the extremes of the C IV emission EW vs blueshift space (Section 3.2), specifically at i) large negative C IV emission blueshift (<-1200 km s^{-1}), ii) small C IV EW (EW < 10 Å) and iii) the region at the bottom-left of the C IV emission space, with relatively high negative C IV emission blueshift and low C IV EW ($\log_{10}$(C IV EW) < $-2.3077 \times 10^{-4} \times$ C IV blueshift + 1.3231) reveal a number of intrinsically pathological quasar spectra and some reconstructions that are clearly sub-optimal. The number of spectra in all three regions is small: 3027 spectra or 2 per cent of the quasar sample. 2283 of the spectra removed in this way are classed as non-BAL quasars by the trough parameterisation code (see Section 2.5) but upon visual inspection include a significant fraction of LoBAL and FeLoBAL objects and their classification (and large, negative blueshift) is often due to insufficient masking. Spectra in these regions are, therefore, excluded from subsequent analysis. A further 189 spectra were excluded because the reconstruction scheme failed to converge due to poor morphing or the reconstructions had reduced-$\chi^2 > 2$. The excluded spectra were distributed evenly across C IV emission space.

The distribution of reduced-χ^2 values for the spectrum reconstructions in our sample is presented inf Fig. 2.5 for the BAL and non-BAL quasars. The median reduced-χ^2 of the non-BAL spectra is 0.89 while for the BAL quasars, divided into AI and BI sub-samples (see Section 2.5) is 0.90 and 0.94, respectively. The covariance between neighbouring pixels in the SDSS spectra reduces the degrees of freedom and we have not accounted for this in our calculation of the reduced-χ^2 such that the distributions in Fig. 2.5 all peak below unity. The exclusion of reconstructions with reduced-$\chi^2 > 2$ was chosen by visually inspecting the reconstructions.

For the remaining 140 448 quasars, each spectrum has the same overall spectral shape and a continuum plus emission line reconstruction is available. An associated mask array contains the wavelengths of pixels where absorption has been identified. Quantification of the absorber properties and the definition of sub-samples of BAL-quasar spectra is now possible.

2.5 Defining the BAL quasar population

The classical definition of a BAL quasar is a quasar with non-zero balnicity index (BI) as defined by Weymann *et al.* (1991):

$$\mathrm{BI} = \int_{3000}^{25000} \left(1 - \frac{f(V)}{0.9}\right) C \, \mathrm{d}V \tag{2.2}$$

with $C = 1$ when $f(V) < 0.9$ continuously for at least 2000 km s^{-1}, otherwise $C = 0$.

Hall *et al.* (2002), seeking a measure to incorporate a more liberal definition of 'absorption', introduced the absorption index (AI) to include absorption closer to the systemic redshift and as narrow as 450 km s^{-1}. Here, $C = 1$ when $f(V) < 0.9$ continuously for at least 450 km s^{-1}.

$$\mathrm{AI} = \int_{0}^{25000} \left(1 - \frac{f(V)}{0.9}\right) C \, \mathrm{d}V. \tag{2.3}$$

Figure 2.6 illustrates the BI and AI calculations for an example spectrum with two BI troughs (1 and 2) and a third AI-only trough. The third trough is wider than 2000 km s^{-1} but not all of this absorption exists above the minimum 3000 km s^{-1} velocity to satisfy the BI conditions.

The DR14Q catalogue contains measurements of BI but the updated redshifts used in this investigation as well as our own reconstructions mean some spectra change classification based on the BI and AI values. We remeasured the BI and AI using Python code written by Rogerson (2019) with minor modifications, allowing us to use our reconstructions to produce the normalised spectra, $f(V)$, in Equations 2.2 and 2.3. Each pixel in the normalised spectra has a value calculated using the inverse-variance weighted flux within a five-pixel window, thereby reducing the effect of single-pixel noise spikes. The code also calculates a variety of individual absorption trough measurements including minimum and maximum ejection velocities and trough depth. Discussion of the additional trough measurements is included in Section 3.2.4.

We compare our BI values with those in the DR14Q catalogue in Fig. 2.7. The redshift changes have primarily affected narrow troughs near to the minimum (3000 km s^{-1}) and maximum (25 000 km s^{-1}) velocity boundaries used for the BI measurements; more or less

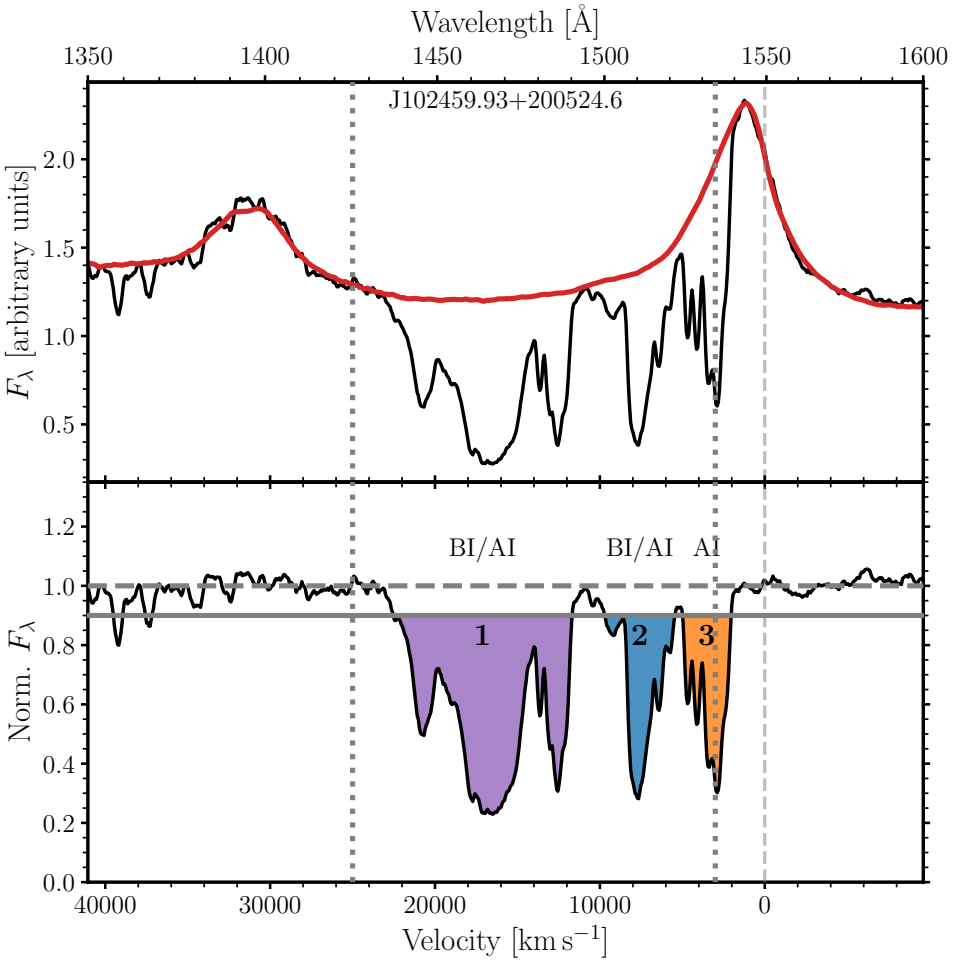

Figure 2.6: Example BAL quasar spectrum and reconstruction (top panel) alongside the normalised spectrum (bottom panel) in velocity space, inverse-variance weighted with a window of five pixels. The grey, dotted vertical lines mark the minimum and maximum velocities considered in the calculation of BI. The dashed, grey line at zero velocity marks the laboratory wavelength of C IV from which the AI measurement is calculated. Troughs 1 and 2 (purple and blue, respectively) have BI (also AI) = 4500 and 1200 km s^{-1} with both troughs below 0.9 contiguously for over 2000 km s^{-1} (10 800 and 4140 km s^{-1} wide, respectively). The third trough satisfies the AI conditions (AI = 1100 km s^{-1}) but not BI due to only 1960 km s^{-1} of the trough width occurring above 3000 km s^{-1}, although significant absorption at velocities below 3000 km s^{-1}exists with a total trough width of 2900 km s^{-1}.

of the absorption is shifted into the BI velocity-window. In particular, if the C IV emission is considered when calculating the redshifts of BAL quasars with abrupt onset of absorption in the blue half of the line, these quasars can have systematically higher redshifts in SDSS. Our statistically lower redshifts lead to less of the absorption appearing at velocities > 3000 km s^{-1} and we can calculate lower or even zero BI.

Differences in the continuum level of the component reconstructions can also result in classification switches. Here, changes result as the contribution of absorption to the BI calculation depends sensitively to the absorption-depth threshold, $f(V) < 0.9$ continuously for 2000 km s^{-1}. In Fig. 2.8 we illustrate these effects by considering the 2359 spectra for which DR14Q listed zero BI whereas we measure BI>0. As a result, using the BI-definition

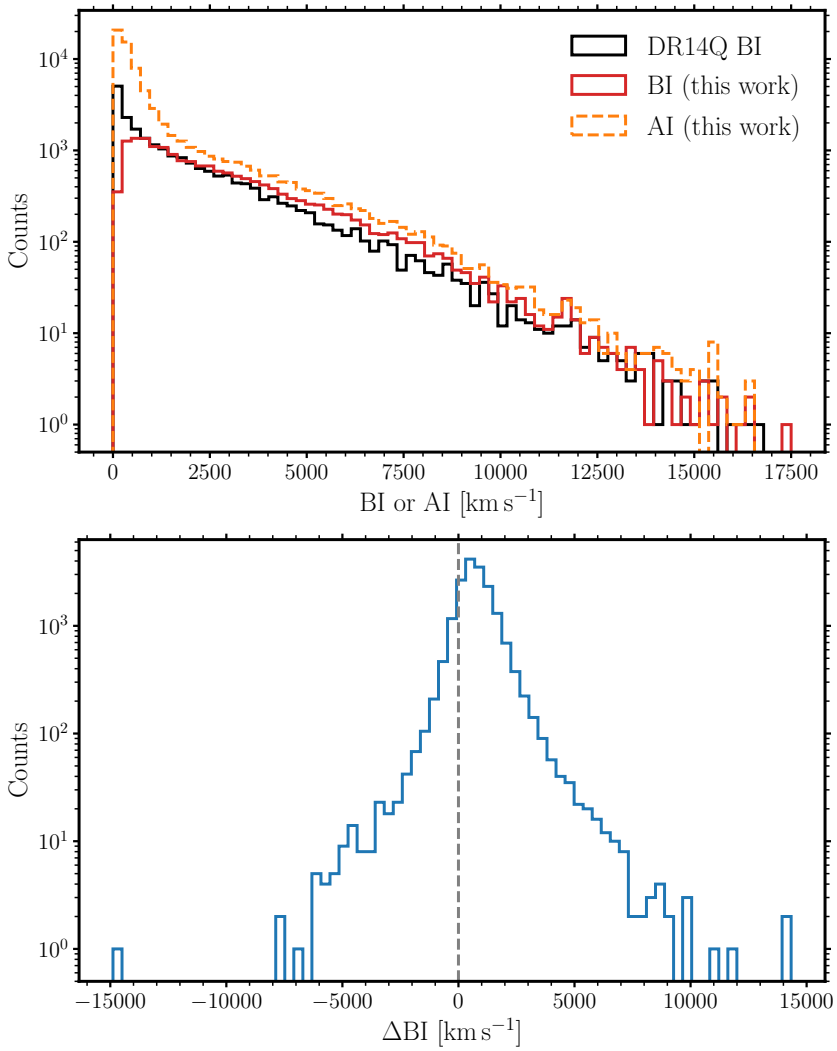

Figure 2.7: Comparison of the BI_{DR14Q} values with our BI values. Top: counts of BI_{DR14Q} and BI and AI calculated for this investigation. Bottom: $\Delta BI = BI - BI_{DR14Q}$. For visualisation purposes, we have removed BI=0 or AI=0 quasars from each of the histograms. In this work, the calculated BI values are, on average, 700 km s^{-1} larger than those in DR14Q. Below 1000 km s^{-1}, there is a decrease in the number of BI-defined BAL quasars according to our measurements and compared to the DR14Q values, which we believe is a result of changes in redshift. Above 1000 km s^{-1} there are more BI-defined quasars due to higher continua in our spectrum reconstructions.

we gain 1503 BAL quasars while the 2359 objects in Fig. 2.8 become non-BAL quasars.[6]

We are also able to compare the AI measurements to those in DR12Q BAL catalogue (Pâris *et al.*, 2017). Trump *et al.* (2006) define the reduced-χ^2 for each AI trough in order to remove false-positive troughs which are the result of noise:

$$\chi^2_{\text{trough}} = \sum \frac{1}{N} \left(\frac{1 - f(V)}{\sigma} \right)^2 \tag{2.4}$$

where N is the number of pixels in the trough. We adopt the requirement for $\chi^2_{\text{trough}} \geq 10$

[6]While we are confident regarding the use of improved redshifts and reconstructions, none of the results presented in the next section depend on the exact definition of the BAL-quasar sample.

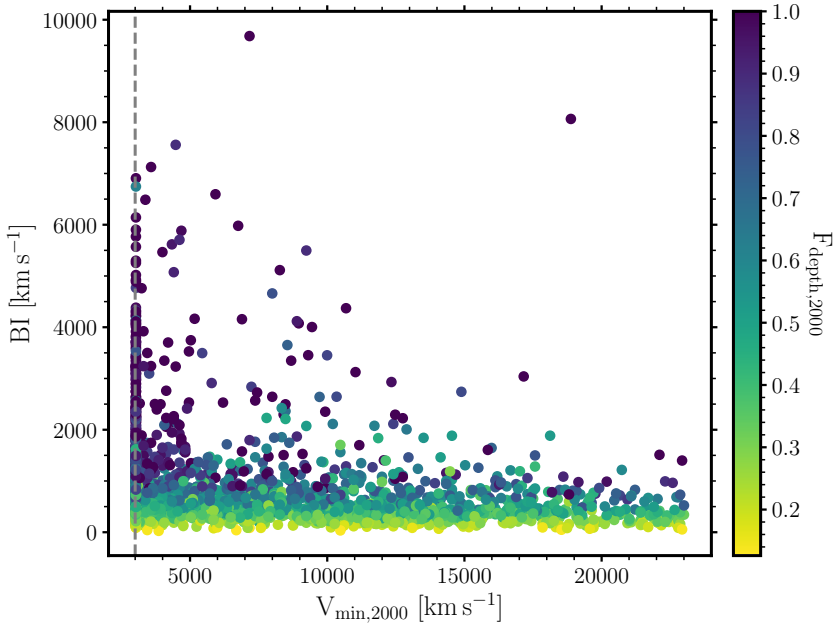

Figure 2.8: Our BI values against our calculations of the minimum ejection velocity with points coloured by trough depth for the 2359 spectra with BI>0 but zero $\mathrm{BI_{DR14Q}}$. Most of these spectra have minimum velocities close to the 3000 km s^{-1} cut-off where redshift differences are responsible. The spectra with large $V_{\rm min}$ have shallow troughs and changes in reconstruction due to continuum reconstructions dominate.

as Trump *et al.* (2006) suggest and Pâris *et al.* (2017) implement. Differences in the sample of DR12Q AI-defined objects and our sample arise from the changes in redshift and continuum level as for the BI-defined samples. In addition, for the spectra included in DR12Q, our AI-defined sample includes a significantly larger number of quasars. We believe the difference is the result of Pâris *et al.* (2017) presenting the AI measurements only for spectra flagged as BAL-quasars through visual inspection. The interpretation is supported by Pâris *et al.* (2017) noting that they have an additional ≃27 000 spectra with non-zero AI not reported in the DR12Q BAL catalogue, which itself contains just ≃22 000 quasars with AI>0.

We exclude 1668 LoBAL quasars from our sample (in addition to those in outlying regions of C IV emission space), defined by a positive $\mathrm{BI_0}$ of Al III troughs where $\mathrm{BI_0}$ is a modified balnicity index where the integral in Equation 2.2 starts at 0 km s^{-1}. An additional 18 FeLoBAL quasars are also removed from the sample by means of the BAL mask (Section 2.4.3): spectra with more than one third of pixels redward of C IV masked are flagged as potential FeLoBAL quasars. The final sample of quasars thus numbers 138 762, with 73 806 of those defined as non-BAL quasars, 14 887 classically-defined BAL quasars (positive BI) and a further 50 069 with positive AI but a BI of zero.

2.5.1 Two AI populations

Upon plotting the distribution of AI in log space (Fig. 2.9), we observe two populations not unlike Knigge *et al.* (2008, see their fig. 1), although note that those authors adopt the AI

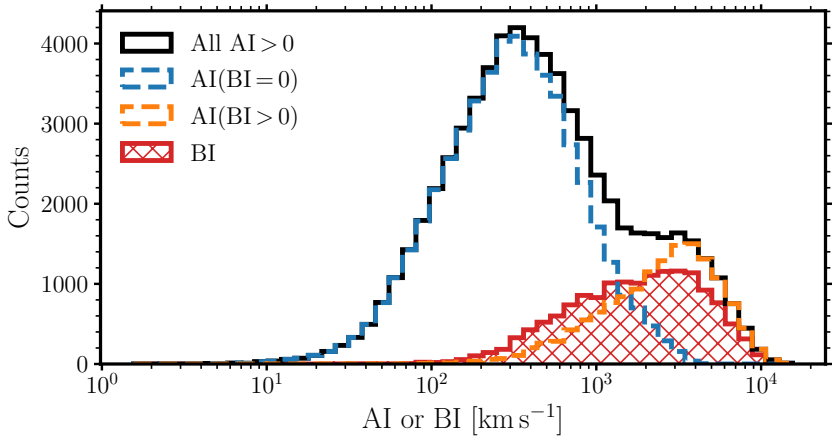

Figure 2.9: AI and BI distribution for quasars with AI>0 (black). The x-axis is the BI or AI measurement described in Equations 2.2 and 2.3. The AI population is divided into quasars with zero BI (blue; left column of Fig. 3.9 where we discuss the trough parameters) and non-zero BI (orange; middle column of Fig. 3.9). The form of the AI-distribution suggests strongly that two populations of absorbers contribute. The BI distribution for quasars with BI>0 is also plotted (red, hatched; right column of Fig. 3.9) which overlaps with the AI(BI>0) population since many of the same spectra appear in both populations. The AI(BI>0) distribution is shifted to the right with respect to the BI distribution due to the inclusion of absorption below 3000 km s^{-1}.

prescription of Trump *et al.* (2006) which includes only absorption wider than 1000 km s^{-1} and extends the 25 000 km s^{-1} maximum velocity to 29 000 km s^{-1}. The large-AI population of quasars is dominated by spectra with positive BI (AI(BI>0); e.g., troughs 1 and 2 in Fig. 2.6) whereas the classically-defined non-BAL quasars dominate the low-AI population (AI(BI=0)). The distribution of BI and AI(BI>0) overlap since many of the spectra, thus with the same trough measurements, appear in both samples. The shift of the AI(BI>0) toward larger values as compared to the BI values is a result of the minimum velocity cut-off on the BI. The number of quasars in the AI(BI>0) population is also lower than the number in the BI population due to the $\chi^2_{\rm trough} > 10$ requirement of the AI troughs. The properties of the AI(BI=0) and AI(BI>0) samples are discussed later in Section 3.2.4.

2.6 Conclusions

Using mean-field independent component analysis, we have successfully reconstructed the ultraviolet spectra of both high-ionisation BAL and non-BAL quasars from the SDSS DR14 quasar catalogue with redshifts $1.56 \leq z \leq 3.5$ and S/N ≥ 5; $\simeq$144 000 quasar spectra in total (Fig. 2.1). Using our reconstructions and employing improved redshifts (Fig. 2.3), we have redefined the BAL quasar population (Fig. 2.7) and found evidence for two AI-defined populations, in agreement with Knigge *et al.* (2008): BI=0 and BI>0 quasars (Fig. 2.9).

The spectrum reconstructions and BAL classifications are critical for the investigations presented in the remaining chapters of this thesis.

Chapter 3

BAL and Non-BAL Quasars

Summary

Using the quasar spectrum reconstructions introduced in the previous Chapter we investigate the outflow properties, evident both in absorption and emission, of high-ionisation BAL and non-BAL quasars. The reconstructions allow the kinematic properties of the C IV λ1549 emission line to be compared directly for both non-BAL *and* BAL quasars. C IV emission blueshift and equivalent-width (EW) measurements are thus available for both populations. Comparisons of the emission-line and BAL trough properties reveal strong systematic correlations between the emission and absorption properties. The dependence of quantitative outflow indicators on physical properties such as quasar luminosity and luminosity relative to Eddington-luminosity are also shown to be essentially identical for the BAL and non-BAL populations. There is an absence of BALs in quasars with the hardest spectral energy distributions (SEDs), identified by the presence of strong He II λ1640 emission, large C IV λ1549-emission EW and no measurable blueshift. In the remainder of the C IV emission blueshift versus EW space, BAL and non-BAL quasars are present at all locations; for every BAL quasar it is possible to identify non-BAL quasars with the same emission-line outflow properties and SED-hardness. The co-location of BAL and non-BAL quasars as a function of emission-line outflow and physical properties is the key result of our investigation, demonstrating that (high-ionisation) BALs and non-BALs represent different views of the same underlying quasar population.

This Chapter is based on the article:

A. L. Rankine, P. C. Hewett, M. Banerji, G. T. Richards

BAL and non-BAL quasars: continuum, emission and absorption properties establish a common parent sample

MNRAS, Volume 492, Issue 3, March 2020, Pages 4553–4575

All work presented in this Chapter is my own, completed with guidance and support from my co-authors.

3.1 Introduction

Following an original observation by Gaskell (1982), over the past decade increasing attention has been devoted to quantifying the outflow signatures evident from the high-ionisation emission lines in the ultraviolet (e.g., Sulentic *et al.*, 2000; Leighly, 2004; Richards *et al.*, 2011) – particularly the blueshifting of the prominent C IV λ1549 emission.

In a number of models the properties of outflowing material are orientation dependent, e.g., relative to the black-hole spin axis, and the probability a quasar is observed to possess BAL features depends on viewing angle. There is, however, still no agreement on whether BALs do arise as the result of viewing angle or represent a particular phase in the fuelling-outflow cycle, with the wind potentially clearing the absorbing gas from the galaxy as the quasar transitions to a non-BAL quasar.

The focus of this Chapter are the far more common HiBAL objects amongst the BAL quasar population and we exclude consideration of the much smaller fractions of LoBAL and FeLoBAL quasars. Careful comparisons of the emission-line properties of HiBAL and non-BAL quasars have been undertaken (e.g., Weymann *et al.*, 1991; Reichard *et al.*, 2003; Baskin *et al.*, 2013, 2015). Results of such investigations have shown that, in general, the UV and optical SEDs, unaffected by the presence of BAL troughs, of BAL and non-BAL quasar populations are very similar. Relatively weak emission features, however, which are diagnostics of the far-UV ionising spectrum, such as He II λ1640, have been found to show systematic differences between the populations (Baskin *et al.*, 2013). To date, the strong absorption present in BAL quasars has precluded a direct comparison of the kinematic properties of high-ionisation ultraviolet emission lines, such as C IV λ1549, in the BAL and non-BAL quasar populations. As a consequence, investigations of the outflow properties of luminous quasars have been confined to evidence from *either* absorber- *or* emission-properties.

The key aim of this Chapter is to provide the first direct comparison of the underlying ultraviolet spectral energy distributions (SEDs) of BAL and non-BAL quasars and thus to investigate outflow properties using *both* absorber and emission diagnostics. The ultimate goal is to use the relationships between the absorption- and emission-outflow properties to constrain the geometry and physical parameters of a disc wind or other models. In this Chapter, however, we concentrate on presenting the observational results for a large sample of BAL and non-BAL quasars.

With the SDSS spectrum reconstructions described in Chapter 2 and having defined the BAL – both AI and BI – and non-BAL quasar populations we perform an investigation into the rest-frame UV properties of the populations and investigate the relationship between the C IV emission outflow signature and the properties of the BAL troughs.

A comparison of the C IV emission space for the BAL and non-BAL quasars, and various other quasar properties are presented in Sections 3.2.1 to 3.2.3. Correlations between the

BAL trough parameters and the C IV emission profile are described in Section 3.2.4 before a short discussion of the implications in Section 3.3. An overview of the main conclusions is included in Section 3.4.

3.2 Results

3.2.1 C IV emission line profile

From the component reconstructions, we can parameterise the C IV emission of both the BAL and non-BAL quasars via a non-parametric approach similar to that of Coatman *et al.* (2016, 2017). A power-law continuum $f(\lambda) \propto \lambda^{-\alpha}$ is fitted to the reconstruction using the median values of F_λ in the two wavelength regions 1445–1465 Å and 1700–1705 Å. The model continuum is subtracted from the spectrum in the window 1500–1600Å and the emission-line flux computed over the same wavelength interval.[1] The wavelength which bisects the cumulative total line flux, $\lambda_{\rm half}$, is determined and converted to a velocity to obtain the blueshift of the emission via

$$\text{C IV blueshift} = c \times (\lambda_r - \lambda_{\rm half}) / \lambda_r \tag{3.1}$$

where c is the velocity of light and λ_r is the rest-frame wavelength of the emission line, in this instance 1549.48 Å for the C IV doublet. Positive values correspond to outflowing material towards the observer. The equivalent width (EW) of the emission as well as the location and value of the peak of the line are also calculated.

Figure 3.1 shows the C IV EW versus the C IV blueshift (hereafter the C IV emission space) for the samples of non-BAL and BAL quasars. Let us first consider the non-BAL quasar population: consistent with Richards *et al.* (2011), weak lines (low EW) are often highly blueshifted, providing strong evidence of outflows, while strong lines are close to symmetric (zero blueshifts). As Richards *et al.* (2011) point out, however, the relationship is not one-to-one as there are quasars with low blueshifts and low EWs. Note also that non-BAL refers here to quasars with both AI=0 and BI=0, i.e., no absorption present. If, however, the AI>0 quasars (still BI=0) are included, the non-BAL C IV distribution does not in fact change significantly. Composite non-BAL quasars constructed from spectra in three regions of C IV emission space are presented in the top panels of Fig. 3.2. In detail, a high-EW composite is generated from spectra with C IV EWs and blueshifts of 103-116 Å and 262–787 km s^{-1}, respectively; a low-EW, low-blueshift composite from 23–29 Å and -262–+262 km s^{-1}; and a low-EW, high-blueshift composite from 23–29 Å and 2360–2890 km s^{-1}. The spectra are

[1] For a small number of quasars (1157) with more than 15 per cent of the line flux blueward of the short wavelength limit the window is extended down to 1465 Å to include the majority of the total C IV emission flux.

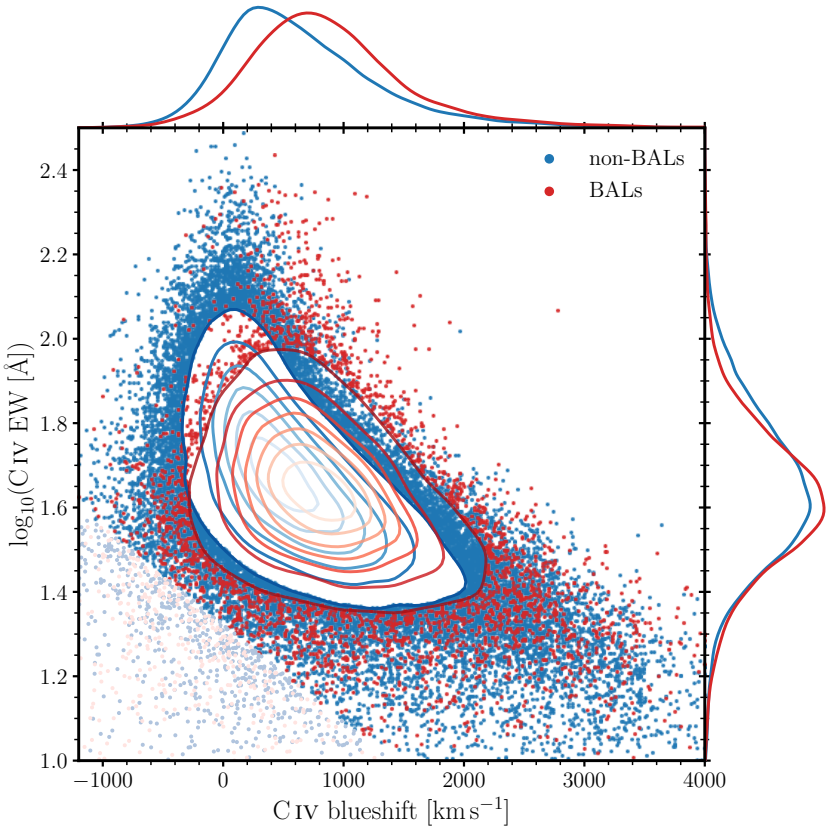

Figure 3.1: C IV emission space for the sample of non-BAL quasars (blue contours/dots) and classically-defined BAL quasars (red contours/dots). Marginalised distributions of blueshift and EW are also shown. The faint points in the sparsely populated lower left of the figure have been excluded from the analysis (Section 2.4.3). The two populations are distributed very similarly within the C IV emission space except at high-EW and low blueshift where there is a notable lack of BALs at the lowest blueshifts.

smoothed using inverse-variance-weighting over a seven pixel window. The close to constant pixel-by-pixel median absolute deviation (MAD), shown as the shaded regions, redward of C IV is almost entirely due to the finite S/N of the spectra.[2] Such composite spectra, covering the full occupied region of the C IV emission space, are available to view in an interactive plot online.[3] It should be noted that the BAL and non-BAL samples are not matched in any way, e.g., in luminosity; however, as will be discussed in Sections 3.2.2 and 3.2.3, various quasar properties are found to be strongly correlated with location in C IV emission space and in the same fashion across the BAL and non-BAL populations.

The full spectrum reconstructions for the BAL quasar population allow a direct comparison of the non-BAL and BAL quasar populations within the C IV emission space (Fig. 3.1) and the bottom panels of Fig. 3.2 contain composite BAL quasars taken from the same areas in the C IV emission space as the non-BAL quasar composites above. The same

[2]Spectrum S/N $\simeq$ 6, increased by $\sqrt{7}$ from the smoothing. Then, with MAD = σ/1.5, the amplitude of MAD/reconstruction is $\simeq \pm 0.04$ in Fig. 3.2.

[3]Available as supplementary material for Rankine *et al.* (2020) at MNRAS online or at `https://people.ast.cam.ac.uk/~alr53/BALs_nonBALs/CIV_BAL_nonBAL.html`

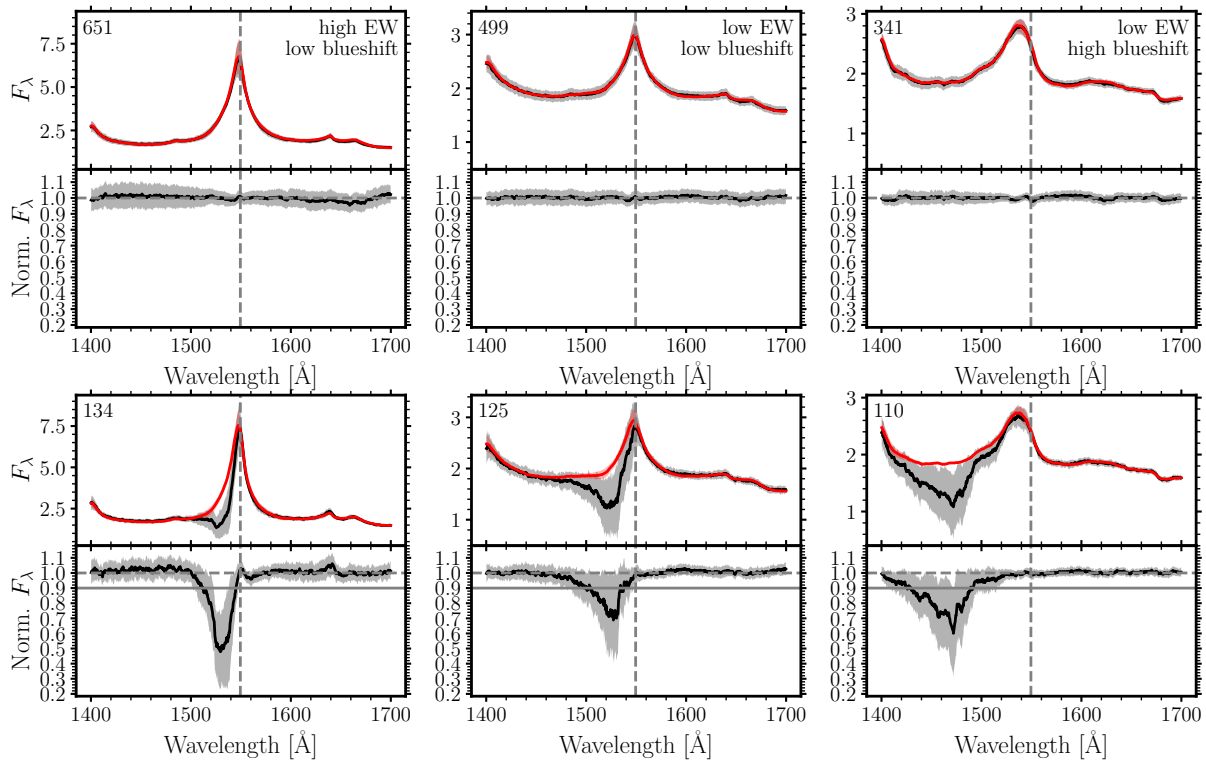

Figure 3.2: Composite spectra and reconstructions of non-BAL (top) and BAL quasars (bottom) for select regions in C IV emission space. Left: high-EW and low-blueshift C IV; middle: low-EW and low-blueshift; right: low-EW and high-blueshift C IV. The number of spectra contributing to each composite is indicated in the top left. In the top panel of each pair, the black line is the median composite SDSS spectrum and the red is the composite reconstruction. The grey and red shaded regions mark the pixel-by-pixel median absolute deviation of the spectra and reconstructions, respectively. The lower panel of each pair presents the composite spectrum normalised by the composite reconstruction. The shaded region is the median absolute deviation of the normalised spectra. The vertical, dashed, grey line corresponds to the rest wavelength of C IV and the horizontal, solid grey line in the normalised BAL quasar panels marks $f(V) = 0.9$, the flux below which BAL troughs contribute to BI and AI calculations. Note that all panels containing the normalised spectra have the same y-scale for comparison. Whilst the C IV emission profiles vary in C IV emission space by design, the BAL troughs also vary systemically. Composite non-BAL and BAL spectra are available to view in an interactive plot of the C IV emission space[3].

C IV emission line shapes are apparent as for the non-BAL quasars. The BAL quasar composites show systematically different BAL trough properties moving around the C IV emission space (see Section 3.2.4). Again, an interactive plot is available for the BAL quasars[3]. The increase in the pixel-by-pixel MAD (shaded regions) within the troughs highlights the diversity in the absorber properties at a given velocity. The diversity of troughs is particularly evident in spectra with weak and blueshifted C IV emission (lower right region of Fig. 3.1), an observation made in an important early paper discussing BAL quasar properties by Turnshek (1988). We find that averaging over spectra possessing relatively-deep individual troughs at different velocities results in the composites showing weak but broad BAL troughs. The kinematics and properties of BAL troughs are explored more fully in Section 3.2.4.

As discussed in Section 2.3 the probability that a BAL quasar is included in the DR14 catalogue as a function of SED, magnitude and redshift is not available. The level of uncertainty in the spectrophotometry of the DR14 quasar spectra also makes consideration of the amount of reddening experienced by the BAL quasars far from straightforward. As a consequence, the quantitative assessment of the intrinsic frequency of BAL quasars as a function of their BAL trough properties and reddening is not possible (cf. Allen *et al.*, 2011, particularly figure 22). Nonetheless, it is instructive to review whether the observed fraction of BAL quasars in the sample changes across the C IV emission parameter space. $f_{\rm BAL}$ is defined as

$$f_{\rm BAL} = \frac{N_{\rm BAL}}{N_{\rm BAL} + N_{\rm non\text{-}BAL}}. \tag{3.2}$$

$N_{\rm BAL}$ and $N_{\rm non\text{-}BAL}$ are the absolute number of BAL and non-BAL quasars and depend on the measure used to select BAL quasars. Here we choose to employ the classic BI>0 definition to give the BAL quasar sample, while the non-BALs are selected to possess both BI=0 and AI=0. Figure 3.3 shows $f_{\rm BAL}$ over the C IV emission space that includes both BAL and non-BAL quasars. For an extended range in C IV emission EW, at constant EW, $f_{\rm BAL}$ increases as the C IV emission blueshift increases. If instead we consider the fraction of quasars with *any* absorption greater than 450 km s^{-1} wide and below 0.95 times the continuum limit, $f_{\rm BAL}$ increasing as C IV emission blueshift increases still holds true but now there are quasars with absorption populating the high-EW, zero-blueshift region of C IV emission space. For the reasons discussed above, caution should be taken when interpreting the quantitative behaviour of $f_{\rm BAL}$ but the behaviour is consistent with an increased probability a quasar with a given C IV EW is seen as a BAL as the C IV emission outflow signature increases. It is difficult to say here whether the increase in the BAL fraction is due to more outflowing gas along our line-of-sight or if it is a result of more momentum being imparted to the gas; however, this empirical observation may be further consistent with the theoretical wind model of Giustini & Proga (2019), where the probability of a quasar hosting a radiation line driven wind increases with increasing accretion rate and BH mass.

3.2.2 C IV and other UV emission lines

The composite spectra allow us to compare the BAL quasars to the non-BAL quasars in different regions of C IV emission space. Figure 3.4 shows the composites in Fig. 3.2 over the wavelength range 1260–3000 Å. The BAL and non-BAL composite reconstructions in the top panel of Fig. 3.4 are extremely similar across the whole wavelength range. The composite spectra themselves are also very similar, apart from the presence of troughs in the BAL spectra, in agreement with Weymann *et al.* (1991) and Matthews *et al.* (2017). There are, however, subtle differences in some of the emission lines at certain areas in C IV emission space which can only be seen when dividing the BAL spectra (reconstructions) by the non-BAL spectra (reconstructions) as shown in the bottom panel. Note that the y-scale in the bottom panel has been chosen to illustrate low-amplitude spectral differences.

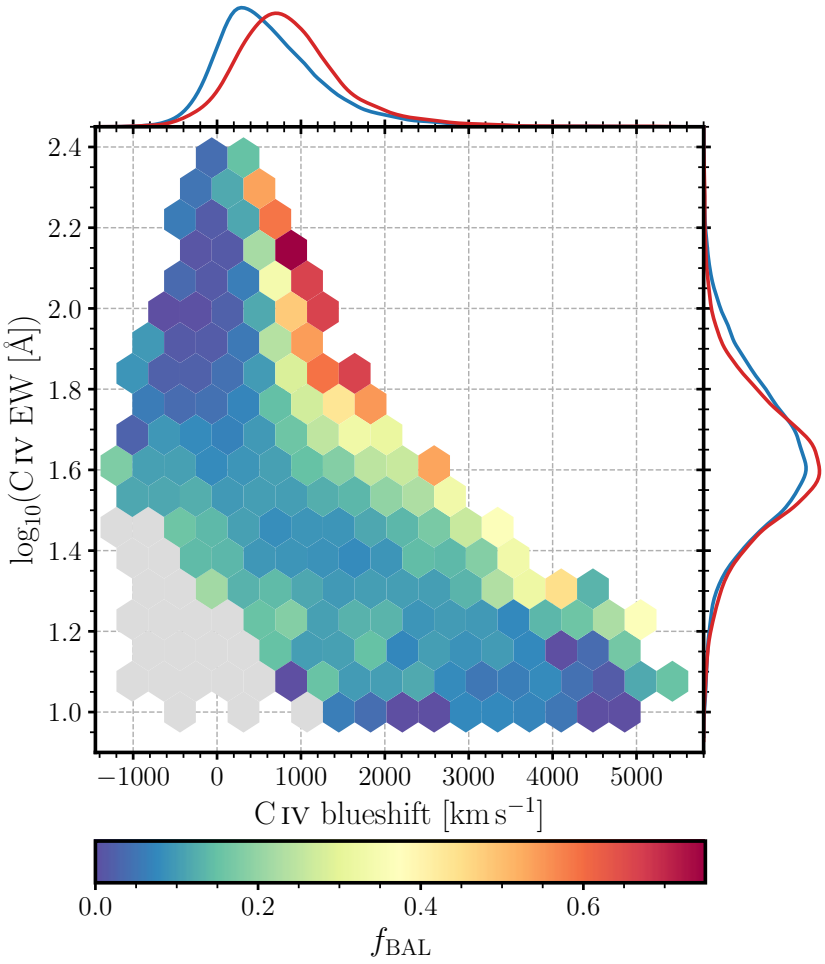

Figure 3.3: The observed fraction of quasars that are classically-defined BAL quasars as a function of the C IV emission properties. Only bins with ten or more quasars are plotted. The grey hexagons indicate the sparsely populated region of C IV emission space excluded from analysis. As discussed in the text, the intrinsic fraction of BALs is not known, however, at fixed EW, the probability a quasar possesses BAL troughs increases with increasing blueshift suggesting that the fraction of quasars with signatures of outflows in absorption increases with increasing evidence of outflows in emission. It is true that the fraction of quasars that are BALs, at a particular location in C IV emission space, is highest at high-EW and positive-blueshift; however, these quasars have low BIs and the relative number of BAL quasars here is low compared to that at higher C IV blueshifts and lower EWs, as highlighted by the marginal distributions (same as for Fig. 3.1).

Consider first the direct empirical differences evident in the BAL/non-BAL quasar spectrum ratios. The BAL absorption blueward of the C IV and Si IV emission is most evident as expected. All three composites also show a systematic difference in Mg II λ2800 emission with the BAL possessing weaker emission, although the reduction is small. The difference has been seen in other investigations (see figure 8 in Baskin *et al.*, 2015, for example) but is particularly evident here. Otherwise, the two composites drawn from the lower C IV EW regions show no spectral differences greater than ≃2 per cent shortward of the C IV emission line.

The composite from the high C IV EW and low C IV blueshift region does, however, possess features coincident with wavelengths of prominent emission lines: peaks are present

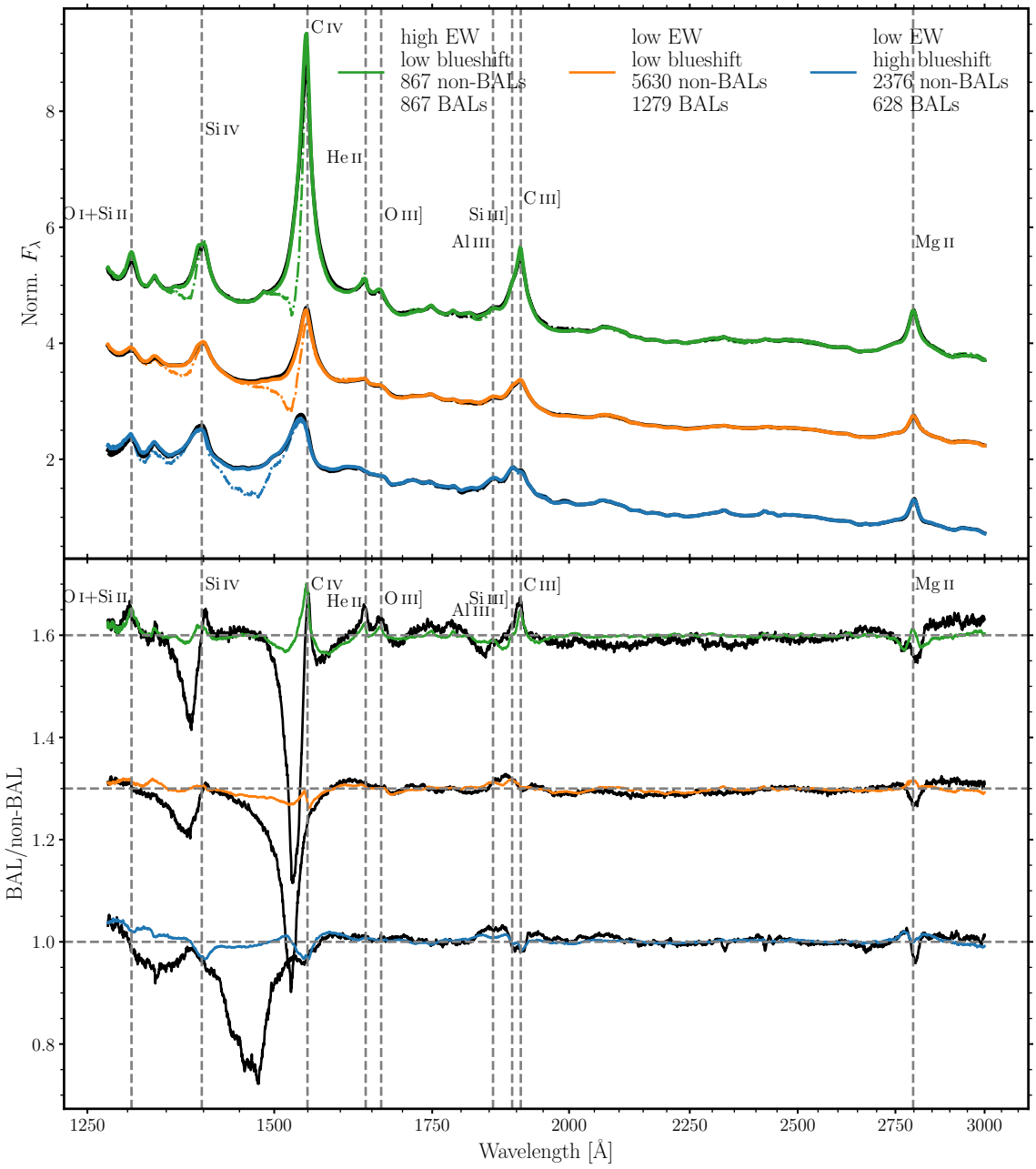

Figure 3.4: Composite spectra and reconstructions of the quasars in and surrounding the three EW and blueshift regions used to produce Fig. 3.2 (top panel). The size of the areas in EW and blueshift have been extended to increase the number of quasars contributing to each composite. The BAL quasars follow the colours in the legend whilst the non-BAL quasars are plotted in black. The composite BAL (dot-dashed, coloured lines) and non-BAL (dot-dashed, black lines) quasar spectra are also plotted. Almost identical composites and reconstructions, such that the dot-dashed spectra are hardly visible underneath the reconstructions, mean the reconstructions are capturing the pertinent features in the spectra. The high-EW, low-blueshift composites have been shifted up by 1.5 and the low-EW, low-blueshift composite shifted up by 3 for presentation purposes. The bottom panel contains the BAL quasar composite spectra (reconstructions) divided by the non-BAL quasar composite spectra (reconstructions) in black (legend colours). Note that the y-scale has been chosen to emphasise even small differences between spectra (reconstructions). The high-EW composite and low-EW, low-blueshift composite have been shifted up by 0.6 and 0.3, respectively. Identical BAL and non-BAL quasar composite spectra (reconstructions) would produce divided spectra (reconstructions) of unity.

in the BAL/non-BAL quasar spectrum ratio at O I+Si II, Si IV, C IV, He II, [O III] and C III]. The location of quasars within the C IV emission space means that the C IV EWs are the same and care has been taken to ensure that both the distributions of C IV EW and blueshift contributing to the non-BAL and BAL composites are carefully matched in order to take account of the differing distributions of BAL and non-BAL quasars in the top-left of C IV emission space (see Fig. 3.1, and Appendix B for a discussion regarding the claim that there are few BAL quasars at the highest C IV EWs). For each BAL quasar contributing to the high-EW composite, the non-BAL quasar with the most similar C IV properties was selected to contribute to the non-BAL composite. The peak differences in emission-line strength are not large, a maximum of 10 per cent, but are highly significant. Inspection of the ratio spectrum reveals systematic reductions in the BAL spectrum to the blue and red of several of the emission-line core excesses. The BAL quasar emission lines are narrower, in FWHM, than those of the non-BAL quasars by $\simeq$14 per cent. The origin of the emission-line differences are therefore due to the BAL spectra possessing slightly narrower emission-line profiles than the non-BAL spectra, potentially due to the BAL quasars with high C IV EWs being viewed more face-on than their non-BAL counterparts. Alternatively, these BAL quasars may have smaller black hole masses. As far as we are aware the observation represents a new result. In the low-EW, high-blueshift composites, the converse is true but with less significance: the BAL quasar C IV emission lines are wider in FWHM by $\simeq$7 per cent.

Moving to the BAL/non-BAL reconstruction ratio spectra, the effectiveness of the reconstruction scheme can be assessed via comparison with the features evident in the BAL/non-BAL spectrum ratios, in particular the differences in emission lines between the two populations. If the reconstructions were perfect the ratio spectra would essentially mimic the features seen in the spectrum ratios, other than at wavelengths affected by BAL troughs. Such is very definitely not the case across the Mg II λ2800 line. The reason, however, is due to the Baldwin effect, i.e., the anti-correlation between emission line EW and luminosity (Baldwin, 1977), which we have chosen not to remove. In more detail, the MFICA components were generated using quasars at $z = 2.0-2.3$ (Section 2.4.3), thereby defining the relative emission-line strengths for the ultraviolet and Mg II lines. The quasars with the wavelength coverage of Mg II emission that contribute to the composites in Fig. 3.4, however, have a significantly lower mean redshift, hence lower luminosity and thus higher emission-line EWs. The reconstruction emission-line strength for each quasar is dominated by the C IV emission and other lines in the far ultraviolet.

The Baldwin-effect induced mismatch to the Mg II emission aside the reconstruction-ratio spectra follow the spectrum ratios very closely. Away from the Si IV and C IV BAL troughs the reconstructions are within 2 per cent of the actual composite spectra. The reproduction of the individual emission-excesses for the BAL quasars in the top composite is striking. The similarities between the composite ratio spectra and the composite ratio reconstructions for all three regions in the C IV emission space highlight the quality of our reconstruction scheme.

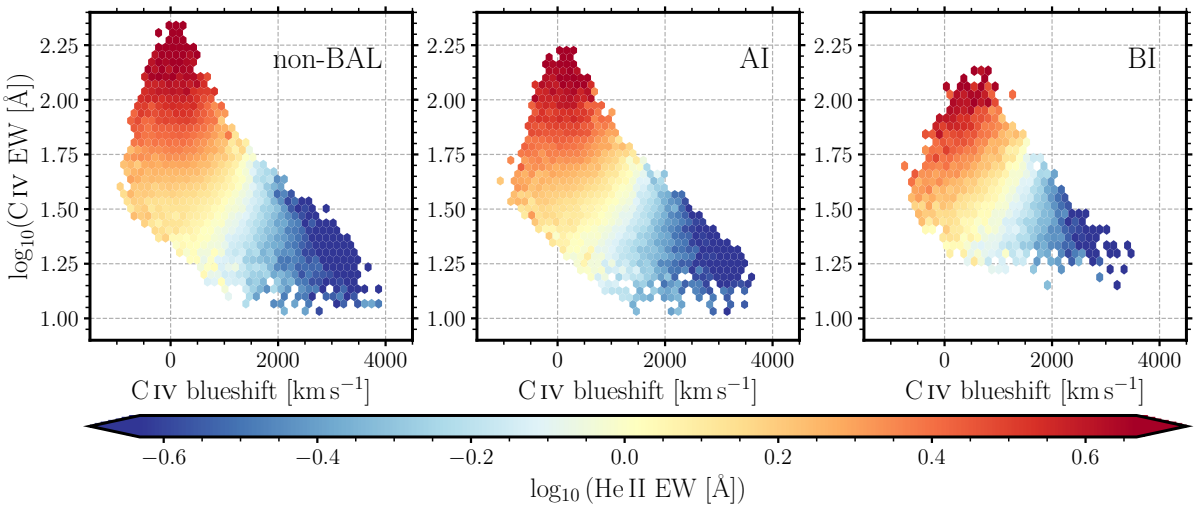

Figure 3.5: C IV emission space with hexagons coloured by median He II EW for the non-BAL quasars (left), AI-defined quasars (middle; black histogram in Fig. 2.9) and BI-defined BAL quasars (right; red, hatched histogram in Fig. 2.9). Only hexagons with ≥ 5 quasars are plotted. The spectra in the lower left of C IV emission space that were excluded and previously plotted as grey hexagons (Fig. 3.3) are not plotted here. The lower C IV coverage in the BI-sample is a result of fewer quasars in this population. The He II-EW distributions are extremely similar in all three populations.

High He II EW is indicative of a stronger soft X-ray spectrum (Leighly, 2004). Baskin *et al.* (2013, 2015) noted the decrease in He II λ1640 strength with increasing C IV blueshift by means of BAL and non-BAL quasar composites. With our reconstructions, we have been able to consider the relationship between the C IV and He II on an object-by-object basis. We calculate the He II λ1640 EW between 1620 and 1650 Å (identical to Baskin *et al.*, 2013) following the same procedure as for the C IV doublet but using the windows 1610–1620 Å and 1700-1705 Å for the power-law estimation. Our observations are in agreement with Baskin *et al.* (2013, 2015) and the hypothesis that disc winds form only when the ionising quasar SED is soft enough that electrons remain bound to nuclei and radiation line-driving contributes to the acceleration of material. The dependence of He II EW as a function of location in C IV emission space confirms the anti-correlation between the hardness of the ionising SED and the strength of outflows seen in both absorption and emission. A new result is the demonstration that the systematic He II EW trends for the non-BAL, AI- and BI-defined BAL quasar populations (Fig. 3.5) are close to identical.

3.2.3 Black hole mass and luminosities

The bolometric luminosity, $L_{\rm bol}$, has been calculated from the monochromatic luminosity at 3000 Å or at 1350 Å[4] for spectra where 3000 Å is not present, using the bolometric corrections $\mathrm{BC}_{3000} = 5.15$ and $\mathrm{BC}_{1350} = 3.81$ from Shen *et al.* (2011). $L_{\rm bol}$ is displayed in Fig. 3.6 as

[4]Spectrophotometric variations in the DR14 spectra contribute a ±10 per cent uncertainty to the luminosity measurements but the factor is small relative to the dynamic range present in the quasar sample.

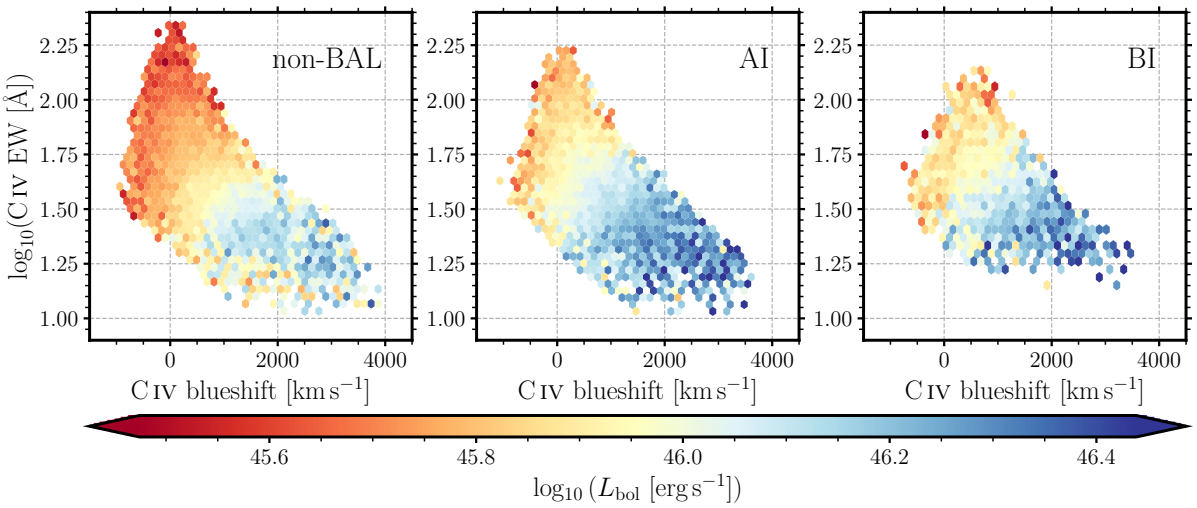

Figure 3.6: As for Fig. 3.5 with hexagons occupied by five or more quasars coloured by median $L_{\rm bol}$. Similar systemic trends within the C IV emission space are present in all three populations.

a function of location in C IV emission space for the non-BAL, AI- and BI-defined quasar populations. In agreement with the Baldwin Effect (Baldwin, 1977), albeit over a smaller dynamic range of luminosity, there is an anti-correlation between $L_{\rm bol}$ and C IV EW at fixed blueshift. $L_{\rm bol}$ also increases towards the high-blueshift end of the C IV emission space in all three of the populations. The three populations have very similar luminosities (median $\log_{10}(L_{\rm bol})$=45.9, 46.0 and 46.0 for the non-BAL, AI and BI quasars respectively).

Consideration of the intrinsic luminosities of the populations would require accurate extinction estimates for the quasars which are not available. It is, however, likely that the quasars with absorbers possess modest $E(B-V)$ values (see Allen *et al.*, 2011, section 8.5). Adopting an average $E(B-V)=0.05$ for BAL quasars (from Allen *et al.*, 2011), BAL quasars are predicted to appear 25 per cent fainter at 3000 Å and 46 per cent fainter at 1350 Å. The reference-wavelength transition occurring at $z \simeq 2.3$ when 3000 Å rest-frame moves beyond the red limit of the SDSS spectra. The intrinsic luminosities of the BAL quasar samples should thus be larger by ≃0.12 ($z \leq 2.3$) and 0.27 ($z \geq 2.3$) in $\log_{10}(L_{\rm bol})$. The factors are modest relative to the dynamic range in luminosity present in the quasar samples and should not affect the trends within the C IV emission space. Again, the systematic trends within the C IV emission space for all three populations closely mimic each other.

Only C IV λ1549-emission is present in all the quasar spectra, thus we derive black hole mass (BHM) estimates from the C IV line via equation 6 of Coatman *et al.* (2017) and reproduced here:

$$\mathrm{BHM} = 10^{6.71} \left(\frac{\mathrm{C\,IV\ FWHMc}}{10^3\,\mathrm{km\,s^{-1}}} \right)^2 \left(\frac{\lambda \mathrm{L}_\lambda(1350\,\text{Å})}{10^{44}\,\mathrm{erg\,s^{-1}}} \right)^{0.53} \mathrm{M}_\odot, \tag{3.3}$$

where the FWHM of the C IV line is measured non-parametrically from the reconstructions. We employ the correction of Coatman *et al.* (2017, their equation 6 and reproduced here in Equation 3.4) to obtain the corrected FWHM (FWHMc) to account for the excess, non-

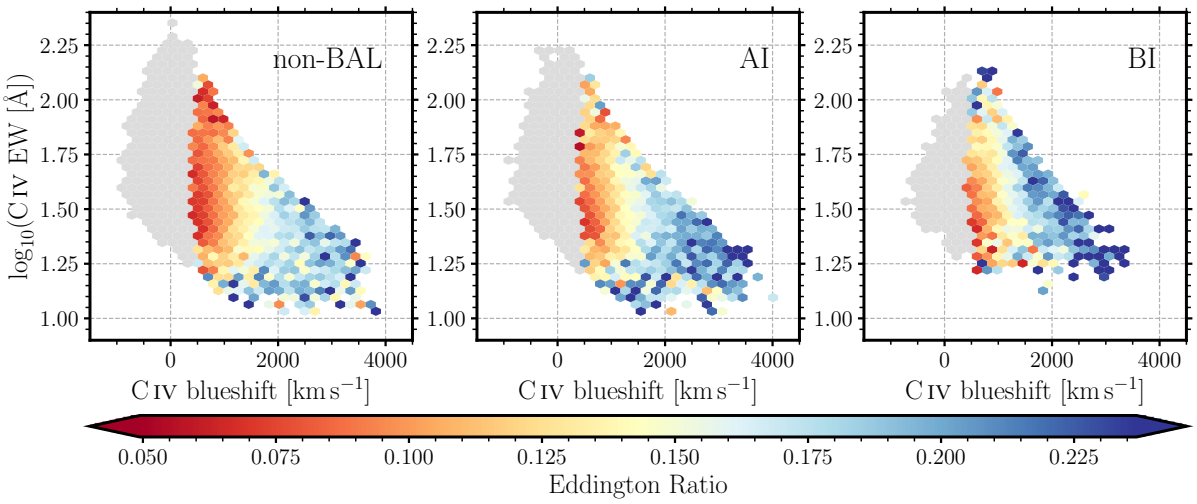

Figure 3.7: As for Fig. 3.5 with hexagons occupied by five or more quasars coloured by median Eddington ratio. We only plot the Eddington ratio for spectra with C IV blueshift > 500 km s^{-1} for which we correct the black hole masses using Coatman *et al.* (2017). The Eddington ratio increases with C IV blueshift for all three populations but is slightly lower at fixed C IV parameters for the non-BAL population compared to the AI- and BI-defined samples (see also Fig. 3.6).

virial, blue emission for quasars with C IV blueshift > 500 km s^{-1}. The correction takes the form

$$\mathrm{FWHMc} = \frac{\mathrm{FWHM}}{0.41\frac{\mathrm{Blueshift}}{10^3\,\mathrm{km\,s^{-1}}} + 0.62}\,\mathrm{km\,s^{-1}}, \tag{3.4}$$

and we use the C IV blueshifts described in Section 3.2.1. The Coatman *et al.* (2017) correction is not well-defined for modest positive blueshifts or negative blueshifts of any size. As a consequence, the mass-correction has not been applied where the C IV blueshift < 500 km s^{-1}. The authors also note that the largest uncertainty in the black hole mass estimates stems from the determination of the quasar redshift and thus the blueshift. In the most pessimistic scenario, taking the maximum differences in redshifts as compared to SDSS as 1000 km s^{-1} for a quasar with a blueshift of 1000 km s^{-1}, leads to a change in the black hole mass by 79 per cent (see table 4 of Coatman *et al.*, 2017) if we were to instead use the SDSS pipeline redshifts. However, this 79 per cent error would affect only a maximum of 7 per cent of our quasar sample given the distributions in C IV blueshift and redshift changes.

From the black hole mass estimates we compute the Eddington luminosity, L_{Edd}, and thus the Eddington ratio using L_{bol} from above, which we present as a function of C IV emission space in Fig. 3.7. Since the Eddington ratio depends on the Eddington luminosity which, in turn, depends on the black hole mass, we have only plotted the Eddington ratio for spectra with C IV blueshift > 500 km s^{-1}. The Eddington ratios of the non-BAL, AI- and BI-defined quasars are similarly distributed in C IV emission space, indicating that quasars with evidence for the strongest outflowing winds based on their emission-line properties have the highest L/L_{Edd}.

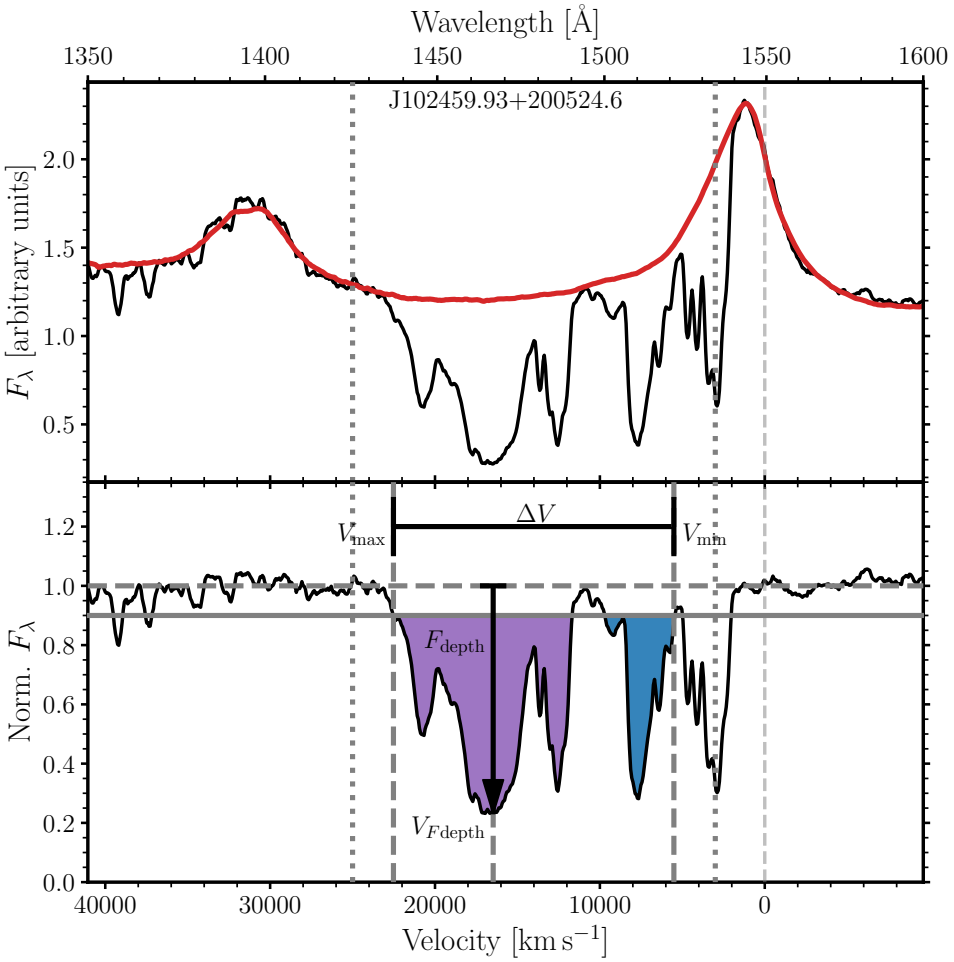

Figure 3.8: As for Fig. 2.6 but now with only the BI troughs shaded for clarity. The measured trough parameters for this spectrum are marked in the lower panel (see Table 3.1 for descriptions of each parameter).

3.2.4 BAL trough parameters

In Fig. 3.2 and the interactive plot[3], we see the systematic trend in BAL trough properties with location in C IV emission space. Strong and symmetric C IV is often accompanied by relatively narrow and deep troughs while spectra with weak- and blueshifted-emission have broader and more diverse troughs. To investigate any systematic relationships between absorber-trough and emission-line properties, various trough parameters are measured. Each trough is defined as a region where the BI (or AI) conditions are met. Table 3.1 lists the parameters and they are illustrated using an example spectrum in Fig. 3.8. Where spectra have multiple troughs, the parameters pertaining to individual trough measurements are reported as follows: we report the minimum $V_{\rm min}$ (i.e., the lowest velocity for which there is broad absorption); the maximum $V_{\rm max}$ (i.e., the highest velocity for which there is broad absorption); the deepest trough $F_{\rm depth}$ measurement and the accompanying $V_{F\rm depth}$, and the widest trough $V_{\rm width}$.

In Fig. 3.9 we present the AI and BI trough parameters as a function of location in C IV emission space. Considering the two populations of AI>0 quasars (Fig. 2.9), we split the AI

Table 3.1: BAL trough parameters. All parameters with the subscript 450 pertain to troughs wider than 450 km s^{-1} (e.g., N_{450}). Matching parameters also exist, with the subscript 2000, for troughs wider than 2000 km s^{-1}, e.g., N_{2000}.

Name	Unit	Description
BI	km s^{-1}	Balnicity index (Equation 2.2)
AI	km s^{-1}	Absorption index (Equation 2.3)
N_{450}		Number of troughs
$V_{\rm min,450}$	km s^{-1}	Minimum velocity of trough
$V_{\rm max,450}$	km s^{-1}	Maximum velocity of trough
ΔV_{450}	km s^{-1}	Range of velocities with absorption
$V_{\rm width,450}$	km s^{-1}	Width of trough
$F_{\rm depth,450}$	Normalised flux units	Trough depth
$V_{F\,\rm depth,450}$	km s^{-1}	Velocity of deepest part of trough

trough parameters into the two populations: AI troughs in spectra with BI=0 (AI(BI=0)), left panels; blue histogram of Fig. 2.9), and AI parameters for spectra with BI>0 (AI(BI>0)), middle panels; orange histogram of Fig. 2.9). The right-hand panels contain the BI trough parameters. By definition, almost all of the spectra with BI>0 have AI>0 and so appear in the middle and right panels.[5] The extent in velocity of the absorption troughs therefore increases systematically moving from left to right in Fig. 3.9.

From first glance at Fig. 3.9, the AI(BI=0) and AI(BI>0) trough systematics differ, while the latter are almost identical to the BI trough systematics, reinforcing the evidence for the existence of two AI populations described by Knigge *et al.* (2008) and presented in Fig. 2.9. For spectra in the middle panels with only one AI trough, the AI trough parameters are identical to the BI trough parameters in the right panels except where $V_{\rm min,450} < 3000$ km s^{-1}. It is also possible for there to be more than one AI trough per spectrum in the middle panels; however, only one of these AI troughs has to satisfy the BI conditions for the object to be included in the right panels, thus the AI and BI trough parameters will differ. Approximately 54 per cent of the spectra in the middle panel have more than one trough.

In the top row of panels we see the dependence of absorption-outflow strength within the C IV emission space, via the AI and BI measures. Clear differences exist between the AI(BI=0) and the BI troughs. While the BI troughs become stronger with increasing C IV emission blueshift, the AI(BI=0) troughs show this same trend at fixed high-EW but at low-EW the AI measures decreases for large C IV blueshifts.

The left panel of the second row, showing the dependence of trough depth explains the AI(BI=0) behaviour in the top row – i.e., at $\log_{10}$(C IV EW) $\lesssim 1.6$ the troughs become shallower as C IV blueshift increases thus AI also decreases (Equation 2.3). The opposite is

[5]There is, however, a small fraction of the BI troughs ($\simeq$4 per cent) that have AI=0 due to $\chi^2_{\rm trough} < 10$ while there is no $\chi^2_{\rm trough}$ requirement for the BI troughs.

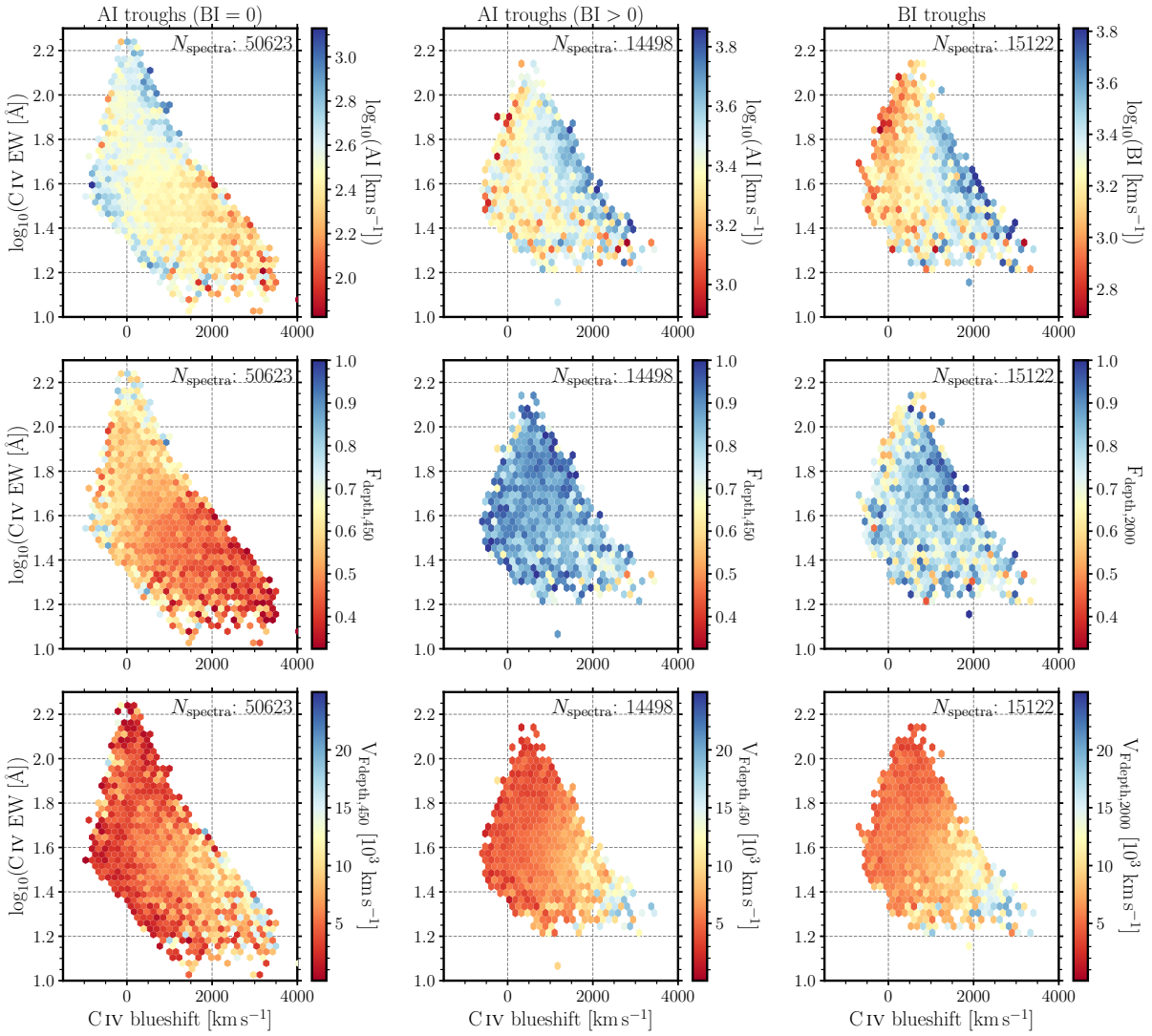

Figure 3.9: The AI- and/or BI-defined quasar populations binned in C IV emission profile space where each hexagonal bin is coloured by trough parameters outlined in Table 3.1. Left panels: AI trough parameters for spectra with BI=0; middle: AI trough parameters for spectra with BI>0; right: BI trough parameters for classically-defined BAL quasars. The quasars have been binned in C IV emission space and the median trough parameter in each bin plotted on the colour axis, for bins with at least five quasars. The number of spectra contributing to each panel is noted in the top right of every panel; each row has the same number of spectra. From top to bottom, AI or BI, $F_{\rm depth}$ and $V_{F\rm depth}$. The figure continues overleaf with $V_{\rm min}$, $V_{\rm max}$, ΔV and $V_{\rm width}$. The dot-dashed lines in the lower right panel locate the boundaries in C IV emission space used to produce the absorber-restframe composites in Fig. 3.10. The structure of both the AI- and BI-defined troughs vary systematically, but differently, in C IV emission space.

true at high C IV EW. If there is any such systematic present for the BI-defined troughs it is far less significant, in contrast to what is seen in the composite troughs in Fig. 3.2. The weakening of the troughs in the composite spectra is a result of averaging out the individual troughs which are more diverse in velocity structure at higher C IV blueshift and lower EW. The comparable depths of the troughs is clear in Fig. 3.10 which shows absorber-restframe composites of the BI-defined BAL spectra in different regions of C IV emission space. Baskin *et al.* (2015) presented similar absorber-frame composites and found trough depth not to be correlated with He II-EW (see their fig. 7), in agreement with what we present here in C IV emission space.

The trends evident in the third, fourth and fifth rows, all showing measures of the absorber trough velocities are however far more similar. For both AI- and BI-defined troughs the minimum and maximum velocities where absorption is present and the velocity of maximum absorption-depth all show strong systematics as a function of C IV blueshift. As the strength of the emission-outflow signature increases, the velocities of the absorbers increase. Very few objects have $V_{F\,\mathrm{depth}}$ at very large velocities (even at high C IV blueshift) – i.e., the deepest part of each trough often occurs in the lower-velocity half of the trough – and this can also be seen in Fig. 3.10. Hamann *et al.* (2019, see their fig. 4) observed these skewed absorption profiles in composites binned by BI. For both AI- and BI-defined samples, the highest-velocity troughs are in quasars with the highest Eddington ratio as observed in Fig. 3.7.

The sixth and seventh row, examining the behaviour of the velocity-extent (ΔV) and -width (V_{width}) of all and individual absorbers, respectively, within the spectra, provide insight into the systematic differences between the AI(BI=0) and BI-defined absorbers. For the BI-defined absorbers as the C IV emission blueshift increases, the trough velocities increase and the trough velocity-extent increases, as would be expected for an accelerating wind. The BAL troughs present in spectra in the lower right of C IV emission space are much broader than those in spectra at the upper left. Whereas, for the AI(BI=0) absorbers, the velocities increase as the C IV blueshift increases but the velocity-extent of the absorbers is close to constant. 16 390 AI-defined quasars have multiple troughs and in many they are separated extensively in velocity, up to 24 950 km s^{-1}. In the AI(BI=0), AI(BI>0) and BI quasar populations, 67, 46 and 83 per cent of the quasars, respectively, have only one trough. Spectra with more than one trough typically have large trough velocities to allow for a second trough at lower velocities and thus have large C IV blueshifts. Many of the AI(BI>0)-quasars have a BI-defined trough (therefore also AI-defined) and a second AI-defined trough, accounting for the high fraction of spectra with $N_{450} > 1$.

The AI(BI=0) spectra are dominated by single, relatively narrow, troughs such that BI=0. These narrow troughs appear in spectra with the full range in C IV blueshift as evidenced by the swathe of constant and low AI, ΔV_{450} and $V_{\mathrm{width,450}}$ in the AI(BI=0) plots. We can test the hypothesis that the AI(BI=0) absorbers are different from the AI(BI>0) absorbers

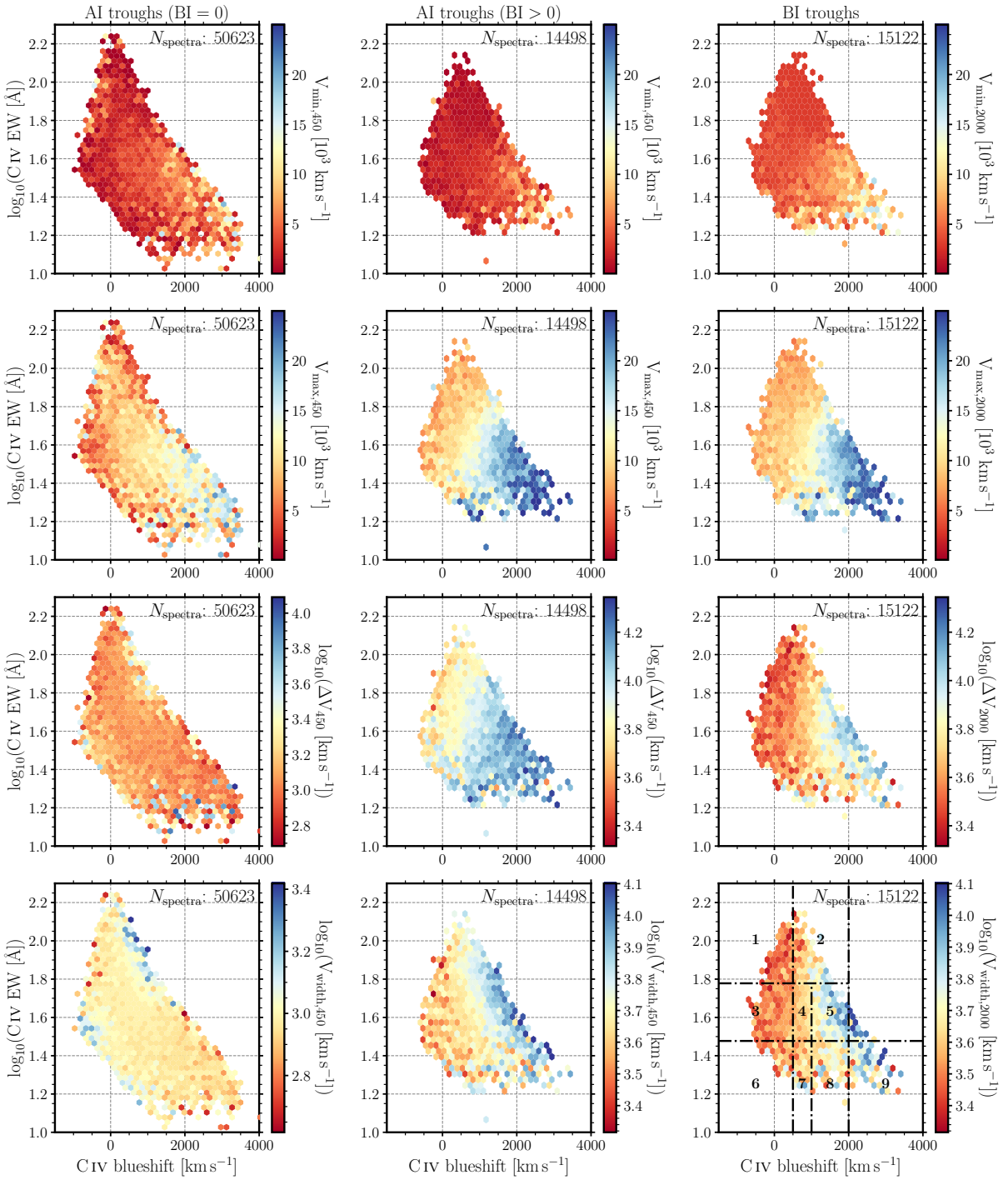

Figure 3.9: *continued*

rather than just much narrower by investigating the structure of the zero-BI troughs. We select 18 740 AI(BI=0) quasars with only one AI-trough and generate a mean composite of the spectra shifted to the rest-frame of the maximum absorption-depth. A well-defined C IV doublet is observed (Fig. 3.11). In many cases, the 450 km s^{-1} minimum velocity required by the AI measurement is sufficiently narrow to include narrow absorption lines (NALs) with very different internal kinematic properties compared to BI-defined absorbers. The AI-defined absorption is participating in the outflows but we conclude that AI(BI=0) absorbers

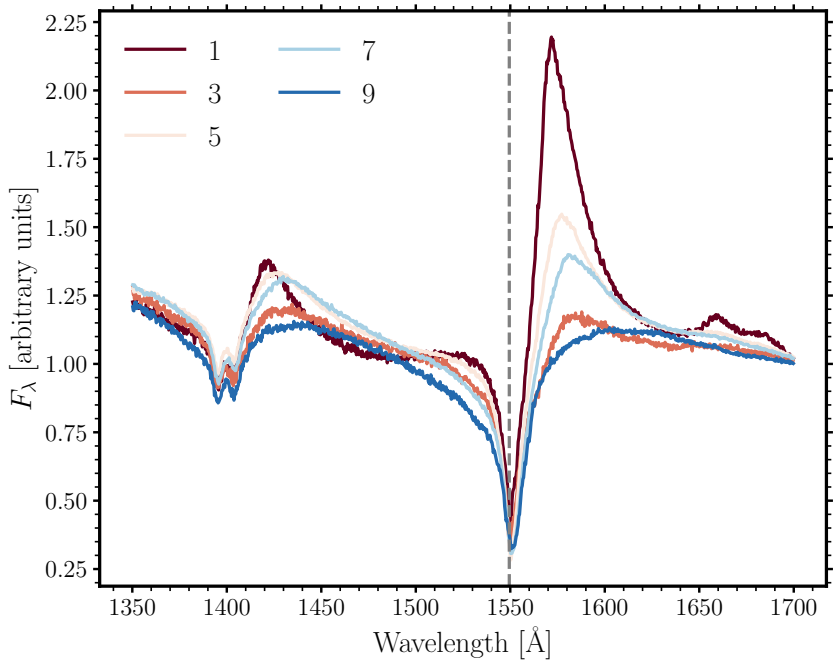

Figure 3.10: Median absorber-restframe composites of the 14 887 BI-defined quasar spectra. Where spectra have more than one trough, the deepest trough is selected. The numbering of the composites matches that of the C IV regions in the lower right panel of Fig. 3.9; however only plotting the odd-numbered composites for clarity. The BI-defined troughs extend to larger velocities at higher C IV blueshifts with the maximum velocity increasing more rapidly than the minimum velocity or the velocity of the deepest part of the trough. The depth of the troughs does not vary systematically in C IV emission space.

are dominated by material in structures with velocity spreads of ≃few-hundred km s^{-1}, very different from much of the material giving rise to the classical BI-defined troughs.

We have yet to consider the high-EW, low-blueshift ($\lesssim$1000 km s^{-1}) region of C IV emission space. Inspection of the ΔV distribution for the AI(BI=0) troughs shows increased ΔV at high C IV EW. Some of these troughs have $V_{\rm width,450} > 2000$ km s^{-1} but have BI=0 as most of the absorption is below 3000 km s^{-1}. In contrast with the NALs discussed above, as the C IV blueshift increases, over an admittedly small range of velocities present at high EW, AI and $V_{\rm width,450}$ increase whilst the troughs deepen ($F_{\rm depth,450}$ increases). In other words, while the minimum velocity remains constant, the maximum velocity increases. The original BI calculation was designed with the 3000 km s^{-1} starting velocity to exclude strong associated absorbers which are believed to result from a different phenomenon compared to the BAL troughs (Weymann *et al.*, 1991). In the circumstances, the use of a BI$_0$ definition for absorbers (where the BI metric is extended down to zero velocity) will include a larger fraction of absorbers resulting from outflows but at the expense of including true 'associated absorbers'.

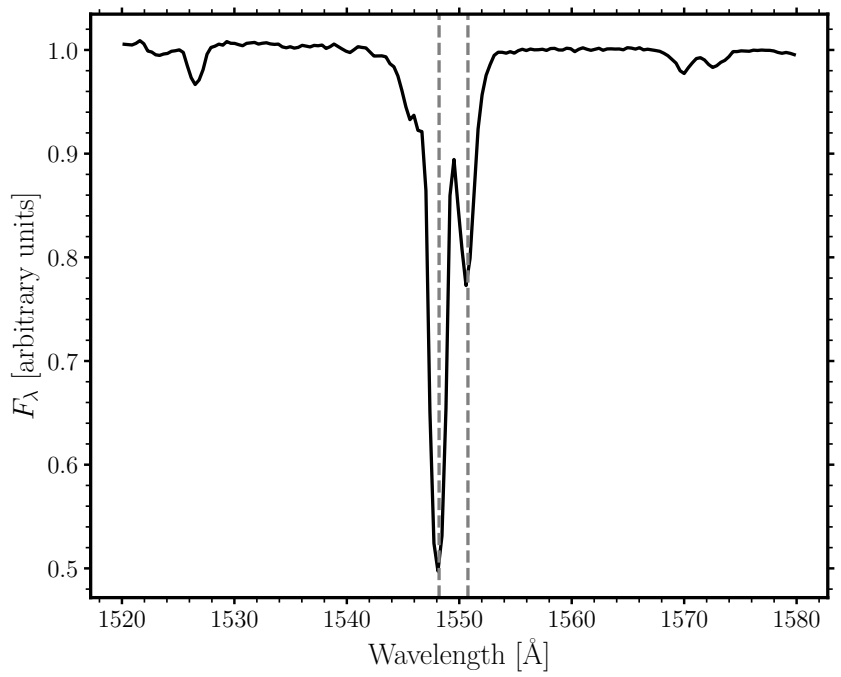

Figure 3.11: Mean normalised composite of 18 740 single, AI(BI=0) troughs shifted to the rest-frame of the deepest part of the trough. The composite is dominated by the well-defined deep, narrow absorption in which both features in the C IV $\lambda\lambda$1548,1551 doublet are seen. Additional weaker absorption is present in some troughs, explaining the broader depression, particularly to shorter wavelengths.

3.3 Discussion

The main aim of this Chapter is to present the observational differences and similarities between the ultraviolet spectra of non-BAL and BAL quasars, including the outflow signatures evident in the C IV λ1549 emission. Our approach has been designed to allow a direct investigation of the systematics observed in the absorption- and emission-outflow properties for the non-BAL and high-ionisation BAL populations as a whole. In short, we can definitively locate BAL quasars in C IV emission-line parameter space, even in the face of significantly absorbed C IV profiles. The results should provide constraints on models, particularly in the case of disc winds.

3.3.1 Quasar physical properties

The observational manifestation of outflows observed in absorption and emission are quite different, particularly in terms of the solid angle over which material contributes to the spectrum. Broad and narrow absorption occurs due to gas present along a particular line of sight. For absorbing structures of limited physical extent, a small change in viewing angle may result in very different observed absorber properties. Similar changes may result temporally due to rapid motion of absorbing material across the line of sight or changes in the ionisation parameter. Emission-line properties instead derive from gas covering a

much larger solid angle from the perspective of the observer. Photons produced by emission, in gas participating in an outflow, over a significant angle contribute to the observed spectrum and small changes in viewing angle are not, in general, expected to result in significant changes to the emission-line spectrum. Observed emission-line changes due to larger angular variations in viewing angle are of course potentially powerful probes of non-spherical geometries, including disc-wind models.

A main result is the similarity in the observed ultraviolet-emission and physical properties between the BAL and non-BAL quasar populations. For every BAL quasar with a certain black hole mass, bolometric luminosity, Eddington ratio, C IV emission profile and He II λ1640 EW, there exists a non-BAL quasar with essentially identical properties, consistent with the two objects possessing the same orientation and/or geometry. Matthews *et al.* (2017) suggest that BAL quasars can be observed at similar inclinations to non-BAL quasars. The converse is not always true; while for the majority of the C IV emission space one can find a BAL quasar for each non-BAL quasar of specified properties, there is a lack of BAL quasars possessing large C IV emission EW, no significant C IV emission blueshifts and hard SEDs.

Richards *et al.* (2011) used the observed relation between the blueshift of the C IV emission and the morphology of the C III] λ1908-Si III] λ1892-Al III λ1857 complex[6] to deduce the locations of BAL quasars within the C IV emission space. The conclusions of Richards *et al.* (2011) are consistent with the results presented here but now far more information is available about the location of BAL quasars in the C IV emission space as a function of the BAL trough properties (see Fig. 3.9 in particular).

The distribution of quasars in C IV emission space (Fig. 3.1) can be explained by a disc-wind model (e.g., Richards *et al.*, 2011); the Doppler blueshifted emission is thought to occur in an outflowing wind component, thus spectra with symmetric and high-EW C IV show little to no evidence of a disc-wind and instead are dominated by disc emission. Quasars with extremely blueshifted emission are all weak-lined. Evidence from the strength of C IV and He II-emission (see below) indicates that quasars at the top-left of the C IV emission space have the hardest SEDs, with a systematic softening of the ionising continuum moving towards the bottom right. In a scenario where line-driving is important for producing the wind, only when the number of high-energy ionising-photons is small enough that electrons remain bound to nuclei can the wind be accelerated to high velocities. As a consequence, quasars with strong C IV emission *and* high blueshift are not found.

As a recombination line, He II λ1640 can be used as an indicator of the number of ionising photons with energies above 54 eV, i.e., as an SED-hardness diagnostic. In the line-driven wind scenario, only the spectra with the lowest He II EW, thus fewest high-energy ionising-photons, are able to produce the strongest disc-winds. Baskin *et al.* (2013, 2015)

[6] A similar approach has been adopted here (see Appendix A) to determine the priors adopted for the reconstruction of the C IV emission profiles.

have quantified the strength of the dependence of BAL trough properties as a function of the He II-emission EW (broader and faster-moving troughs are observed when He II is weak). The systematic behaviour of He II-emission as a function of C IV blueshift for non-BAL quasars has also been identified by Baskin *et al.* (2015). Again, our results (Fig. 3.5) for the strength of He II-emission in the BAL and non-BAL populations across the C IV emission space show striking systematic behaviour and demonstrate the very close similarity in properties for BAL and non-BAL populations.

Simple comparisons of emission-line properties for the BAL and non-BAL populations as a whole will show differences as a result of the lack of BAL quasars with hard SEDs and strong, symmetric C IV λ1549 emission. The dearth of BAL quasars at the top left of the C IV emission space (Fig. 3.1) has naturally led to the conclusion that BAL quasars are more common among the quasar population with softer SEDs. Our analysis indicates the situation is somewhat more complex as BAL quasars exist across the entire remainder of the C IV emission space occupied by the non-BAL quasars. While SED-hardness is important, a stronger emission-outflow signature at fixed C IV EW is also relevant for increasing the probability that a quasar is a BAL quasar (Fig. 3.3). Overall, therefore, a key conclusion from the results presented in Section 3.2, is that, when an outflow is present, i.e., C IV blueshift > 0, the physical properties (including L, $L/L_{\rm Edd}$, SED-hardness) and ultraviolet emission-line properties of the non-BAL and BAL populations are essentially indistinguishable.

3.3.2 Absorber properties

Knigge *et al.* (2008) were the first to propose the existence of two-populations of absorbers among quasars with positive AI values. In our absorber classification a physically significant difference is evident between the AI(BI=0))-defined absorbers and those defined by AI(BI>0). Row five of Fig. 3.9 shows how, independent of the AI- or BI-value of troughs, the maximum absorber outflow velocity increases with increasing C IV emission blueshift. Row six, however, reveals a clear difference in the velocity extent of troughs, with AI(BI=0)-defined absorbers possessing a constant velocity width (ΔV), while the AI(BI>0) absorbers show a strong systematic trend of increasing ΔV with increasing maximum outflow velocity. The latter behaviour is consistent with outflowing absorbing material in an accelerating wind. The composite absorption spectrum of the AI(BI=0)) absorbers (Fig. 3.11) by contrast shows both components of the C IV $\lambda\lambda$1548,1551 doublet are visible. The typical velocity-spread within the absorber structures, independent of outflow velocity, must, therefore, be no more than $\simeq$250 km s^{-1}.

It is in the high-EW region of C IV emission space where quasars have the hardest ionising SEDs that we observe slightly narrower emission lines in the BAL quasars than the non-BALs (Fig. 3.4). If absorption is present in these spectra, it is typically deep and also narrower than the majority of the BI-defined troughs but is amongst the broader AI-defined

troughs. The narrower emission lines and hard SEDs, combined with the differing trough systematics, could suggest a different orientation of the quasars or a different outflow-driving mechanism (Richards, 2012) from that of the outflows traced by the absorption seen in all other areas of C IV emission space. Alternatively, certain sight-lines may probe different parts of the outflows, which may be dominated by different driving mechanisms.

The investigation presented here has focussed on quasars with BAL troughs while a study of the outflow properties of narrow C IV absorption lines in non-BAL and BAL quasars was undertaken by Bowler *et al.* (2014). Results included the detection of line-locked absorbers but, most relevant to findings presented here, also showed that the kinematics and population statistics of narrow absorbers in the non-BAL and BAL quasar sub-populations were similar. Combining the results with those presented here leads to a picture where, in respect of outflow signatures, the non-BAL and BAL quasar populations possess the same emission and NAL outflow properties strongly suggesting a direct link between apparent 'non-BAL' and 'BAL' quasars. We present further investigation of the narrow absorption line properties of non-BAL and BAL quasars in the next Chapter.

While the results in Section 3.3.1 support the idea that BAL quasars have the same parent population as non-BALs (Richards, 2006), it is clear that the properties of the absorption troughs change significantly across the C IV emission space, which is an observation that is expected from theory (see Giustini & Proga, 2019). The observation may be important in the context of understanding the origin of 'BAL quasars' as population statistics, such as the fraction of quasars classified as BALs, are potentially a strong function of the BAL definition. Put another way, BAL quasars can be found across nearly the full C IV emission space but BAL trough properties change in such a way that grouping all BALs together into the same subclass of objects may restrict the physical insight that can be gained into the origin and properties of outflows.

3.4 Conclusions

By reconstructing the quasar spectra, we have recovered the intrinsic C IV emission of BAL quasars even where said emission is heavily absorbed. This has allowed us to, for the first time, place the BAL quasars alongside the non-BAL quasars in C IV emission profile space (Fig. 3.1). We find that for every BAL quasar with certain C IV emission properties, there exists a non-BAL quasar with the same properties. The converse is not necessarily true; there are almost no BAL quasars at the highest EWs in C IV emission space with zero blueshift, compared to the non-BAL quasars.

In addition to C IV emission, BAL and non-BAL quasars are extremely similar in respect of their He II λ1640 EW, bolometric luminosity, and Eddington ratio (Figs. 3.5–3.7). The similarities in properties, some measured from the reconstructed emission spectra, suggest that the broad absorption observed in BAL quasars is the result of clumpy, outflowing

gas along the line-of-sight (broadly consistent with Yong *et al.*, 2018) and that all quasars – barring perhaps those with the hardest ionising-SEDs at the highest C IV emission EWs and lowest blueshifts – have the potential to be seen as BAL quasars but with varying probability (Fig. 3.3). The trough parameters also vary systematically in C IV emission space (Fig. 3.9), and we have gained insight into the trough-structure of the two AI-defined populations. At the highest C IV EWs, the BAL quasars have slightly narrower emission lines compared to the non-BAL quasars (Fig. 3.4) and it is also these BAL quasars that have quite different troughs from the rest of the BAL quasars – deep, narrow and close to systemic velocity – which perhaps could suggest a different driving mechanism of the outflows and/or a different quasar orientation.

Virtually every paper on BAL quasars starts by noting the two main hypotheses, which are that BALs are ubiquitous in the quasar population but have only a ∼20 per cent covering fraction or that they represent a distinct 20 per cent of the quasar population (with nearly 100 per cent covering fraction). With this Chapter we argue that the question is largely resolved (at least for high-ionisation BALs): the similarity of BAL and non-BAL quasars demands that BALs are not a distinct class of quasars. Rather, BAL quasars are normal quasars observed along a particular line of sight or at a particular time. Conceivably, both may be true given that BAL troughs can be transient (e.g., Capellupo *et al.*, 2012; Rogerson *et al.*, 2018; Yi *et al.*, 2019). Models invoking non-spherical geometries and particular viewing angles, e.g., BALs seen when the line-of-sight probes just above/below some form of obscuring torus, are not straightforward to reconcile with the strong systematic relationship between absorber and emission-line kinematics across the full range of C IV emission properties.

Chapter 4

Narrow Absorption Lines

Summary

This Chapter focuses on the narrow absorption lines (NALs) in our sample of SDSS quasar spectra. We explore the properties of the NALs in the C IV emission space, finding that for both non-BAL and BAL quasars the velocity of the outflowing NALs increase as the C IV blueshift increases. The velocity of line-locked systems, which are evidence of radiation line-driving, also increases as blueshift increases. We also explore the properties of the NALs detected within the BAL troughs and find them to be tracing gas with the same ionisation state as the NALs found outside the BAL troughs. The similarities between the NALs in BAL and non-BAL quasars provides further evidence that BAL and non-BAL quasars are drawn from the same parent population. We suggest that the majority of absorption troughs with zero Balnicity Index but positive Absorption Index are in fact high-EW C IV NALs. With this Chapter, a main result of this thesis is the correlation between the outflow signatures seen in absorption – broad and narrow – with the emission outflow signature.

The investigation presented in this Chapter is not yet published. P. C. Hewett performed the initial NAL search with the Gaussian templates detailed in Section 4.2.

4.1 Introduction

The final outflow signature that we are yet to discuss in any detail are the narrow absorption lines (NALs). The location, structure, and mechanics of quasar outflows are by no means solved; however, the discovery of NALs inside BAL troughs (Bowler *et al.*, 2014; Mas-Ribas & Mauland, 2019) points to a wind with varying density along our line-of-sight over a significant velocity range, and many simulations also produce complex structures (e.g., Proga *et al.*, 2014).

The mechanism for driving quasar outflows is not yet determined, but, as mentioned in Chapter 1, a combination of processes including magnetic fields and radiation line-driving could be plausible. Unambiguous evidence of the latter is the detection of line-locked NAL systems in quasar spectra. Simulations (Chelouche & Netzer, 2003) have suggested that line-locking is common in radiatively-driven outflows. It had been suggested that non-BAL quasars did not show extensive evidence of line-locking based on arguments that velocity separations comparable to line-locked systems were occurring purely by chance and that low-velocity ejections were favoured such that the small velocity separations were not significant (Sargent & Boroson, 1977). The statistics have since improved and Bowler *et al.* (2014) discovered that line-locking is as likely in non-BAL quasars as it is in BAL quasars. The similarities between the BAL and non-BAL quasar populations in Chapter 3 is supported by the finding in Bowler *et al.* (2014) that there is no detectable difference in the ionisation state of the gas responsible for the NALs between the BAL and non-BAL quasars. For both populations the ionisation parameter of the outflowing gas was seen to decrease as the NAL velocity increased, and the authors attribute this effect to an accelerating outflow (see also Chen *et al.*, 2021; Perrotta *et al.*, 2018).

Chen *et al.* (2021) claim that the ionisation state of high-velocity (0.1–0.2c) line-locked systems is higher than of the single absorbers at the same velocities; however, they do not account for the contamination by low-ionisation intervening systems that will dominate the high-velocity NALs (which they estimate account for 66–86 per cent of the high-velocity NALs). Bowler *et al.* (2014), on the other hand, deliberately corrected the absorption properties for the presence of intervening absorbers and observed no differences between the properties of the doublet and triplet systems over the range of NAL velocities dominated by outflowing systems.

In this Chapter, we describe an investigation of the C IV NAL systems, both single and line-locked, in the context of the C IV emission space in an effort to link the outflow signatures seen in absorption with those in emission. In Section 4.2, we present the procedure of finding and fitting the NALs in both the non-BAL and BAL quasars. We use the spectrum reconstructions presented in Chapter 2 to improve the detection of absorbers particularly within the C IV emission line profile. Our analysis benefits from the size of the quasar sample, having selected the quasars from the SDSS DR14 quasar catalogue (Pâris *et al.*, 2018).

The average S/N per pixel is lower for the DR14 objects (due to the fainter magnitude limit; see Section 2.3) than for DR7 which was utilised by Bowler *et al.* (2014); however, in Section 4.3 we are able to perform a novel investigation into the properties of the absorbers detected inside and outside the BAL troughs. Here, we also explore the distribution of the C IV doublets in C IV emission space and compare the BAL and non-BAL quasars. Section 4.4 discusses the properties of the line-locked systems in the context of the C IV emission space and again compares the BALs with non-BAL quasars and the in-trough with out-of-trough absorption.

4.2 Finding and fitting C IV NALs

4.2.1 NAL search

We use the quasar sample from Chapters 2 and 3 which have redshifts $1.5 < z < 3.5$ and average S/N ≥ 5 per pixel. The first step in finding and fitting the NALs is to create the absorption spectrum that can then be searched for single Gaussian profiles. For each quasar in our sample, the reconstruction is subtracted from the spectrum to create a difference spectrum which is then median-filtered with a 201-pixel window to remove any low-level (up to a few per cent) differences between the spectrum and reconstruction. This median-filtered spectrum is then subtracted from the difference spectrum to leave behind the signature of any narrow absorbers. The resulting absorption spectrum is searched for single Gaussian absorber components in a similar manner to that in Bowler *et al.* (2014)[1] and the procedure is summarised briefly here. Gaussian templates of different widths (FWHMs $\approx$ 162, 203, 244, 325 km s^{-1}) are centred at half-pixel intervals between 1381 Å and 1568 Å and the best-fitting template is selected using the template with the minimum χ^2. The final candidate list contains Gaussian absorption profiles with 3-σ detections. The search for C IV doublets and triplets could be conducted with templates that have two and three components to maximise the S/N of detections, however, the search was deliberately performed via the identification of individual absorption components in order to simplify the statistics of the detections.

With a list of absorber candidates and their locations in each spectrum, we then fit Gaussian profiles to each candidate using the Python package LMFIT with more freedom in the parameter values than was allowed during the initial template-fitting search.

C IV doublets are then found by searching for components that are separated by $\sim 497 \pm 69$ km s^{-1} (the velocity separation of the 1548 Å and 1551 Å C IV components with an error of the width of an SDSS pixel). Each doublet is then also considered part of a triplet system if there is a third absorption component located $\sim 750 \pm 69$ km s^{-1} from the mean velocity of the doublet.

[1]The search was performed using code that was employed in Bowler *et al.* (2014).

In addition to the search presented above using the reconstruction-based absorption spectrum, the AI- and BI-classified quasars are searched a second time with a different absorption spectrum. The goal of this second search is to find absorption systems within the BAL troughs and this is achieved by creating an absorption spectrum where the broad absorption has been removed. The absorption spectrum is defined by median-filtering each quasar spectrum with a 41-pixel window and subtracting this from the original spectrum, as in Bowler *et al.* (2014). With the absorption spectra created, the routine for locating the C IV NALs can proceed as detailed above.

4.2.2 Absorption in and out of troughs

Each BAL quasar spectrum was searched twice for NALs: first with the reconstruction-based continuum and second with the 41-pixel median-filtered spectrum. We aim to use the reconstruction-based continuum for NALs outside of the broad absorption troughs and only default to the median-filtered spectrum continuum for regions of the spectra within troughs. We use the trough parameters defined in Section 3.2.4 to split each spectrum into in/out troughs and include NALs in the final sample that have been detected using the appropriate continuum for that spectrum segment.

For the BI-selected BAL quasars, determining which NALs are in and outside of BAL troughs is relatively straightforward. Using the trough parameters defined in Section 3.2.4, each BI trough has a width of at least 2000 km s^{-1}– much wider than an individual C IV doublet.

For the AI(BI=0) quasars, defining the set of in-trough absorption is more complicated. Knigge *et al.* (2008) found two populations of AI quasars: those with high AI-index typically had BI>0 (AI(BI>0)) and those with low AI-index typically had BI=0 (AI(BI=0)). We were able to reproduce the result with our BAL classifications (see Section 2.5.1 and Fig. 2.9). Additionally, the mean composite of the AI(BI=0) quasars in the trough's rest-frame in Fig. 3.11 is a clear demonstration that many of the AI(BI=0) troughs are in fact coincident with the location of a narrow C IV absorption line. For this reason we use the reconstructions to define the continuum of the NALs that are in AI(BI=0) troughs with the deepest part above 3000 km s^{-1} (below this velocity many of the troughs are actually quite wide but have BI = 0 because of the minimum starting velocity of the BI classification). There is the possibility that some AI troughs that are wider than a C IV doublet and just narrower than the BI threshold are not treated appropriately; however, the majority of AI troughs are actually quite narrow – consistent with doublet and triplet widths (see Appendix C).

Table 4.1: Doublets with $\beta < 0.08$ and triplets with $0.01 < \beta < 0.1$ in the final sample. Columns 2 and 4 contain the number of doublet and triplet systems, respectively. Columns 3 and 5 describe the fraction of quasars with at least one absorption system.

		Doublets		Triplets	
	No. quasars	N	$F_{\rm qso}$	N	$F_{\rm qso}$ [a]
non-BAL	76 150	25 255	0.28	109	0.010
AI	50 698	44 245	0.58	1296	0.054
BI	15 161	12 179	0.53	366	0.057

[a]As a fraction of the number of quasars with one or more doublets in the triplet β-range.

4.2.3 Final NAL sample

We restrict the final NAL sample based on the following criteria applied to each single Gaussian absorber:

1. absorber S/N ≥ 3 where the noise is the SDSS pixel noise;
2. absorber EW ≤ 4 Å;
3. absorbers outside troughs must have EW ≥ 0.1 Å but the threshold is not applied for absorbers within troughs;
4. Gaussian FWHM $150 \leq \sigma \leq 340$ km s^{-1} where the minimum is set by the resolution of the SDSS spectra and the maximum by the width above which the doublet components become blended together and are no longer detected as two distinct absorbers;
5. and reduced-$\chi^2 \leq 5$ which is deliberately lenient to allow the inclusion of particularly high-S/N absorbers and to account for the frequent presence of a second close absorber affecting the adjacent 'continuum' region.

Additionally, doublets are only included in the final sample if they have $\beta < 0.08$ where β is the velocity of the NAL, v, with respect to the systemic velocity as a fraction of the speed of light. Triplets with $0.01 < \beta < 0.1$ are included in the sample (see Section 4.4). Of the 76 150 non-BAL quasars, 21 302 have at least one C IV doublet, and 109 have at least one triplet. There are 50 698 AI(BI=0) quasars in our sample, with 29 601 having a doublet and 1276 with a triplet. The classically-defined BAL quasars number 15 161, 8027 of which have at least one doublet and 358 have a triplet. Table 4.1 summarises the NAL sample. Overall, the BI quasar population has a higher incidence of NALs detected compared to the combined non-BAL+AI population. Chen *et al.* (2020) also found more NALs in their BAL population compared to their non-BAL sample. The high incidence of NALs in the AI population alone is due to the high probability a quasar is classified as AI when a NAL is present.

4.3 C IV doublets

4.3.1 β-distribution

In Fig. 4.1 we plot the β distribution for the C IV doublets in our quasar sample. The overall shape of the distribution in the left-hand panel is similar to what is found across various NAL investigations (Wild *et al.*, 2008; Bowler *et al.*, 2014; Chen *et al.*, 2020). The sharp peak at $\beta = 0$ is populated by associated absorption systems; outflowing NALs are expected to populate the $0.01 < \beta < 0.05$ region; and intervening systems dominate at $\beta > 0.05$. The intervening NALs should be uniformly distributed in β and it is possible to estimate the contamination of the outflowing and associated populations by intervening systems. We make an estimate of the fraction of doublets in the β range 0.01–0.05 that are outflowing as opposed to intervening by considering the number of absorbers (which are likely intervening) at $\beta = 0.06$–0.08 in the non-BAL population. The number of intervening systems should be constant with β, thus subtracting twice[2] the number of systems at $0.06 < \beta < 0.08$ from the number of systems between $0.01 < \beta < 0.05$ provides an estimate of the number of outflowing systems for each quasar population. The fraction of systems with $0.01 < \beta < 0.05$ that are outflowing in the non-BAL, AI and BI quasars is 33.2, 90.1, and 88.3 per cent, respectively. For reasons that will become apparent later, we note that the combined non-BAL+AI population has an estimated outflowing fraction of 80.1 per cent. There is a significant increase in the fraction of NALs that are outflowing for the AI and BI population. In the cases where we compare BAL and non-BAL NAL properties, we consider the results in the context of the different contamination fractions and cannot make any quantitative claims about the ionisation state of the gas, for example.

Some discussion should be had on the effect of BAL-classification on the detection of NAL systems. As a reminder, the BI-classification runs from 3000–25 000 km s^{-1} ($\beta = 0.01$–0.08) and defines a trough to be a minimum 2000 km s^{-1}-wide contiguous region of spectrum falling below 0.9 of the continuum level. The AI-classification covers 0–25 000 km s^{-1} and includes troughs with a minimum width of 450 km s^{-1}. The maximum velocity for the BAL-classification is such as to avoid confusion with Si IV absorption. The doublet search extends beyond $\beta = 0.08$ which leads to a modest apparent excess of C IV doublets due to chance coincidences of components of Si IV doublets particularly close to the Si IV absorption close to systemic velocity. Additionally, there is an apparent increase in the number of non-BAL NALs and a decrease in AI NALs at $\beta > 0.08$ since no NALs will be classified as AI troughs regardless of the EW of the absorption. For these reasons, when considering the C IV doublets we place a maximum $\beta = 0.08$.

For the sample of AI quasars, the definition of in or out of an AI trough leads to a different distribution of NAL velocities than would be expected from just using the AI trough param-

[2] factor of two to account for the 'outflowing' beta range being twice the width of the range $\beta = 0.06$–0.08

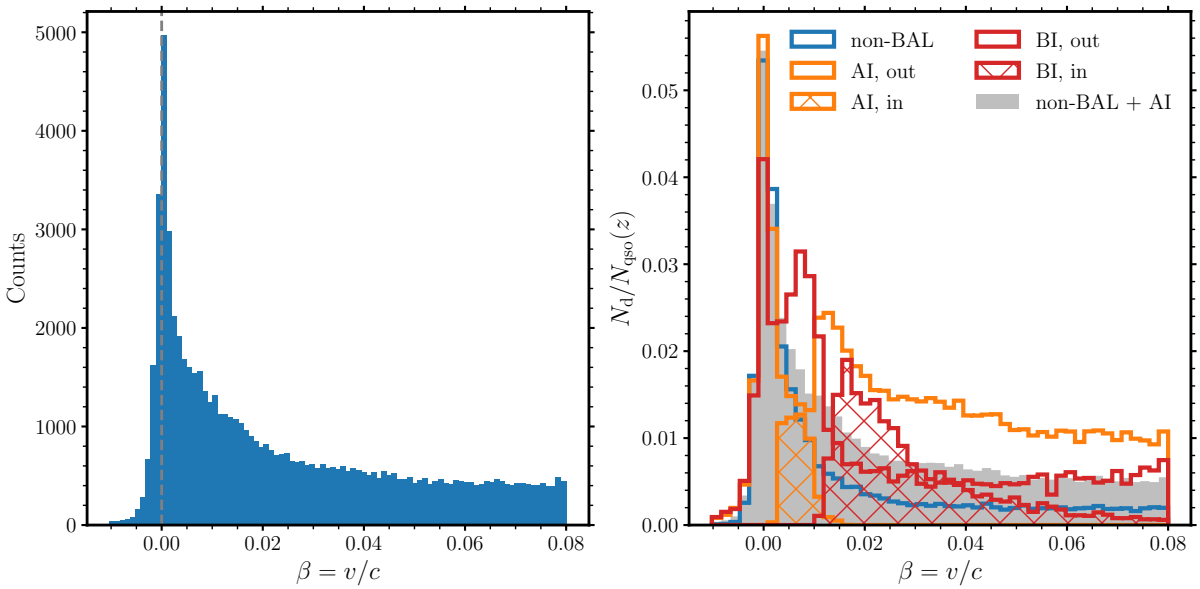

Figure 4.1: C IV doublet β distribution for all quasars (left) and for the non-BAL, AI(BI=0), and BI-defined quasars (right). In the left-hand panel, the sharp peak at $\beta = 0$ contains the associated absorbers. We define the outflowing NALs as having $0.01 < \beta < 0.05$. At $\beta > 0.05$ the NAL population is dominated by intervening absorption systems and is essentially flat. In the right-hand panel, the doublet count in each bin is normalised by the number of quasars with spectral coverage of that β and defined as non-BAL, AI, or BI quasars as appropriate. The AI and BI NAL populations are also split into in-trough and out-of-trough NALs (see text for details).

eters. There is the strong peak of associated absorbers at $\beta = 0$, the majority of which are classed as out-of-trough. The only in-trough NALs are occurring between $\beta = 0$ and ~0.01. While many NALs at $\beta > 0.01$ are coincident with AI troughs, all of these NALs are classed as out-of trough with our definition.

Also plotted in the right-hand panel is the combined non-BAL+AI population of NALs which will be considered throughout this Chapter for reasons mentioned previously. The results of Knigge *et al.* (2008) which were supported by our investigation of the AI(BI=0) quasars and the composite AI-trough in Fig 3.11 lead us to conclude that the majority of the AI troughs are C IV NALs with EWs large enough to satisfy the AI definition. The higher percentage of systems that are outflowing in the AI population than the non-BAL population, reported previously, is consistent with this conclusion given that the number density of intervening systems is expected to drop off rapidly as EW increases (Cooksey *et al.*, 2013).

The β-distribution of NALs in the BI quasars is also dependent on the BI-classification. Like all of the other sub-populations of quasars, the associated absorbers at zero velocity are present. The excess doublets below 0.01 is mostly due to the BI classification starting at $\beta = 0.01$ and so no NALs in the BI quasars will be in troughs at $\beta < 0.01$. The β distribution of the in-trough BI NALs is governed by the location in velocity space of the BI troughs.

4.3.2 Composite NAL spectra

The majority of the absorbers in our sample are low-S/N and thus do not facilitate an investigation on the individual absorber properties. Composite absorption spectra in the rest-frame of the C IV doublets however, allow the average NAL properties to be explored for various sub-populations. The median composite spectra presented in Fig. 4.2 of the BI and non-BAL+AI doublets are constructed as follows.

First, a 41-pixel median filter is applied to each spectrum to create the continuum. The same continua were used in the process of identifying the NAL absorption in BAL troughs and here we do the same to all spectra in our sample to ensure that the continuum, against which the NALs are detected, is defined using the same definition for all samples. The continuum is then divided into the quasar spectrum leaving the absorption spectrum. Finally, the median composite spectra are generated by moving each absorption spectrum to the rest-frame of the absorber (using a nearest-pixel approach to avoid re-binning) and calculating the median flux in each pixel. Spectra with more than one C IV doublet contribute to the composite for each doublet at each NAL's rest-frame. The number of absorbers is generally large; however, the Mg II in the composites, where there are significant contributions from absorbers at redshifts $z_{\rm abs} > 2.3$, can be unreliable due to the very low spectrum-S/N at observed wavelengths > 9300 Å. All composites presented in this Chapter are median composites but we have checked that they are in good agreement with the mean composites.

The composite spectra in Fig. 4.2 are created from the outflowing NALs at $0.01 < \beta < 0.05$. The excess flux above unity around the absorption features is an artefact of the 41-pixel median-filter used in the continuum-generation. The redshift range and wavelength limits of the spectrograph result in fewer quasars contributing to the Lyβ and Mg II absorption lines than the C IV system; however, the presence of these and other species in the absorption spectra highlight that the majority of the doublets in our sample are indeed real. We make no claim about the ionisation state of the gas from Fig. 4.2 since the composite spectra cover a large range in velocity space ($0.01 < \beta < 0.05$) and different quasars contribute to the composite of the different absorption features. However, Bowler *et al.* (2014) found that the N V:C IV EW ratio decreased as β increased while the Mg II:C IV increased for the BAL and non-BAL quasars alike, suggesting a lower-ionisation parameter of the gas as NAL velocity increases. In the intervening systems, Bowler *et al.* (2014) measure N V:C IV < 0.01 and Mg II:C IV ≈ 0.62, compared to 0.31 and 0.42, respectively, in the range $\beta = 0.02$–0.03 (see their table 5). The median β is significantly larger for the non-BAL+AI sample than the BI sample which leads to the median BAL doublet system tracing a higher ionisation state than the median non-BAL doublet. Additionally, the higher fraction of non-BAL+AI doublets that are potentially intervening (∼19.9 per cent compared to ∼11.7 per cent of the BI NALs) and are therefore tracing gas of a much lower ionisation state means that the median non-BAL N V:C IV and Mg II:C IV EW ratios more closely resemble the intervening EW

ratios (N V:C IV ≈ 0.06 and Mg II:C IV ≈ 0.28) compared to the BI values (N V:C IV ≈ 0.30 and Mg II:C IV ≈ 0.07). Upon binning in β, we produce similar results to Bowler *et al.* (2014). The lack of a minimum EW for the doublets found inside troughs is also partly responsible for the significantly weaker Mg II absorption in the BI composite.

Based on the similarities in emission properties found between the BAL and non-BAL quasars in Chapter 3 and the results from Bowler *et al.* (2014) that the absorber systems in BAL quasars show the same trends in ionisation parameter as in the non-BAL quasars, we predict that the absorber systems appearing in and out of troughs in the BAL population will show the same level of ionisation. In Fig. 4.3 we test this hypothesis by plotting the continuum-normalised composite NAL doublets in and out of BAL troughs for the BI quasar population.

Before discussing the results of this test, it is important to first note the remaining differences when detecting NALs in and out troughs. The additional broad absorption causes the effective local continuum to be much lower. For our sample, the continua of the BI out-of-trough NALs are on average a factor of $\sim$1.7 higher than the in-trough continua. For absorption lines detected at moderate S/N the EW of the lines is preserved, independent of whether in or out of a trough. At low S/N, however, the absorption-line detection threshold corresponds to a limit on the area of the line rather than the EW. The noise is dominated by contributions from the sky and, other than for very bright quasars, is thus independent of whether the absorption line is in or out of a trough. As a consequence, absorption lines detected close to the S/N = 3 threshold within BAL troughs possess EWs a factor of 1.7 larger than those detected out of the troughs. Absorber EWs in composite spectra, including significant numbers of low S/N absorbers detected within troughs, are, therefore, of somewhat higher EW compared to out of trough absorbers. The systematic effect is compensated somewhat by the lack of a minimum threshold on the EW for absorption lines within troughs. The first effect dominates for absorption within significant troughs and the C IV and N V lines are slightly stronger in Fig. 4.3, while for lines outside of troughs the lack of the EW threshold leads to weaker lines, as evident from the difference in the depths of the Mg II absorption.

4.3.3 Doublets in C IV emission space

The C IV emission space has been used throughout this thesis as an indicator of the strength of any wind relative to the strength of the classic broad line region component. Here, we examine the relationship between the C IV doublets and C IV emission space. Before we do so, however, we showed in Figs. 3.6 and 3.7 that the bolometric luminosity and Eddington ratio both increase towards the lower-right of C IV emission space which leads to an increase in the average continuum S/N at high C IV blueshifts for our flux-limited quasar sample. The NAL detection function will thus change across C IV emission space with a higher detection fraction at the bottom-right of the space where the S/N is greatest.

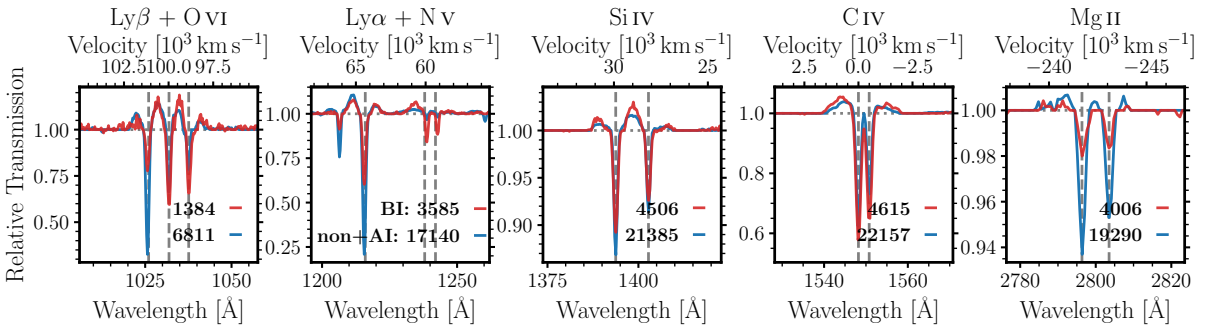

Figure 4.2: Median composite of the BI (red) and non-BAL+AI quasar (blue) doublets at $0.01 < \beta < 0.05$ in the doublet rest-frame. The number of spectra with the appropriate wavelength coverage is noted in the panels' legends. The presence of other species in absorption confirms that the doublets are real. Dashed vertical lines mark the wavelengths of the species visible in each panel.

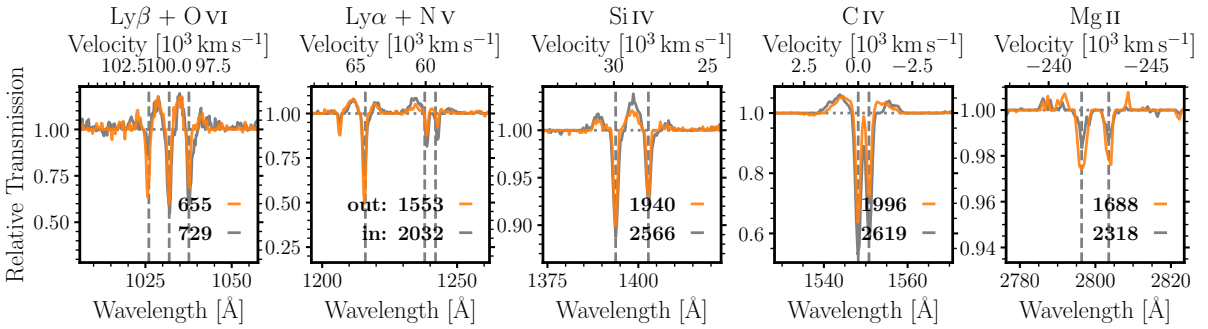

Figure 4.3: Median composite of the BI-quasar doublets at $0.01 < \beta < 0.05$ in the doublet rest-frame. Doublets that are detected in troughs contribute to the grey composite spectra, and those out of troughs to the orange spectra. With selection effects in mind (see text), there appears to be no difference in ionisation state of the gas producing the absorption in BAL troughs from that out of the BAL troughs.

Figure 4.4 contains the mean number of associated, outflowing, and intervening doublets per quasars in C IV emission space. The top row shows the distribution of NALs between $0 < \beta < 0.01$ where associated absorbers dominate. The average number of doublets per quasar increases towards the top-left of C IV emission space for both the non-BAL+AI and BI quasars. The lower incidence of associated NALs in the region of C IV emission space where disc-winds are thought to strongest, could be an indication that the gas responsible for the absorption has been blown out from the galaxy. Alternatively, Stone & Richards (2019) proposed that the presence of $\beta \simeq 0$ NALs is an indication of an edge-on orientation (or as close to edge-on without being obscured by some dusty torus) based on an investigation of the FIRST radio properties of quasars and their NALs. They found an excess of 'steep' radio-spectrum objects at $\beta \simeq 0$ and, assuming that a steep spectrum is an indication of an edge-on orientation of the radio jets and therefore the quasar, the authors suggest that the $\beta \simeq 0$-NALs are detected in edge-on objects. If $\beta \simeq 0$-NALs are an indication of edge-on orientation then it could be argued that the high-EW, low-blueshift region of C IV emission space contains more edge-on systems.

The bottom row covers $0.01 < \beta < 0.05$ which is populated by outflowing (and interven-

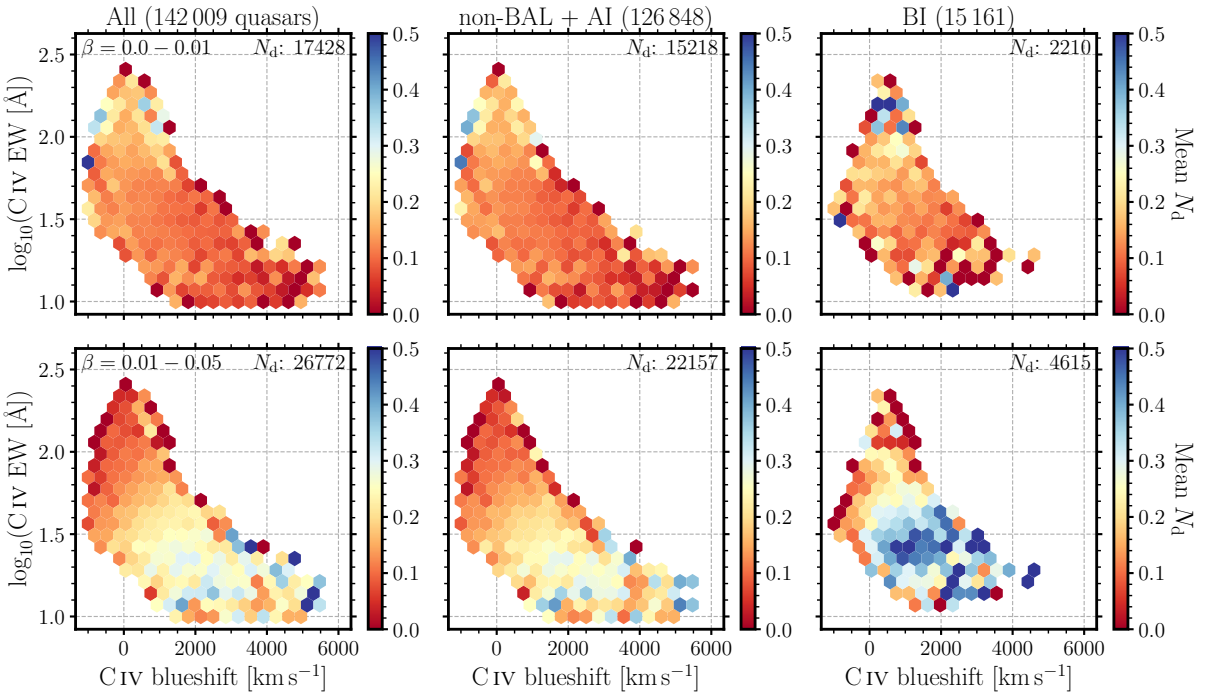

Figure 4.4: Mean number of C IV doublets per spectrum in different velocity ranges as a function of location in C IV emission space for all quasars (left), non-BAL and AI quasars (middle), and BI quasars (right). Only hexagons with 5 or more quasars are plotted. The top row contains the doublets at $\beta = 0.0$–0.01 where the associated systems dominate. The number of associated systems decreases from the top-left to bottom-right of C IV emission space. $\beta = 0.01$–0.05 contains a significant fraction of outflowing systems and is covered by the bottom row. Conversely to the associated systems, the number of doublets increases from the top-left to bottom-right. Colour bars are identical on every axis.

ing) NALs. Here, the mean number of absorbers is increasing towards the bottom-right where winds are expected to be strongest. In Chapter 3 we found that the BAL trough parameters, including the balnicity index correlated with location in C IV emission space, showing more absorption at higher C IV blueshifts. We thus predicted that the NAL outflow signature will increase as C IV blueshift increases which is what we observe. Moreover, the similarities between the BAL and non-BAL quasars we described in the same Chapter and the nature of the NAL detection in Bowler *et al.* (2014) in the BAL and non-BAL quasars lead us to expect that the distribution of outflowing NALs in BALs and non-BAL quasars should be similar. The middle and right-hand panels in the bottom row show that while the non-BAL+AI and BI quasar populations do both show an increase in the number of NALs per quasar as C IV blueshift increases and EW decreases, the number of NALs in the BI quasars is approximately twice what is seen in the non-BAL+AI population at the highest blueshifts. We calculated in Section 4.3.1 that a larger fraction of the doublets may be outflowing – as opposed to intervening – in the BI population compared to the non-BAL+AI population which could account for the stronger trend across the C IV emission space for the BI quasars. A model where the sight-lines that produce BALs have a higher likelihood of producing NALs in order to explain the higher overall incidence of NALs in the BAL quasars is

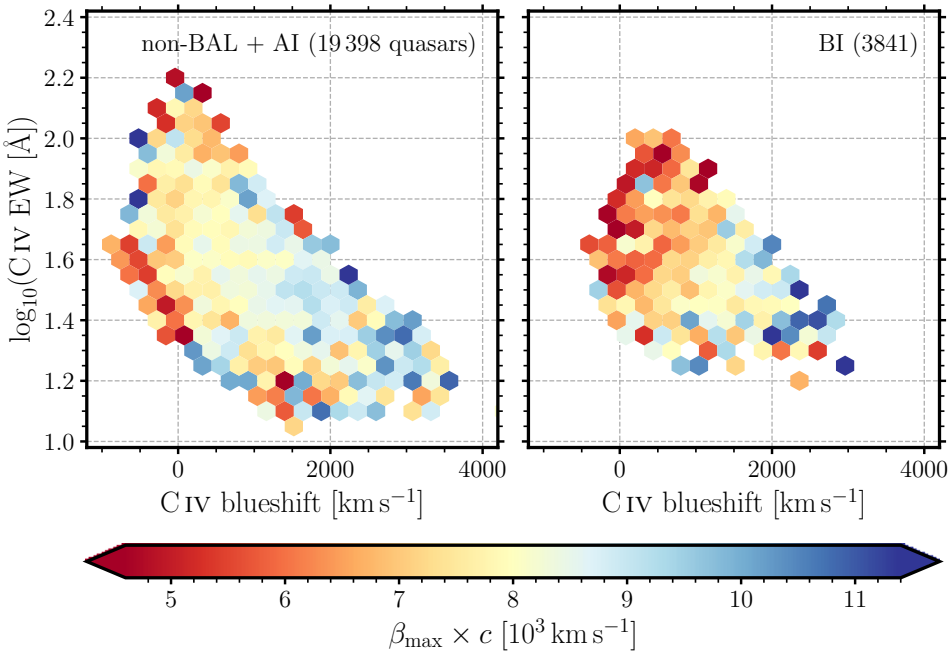

Figure 4.5: Maximum velocity of the outflowing ($0.01 < \beta < 0.08$) C IV doublets as a function of location in C IV emission space for the non-BAL+AI quasars (left) and the BI BALs (right) with at least one C IV doublet. Each hexagon is colour-coded by the median maximum NAL velocity of the quasars in that bin and only bins with at least 5 quasars are plotted. In both populations the overall trend is an increasing maximum velocity as C IV blueshift increases.

one plausible scenario and is indicative of the highly structured nature of quasar outflows.

The systematic increase in S/N across the C IV emission space does not account for all of the trends in Fig. 4.4. An investigation into the detection rate of the intervening systems across the space revealed that the S/N selection effect is weak. The average number of absorbers with $0.06 < \beta < 0.08$ per quasar increases from ∼0 in the top-left of C IV emission space to ∼0.15 in the bottom-right for all quasars (c.f. the increase to ∼0.25 in the bottom-left panel of Fig. 4.4 and also to ∼0.4 in the BI quasars).Accounting for the S/N effect in the bottom row would not remove the observed trends and cannot remove the differences between the BI and non-BAL+AI populations. Additionally, the fact that, in the top row, the absorber counts decrease towards the bottom-right where the S/N is greatest give us confidence that the S/N selection effect is small. This opposing trend in the top row would only grow stronger by accounting for the S/N effect.

In Chapter 3, we discovered that the AI and BI trough velocities varied systematically in C IV emission space. With our finding that the majority of the AI troughs are C IV NALs, it is perhaps not surprising that the relationship between location in C IV emission space and NAL velocities is similar to that with the AI trough parameters (see Fig. 3.9). In the left-hand panel of Fig. 4.5 we plot the maximum NAL velocity in the non-BAL+AI quasar population in C IV emission space and find that the observed trend is particularly reminiscent of $V_{\mathrm{max,450}}$ of the AI(BI=0) quasars in Fig. 3.9.

The right-hand panel contains the velocities of the C IV doublets found in the BI quasars. The median of the maximum NAL velocity in each hexagon in the non-BAL and BAL populations can be seen to increase as the C IV blueshift increases which is again consistent with BAL quasars being drawn from the same parent population as the non-BAL quasars. The larger fraction of truly outflowing NALs in the BI population could account for the stronger trend across the space compared to the non-BAL+AI populations. In addition to the median, the mean and mode of the maximum NAL velocity increase towards the high blueshift end of C IV emission space, suggesting that the increase in velocity is not purely the result of the existence of a population of high-velocity NALs in spectra with large C IV blueshifts but instead a shift in the whole distribution of NAL velocities as blueshift increases.

4.4 Line-locked systems

Bowler *et al.* (2014) found line-locked C IV systems in both BAL and non-BAL quasars with similar incidence rates. These triplets were detected in outflows up to 20 000 km s^{-1} and Chen *et al.* (2021) has since searched for and found line-locked absorption up to outflow velocities of 60 000 km s^{-1}. Bowler *et al.* (2014) also find no differences between the doublet and triplet absorber properties. With these discoveries in mind, we expect that the trends observed in the C IV emission space with the C IV doublets will be similar to what is observed in the line-locked absorbers. We also do not expect to see any differences between the line-locked systems in the non-BAL and BAL quasar population, nor any differences between those found in BAL troughs to those outside.

We limit our search for line-locked NALs to $0.01 < \beta < 0.1$. The high-velocity limit is higher than for the outflowing doublets due to the reduced risk of contamination by three coincident Gaussian profiles, true doublet plus one coincident Gaussian absorption line, or two coincidentally overlapping doublets. Neither do we have contamination by true line-locked but intervening systems since the construction of a line-locked system is direct evidence of radiation-line driving and so any line-locked system is an outflowing system. In fact, any contamination by spurious Gaussian profiles can be seen in the relative depths of the two Si IV doublets line-locked at 500 km s^{-1} in Fig. 4.6. Note that the BI composite is noisier than the non-BAL composite given the factor of ∼3.3–4.0 more quasars in the non-BAL composite from Lyβ to Mg II. Taking the ratio of the blue components of the two Si IV doublets (1393.76 Å), we estimate that 1404 (∼ 0.99 per cent) of the 1405 non-BAL+AI triplets and 363 (∼ 0.99 per cent) of the 366 BI triplets are real. We keep the minimum $\beta = 0.01$ due to the high number density of C IV doublets at $\beta < 0.01$ which would lead to a higher fraction of coincident doublets contaminating the triplet population.

It is clear from the composites in Fig. 4.6 that the absorption of the low-ionisation Lyα and Lyβ is markedly stronger in the non-BAL composite (the Lyα is a factor of ∼1.9 stronger) and the high-ionisation N V weaker. The median β of the non-BAL quasar composite is

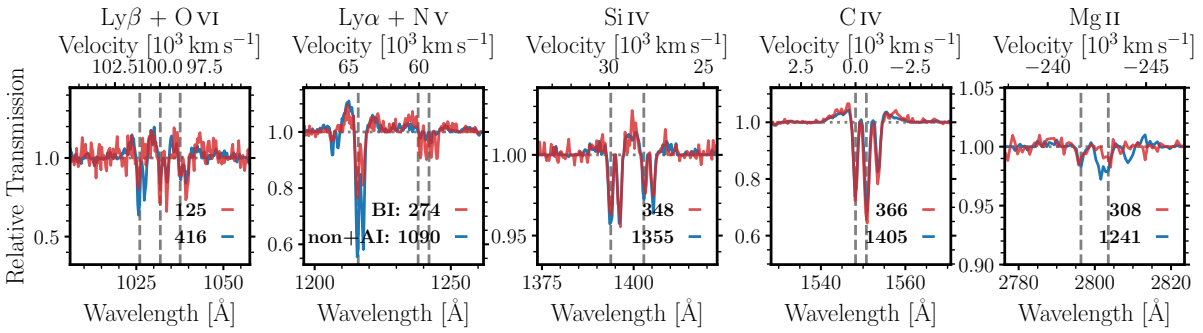

Figure 4.6: Median composite of BI (red) and non-BAL+AI (blue) triplets at $0.01 < \beta < 0.1$ in the triplet rest-frame. The presence of the two Si IV doublets with essentially identical EWs show that the triplet sample contains almost no cases where the C IV triplets are due to chance coincidences of unrelated absorbers. Dashed vertical lines mark the wavelengths of the species visible in each panel. The absorption from the line-locked system can be found 500 km s^{-1} to the right of the vertical lines.

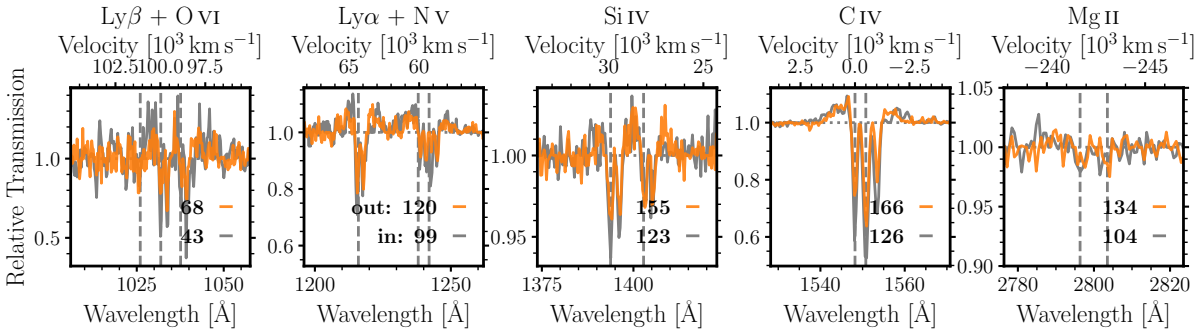

Figure 4.7: Median composite of the BI-quasar triplets at $0.01 < \beta < 0.08$ in the triplet rest-frame. The β interval is chosen in order to compare the C IV triplets that are detected in troughs (grey) to those out of troughs (orange). There are no discernible differences between the line-locked absorption in troughs and out of troughs.

≈ 0.038 which is greater than the median $\beta \approx 0.029$ of the BI composite. The differing strengths are consistent with the decreasing ionisation parameter with increasing β reported by Bowler *et al.* (2014) (see also their figs. 7 and 8). Bowler *et al.* (2014) would predict that the Mg II absorption in this non-BAL composite should also be deeper, which appears to be true in Fig. 4.6, however, the low-S/N of the BI composite precludes a definitive comparison.

Just as with the doublets, we expect the line-locked systems inside BAL troughs to be identical to those outside, modulo the effect of the differing local continua. In Fig. 4.7, we show that this is indeed the case and suggests that gas entrained in the much more extensive wind traced by the BALs has the same properties as the outflowing gas outside of the BALs.

With line-locked systems being direct evidence of radiation line-driving, a prediction of our model is that the velocity of the triplet systems will correlate with the C IV blueshift. Ideally, we would divide the population of triplets into BAL and non-BAL quasars and investigate the incidence of triplets across C IV emission space or the maximum velocity;

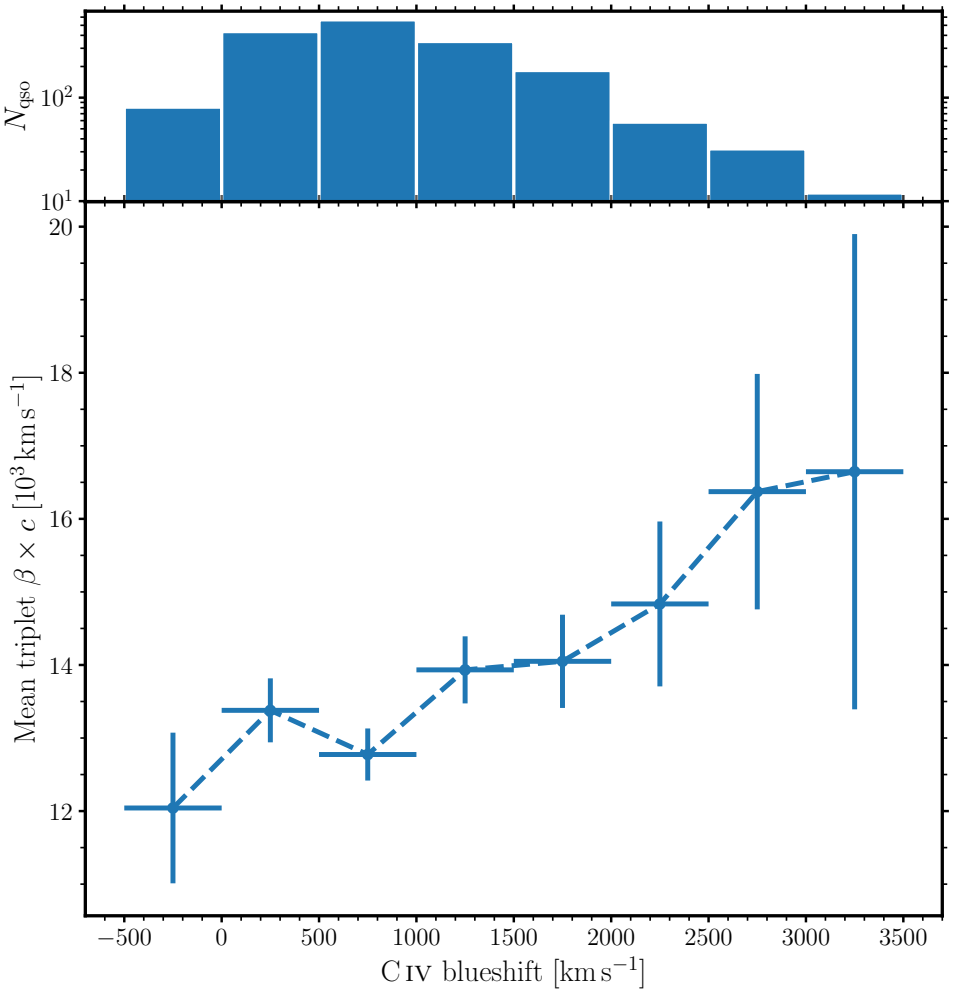

Figure 4.8: Mean triplet velocity in bins of C IV blueshift for $0.01 < \beta < 0.1$. For the 28 quasars with two triplets, the highest velocity NAL is selected. The top panel contains the number of quasars in each blueshift bin. The error bars show the bin width and the standard error on the mean. The mean triplet velocity is consistent with an increased triplet velocity as C IV blueshift increases.

however, we do not have a large enough sample to produce plots like Figs. 4.4 and 4.5. In Fig. 4.8 we have instead plotted the mean triplet velocity in bins of C IV blueshift for the non-BAL+AI and BI quasar samples combined. The maximum triplet velocity is chosen for the 28 quasars with more than one triplet. The triplet velocity is seen to increase as C IV blueshift increases from ∼12 000 km s^{-1} at zero blueshift up to ∼16 000 km s^{-1} at blueshifts of ∼3000 km s^{-1}. From Figs. 4.6 and 4.8 it is clear that radiation line-driving is important in both BAL and non-BAL quasars.

4.5 Conclusions

We have investigated the narrow C IV absorption line systems in our sample of BAL and non-BAL quasars, making use of the spectrum reconstructions. We have searched for C IV NALs in and out of BAL troughs and considered the incidence and velocity of the doublets

and line-locked systems in the context of the C IV emission space. Our main results are as follows:

- The majority of AI(BI=0) troughs, as defined by the Absorption and Balnicity indices, are C IV NALs and line-locked systems.
- Doublets at $0.0 < \beta < 0.01$ where NALs tracing gas associated with the quasar environment or host galaxy dominate have a higher incidence at low C IV blueshifts and high C IV EWs and this is true for the non-BAL quasars and BI quasars (top row of Fig. 4.4). Possible scenarios include the gas being blown out of the galaxy when the C IV blueshift is high and winds are strong, or the low-velocity NALs are an indicator of an edge-on orientation (Richards *et al.*, 2021) and quasars at high-C IV EW are more likely edge-on.
- Doublets at $0.01 < \beta < 0.05$ which are thought to be outflowing show increasing NAL velocities as C IV blueshift increases (Fig. 4.5). Therefore, NALs are faster when the outflows traced by emission are strongest.
- The velocity of the line-locked systems, which are evidencing radiation-line driven outflows, is also increasing as the emission outflow signature increases highlighting the importance of line-driving in both quasar populations (Fig. 4.8).
- We find that the doublets and triplets found in BAL troughs do not appear to show any differences in ionisation state from those outside troughs (Figs. 4.3 and 4.7).

SDSS DR16 (Lyke *et al.*, 2020) contains an additional ≈225 000 quasars – a 42 per cent increase on the DR14 catalogue size. Performing similar analyses with DR16 in the future would thus improve the statistics of the line-locked NALs.

The investigation presented in this Chapter provides further evidence that BAL and non-BAL quasars are drawn from the same population given the similarities in their NAL properties. A main result of this thesis is that the emission, broad absorption and narrow absorption signatures of outflows are all correlated with each other: as the C IV emission blueshift increases, the velocities of the BALs and NALs also increase. Modelling these results is beyond the scope of this Chapter and thesis but is an important next step in understanding quasar outflows and their effect on the galaxy evolution.

Chapter 5

LOFAR-Detected Quasars in C IV Emission Space

Summary

We present an investigation of the low-frequency radio and ultraviolet properties of a sample of ≃10 500 quasars from the Sloan Digital Sky Survey Data Release 14, observed as part of the first data release of the Low-Frequency-Array Two-metre Sky Survey. We employ the reconstructions from Chapter 2 to parameterise the C IV λ1549-emission line that is used to infer the strength of accretion disc winds, and the He II λ1640 line, an indicator of the soft X-ray flux. We find that radio-detected quasars are found in the same region of C IV blueshift versus equivalent-width space as radio-undetected quasars, but that the loudest, most luminous and largest radio sources exist preferentially at low C IV blueshifts. Additionally, the radio-detection fraction increases with blueshift whereas the radio-loud fraction decreases. In the radio-quiet population, we observe a range of He II equivalent widths as well as a Baldwin effect with bolometric luminosity, whilst the radio-loud population has mostly strong He II, consistent with a stronger soft X-ray flux. The presence of strong He II is a necessary but not sufficient condition to detect radio-loud emission suggesting some degree of stochasticity in jet formation. Using energetic arguments and Monte Carlo simulations, we explore the plausibility of winds, compact jets, and star formation as sources of the radio quiet emission, ruling out none. The existence of quasars with similar ultraviolet properties but differing radio properties suggests, perhaps, that the radio and ultraviolet emission is tracing activity occurring on different time-scales.

This Chapter is based on the article:

A. L. Rankine, J. H. Matthews, P. C. Hewett, M. Banerji, L. K. Morabito, G. T. Richards

Placing LOFAR-detected quasars in C IV emission space: implications for winds, jets and star formation

MNRAS, Volume 502, Issue 3, April 2021, Pages 4154–4169

J. H. Matthews was instrumental in producing the bootstrapped curves in Fig 5.8 as well as the wind and SFR $L_{\rm bol}$–L_{144} relations and galaxy evolutionary tracks in Fig. 5.10. Matthews produced Fig. 5.9 and conducted the Monte Carlo simulations outlined in Section 5.4.1 and produced the corresponding Fig. 5.11.

5.1 Introduction

Quasars and active galactic nuclei (AGN) are widely considered important in galaxy formation models, interacting with their host galaxies via collimated radio jets or wide-angled winds launched from the accretion disc. Both winds and jets are produced across all black hole masses; however, their connection to accretion processes and disc physics is unclear.

As discussed in previous Chapters, accretion disc winds are most evident via the BALs observed in quasar ultraviolet/optical spectra. Also evidence of disc winds is the blueshifting of the C IV emission line. It is not yet clear how direct the connection is between the C IV blueshift and the BALs; however, the strong correlations between the BAL and emission-line properties reported in Chapter 3 suggest that BAL quasars are drawn from the same parent population as non-BAL quasars.

AGN jets are studied through their radio emission, and radio sources can be categorised based on their morphology, radio-loudness, and optical spectra (among other properties). Results showing bimodality in the distribution of radio-loudness – the ratio of radio to optical luminosity – by Kellermann *et al.* (1989) lead to the authors defining the radio-loud population of quasars (see also Strittmatter *et al.*, 1980). A series of studies have investigated the distribution of radio-loudness and whether or not a clear bimodality exists. Generally, it is clear that the distribution cannot be fit by a single Gaussian, but the evidence for a true bimodality or dichotomy is debated (Falcke *et al.*, 1996; Brotherton *et al.*, 2001; Ivezić *et al.*, 2002; White *et al.*, 2007; Miller *et al.*, 2011; Baloković *et al.*, 2012; Gürkan *et al.*, 2019). What is known is that the radio-loud population is dominated by quasars with powerful jets which have inflated large radio lobes; however, the importance of compact jets, winds, and star formation in producing the radio emission of the radio-quiet quasars is still unclear (see Panessa *et al.*, 2019, for a review).

The radio-loud AGNs can be split into high and low excitation radio galaxies (HERGs and LERGs) as determined by the optical emission line properties (Laing *et al.*, 1994; Tadhunter *et al.*, 1998; Buttiglione *et al.*, 2010; Best & Heckman, 2012). HERGs typically refer to AGNs in 'quasar-mode' in which the black hole is thought to accrete from an optically thick and geometrically thin accretion disc. This mode can also be called 'radiative-mode' owing to the disc's radiative efficiency. LERGs, on the other hand, are observed to have highly energetic radio jets but an absence of strong emission lines that are otherwise present in HERGs. Best & Heckman (2012) find HERGs and LERGs across all radio luminosities, although with HERGs found preferentially at high radio luminosities, and they suggest that Eddington fraction may be the main driver of the HERG/LERG dichotomy. Additionally, the Fanaroff & Riley (1974) classification scheme splits radio galaxies into Fanaroff–Riley type I (FR I) or Fanaroff–Riley type II (FR II) based on their morphology. The morphological class depends on radio luminosity, with FR II sources more common at high luminosity (Fanaroff & Riley, 1974; Ledlow & Owen, 1996), implying that jet power is one important

factor, although more recent results have shown that a luminosity break between FR I/II sources is far from clear (Best, 2009; Mingo *et al.*, 2019). It has been suggested that the FR I/II dichotomy might be driven by accretion rate or black hole spin (Baum *et al.*, 1995), or differences in the host galaxy or environment (Bicknell, 1995; Kaiser & Best, 2007). There is growing evidence that environment is important (Hill & Lilly, 1991; Gendre *et al.*, 2013; Miraghaei & Best, 2017; Mingo *et al.*, 2019), whereby jets with similar radio powers are more likely to be disrupted in denser environments thus becoming morphologically classed as FR Is (see e.g. Mingo *et al.*, 2019; Hardcastle & Croston, 2020, for discussions).

The radio-quiet sources are arguably less well understood than the radio-loud ones, since they are fainter and harder to spatially resolve. Star formation produces radio emission (e.g Condon, 1992; Thompson *et al.*, 2006; Becker *et al.*, 2009), and jets and star formation must contribute at some level to the radio-quiet emission, with possible other contributions from disc winds (Stocke *et al.*, 1992; Blundell & Kuncic, 2007; Zakamska & Greene, 2014) and X-ray coronae (Laor & Behar, 2008; Raginski & Laor, 2016). A review of these processes is provided by Panessa *et al.* (2019). Whatever the origin of the emission, properly characterising the radio-quiet population is critical for understanding the connection between quasar outflows and star formation. It is possible to rule out star formation as the source of radio emission in sources where the flux measured on arcsec scales matches that on milli-arcsec scales (e.g., Blundell & Beasley, 1998); however, this requires high resolution radio observations. In addition, the well-known correlation between far-infrared luminosity and radio luminosity, the far-infrared radio correlation (Helou *et al.*, 1985; Yun *et al.*, 2001; Calistro Rivera *et al.*, 2017; Gürkan *et al.*, 2018; Read *et al.*, 2018) means that radio luminosity can be used as a star formation rate estimator in certain cases; understanding the level at which this correlation is contaminated from AGN-driven mechanisms is again important.

Although there have been attempts to combine winds and jets within a unified framework (e.g. Giustini & Proga, 2019), the issue of how, in detail, jets and winds are produced, related, and connected to the accretion disc remains fundamentally unclear. The C IV blueshift can be used as an indicator of wind strength, with quasars exhibiting large and positive blueshifts thought to host stronger accretion disc winds. Observations of radio-loud quasars act as a probe of jet physics, whereas the C IV emission space is used to infer properties of the accretion disc, broad-line region (BLR) and disc winds. Combining these data therefore allows the connection between the AGN disc, jets, and winds to be studied. By investigating the radio properties of Sloan Digital Sky Survey (SDSS) DR7 quasars from the Faint Images of the Radio Sky at Twenty-Centimetres (FIRST) survey (Becker *et al.*, 1995), Richards *et al.* (2011) were able to show that radio-loud quasars are concentrated at low C IV blueshifts, thus suggesting radio-loud quasars often have little to no outflowing wind. This behaviour is broadly consistent with the relative scarcity of radio-loud BAL quasars (Stocke *et al.*, 1992; Becker *et al.*, 2000; White *et al.*, 2007; Morabito *et al.*, 2019). Richards *et al.* (2011) also found radio-quiet quasars with low blueshifts and, in fact, very

similar UV spectral energy distributions (SEDs) to the radio-loud quasars. Also using FIRST and SDSS, Kratzer & Richards (2015), were able to show that the mean radio-loudness decreases with increasing C IV blueshift and argue that radio-loud and radio-quiet quasars should not be compared without first taking into account non-radio properties. Stone & Richards (2019) investigated instead the narrow C IV absorbers associated with the quasar and found them to be as common in radio-quiet quasars as they are in radio-loud quasars, suggesting that whatever physics governs the associated absorbers – whether they are evidence of a failed accretion disc wind (e.g., Vestergaard, 2003) or winds from star formation on kilo-parsec scales (Barthel *et al.*, 2017) – it is unrelated, at least directly, to the radio emission (see also Chen *et al.*, 2020, who found no correlation between the number of absorbers in quasar spectra and radio-loudness).

Owing to the sensitivity of FIRST, Richards *et al.* (2011) were only able to investigate the relationship between the UV and radio properties of the radio-loud population. With the advent of the high-sensitivity Low-Frequency Array (LOFAR; van Haarlem & et al., 2013), it is now possible to probe the radio-quiet population in more detail (e.g. Gürkan *et al.*, 2015, 2018, 2019; Morabito *et al.*, 2019; Rosario *et al.*, 2020). By combining LOFAR data with the C IV emission line, we can therefore consider the relative contributions of winds, star formation, and compact jets in the radio-quiet population and their relation to disc and outflow processes. In addition, we can confirm whether or not the radio-loud population behaves in the same way when observed at lower radio frequencies. Such an approach can, in principle, lead to greater insight into quasar feedback and fuelling by untangling the radio emission produced by star formation from that of jets and winds, while simultaneously studying the connection between star formation and the quasar accretion properties.

In this study, we have investigated the relationship between the low-frequency radio emission and the rest-frame UV properties, in particular the C IV and He II emission line properties of quasars observed by SDSS and part of the LOFAR Two-metre Sky Survey (LoTSS). The Chapter is structured as follows. In Section 5.2, we describe the observational data used in this study. The results are presented in Section 5.3 before a discussion of their implications in Section 5.4. We define the spectral index, α, such that flux density $F_\nu \propto \nu^\alpha$, and use this definition throughout the Chapter.

5.2 Observational data

The LoTSS (Shimwell *et al.*, 2017) is a low-frequency (144 MHz), high-sensitivity (median of 71 μJy beam^{-1}) survey with the aim of observing the entire northern sky. The first data release (LDR1; Shimwell *et al.*, 2019) covers over 400 deg^2 of the Hobby-Eberly Telescope Dark Energy Experiment (HETDEX) Spring field and contains almost 320 000 radio sources. The value-added catalogue contains optical identifications and morphological classifications (Williams *et al.*, 2019) as well as photometric redshifts and rest-frame magnitudes by com-

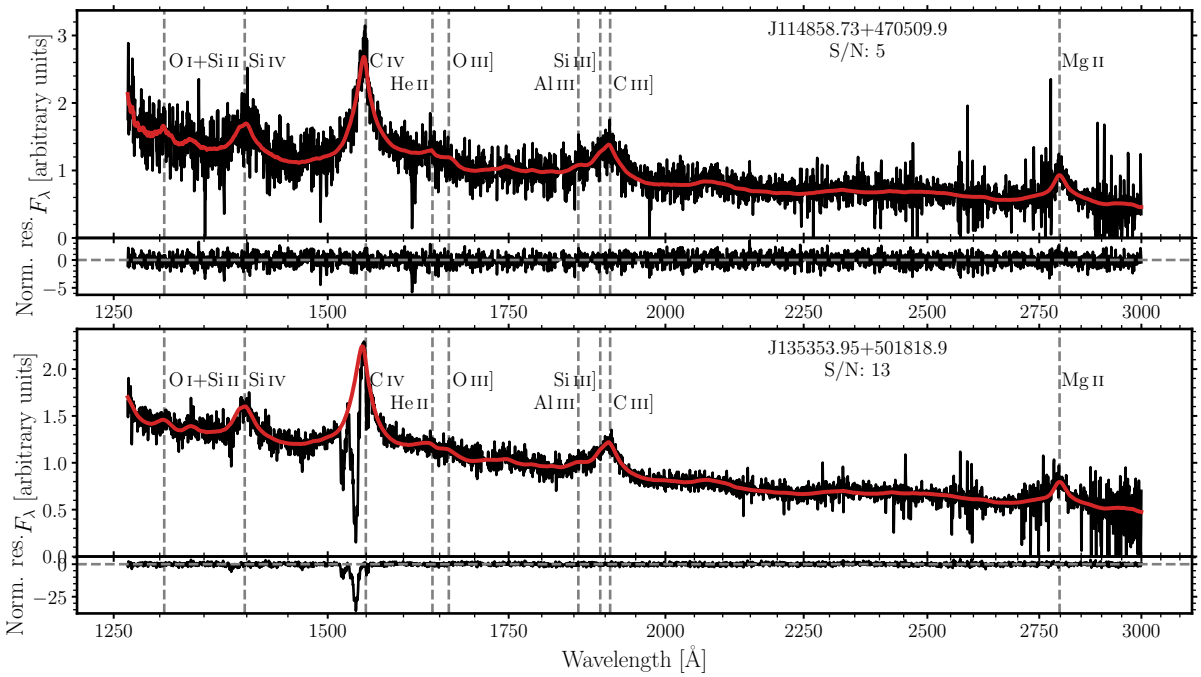

Figure 5.1: Two examples of SDSS DR14 spectra and the reconstructions from Chapter 2. The top panels contain an example of a low-S/N (S/N ≃ 5) quasar spectrum (black) and its reconstruction overplotted in red. The residuals normalised by the noise [i.e., (spectrum−reconstruction)/noise] are also shown. In low-S/N spectra, the reconstructions provide more robust measurements of the emission line parameters, in particular the C IV blueshift (calculated from the flux-weighted median wavelength of the C IV emission) and equivalent width (see Section 5.3.1 for details). The bottom panels contain an example of a quasar spectrum with significant absorption of the C IV line. In such cases, the ICA components use priors based on the properties of the C III] λ1909 complex to reconstruct the intrinsic C IV emission.

bining Pan-STARRS and WISE data (Duncan *et al.*, 2019). Using data from LoTSS allows us to investigate the low-frequency radio properties of SDSS quasars and examine trends with their emission line properties. One of the great advantages of LOFAR is its lower observing frequency compared to surveys such as the FIRST survey (Becker *et al.*, 1995). For 5σ detections, FIRST has a flux limit of 1 mJy at 1.4 GHz. LOFAR meanwhile, has a flux limit of 0.35 mJy at 144 MHz (Rosario *et al.*, 2020). However, LOFAR is effectively 10 times more sensitive than FIRST to a compact radio source with $\alpha = -0.7$ (Shimwell *et al.*, 2019), with the difference greater for steeper spectrum sources.

Our quasar sample was defined by identifying quasars in the SDSS DR14Q catalogue (Pâris *et al.*, 2018) lying within the ≃400 deg^2 area of LDR1. To do this, we used the multi-order coverage map generated by Morabito *et al.* (2019), allowing us to match the LoTSS DR1 sample with SDSS DR14 quasars using the Pan-STARRS positions in the value-added catalogue from Williams *et al.* (2019). SDSS DR16Q (Lyke *et al.*, 2020) was published during the time of writing. Our analysis for the DR14 quasars is made possible by our previous work on reconstructing the spectra. Additionally, using DR16 would lead to an increase in total sample size of only 15 per cent and an increase in the detected sample of only 8 per cent within the redshift range of interest. Thus, using DR16 would require a substantial

additional effort without changing our overall results. For these reasons, we chose not to use DR16. The spectrum signal-to-noise ratio (S/N) of the SDSS DR14Q quasars covers an extended range, with bright objects observed with S/N>20 per 69 km s^{-1} pixel while quasars detected close to the SDSS-survey magnitude-limit possess S/N $\lesssim 2$.

Ten-thousand four-hundred and thirty-eight of the 24 357 quasars here are included in the sample used in Chapters 2 and 3. The majority of the additional quasars possess spectrum S/N below the threshold of five imposed for the sample in those Chapters. At such low S/N, redshift determinations using the MFICA-scheme can possess large errors. Systemic redshifts were therefore estimated using a set of 27 quasar templates spanning the full range of morphologies of the C III]-emission complex shown in Fig. A.2, which, again, deliberately exclude the C IV-emission line. The analysis presented in the rest of this Chapter uses the quasars with S/N ≥ 5. The analysis was also repeated using the sample over the full spectrum S/N range and the results of the Chapter were unchanged.

Once systemic redshift estimates are available, the quasar spectra were reconstructed using the same ICA-scheme presented in Chapter 2. See Fig. 5.1 for two example spectra and their reconstructions. The spectrum-reconstructions essentially eliminate the uncertainties resulting from the presence of absorption features coincident with the C IV-emission. The effective S/N of the reconstructions is also significantly improved relative to the observed spectra. C IV- and He II- emission parameters and bolometric luminosities were calculated from the spectrum reconstructions. As a reminder, bolometric corrections $BC_{3000} = 5.15$ and $BC_{1350} = 3.81$ from Shen *et al.* (2011) were applied, as appropriate, to the rest-frame 3000 Å monochromatic luminosity or to the 1350 Å luminosity if 3000 Å is not available in the spectra.

The S/N ≥ 5 quasar sample contains 10 547 quasars with redshifts $1.5 \leq z \leq 3.5$ from the SDSS DR14Q catalogue within the $\simeq$400 deg^2 of LDR1. Approximately 96 per cent of the quasars (10 163) have reliable reconstructions and C IV measurements based on the criteria detailed in Section 2.4.3. 1662 of the quasars have $\geq 5\sigma$ LOFAR detections using the peak flux densities from the value-added catalogue of Williams *et al.* (2019). 1528 of the 1662 detected quasars ($\simeq$92 per cent) possess reliable ICA-based reconstructions. Our final quasar sample is formed by the 10 163 quasars with S/N ≥ 5 and reliable reconstructions. A summary of the quasar sample is presented in Table 5.1.

BAL quasars make up only $\simeq$10 per cent of our sample and small-number statistics preclude an effective investigation of the radio and ultraviolet emission properties of the BAL quasars alone. A key result of Chapter 3 was the high degree of similarity in the ultraviolet emission properties of the BAL and non-BAL quasar populations. The comparison of the two populations was possible because of the effectiveness of the spectrum reconstruction scheme. We therefore use the spectrum reconstructions for the combined populations in our analysis, although none of the conclusions presented in this Chapter change if the analysis is confined to the non-BAL quasar population.

Table 5.1: S/N ≥ 5 quasar sample

	Number	Fraction
All quasars	10 547	1
LDR1 detected	1662	0.16
LDR1 detected, reliable recons.	1528	0.14

5.3 Results

5.3.1 Radio detected sources in C IV emission space

In this section, we present the distribution of LOFAR-(un)detected quasars in the plane of C IV λ1549 equivalent width (EW) against blueshift; hereafter referred to as the C IV emission space. The C IV parameters are calculated in the same manner as in Section 3.2.1. In summary, a non-parametric approach is taken whereby the EW of the line is calculated by integrating the continuum-subtracted spectrum reconstructions relative to the power-law continuum. The use of the reconstructions means that there is no requirement for fitting Gaussian profiles to the spectra. The blueshift of the line is calculated from the flux-weighted median wavelength of the C IV emission relative to the systemic velocity of the quasar. The C IV blueshift is often used to infer the strength of outflowing winds emanating from the accretion disc (e.g. Richards *et al.*, 2011) with quasars with large blueshifts having strong winds.

The distributions of LOFAR-detected and undetected quasars in C IV emission space are shown in Fig. 5.2. The general distribution of all quasars in figure is consistent with that seen in previous chapters: quasars can either have strong C IV emission (large EW) *or* strong C IV outflows (large blueshifts), but not both. However, quasars with weak emission and no outflow signature also exist. Note that the sharp diagonal line in Fig. 5.2 is the result of excluding quasars in the sparsely populated low-blueshift, low-EW corner of C IV emission space.[1] Upon dividing the sample into quasars with and without LOFAR detections (see Section 5.2), it is evident that LOFAR-detected and undetected quasars can be found across the same region of C IV emission space. However, Fig. 5.3 shows that the radio-detection fraction increases with blueshift from ≃12 per cent at ≃ 0 km s^{-1} to ≃40 per cent at ≃ 3000 km s^{-1}.

Is the correlation between radio-detection fraction and C IV blueshift a selection effect? Our quasar sample is dominated by objects targeted in SDSS-III/BOSS and SDSS-IV/eBOSS. The target selection for the former survey maximised the surface density of quasars at $z > 2.15$ (Ross *et al.*, 2012) while the latter's target selection was designed to achieve a surface densities of ∼70 deg^{-2} quasars for $0.9 < z < 2.2$, ∼3–4 deg^{-2} for $z > 2.1$ and

[1] Quasars in this area of C IV emission space are typically FeLoBALs, have pathological spectra or have sub-optimal reconstructions (see Section 2.4.3 for details).

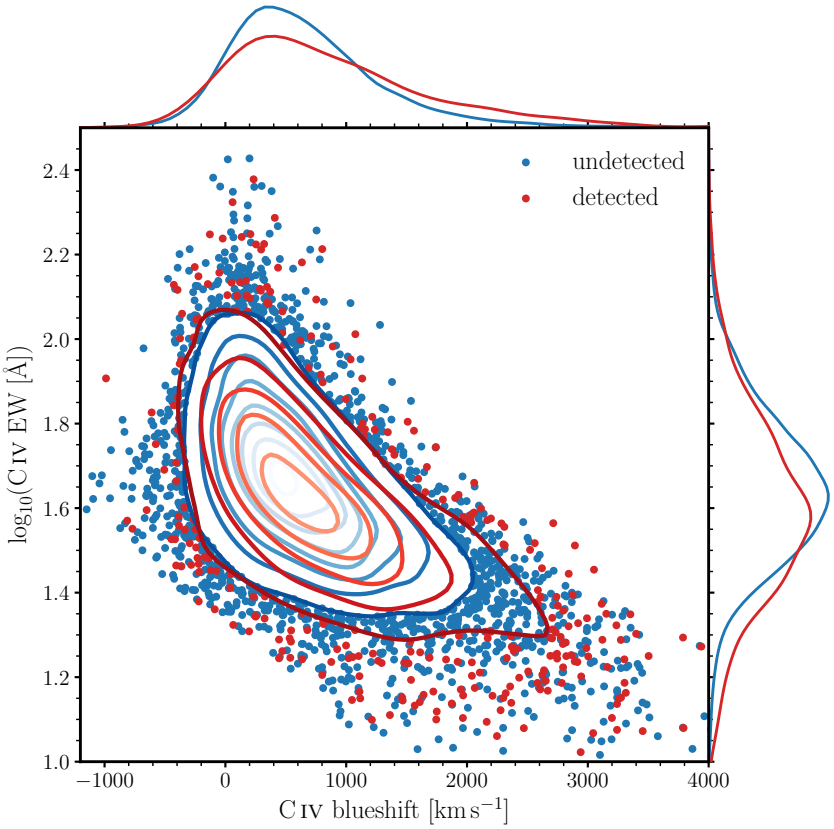

Figure 5.2: Distribution of quasars detected (red dots/contours) and undetected (blue dots/contours) by LOFAR in C IV emission space. The detected and undetected quasars populate the same region of C IV space.

included targets with FIRST detections (Myers *et al.*, 2015). Our sample includes quasars at $1.5 \leq z \leq 3.5$ and there is a mild correlation between C IV blueshift and (cosmological) redshift. However, we are cautious not to quantify any evolution of the detection fraction with redshift owing to potential selection effects resulting from the different target selections adopted by SDSS-III and -IV (but see Appendix D where we show that the detection and radio-loud fractions as a function of C IV blueshift do not change qualitatively with redshift). We also test excluding the 14 quasars targeted purely for their FIRST detections as well as limiting the sample to only BOSS quasars targeted as part of the CORE sample and observe no qualitative changes in the detection or radio-loud fractions as a function of C IV blueshift (see Appendix E).

Conversely, C IV blueshift is known to increase with bolometric luminosity (see contours in Figs. 3.6 and 5.4) and the radio-detection fraction also increases with $L_{\rm bol}$. However, Fig. 5.4 illustrates that the increase of radio-detection fraction is empirically found with both $L_{\rm bol}$ and blueshift. The trend of increasing radio-detection fraction with $L_{\rm bol}$ is stronger than with C IV blueshift but at fixed luminosity there is still a tendency for the radio-detection fraction to increase with blueshift. We have checked that the dependence of C IV blueshift on radio-detection fraction is still apparent when restricting the sample to quasars with $\log_{10} L_{\rm bol} < 45.5$. However, at luminosities $\log_{10} L_{\rm bol} > 45.75$ the detection

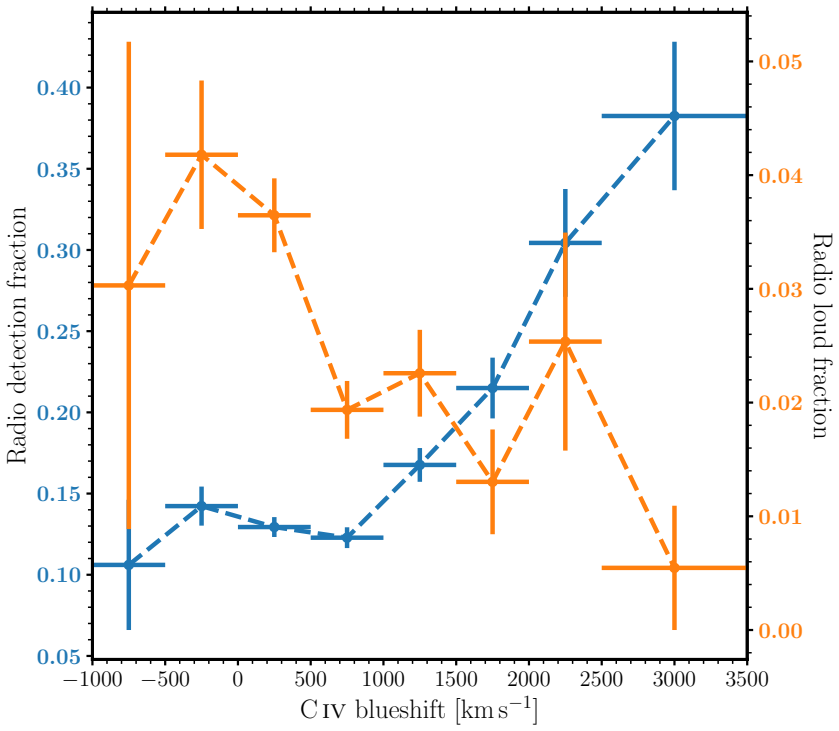

Figure 5.3: Radio-detection fraction (blue; left axis) and radio-loud fraction (orange; right axis) as a function of C IV blueshift in bins of 500 km s^{-1}, with the two highest blueshift bins combined. 1σ uncertainties are calculated using Poisson errors. Note that the scales of the left and right axes are different. While the radio-detection fraction increases with blueshift, the radio-loud fraction decreases but with a more shallow gradient.

fraction first decreases and then increases with increasing blueshift. This change in the behaviour of the detection fraction at low blueshifts is a result of removing quasars with large C IV EWs from the sample when excluding quasars with low $L_{\rm bol}$ (see Fig. 3.6) thus preferentially removing undetected quasars at low blueshifts (see Fig. 5.2). Hinted at in Figs. 5.2 and 5.4 is that the radio detection trend with blueshift at fixed EW is likely more complex than the simple monotonic increase observed in the whole sample. It should be stressed that here we are investigating a few key variables, namely C IV blueshift, He II EW, and bolometric luminosity, that are providing particular projections in what is likely a multidimensional parameter space.

5.3.2 The radio-loud fraction

radio-loudness, defined as

$$R = \frac{L_{\rm rad}}{L_{\rm opt}}, \tag{5.1}$$

with radio luminosity $L_{\rm rad}$ and optical luminosity $L_{\rm opt}$, has often been used as a proxy for dividing radio sources into two populations: radio-loud sources have powerful, large-scale FR II-type jets (Fanaroff & Riley, 1974), and radio-quiet sources can have FR I jets but also other radio emission mechanisms (which can include star formation).

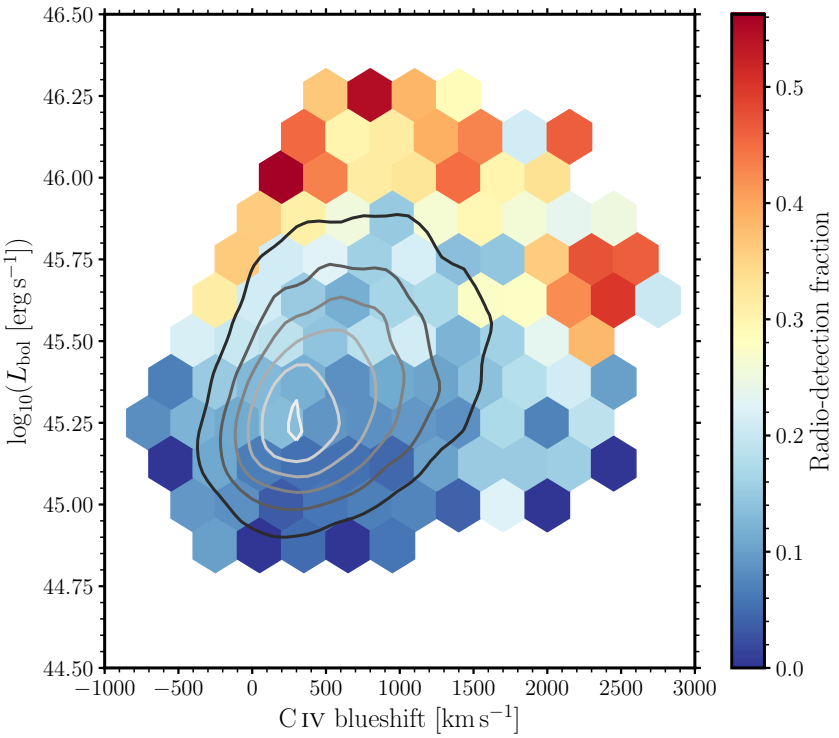

Figure 5.4: Radio-detection fraction as a function of C IV blueshift and bolometric luminosity. Bins with 10 or more quasars are plotted and the contours illustrate the distribution of objects in C IV blueshift-$L_{\rm bol}$ space. The detection fraction increases with blueshift and $L_{\rm bol}$. While this trend is stronger with the latter, there is still a trend of increasing detection fraction with blueshift at constant $L_{\rm bol}$.

A threshold that minimises the overlap in each sample can be used as a crude cut to separate radio-quiet from radio-loud sources, although with contamination in both samples. An appropriate value is often identified from a dip in the overall distribution of radio-loudness, and the classical radio-loud threshold is $\log_{10} R = 1$ at 5 GHz (Kellermann *et al.*, 1989). We have extrapolated this threshold to 144 MHz using the typical synchrotron spectral index of −0.7 to define a radio-loud threshold of $\log_{10} R = 2$ for our sample. Figure 5.5 provides an illustration of example radio SEDs and their corresponding radio-loudness measurements.

In Fig. 5.6, we again show the C IV emission space, now dividing the quasar sample into radio-loud and radio-quiet sources. Here we use the SDSS i-band magnitude, corresponding to rest-frame 2500 Å for the median redshift of the sample, to calculate the optical luminosity. Radio luminosities are calculated from the integrated flux densities in LDR1 and utilise the ICA- and template-derived spectroscopic redshifts described in Section 5.2. Both radio and optical luminosities are k-corrected to $z = 0$ using spectral indices −0.7 and −0.5, respectively. In addition to the detected radio-quiet quasars, we also included the undetected radio-quiet sources by estimating the upper limit on $\log_{10} R$ by calculating the radio luminosity at the flux limit of 0.35 mJy for the undetected objects. Eight-thousand six-hundred and thirty-one undetected objects with an upper limit of $\log_{10} R < 2$ are included in the radio-quiet population for the remainder of this subsection. Four undetected

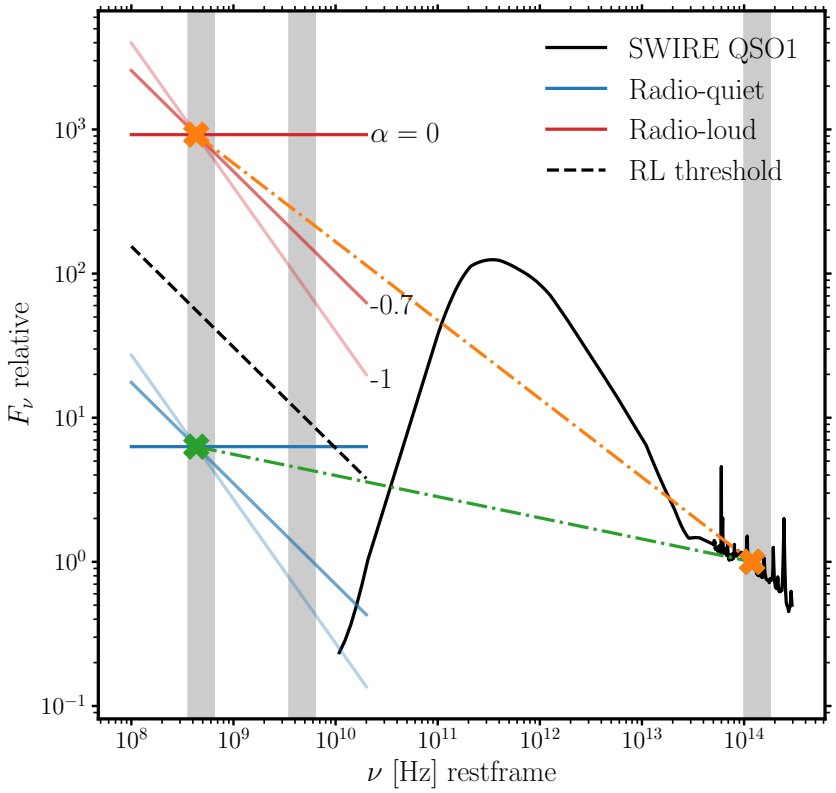

Figure 5.5: Radio-to-UV SEDs in the quasar rest-frame. The vertical grey bands, from left to right, represent the observed frequencies of LOFAR, FIRST, and SDSS i-band for the redshift range of the sample ($1.5 < z < 3.5$). The FIR-UV template (black) is the QSO1 template from the SWIRE library (Polletta *et al.*, 2007), normalised in the i-band. Radio-loud and radio-quiet SEDs with spectral indices $\alpha = 0, -0.7, -1$ are plotted in red and blue, respectively. The orange (green) crosses and dot-dashed lines mark the observed LOFAR and i-band fluxes for a $\log_{10} R = 3$ ($= 0.8$) source at $z = 2$. The radio-loud threshold is plotted as the black dashed line where the classical $\log_{10} R = 1$ threshold has been extrapolated from 5 GHz to 144 MHz. It is clear from the $\alpha = 0$ radio-quiet SED that assuming a spectral index and extrapolating the radio-loud threshold from 5 GHz could lead to movement for some sources across the threshold between surveys.

quasars have upper limits of $\log_{10} R > 2$ with the potential to be radio-loud and thus are not included in either sample. While radio-loud quasars are present at all locations in C IV emission space, they are concentrated at low C IV blueshifts ($< 500\,\mathrm{km\,s^{-1}}$). The radio-loud fraction (RLF) is calculated from

$$\mathrm{RLF} = \frac{N_{\mathrm{RL,det}}}{N_{\mathrm{RL,det}} + N_{\mathrm{RQ,det}} + N_{\mathrm{RQ,undet}}}, \tag{5.2}$$

where the denominator includes the number of undetected radio-quiet quasars ($N_{\mathrm{RQ,undet}}$) as well as the number of detected radio-quiet ($N_{\mathrm{RQ,det}}$) and radio-loud ($N_{\mathrm{RL,det}}$) quasars. The radio-loud fraction as a function of C IV blueshift is presented in Fig. 5.3 and is shown to decrease from around 4–5 per cent to < 1 per cent as blueshift increases from $\simeq 0$ to $\simeq 3000\,\mathrm{km\,s^{-1}}$, in qualitative agreement with Richards *et al.* (2011) and Kratzer & Richards (2015) using FIRST.

We experimented with different radio-loud thresholds and although the results change

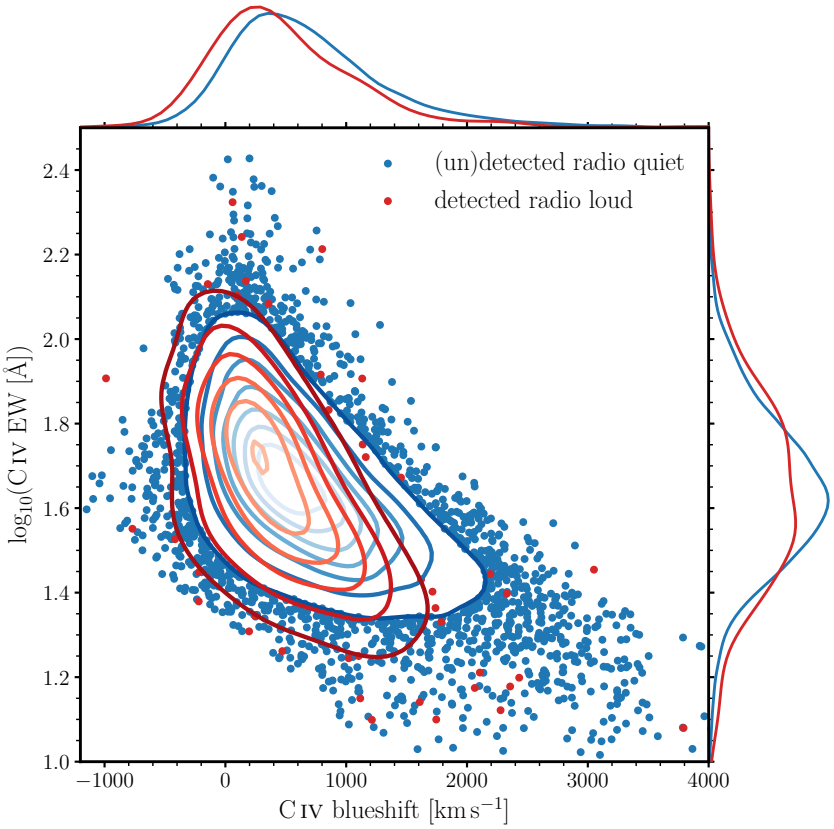

Figure 5.6: Radio-loud (red dots/contours) and radio-quiet (blue dots/contours) quasars in C IV emission space. Radio-loud and radio-quiet quasars can be found in the same region of C IV space that the undetected quasars populate but the radio-loud quasars are skewed towards lower C IV blueshifts than the radio-quiet sources.

quantitatively, the conclusions of this Chapter are unchanged. In particular, we investigated radio-loud thresholds of $\log_{10} R = 1.8$ and 2.8, for which the overall radio-loud fraction changed to ~ 0.037 and ~ 0.014, from ~ 0.029 for $\log_{10} R = 2$. At the low frequency of 144 MHz investigated here, the lobes tend to dominate the radio emission (Blundell *et al.*, 2000) in the radio-loud sources and so by increasing the radio-loud threshold, the radio-loud sample will be biased towards steeper spectrum sources (more negative spectral indices) which are likely to be more edge-on. Despite this, the trends presented in Fig. 5.3 and throughout the Chapter do not change qualitatively.

The design goal of FIRST was to achieve sufficient sensitivity to detect sources above the break in the radio logN-logS curve which include essentially all radio-loud objects bright enough to be included in the SDSS spectroscopic quasar survey (see Becker *et al.*, 1995, section 3.2). For 5σ detections, FIRST has a flux limit of 1 mJy at 1.4 GHz, as compared to LOFAR's 0.35 mJy at 144 MHz (Rosario *et al.*, 2020). As a result, FIRST is mostly sensitive to the radio-loud population, and all FIRST-detected sources are also detected in LOFAR unless they have inverted spectra with $\alpha \gtrsim 0.46$. Not all LOFAR-detected, radio-loud sources are detected in FIRST, due to the combination of sensitivity and observing frequency — such sources can either be fainter overall, or sufficiently steep spectrum such that they

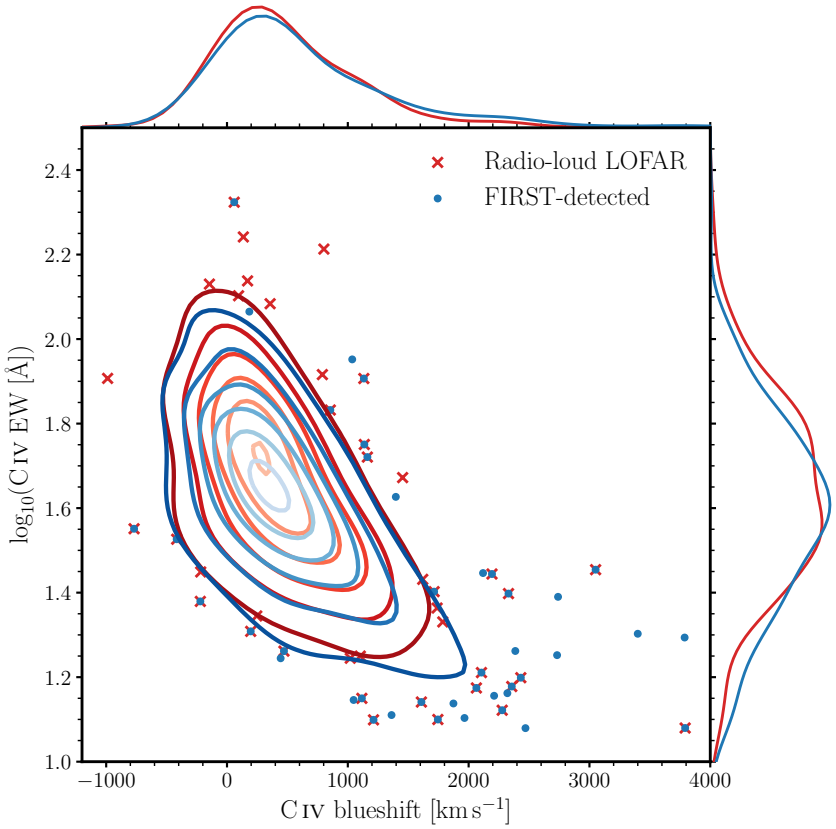

Figure 5.7: The distribution of FIRST-detected sources (blue dots/contours) is identical to the distribution of radio-loud sources in LOFAR (red crosses/contours; same as in Fig 5.6) in C IV emission space. All FIRST-detected sources are also detected in LOFAR unless they have inverted spectra with $\alpha \gtrsim 0.46$.

could not be detected by FIRST. We have matched the SDSS quasars that are in the LOFAR footprint to FIRST using the nearest-neighbour LOFAR–FIRST matching procedure described in section 2.4 of Morabito *et al.* (2019). Figure 5.7 demonstrates that the radio-loud sources that are detected in LOFAR have an extremely similar distribution in C IV emission line space to the FIRST-detected sources. This similarity suggests that the LOFAR-detected radio-loud sources are an extension of the FIRST-detected population studied by Richards *et al.* (2011), even though these sources have fainter radio emission at 1.4 GHz compared to FIRST-detected objects. Equivalently, it implies that, when a reasonable radio-loudness cut is applied, the two observing frequencies are tracing similar AGN phenomena since the location in C IV emission space is predicated upon the properties of the quasar which could be related to the origin of the radio emission. Additionally, the similar distributions of the LOFAR-detected and FIRST samples when changing the radio-loud threshold implies that the exact value for the threshold does not significantly affect the results.

5.3.3 Radio properties in C IV emission space

Figure 5.8 contains the C IV emission space populated by the LOFAR-detected quasars, revealing trends with blueshift for various radio properties. The radio luminosity (left-hand

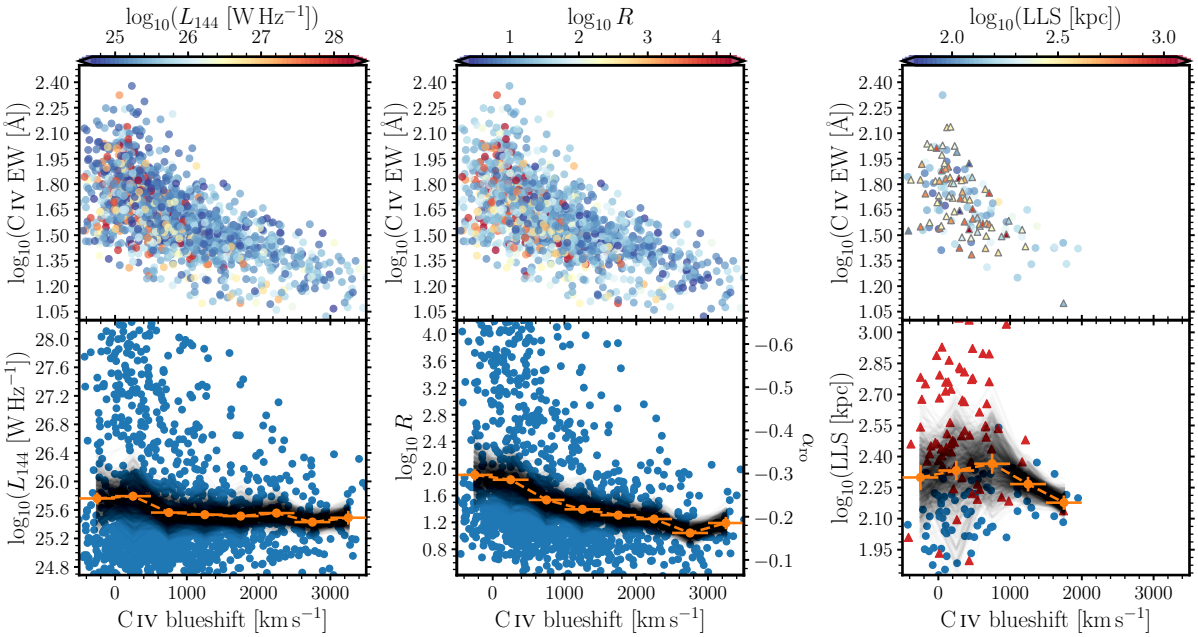

Figure 5.8: Top: C IV emission space for detected sources with points coloured, from left to right, by $\log_{10} L_{144}$, $\log_{10} R$ and (resolved) largest linear size. Bottom: The respective radio property of the detected sources in the top panels against C IV blueshift (blue points). Note that the middle panel with $\log_{10} R$ on the left y-axis has the corresponding $\alpha_{\rm ro}$ values on the right y-axis. Quasars with LOFAR Galaxy Zoo sizes (see text for details) are plotted as triangles in the right-hand panels (and red in the bottom panel). The mean log radio-property in bins of width 500 km s^{-1} are plotted in orange with the standard error on the mean. The grey lines are 1000 'bootstrapped curves': the number of objects in each bin is controlled by randomly choosing N objects per bin, where N is the number of objects in the highest C IV blueshift bin, and plot the mean.

panels) reveals that low-luminosity radio emission can be found in quasars across the C IV emission space but quasars with high-luminosity radio emission typically exist at the low-blueshift end of observed C IV emission profiles. We ascertain that the lack of radio-bright quasars with high blueshifts is not an artefact of fewer quasars overall in this region of C IV emission space by performing bootstrap sampling in bins of width 500 km s^{-1}, where the number of samples in each bin is controlled by the number of objects in the highest C IV blueshift bin. The mean log radio-luminosity of the samples in each bin is calculated. The bootstrapping is repeated 1000 times, producing the 1000 grey curves in the lower left-hand panel of Fig. 5.8. The curves are consistent with no maximally-luminous sources at high blueshift and in qualitative agreement with the trend in the mean radio luminosity of decreasing L_{144} with increasing blueshift in the whole population. Note that the calculation of the mean and bootstrapping is performed using the log of the radio parameters, but conclusions based on the panels in Fig. 5.8 are unchanged if the analysis is performed on the linear radio parameters.

The bolometric luminosity is known to increase with blueshift (see Fig. 3.6 and the contours in Fig. 5.4). However, the decrease in the mean of $\log_{10} R$ with blueshift (middle panels of Fig. 5.8) demonstrates that quasars with little to no outflowing component of C IV are, on average, more radio-luminous relative to their optical luminosity than the quasars with

a significant outflowing component. We have verified that this correlation with blueshift holds even after taking the increasing average optical luminosity into account, as would be expected from the fact that the mean radio luminosity also decreases with blueshift (left-hand panel of Fig 5.8). Again, the bootstrap sampling of $\log_{10} R$ illustrates the decreasing average radio-loudness with increasing blueshift (consistent with Kratzer & Richards, 2015) is not caused by fewer quasars at high blueshifts. Alongside $\log_{10} R$, we calculate $\alpha_{\rm ro}$, the radio-to-optical spectral index, defined as

$$\alpha_{\rm ro} = \frac{\log_{10}(L_{\rm rad}/L_{\rm opt})}{\log_{10}(\lambda_{\rm opt}/\lambda_{\rm rad})} = \frac{\log_{10} R}{\log_{10}(\lambda_{\rm opt}/\lambda_{\rm rad})}, \tag{5.3}$$

with radio luminosity, $L_{\rm rad}$, at $\lambda_{\rm rad} = 2\,\mathrm{m}$, and optical luminosities derived from SDSS i-band photometry ($\lambda_{\rm opt} = 7625\,\text{Å}$). The radio-loud threshold of $\log_{10} R = 2$ is equivalent to $\alpha_{\rm ro} \simeq -0.31$, with more radio-loud objects having more negative $\alpha_{\rm ro}$ values. We label the right-hand axis of the lower panel of the middle column of Fig. 5.8 with the equivalent $\alpha_{\rm ro}$ values for $\log_{10} R$.

The existence of at least two populations is clear from the bottom left and middle panels of Fig. 5.8. There is a clear division at $L_{144} = 10^{26}\,\mathrm{W\,Hz^{-1}}$ across all C IV blueshifts. On the contrary, a division in radio-loudness appears to be dependent on C IV blueshift suggesting that the radio-loud threshold should decrease with blueshift rather than being a constant value. We choose not to adopt a blueshift-dependent radio-loud threshold in order to be consistent with previous work.

In the right panels of Fig. 5.8, we present the projected largest linear size (LLS) of the resolved radio emission. Where available, the LOFAR Galaxy Zoo sizes (Williams *et al.*, 2019) are used and are presented as triangles (and red in the lower right panel). By design, the quasars selected for analysis with Galaxy Zoo typically have large radio sizes. All other radio sizes are calculated from twice the full width at half-maximum of the deconvolved major axis [see section 2.1 of Hardcastle *et al.* (2019) for why the doubling is required] presented as (blue in lower right panel) circles. There is a trend of decreasing LLS with increasing blueshift, and, at high blueshifts, there are no sources large enough to be resolved by LOFAR. LoTTS has a resolution of 6 arcsec, which corresponds to $\sim 50\,\mathrm{kpc}$ at $z = 2$, similar to FIRST, and is of the order of host galaxy scales. The sources with measurements from LOFAR Galaxy Zoo extend much farther than typical host galaxy sizes, with the largest LLS $\simeq 1\,\mathrm{Mpc}$. The smaller resolved sources are also larger than the host galaxies.

In Fig. 5.8, we plotted mean radio luminosity in bins of C IV blueshift, but the mean can be misleading since there are multiple radio populations contributing. The black points in Fig. 5.9 show the mean and median values of $\log_{10}(L_{144})$ in bins of blueshift for the whole sample, showing a decreasing mean $\log_{10}(L_{144})$ and a flat or perhaps marginally increasing median $\log_{10}(L_{144})$ as C IV blueshift increases. Also in Fig. 5.9, we plot mean and median $\log_{10}(L_{144})$ against C IV blueshift after applying cuts to the sample of $\log_{10} R < 2$ and, separately, $L_{144} < 10^{26}\,\mathrm{W\,Hz^{-1}}$ (red and blue points). The cut in $\log_{10} R$ removes the radio-loud

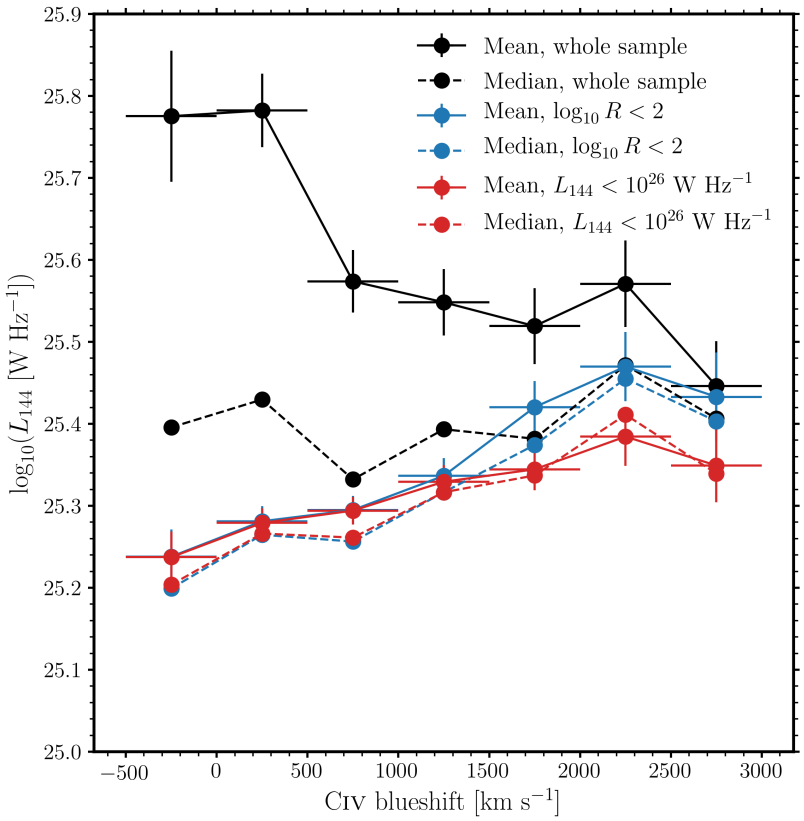

Figure 5.9: The mean and median values of $\log_{10}(L_{144})$ as a function of blueshift, using the same 500 km s^{-1} bins as in Fig. 5.8, with various cuts applied to the data. Error bars show the bin size and the standard error on the mean. The mean and median from the whole sample is shown in black; the mean black curve is identical to that in the bottom left panel of Fig. 5.8. For the whole sample, the mean curve decreases with C IV blueshift as in Fig. 5.8, whereas the median marginally increases. The red and blue curves show the mean and median $\log_{10}(L_{144})$ for sources with $\log_{10} R < 2$ (blue) and $L_{144} < 10^{26}$ W Hz^{-1} (red). The radio-quiet and low-luminosity sources evolve differently across C IV emission line space to the luminous, radio-loud population.

population shown in the middle panels of Fig. 5.8. The luminosity cut removes mostly radio galaxies with powerful jets; however, less powerful jets do exist down to $L_{144} \simeq 10^{22}$ W Hz^{-1} (see fig. 5 of Mingo *et al.*, 2019). Both cuts produce increasing mean and median L_{144} with blueshift illustrating that the low-luminosity and radio-quiet quasars correlate with blueshift in a different manner from the luminous and radio-loud population. Different correlations for different populations is consistent with the differing trends in radio-detection and radio-loud fractions observed in Fig. 5.3.

5.3.4 He II properties and size-luminosity diagrams

The strength of the He II λ1640 recombination line is indicative of the strength of the soft X-ray SED (Leighly, 2004). The strong anticorrelation between C IV blueshift and He II EW in described in Section 3.2.2 (see also Baskin *et al.*, 2013, 2015) suggests that winds can only be launched in quasars which have weak soft ionising SEDs such that material can be

accelerated by line driving with electrons remaining bound to the nuclei. In this section, we investigate the relationship between the strength of the He II line and the radio emission.

Figure 5.10 (left-hand panel) illustrates the relationship between the He II EW and the radio and bolometric luminosities. There are two populations in $L_{\rm bol}$-L_{144} space: the radio-loud (triangles) and radio-quiet (circles) quasars. The radio-quiet quasars follow the trend of increasing radio luminosity with increasing bolometric luminosity, which is by definition for the upper envelope of the radio-quiet quasars since $\log_{10} R$ sets the dividing line between loud and quiet sources. However, the lower envelope of the radio luminosity is also increasing with $L_{\rm bol}$, which, if not a selection effect, suggests that $\log_{10} R$ should be favoured over radio luminosity for defining the radio-loud population (see Baloković *et al.*, 2012). There is also evidence for decreasing SED hardness via the decrease in He II EW as $L_{\rm bol}$ increases. The anticorrelation between $L_{\rm bol}$ and He II EW is not unlike the Baldwin effect (Baldwin, 1977). As expected from the radio-loud definition, the radio-loud quasars are scattered to higher radio luminosities and show no evidence for a trend with $L_{\rm bol}$. Note there is not a sharp dividing line between the radio-loud and radio-quiet populations since $\log_{10} R$ is calculated using L_{2500}, which is determined from the SDSS photometry, while $L_{\rm bol}$ is calculated from the spectra. The radio-loud quasars typically have strong He II emission, indicating a hard ionising continuum, which could suggest that jets and SED shape are correlated with the same underlying physics (see Section 5.4.3).

In the middle panel of Fig. 5.10, we plot the radio luminosity against LLS with points coloured by He II EW. This size–luminosity plot is often referred to as a P-D diagram and is useful for studying the evolution of sources as well as the origin of the radio emission (e.g., Baldwin, 1982; Blundell *et al.*, 1999; An & Baan, 2012; Hardcastle *et al.*, 2019; Hardcastle & Croston, 2020). Again we see two clouds of points: quasars with relatively small ($\lesssim 100$ kpc) and faint radio emission ($\lesssim 10^{26}\,{\rm W\,Hz^{-1}}$), the majority of which are unresolved such that the sizes are upper-limits; and a second cloud of large and bright radio sources ($\gtrsim 100$ kpc and $\gtrsim 10^{27}\,{\rm W\,Hz^{-1}}$). The small-size, low-luminosity cloud covers the full range of He II EWs, while the large and bright cloud in the upper right is populated, almost exclusively, with quasars that have strong He II emission. The distribution of He II EW across the radio-loud and -quiet populations could be a sign that jets are semi-stochastic: they can form in high He II EW sources but are not required to (see Section 5.4.2). The strong correlation between C IV blueshift and He II EW identified in Section 3.2.2 means that Fig. 5.10 is qualitatively unchanged if we replace He II EW with C IV blueshift, allowing it to be inferred that quasars with strong winds do not host bright, extended radio emission. Stocke *et al.* (1992) arrived at this same conclusion using BALs as their evidence for winds. See also Mehdipour & Costantini (2019) who report an anticorrelation between the column density of ionised X-ray winds and the radio-loudness parameter.

We also show a size-luminosity diagram, with points coloured by $\log_{10} R$, in the right-hand panel of Fig. 5.10, together with radio galaxy evolutionary tracks. The tracks are calcu-

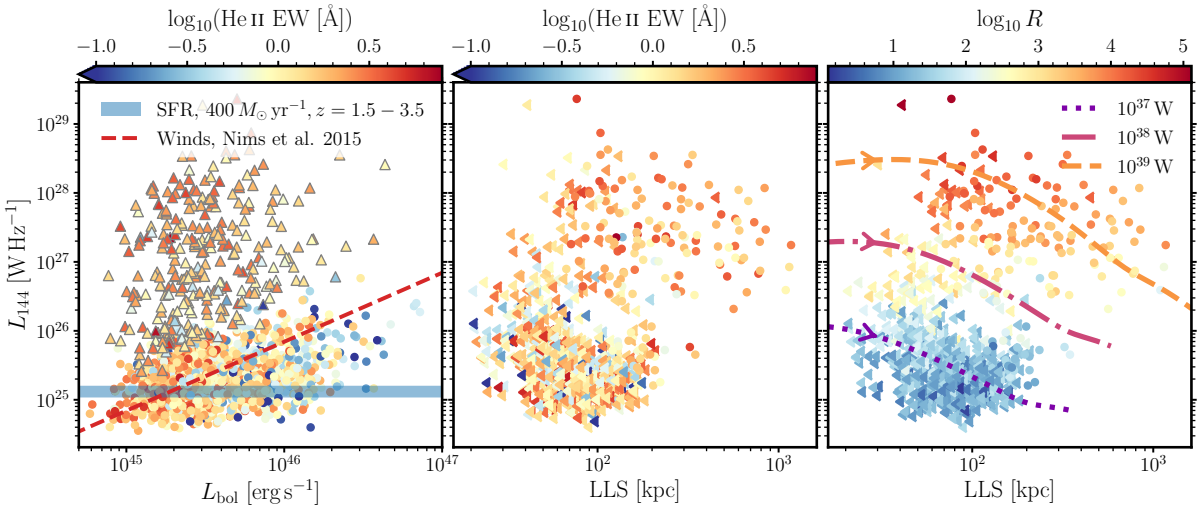

Figure 5.10: Left: Radio luminosity against bolometric luminosity. Circles (radio-quiet) and triangles (radio-loud), all coloured by $\log_{10}$(He II EW). In radio-quiet quasars, radio luminosity is correlated with bolometric luminosity, both of which are anticorrelated with He II EW, covering the full range in He II strength. The radio-loud quasars host more stochastic radio emission and favour strong He II emission. The red dashed line and blue band illustrate the expected radio emission from winds and star formation (see Sections 5.4.1 and 5.4.1). Middle: Radio luminosity against LLS. Circles are resolved sources and leftward arrows are unresolved. All unresolved LLS values are upper limits. Quasars with big/extended and bright radio sources typically have strong He II emission while small/compact and faint radio emission is hosted by quasars with a range of He II line strengths. Right: Same as middle panel but with circles (resolved) and leftward arrows (unresolved) coloured by $\log_{10} R$. Radio galaxy evolutionary tracks calculated from the models of Hardcastle (2018) at $z = 2$ are plotted.

lated from the models of Hardcastle (2018) for three different jet powers (10^{37},10^{38},10^{39} W) and evolved for 500 Myr in an environment defined using the universal pressure profile of Arnaud *et al.* (2010). We conduct the calculations at $z = 2$ and adopt a cluster mass of $M_{500} = 2.5 \times 10^{13}\,M_{\odot}$ with a temperature of $k_B T = 1$ keV. These parameters are chosen so the tracks act as $z = 2$ analogues to the $z = 0$ tracks in figure 8 of Hardcastle *et al.* (2019), and the aim is to give a feel for the size-luminosity evolution of jets with different powers in a group environment. The evolutionary tracks assume a jet-origin for the radio emission; however, we do not argue that this is the case. The right-hand panel of Fig. 5.10 shows that radio-quiet quasars are not simply younger, compact versions of the jetted radio-loud quasars – if the jet power is roughly constant. As sources get larger, their radio luminosity instead decreases for a given jet power, suggesting that any evolutionary link between the two populations would require a substantial change in jet power output. The tracks also show the typical jet powers required to produce the observed L_{144} in radio-quiet and radio-loud sources (although caution should be employed when estimating jet powers from radio luminosity, see e.g., Hardcastle & Croston 2020). Taking the modelled jet powers at face value implies that radio-loud quasars require kinetic powers comparable to their total radiative outputs, whereas the radio-quiet sources can, unsurprisingly, be powered by much weaker jets.

5.4 Discussion

Our investigation into the low-frequency radio and ultraviolet emission line properties of a sample of SDSS quasars allows for a discussion about the origin of the radio emission, the relative importance of jets, winds, and star formation and the physical drivers of the observed trends with C IV and He II properties.

5.4.1 Origin of radio emission

Radio emission can come from multiple different sources. As discussed in the previous section, the radio-loud sources are typically large and luminous, whereas the radio-quiet quasars are often unresolved, suggesting fairly compact sources with low radio luminosities. It is well known that the radio emission in radio-loud quasars is dominated by jets; however, the origin of the radio in radio-quiet quasars is unknown and could be a combination of star formation, winds, and jets (see Panessa *et al.*, 2019, for a review). In this section, we discuss, in turn, the plausibility of these mechanisms as possible sources of the radio luminosities observed in our quasar sample, focusing specifically on the radio-quiet population.

Star formation

Radio emission from star formation can be produced by synchrotron radiation from non-thermal electrons accelerated in supernova remnant shocks, as well as free-free emission from H II regions ionised by massive stars (see Condon, 1992, for a review). At the frequencies considered here, the non-thermal synchrotron component dominates. One way of calibrating the amount of radio emission produced by a given star formation rate (SFR) is from the far-infrared radio correlation (FIRC; Helou *et al.*, 1985; Yun *et al.*, 2001) where the origin of the far-infrared emission is assumed to be from hot dust heated by young stars and supernovae (e.g., Harris *et al.*, 2016). Using spectral modelling combined with LOFAR data, Calistro Rivera *et al.* (2017) find the relationship

$$\frac{\mathrm{SFR}_{144}}{M_\odot\,\mathrm{yr}^{-1}} = 1.455\times10^{-24}\,10^{q(z)}\,\frac{L_{144}}{\mathrm{W\,Hz}^{-1}}, \tag{5.4}$$

where $q(z) = 1.72\times(1+z)^{-0.22}$ is a factor accounting for the redshift evolution of the FIRC. Using this relation, we can estimate the SFR needed to produce the radio emission in the cloud of radio-detected, radio-quiet quasars. These quasars have typical radio luminosities of $L_{144}\sim10^{25}\,\mathrm{W\,Hz}^{-1}$, which from equation 5.4 requires SFR$\simeq300\,M_\odot\,\mathrm{yr}^{-1}$ at $z=2$. This SFR is quite high, but not unreasonable for a quasar in our redshift range; for example, Harris *et al.* (2016) infer $\simeq300\,M_\odot\,\mathrm{yr}^{-1}$ at $z=2-3$ and Stanley *et al.* (2017) find $\simeq50-250\,M_\odot\,\mathrm{yr}^{-1}$ at $z=1.5-2.5$. Harris *et al.* (2016) find their results are consistent with the main sequence

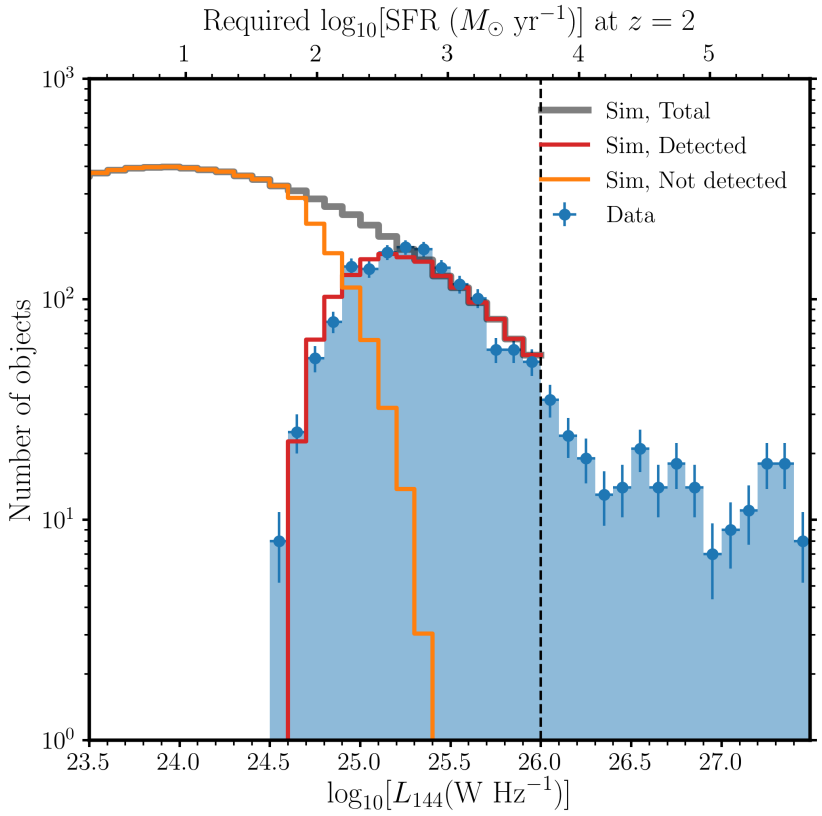

Figure 5.11: A histogram in radio luminosity, showing the sources from our sample compared to the simulated population from the Monte Carlo simulations described in Section 5.4.1. The dotted line marks $L_{144} = 10^{26}$ W Hz^{-1}, above which sources were not included in the simulation (although the data are still plotted). The figure shows that star formation rates of $\simeq 300$ up to 1000s of $M_\odot$ yr^{-1} can plausibly produce the radio emission up to $L_{144} \sim 10^{26}$ W Hz^{-1}. The limitations of the method, which is intended to be illustrative, are discussed briefly in the text. The relation to the radio luminosity function is discussed in Section 5.4.1.

of star-forming galaxies. Higher SFRs ($\gtrsim 1000\,M_\odot$ yr^{-1}) have also been measured in both quasar hosts (Pitchford *et al.*, 2016) and radio galaxies (Drouart *et al.*, 2014). Inevitably, it is the most star-forming radio-quiet quasars that will be radio-detected, so the typical SFR of the bulk of the radio-quiet quasars could still be significantly lower than the SFR required to produce radio emission at the $L_{144} \gtrsim 10^{25}$ W Hz^{-1} level.

To explore the contribution of star formation further, we conducted a simple Monte Carlo (MC) simulation. Our approach is similar in spirit to the MC simulations carried out by Rosario *et al.* (2020), although our method is a little different. We first discard all quasars with $L_{144} > 10^{26}$ W Hz^{-1}, and, for every quasar in the remaining sub-sample, we draw a SFR from a log-normal distribution. We convert this to a rest-frame L_{144} using equation 5.4 and then to an observer-frame flux density, and ask whether this source would be radio-detected at that quasar's redshift, based on its predicted total flux density. The quasars with $L_{144} < 10^{26}$ W Hz^{-1} are mostly unresolved, so their peak and total flux densities are comparable. We find the flux limit of 0.35 mJy quoted by Rosario *et al.* (2020) reproduces the radio-detection fraction fairly accurately when applied as a cut to the total flux density,

so we use this value for our Monte Carlo simulations. We carry out the above process 100 times for each quasar, and renormalise when comparing to the observational data. We can then build a histogram for each pair of SFR distribution moments, masking bins with < 6 counts, and fit for the two moments using a simple χ^2 minimisation.

The results of this exercise are shown in Fig. 5.11. The aim here is not to produce a statistically good fit or infer parameters, rather to ascertain if star formation is a plausible origin of the radio emission in radio-quiet quasars. We found the best-fitting parameters correspond to a median SFR of $\approx 30\,M_\odot\,\mathrm{yr}^{-1}$, a mean SFR of $\approx 420\,M_\odot\,\mathrm{yr}^{-1}$, and a standard deviation in log-space of ≈ 1 dex. The best-fitting reduced-χ^2 was $\chi^2/\mathrm{d.o.f.} \approx 2$. While not formally a statistically acceptable fit, the model reproduces the shape and normalisation of the observed data histogram. As a result, it also produces a radio-detection fraction (≈ 13 per cent) comparable to that observed (with luminous radio sources not included). Our approach is clearly fairly crude; it does not account for a number of systematic effects, such as the SFR dependence on redshift, source structure/morphology, or a different, perhaps multimodal, SFR distribution. Additionally, far-infrared luminosity has been observed to correlate with the C IV blueshift (Temple *et al.*, 2021) which could suggest that, at these redshifts, the far-infrared emission is driven by the AGN, perhaps in the form of kpc-scale AGN-heated hot dust (Symeonidis, 2017). Nevertheless, the simulations still come close to reproducing the observations, suggesting that the radio emission in radio-quiet quasars can plausibly be produced by star formation, provided that median SFRs of $\simeq 30\,M_\odot\,\mathrm{yr}^{-1}$ in all quasars, and $\simeq 300\,M_\odot\,\mathrm{yr}^{-1}$ up to 1000s of $M_\odot\,\mathrm{yr}^{-1}$ in the radio detected sources, can be accommodated. It is also likely that multiple different mechanisms are operating across the population, and we are not accounting for any contributions from winds or jets.

Winds

Disc winds can produce radio emission through free-free emission (Blundell & Kuncic, 2007) or synchrotron emission from shocks (Stocke *et al.*, 1992; Zakamska & Greene, 2014; Nims *et al.*, 2015). In the former case, super-Eddington accretion (and/or possible clumpiness) is generally required to produce high enough radio luminosities to make a significant contribution to the core radio luminosities that are observed, so while free-free emission may be important in some sources, it is generally less efficient at converting kinetic power from a wind into radiation. Considering electron acceleration at shocks, Nims *et al.* (2015) provide an estimate of the radio luminosity produced by a wind with kinetic power $L_k \sim 0.05 L_{\mathrm{bol}}$, suggesting $L_{\mathrm{radio}} \sim 10^{-5} L_{\mathrm{bol}}$. This relationship is plotted in the left-hand panel of Fig. 5.10. To get this estimate, the authors assume 1 per cent of the shock power goes into non-thermal electrons (based on what is observed in supernova remnants) and that these electrons radiate in a 3 mG magnetic field. The kinetic luminosity is also uncertain and the true outflow prevalence or wind covering fraction is not known, both of which would influence the radio emission. Thus, while the assumed values are reasonable guesses, there

is significant room for manoeuvre in the estimated radio luminosity. The fact that the dotted red line coincides with the cloud of radio-quiet points in Fig. 5.10 should therefore be interpreted with caution; it is a demonstration that disc winds possess sufficient power to contribute to radio emission in that regime, but does not constitute actual evidence of such a contribution.

Weak and/or compact jets

Jets from AGN dominate the high luminosity, radio-loud AGN population, but jets also produce radio emission at lower luminosities. For example, Mingo *et al.* (2019) show that, even though FR II radio galaxies are preferentially found at high luminosity, both FR I and FR II jetted sources can be found right down to $L_{144} \sim 10^{22}\,\mathrm{W\,Hz^{-1}}$, significantly below the traditional FR luminosity divide. The lower-luminosity FR I and FR II sources are also more compact. In recent years, a population of compact, lower-luminosity sources thought to be associated with weak jets have been identified (e.g. Sadler *et al.*, 2014; Baldi *et al.*, 2015, 2018), often referred to as 'FR 0' radio galaxies. Various other classes of compact radio galaxies have also been identified. Compact steep-spectrum sources (CSS) and gigahertz peaked sources (GPS) are quite powerful at 1.4 GHz and are generally unresolved in all-sky radio surveys (O'Dea *et al.*, 1991; O'Dea, 1998; Orienti, 2016; O'Dea & Saikia, 2021). These sources could be young or frustrated versions of larger jetted radio galaxies, and might be responsible for some of the more powerful compact, unresolved sources in our sample.

In addition, excess AGN activity has been invoked to explain the differences in radio properties between red and blue quasars (Klindt *et al.*, 2019; Fawcett *et al.*, 2020; Rosario *et al.*, 2020), and Jarvis *et al.* (2019) have demonstrated that many radio-quiet quasars have their radio emission dominated by the AGN rather than star formation (see also White *et al.*, 2015, 2017; Herrera Ruiz *et al.*, 2016; Gürkan *et al.*, 2018; Morabito *et al.*, 2019; Smith *et al.*, 2020). Molyneux *et al.* (2019) also find a connection between ionised galaxy-scale outflows and compact radio emission, suggesting weak or young jets as the cause. As already discussed, however, compact AGN radio emission does not always have to be attributable to jets and could instead be related to winds or some other AGN phenomena. Nevertheless, since the population of jetted radio-loud sources is likely to extend down to lower radio luminosities, we expect some fraction of the radio-quiet sources to have their emission dominated by jets with powers a few orders of magnitude lower than those in the large, luminous sources (see right-hand panel of Fig. 5.10). As mentioned previously, these cannot simply be young versions of the radio-loud population if the jet power is roughly constant.

The multiple possible contributors to radio-quiet emission

The above arguments, and the left- and right-hand panels of Fig. 5.10 in particular, indicate that disc winds, jets, and star formation are all energetically capable of producing

compact, unresolved radio emission with $L_{144} \sim 10^{24-26}\,\mathrm{W\,Hz^{-1}}$. It is hard to distinguish further between the possible contributors, although comparison to the radio luminosity function is instructive. At low redshift and at 1.4 GHz, there is a transition between star-forming galaxies and radio AGN at a break luminosity around $10^{23}\,\mathrm{W\,Hz^{-1}}$ (Mauch & Sadler, 2007; Kimball *et al.*, 2011; Heckman & Best, 2014). This break luminosity probably shifts to higher luminosities in quasar hosts (Condon *et al.*, 2013) and at higher redshift, because the SFR is expected to increase, thus the contribution to the radio greater. The lower observing frequency should also increase individual source luminosities (due to the shape of the radio SEDs) and a higher luminosity transition between star-forming galaxies and radio-loud AGN is indeed measured by Hardcastle *et al.* (2019) using LOFAR data. It is therefore plausible that the apparent break in the histogram of L_{144} in Fig. 5.11 at around $\log_{10}(L_{144}) \approx 26-26.4$ corresponds to the transition between star formation and AGN jets dominating the radio emission. However, there are also multiple overlapping contributions from AGN jet (Jarvis & Rawlings, 2004; Simpson, 2017) – and possibly wind – populations. We therefore do not favour one specific scenario or single origin for the radio-quiet emission, although we discuss what might drive the observed correlations in Section 5.4.3. Furthermore, the relative dominance of AGN and star formation might change as a function of luminosity even in the radio-quiet population. What we can be sure of is that there are *at least two* overlapping populations, so as to explain the clear increase in source numbers below $10^{26}\,\mathrm{W\,Hz^{-1}}$ (Fig. 5.11) as well as the opposing trends shown in Fig. 5.3. This idea is consistent with the studies referenced above and can be studied in more detail with future LOFAR data releases. Multi-wavelength studies of the radio-quiet quasars will help to disentangle the sources of the radio emission in this population.

5.4.2 Stochasticity and time-scales

At a given location in C IV emission space, quasars tend to have very similar rest-frame UV properties; however, radio properties can differ substantially, to the extent that sources are found on both sides of the radio-quiet/radio-loud and LOFAR-detected/undetected divisions at any given location in the parameter space. One way of explaining this is that the radio and UV properties trace stochastic processes operating on different time-scales (Nipoti & Binney, 2005). We can explore this hypothesis further by considering the relevant physical time-scales in the system.

For jets, there are two important time-scales: the first being the time-scale over which the jets grow. Typical advance speeds for FR II sources are of a few per cent of the speed of light (e.g. Harwood *et al.*, 2017) suggesting lifetimes around 100 Myr for a (two-sided) LLS of 600 kpc (assuming the jet-axis is orthogonal to the line-of-sight).

The second important time-scale is the synchrotron cooling time. Whatever the energy source for the radio emission, the radiation is likely to be synchrotron emission from

shock-accelerated electrons. The synchrotron cooling time for electrons with a characteristic emission frequency ν_c is given by

$$\tau_{\rm sync} \approx 108\,{\rm Myr} \left(\frac{B}{10\,\mu{\rm G}}\right)^{-3/2} \left(\frac{\nu_c}{144\,{\rm MHz}}\right)^{-1/2}, \tag{5.5}$$

where B is the magnetic field strength. The value of B here is uncertain and depends on the origin of the radio emission. For large-scale radio galaxies, magnetic field strengths of $\sim 10\,\mu$G are typical (Croston *et al.*, 2005; Harwood *et al.*, 2016). For these characteristic field strengths, and for the radio frequencies considered here (144 MHz for LOFAR and 1.4 GHz for FIRST), we might expect the synchrotron emission to trace jet activity on ≃10–100 Myr time-scales. The picture is more complicated than this as adiabatic expansion and cooling will be more important for some sources as the lobes expand (e.g., Blundell & Rawlings, 2000).

The time-scale for jet growth and $\tau_{\rm sync}$ for the magnetic field strengths above are only applicable to the radio-loud sources; in the radio-quiet sources the corresponding time-scales are different and depend on the mechanism responsible for the radio-quiet emission. Magnetic fields in star-forming galaxies range from μG levels to 100s of μG (Thompson *et al.*, 2006), but in quasar winds there are few observational constraints (although Nims *et al.*, 2015, adopt ~ 3 mG which would reduce $\tau_{\rm sync}$ to ≈ 0.02 Myr). Compact, galaxy-scale jets and quasar-driven winds inevitably have shorter dynamic time-scales than large-scale radio galaxies, while a typical star formation time-scale is ≈ 10 Myr and cannot be too much longer than this for the high SFRs considered here.

To consider the relationship between the UV and the radio emission, we must discuss the time-scales that are important for the UV emission. The UV emission line properties are determined by the physics of the accretion disc, the broad-line region and the putative outflow. One relevant time-scale is the viscous time-scale in a thin α-disc (e.g. Shakura & Sunyaev, 1973; Frank *et al.*, 2002), given by

$$\tau_{\rm visc} \sim 5\times10^4\,{\rm yr}\,\frac{R}{5\,{\rm ld}}\left(\frac{\alpha_{\rm visc}}{0.1}\right)^{-1}\left(\frac{H/R}{0.1}\right)^{-1}\left(\frac{c_s}{10\,{\rm km\,s^{-1}}}\right)^{-1}, \tag{5.6}$$

where $\alpha_{\rm visc}$ is the standard viscosity parameter, H/R is the disc aspect ratio, R is the radius, and c_s is the sound speed, and we have chosen typical values for ≈100 gravitational radii in a thin disc around a $10^9\,M_\odot$ black hole. Other time-scales relevant for the disc are the thermal and dynamical time-scales, both of which are generally much shorter than $\tau_{\rm visc}$ (Frank *et al.*, 2002). In the case of large-scale jets producing the radio emission, $\tau_{\rm sync}$ is much longer than any of the time-scales associated with the disc and BLR.

We can expect that radio emission from large-scale lobes and jets traces longer time-scales than the UV and optical emission from the accretion disc and BLR more trivially from the sizes of, and light travel times across, the respective emission regions. Similarly,

it is fairly natural for the star formation and quasar activity time-scales to be decoupled as discussed by, e.g., Pitchford *et al.* (2016). A disconnect between the radio and UV properties is reasonable if the UV properties change on time-scales shorter than, say, $\tau_{\rm sync}$; for example, if quasars 'flicker', or change between different accretion states. It is well known that quasars exhibit multiwavelength variability on a wide range of time-scales (e.g., Ulrich *et al.*, 1997; Peterson, 2001), and 'changing-look' quasars are a particularly dramatic example of this (LaMassa *et al.*, 2015; MacLeod *et al.*, 2016; Runnoe *et al.*, 2016). Evidence for flickering or intermittent jets can be seen in a number of large-scale radio galaxies (e.g., Konar *et al.*, 2006; Turner, 2018; Maccagni *et al.*, 2020; Shabala *et al.*, 2020). There are also theoretical suggestions that quasars might accrete in sporadic episodes, perhaps lasting only 10^5 yr (e.g., King & Pringle, 2007; King & Nixon, 2015). We suspect that understanding stochasticity and intermittency (in terms of both discs and jets) is important for explaining why two given sources can look nearly identical in their UV spectra but have totally different radio properties, a statement that can be true for both radio-loud and radio-quiet sources.

5.4.3 What physics drives the trends in C IV emission space?

Although there are probably a number of competing factors at work, models for the radio emission must (at least) be able to explain the results shown in Fig. 5.3: the radio-detection fraction increasing with C IV blueshift, and the decreasing radio-loud fraction. Additionally, at a given location in C IV emission space, what determines whether a source is radio-loud, radio-detected but radio-quiet, or radio-undetected? The trend in radio-loud fraction is discussed by Richards *et al.* (2011) and driven by the prevalence of relatively large-scale, powerful AGN jets; relevant also to this discussion is the work by Kratzer & Richards (2015) who investigate dependence of the radio-loud fraction and mean radio-loudness not only on C IV properties, but also with redshift, optical luminosity, 'Eigenvector I', mass, and colour. In contrast to the radio-loud fraction, the trend in radio-detection fraction is instead driven by the mechanism(s) powering the emission in the cloud of radio-quiet sources. We discuss each of these trends in turn with reference to the relevant physics of jets, winds and star formation.

Radio-loud fraction

First, we consider the decrease of the RLF with C IV blueshift, first discussed by Richards *et al.* (2011) and now confirmed at lower radio frequencies. We assume for the purposes of this discussion that the radio emission in the majority of radio-loud sources is produced by radio lobes that have been inflated by jets. If jets are driven by the Blandford & Znajek (1977) mechanism, the jet power proportionality is $Q_{\rm BZ} \propto a_*^2 \Phi_B^2 M_{\rm BH}^2$; here $M_{\rm BH}$ is the black

hole mass, a_* is the dimensionless black hole spin, and Φ_B is the magnetic flux threading the event horizon. As well as having the available spin and magnetic energy, a number of general-relativistic magnetohydrodynamic simulations (GRMHD) suggest that there are other critical ingredients like the presence of an inner disc wind to collimate the flow, and a preference for certain accretion states (see reviews by Blandford *et al.* 2019; Davis & Tchekhovskoy 2020).

Black hole spin is interesting to consider, since higher spins lead to higher radiative efficiencies and an increase in extreme UV (EUV) flux, both because the disc extends closer to the black hole. One possibility is that quasars with lower C IV blueshifts have higher black hole spins that could preferentially produce jets at low blueshifts and explain the decrease of RLF with blueshift. In addition, in high-spin sources the increased EUV flux could lead to a more ionised outflow and BLR. This increase in spin would increase the He II EW and decrease the line-driving force multiplier and outflow strength (we have observed the He II EW to be greatest at low C IV blueshifts; see Fig. 3.5). Thus, spin can go someway to explaining the observed behaviours and the apparent anticorrelation between wind and jet prevalence in C IV emission line space. It is worth noting that, in X-ray binaries, winds and jets appear in distinct, and generally opposite accretion states as defined by spectral hardness and X-ray luminosity (Fender *et al.* 2004; Ponti *et al.* 2012; although see also Muñoz-Darias *et al.* 2019; Higginbottom *et al.* 2020). Körding *et al.* (2006) have attempted to apply similar principles to populations of AGN, but the picture is clearly more complicated, not least because of the range in time-scales involved. Nonetheless, the C IV emission space seems to have potential as a probe of the 'disc-wind-jet' connection in AGN.

Spin is likely to be necessary, but not sufficient, for powerful jet production in AGN. General theoretical arguments for this are given by, for example, Richards *et al.* (2011) and Blandford *et al.* (2019) where a high mass accretion rate can lead to funnelling of material to form the base of a jet. The idea is also supported observationally by the fact that many radio-quiet AGN seem to be spinning rapidly, as inferred from X-ray observations (Reynolds, 2014) and studies based on the Soltan (1982) argument – which states that the luminosity function traces the black hole accretion rate of the Universe – generally find high radiative efficiencies implying high spins (Elvis *et al.* 2002; Yu & Tremaine 2002; Shankar *et al.* 2020; see also Broderick & Fender 2011).

As well as spin, the jet power also depends on the magnetic flux threading the event horizon (Blandford & Znajek, 1977; Tchekhovskoy *et al.*, 2011; Davis & Tchekhovskoy, 2020), which can either be generated in situ (e.g. Liska *et al.*, 2020) or accumulated from the surrounding interstellar medium (e.g., Beckwith *et al.*, 2009). It is not clear how the magnetic flux responsible for jet launch might affect the UV emission line properties, particularly since it may be a state-dependent property of immediate black hole environment, in contrast to the black hole spin that probably changes on longer time-scales. It is also possible that the jets are primarily launched during different accretion states to the 'quasar' state,

in which case the disc might have little memory of the magnetic field configuration during the jet episodes (e.g., Sikora & Begelman, 2013).

Generally speaking, the dependence of jet power on the magnetic flux offers a possible cause of stochastic jet behaviour as discussed in Section 5.4.2. It may also facilitate the hypothesis that black hole spin increases as blueshift decreases. In this framework, spin would increase the probability of producing a powerful jet and control the radio-loud trend with blueshift. Additional physics relating to the accumulation of magnetic flux and/or jet collimation would then determine whether a powerful jet could be launched for a given black hole spin (see also Sikora *et al.*, 2007; Rusinek *et al.*, 2020). These suggestions require severe qualification; there are likely to be multiple degeneracies and it is not possible to draw clear conclusions. Overall, consideration of jet launching theory (i) provides a possible framework in which black hole spin increases towards low C IV blueshifts and high He II EWs; and (ii) supports the idea that stochastic behaviour is expected, which is important for explaining the radio properties of our quasars in C IV emission space.

Radio-quiet quasars and the radio-detection fraction

As described above, the origin of the radio emission in radio-quiet sources is not known and is likely to be attributed to at least two mechanisms. The driving factor behind the trend of increasing radio detection with C IV blueshift depends on this conclusion and the relative contribution of star formation, winds, and jets.

Disc winds might be driving the increased detection fraction with C IV blueshift, even if they are not the dominant cause of radio emission in radio-quiet quasars. If so, the explanation might be fairly straightforward: since C IV blueshifts are thought to be caused by a stronger outflowing component in the BLR, it is fairly natural to expect that they produce disc winds with higher kinetic powers than low blueshift sources. An increased wind power could then produce more radio emission and increase the detection fraction.

Disc wind models for BAL quasars are capable of producing strong UV emission lines (Murray *et al.*, 1995; Matthews *et al.*, 2016, 2020), but, although there have been successful attempts to model C IV blueshifts (e.g., Chajet & Hall, 2013; Yong *et al.*, 2017), we are not aware of a full radiative transfer and photoionisation treatment of their formation. In order to test disc wind models for radio emission, future modelling designed to constrain the kinetic power of outflows associated with blueshifts would be useful, combined with a more detailed treatment of the expected radio emission from wind-driven shocks.

5.5 Conclusions

We have made use of the first data release of the LoTSS to investigate the low-frequency radio emission of a sample of ≃10 500 quasars in the context of their ultraviolet proper-

ties. SDSS spectrum-reconstructions from Chapter 2 allow for reliable measurements of the C IV λ1549- and He II λ1640-emission lines. Our main conclusions are as follows:

- We have investigated the radio properties of quasars throughout the C IV emission space – blueshift versus equivalent width. We have found radio-detected quasars everywhere in C IV emission space that undetected quasars can be found (Fig. 5.2).
- The increased sensitivity of LOFAR relative to surveys such as FIRST enables a unique probe of the radio-quiet population (Fig. 5.7). We discovered an increasing radio-detection fraction with increasing C IV blueshift (Fig. 5.3) – which is used to infer the strength of accretion disc winds. However, the detection fraction trend with blueshift at fixed EW is not as simple as the monotonic increase observed in the whole population (Fig. 5.4 and accompanying text). The radio-loud fraction decreases with increasing blueshift hinting at multiple sources of radio emission that correlate differently with C IV blueshift.
- Radio-loud sources can be found across the same range of C IV emission space as radio-quiet sources, but, consistent with earlier studies, the largest, most luminous and most radio-loud sources are found preferentially at low blueshifts and moderately high C IV EWs (Fig. 5.8).
- Luminous radio sources are also found almost everywhere in C IV emission space, but, consistent with earlier studies, the largest, most luminous and most radio-loud sources are found at low blueshifts and moderately high C IV EWs (Fig. 5.8). It is difficult, however, to separate different sources of radio emission and so care should be taken when performing statistical analysis on the whole population (Fig. 5.9). Additionally, the distribution of radio-loudness as a function of C IV blueshift would suggest that the radio-loud threshold should be a function of blueshift rather than a constant number.
- Comparing FIRST-detected sources to radio-loud sources in LOFAR (Fig. 5.7) reveals that when a reasonable radio-loudness cut is applied, the two populations have very similar distribution in C IV emission space. This result suggests that the observing frequencies are tracing similar AGN phenomena and that radio-loud sources in LOFAR that are either too faint, or have too steep spectra, to be detected by FIRST are an extension of the same population.
- Despite the trends across the parameter space, sources can look identical in the ultraviolet and have completely different radio properties. This inability to differentiate quasars with different radio properties based solely on their ultraviolet properties suggests that the radio does not know about the current state of the accretion disc, as might be expected if the processes are stochastic and the different emission traces different time-scales of activity.

- We find that the radio properties correlate with He II EW. There is a Baldwin effect with luminosity across the radio-quiet quasars, whereas most luminous radio sources have strong He II EW (Fig. 5.10, left-hand panel). Weak He II EW sources (EW $\lesssim 1$ Å) are almost guaranteed to be radio-quiet with luminosities below 10^{26} W Hz^{-1}.

- We explore the possible origin of the radio emission. We find that star formation, disc winds and weak/compact jets are all energetically capable of producing the radio-quiet quasar emission (Fig. 5.10). We explore the possible role of star formation in more detail using Monte Carlo simulations, showing that a broad distribution of SFRs with median $\approx 30\,M_\odot\,\mathrm{yr}^{-1}$ can approximately reproduce the detection fraction and distribution of radio luminosity in the radio-quiet quasars (Fig. 5.11). We infer SFRs in the range of 100s to 1000s of $M_\odot\,\mathrm{yr}^{-1}$ in the radio-detected, radio-quiet sources. Occam's razor might lead one to invoke star formation plus jets as the simplest explanation for the radio emission, but there is plenty of room for other drivers. Multiple overlapping contributions from winds, jets, and star formation are possible (see Section 5.4.1).

Our work further demonstrates the utility of low-frequency radio data for investigations regarding the origin of radio emission, particularly in radio-quiet quasars. Combining LOFAR data with the C IV emission line space has allowed us to investigate the connection between winds, jets, and star formation, as well as their relationship with the AGN accretion disc and BLR. Future data releases from LoTSS covering the full northern sky will therefore be of tremendous value in addressing these questions and studying the relationship between radio emission and the rest-frame UV emission lines in more detail.

Chapter 6

Conclusions and Future Prospects

6.1 Summary

The aim of this thesis is to provide quantitative observations of the various outflow signatures in UV quasar spectra with the intention of providing constraints that can then be applied to theoretical modelling. To that end, we have used the SDSS DR14 quasar population at redshifts $1.5 < z < 3.5$ as our base sample of quasars. In Chapter 2 I described the spectrum reconstruction scheme which implements ICA in order to reconstruct the intrinsic C IV emission even in the face of extensive absorption. The reconstructions were then used as the reference continua for the classification of quasar as either BALs or non-BALs, using the classical Balnicity Index definition as well as the Absorption Index definition.

With the C IV emission properties measured for all quasar populations, we compared the distribution of the BAL and non-BAL quasars in the C IV emission space and found them to be the same (Chapter 3). The similarities between the He II EW – which provides a measure of the flux in the far-ultraviolet, the bolometric luminosity, and Eddington ratio of the BAL and non-BAL quasars lead us to the conclusion that the BAL and non-BAL quasars are drawn from the same population. We suggest that BAL quasars are not a result of a particular viewing angle, just above or below some obscuring torus for example, but instead that they are a result of small differences in the line-of-sight based on the similarities between the UV properties of the two sub-populations.

One of the main conclusions of this thesis is that the properties of the various UV outflow signatures (C IV blueshift, BALs, and NALs) are all correlated. We have shown that the BAL trough parameters, including the minimum and maximum ejection velocities, correlate with the location in the C IV emission line blueshift and equivalent width space. In particular, the velocities in the wind traced by absorption increase as the C IV blueshift increases. We have found a similar correlation between the maximum velocities of the NAL systems and the C IV blueshift (see Chapter 4). The velocities of the line-locked systems also increase with C IV blueshift which illustrates the importance of radiation line-driving in ac-

celerating the wind. The ionisation state of the gas responsible for the narrow absorption lines found outside of and within the BAL troughs are also similar which provides further evidence in support of the BAL and non-BAL quasars being drawn from the same parent population.

In Chapter 5, we investigated the low-frequency radio properties of our quasar sample in the context of the UV properties explored in Chapter 3. The sensitivity of LOFAR allows the detection of a significant fraction of quasars which are classified as radio-quiet and we find that the radio-detection fraction, which is driven by the radio-quiet sources, increases with C IV blueshift whilst the radio-loud fraction, driven by powerful radio jets, decreases. The opposing trends imply that there are at least two sources of radio emission in luminous, high-redshift quasars and that they correlate differently with the C IV emission space. However, we find that the radio-quiet and radio-loud sources do exist across all of the populated C IV emission space. The existence of quasars with similar UV properties and different radio properties could suggest that the UV and radio are tracing quasar activity on different time-scales. The discovery that all of the radio-loud quasars have weak He II emission but that all quasars with weak He II need not be radio-loud leads us to conclude that stochasticity to some degree is involved in jet formation. Additionally, compact/weak jets, star formation, and winds are all plausible sources for driving the trends observed in the radio emission in radio-quiet quasars and we rule out none.

6.2 Future prospects

Previous works have suggested that strong associated absorbers are an indicator of an edge-on orientation (Stone & Richards, 2019; Richards *et al.*, 2021). The NAL catalogue presented in Chapter 4 will allow an investigation into the utility of NALs as an orientation-indicator in combination with radio spectral indices from FIRST and LOFAR where steep-spectrum sources are more likely edge-on. Extending the catalogue to include the SDSS DR16 objects would also improve the statistics of line-locking in the BAL and non-BAL populations.

According to our paradigm, BAL and non-BAL quasars are drawn from the same parent population. Allen *et al.* (2011) observed that with increasing redshift, BAL quasars grow disproportionately redder than their non-BAL counterparts. Whereas the SDSS-derived samples studied by Allen *et al.* (2011) and in this thesis suffer from selection effects due to biases against even moderately red quasars, the infrared-selected quasar population from WISE targeted with 4MOST will enable a direct study of the emission line properties of the moderately reddened quasar population. Such an investigation would test our model, as a statistical difference in emission-line properties between BAL and non-BAL red quasars would suggest intrinsic differences between the populations.

The question of how the activity of the black hole affects galaxy evolution is a fundamental one that can only be answered by combining different diagnostics probing properties

over the very the different physical scales involved. This thesis is an example of the advances that can be made with the greatly improved statistical samples now available, combined with modern statistical analysis techniques. However, samples with full wavelength to faint flux limits are still relatively small. LOFAR will make improvements at radio wavelengths and eROSITA (Merloni *et al.*, 2012; Predehl *et al.*, 2020) is in the process of imaging the entire sky at X-ray wavelengths (0.2–8 keV). While designed to observe > 100 000 galaxy clusters, eROSITA will also image ∼3 million AGN, probing the innermost region of the accretion disc, e.g., X-ray diagnostics such as the in-band spectral index give an indicator of the Eddington fraction (Shemmer *et al.*, 2006; Marlar *et al.*, 2018).

Recent advances made by statistical investigations of quasar variability, including the discovery of changing-look quasars (LaMassa *et al.*, 2015) and the initial results on reverberation mapping and BAL-trough variability, have shown that AGN are not static objects and that some of the time-scales involved are short. Increased baselines are required to investigate variability on longer time-scales and larger sample sizes of quasars being monitored will improve the statistics. LSST (Ivezić & et al., 2019) is expected to image 10–30 million AGN in the optical and produce light curves of close to 1000 epochs. Meanwhile SDSS-V's Black Hole Mapper (Kollmeier *et al.*, 2017) will produce optical spectra for more than 300 000 quasars and will provide time-resolved spectroscopic observations for more than 22 000 of them. The application of the MFICA spectrum reconstruction scheme to the spectra from SDSS-V would aid in the investigation of temporal variability. Large samples of time-resolved observations allow quasar variability to be studied, including the role of outflows, while multi-wavelength observations will help to build a holistic picture of outflows on different scales. The next obvious step is to produce a model for quasar winds that can explain the various observations I have presented in this thesis.

Appendix A

Creation of priors

The correlation between the morphology of the C III] λ1908+Si III] λ1892+Al III λ1857 emission complex and the extent of the blueshift of C IV emission in luminous quasar spectra has been known for some time (see fig. 16 of Richards *et al.*, 2011, and the top panels of our Figure A.1). While the C IV blueshift is a result of shifting the centroid of the line, the observed C III] 'blueshift' is caused by an increase in the ratio of Si III] to C III] emission. Richards *et al.* (2011) used the C III] 'blueshift' to parameterise the blueshift of the absorbed C IV emission in a sample of BAL quasars. Here, we use the C III] 'blueshift' to place priors on the 10 component weights for the BAL quasars since, for the high-ionisation BAL-quasars under investigation, the 1600–2900 Å wavelength interval is free of high-ionisation transitions where broad absorption is observed.

The component-weight priors were constructed using a sample of ∼4000 non-BAL quasars with S/N ≥ 9 per pixel. Similarities between the BAL quasar and non-BAL quasar spectra in the wavelength range 1600–3000 Å allow the non-BAL quasars to be used to infer the BAL quasar component weights. The components covering 1260–3000 Å were fitted to the spectra and the C III] 'blueshift' measured between 1820 and 1970 Å using the recipe detailed in Section 3.2.1. The continuum was fitted using the wavelength intervals 1790–1810 Å and 2015–2035 Å. The middle panels of Figure A.1 show two examples of the component weights against the C III] 'blueshift' for the non-BAL quasar sample. The spectra (and component weights) were binned according to the C III] 'blueshift'. The edges of the bins are drawn on the top four panels in Figure A.1. The correlation between the C III] and C IV is evident in the composite reconstruction for each bin in Figure A.2: with increasing C III] 'blueshift' (increasing bin number), the C IV blueshift also increases. Note also that the C IV EW decreases and that He II λ1640 decreases in strength with increasing blueshift, the latter of which is in agreement with Richards *et al.* (2011) and Baskin *et al.* (2013, 2015).

The median and median absolute deviation (MAD) of each component weight in each bin was calculated (see examples in the bottom panels of Figure A.1). From these measurements, for each C III] 'blueshift' measured in the whole quasar sample, normal priors

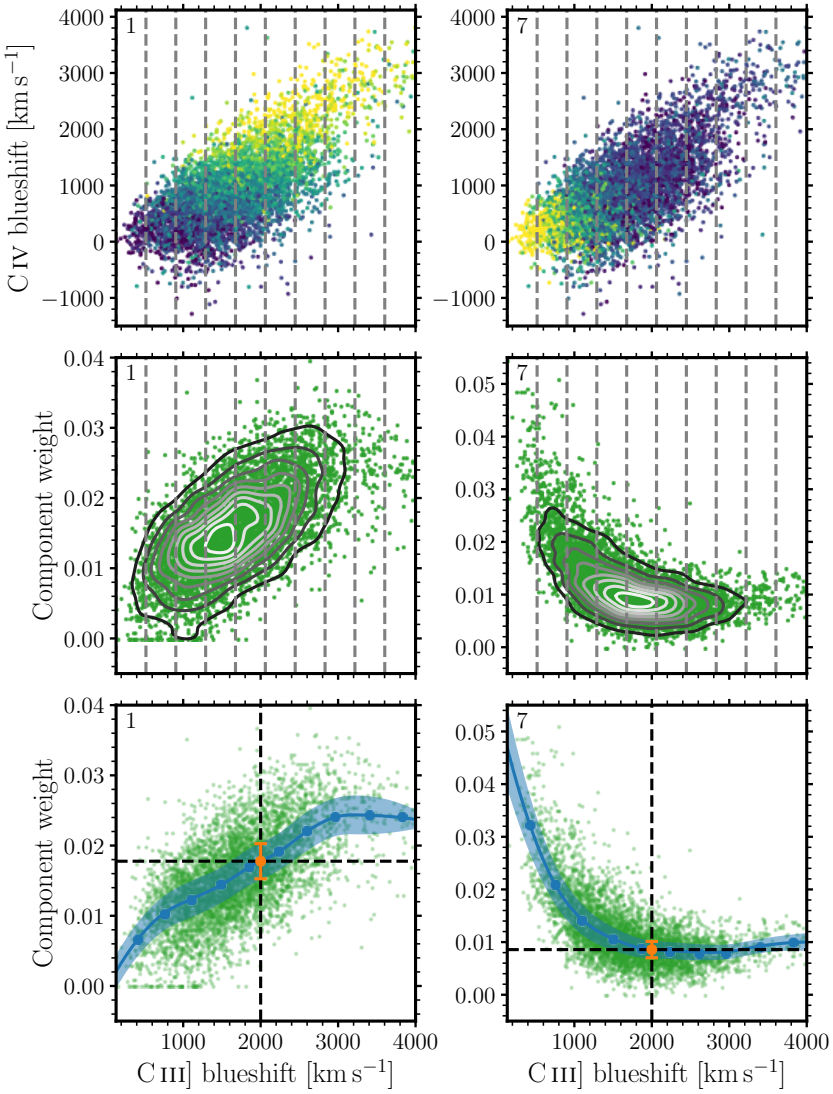

Figure A.1: Priors for first component (left panels) and 7th (right panels) as examples, created from ∼4000 non-BAL quasars. Top: C IV blueshift against that of C III] for the non-BAL quasars, with points coloured by component weight. Vertical grey lines mark the C III] 'blueshift' bin edges. Middle: component weight against C III] 'blueshift'. Grey lines are again the bin edges. Bottom: median component weight in each C III] 'blueshift' bin against C III] 'blueshift' (blue points). The blue line and shaded regions are created via a quadratic spline interpolation of the median and the median absolute deviation component weights. The green points are the same as those in the middle panels. The orange points mark the priors for an example spectrum with a C III] blueshift of 2000 km s^{-1} where the points and errorbars mark the centre and width of the normal priors for each component.

can be created by implementing quadratic spline interpolation via the Python library SciPy (shaded regions in the same panels). As an example, a spectrum with a C III] blueshift of 2000 km s^{-1} will have a normal prior for component 1 (7) with centre 0.018 (0.009) and width 0.005 (0.003).

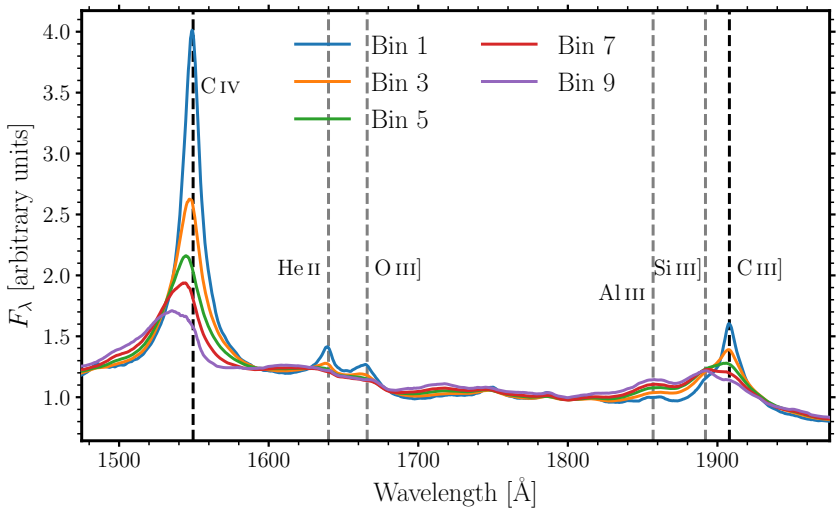

Figure A.2: Non-BAL quasar composite reconstructions for the odd-numbered bins in C III] 'blueshift'. From the first bin to the 9th, as the C III] 'blueshift' increases the C IV blueshift also increases.

Appendix B

The unabsorbed SEDs of BAL and non-BAL quasars

All quasar spectra in our sample, whether BAL or non-BAL, are reconstructed using MFICA components generated from a sample of non-BAL quasars. Much of the BAL spectra blueward of 1600 Å is affected by absorption such that to reconstruct the BAL quasar spectra we rely on the assumption that the correlation between the C IV emission and the spectra redward of 1600 Å of the non-BAL quasars can also be applied to the BAL quasar spectra. To test the validity of the assumption that, excluding absorption, the BAL and non-BAL spectra are similar, we have generated composite BAL and non-BAL spectra for different regions in C IV emission space. The regions are those marked on the C IV emission space in the top right panel of Figure B.1. Pixels masked due to narrow or broad absorption in individual spectra do not contribute to the composites. In regions 1–4, where the distributions of BAL and non-BAL quasars in the C IV emission space differ significantly the objects contributing to each composite have been matched carefully. Specifically, non-BAL composites have been constructed using the same number of spectra contributing to the BAL composite, where each non-BAL spectrum has been selected to lie close to a BAL-spectrum in the C IV emission space.

Figure B.1 presents the composite spectra of the BAL and non-BAL quasars, illustrating that for all regions in C IV emission space the median non-BAL and BAL spectra are remarkably similar. Only by adopting a very contrived model could the results of the comparison (for the two populations) be explained in circumstances where the assumption was not also valid for individual BAL-quasars. There are only slight differences in a few regions, namely 3, 6 and 9, where the continuum blueward of C IV is lower in the BAL composites than the non-BAL composites (1, 2 and 1 per cent difference on average for the three regions) on account of imperfect masking of the absorption troughs. The composite BAL *reconstructions* (lower right panels of Figure B.1) are almost identical to the non-BAL spectra. The improved match comes about because of the continuity over hundreds of $\mathrm{km\,s^{-1}}$ in the reconstruction process further reducing the effect of the modest depression in the

BAL-spectra.

The lack of BAL quasars at high C IV EWs can also be supported here. If a fraction of the non-BAL quasars have absorption in their spectra that is not being detected then the non-BAL spectra in composite 1 of Fig. B.1 would show a depression in the blue wing of the C IV emission. No significant absorption is observed and so we are confident in our ability to detect and mask the absorption, and subsequently reconstruct the intrinsic emission throughout the C IV emission space.

The C IV emission properties computed from the BAL and non-BAL composite spectra and the BAL-reconstructions show only very small differences. Even using the composite spectra themselves, the differences in the C IV EW and blueshift are small, typically only $\simeq$3 per cent in EW and $\simeq$70 km s^{-1} in blueshift. No blueshift difference exceeds 150 km s^{-1} and the most extreme difference in EW occurs for the composites in region 9, where the 2 Å change corresponds to a 9 per cent increase for the BAL composite. The measurements from the BAL and non-BAL reconstructions, used throughout the paper, are even more similar.

The differences in the C IV emission properties between the actual BAL and non-BAL composite spectra are negligible in the context of all measurements presented in the paper. The result provides clear evidence that the assumption regarding the similarity between the BAL and non-BAL SEDs is valid to a high degree of accuracy for the two populations.

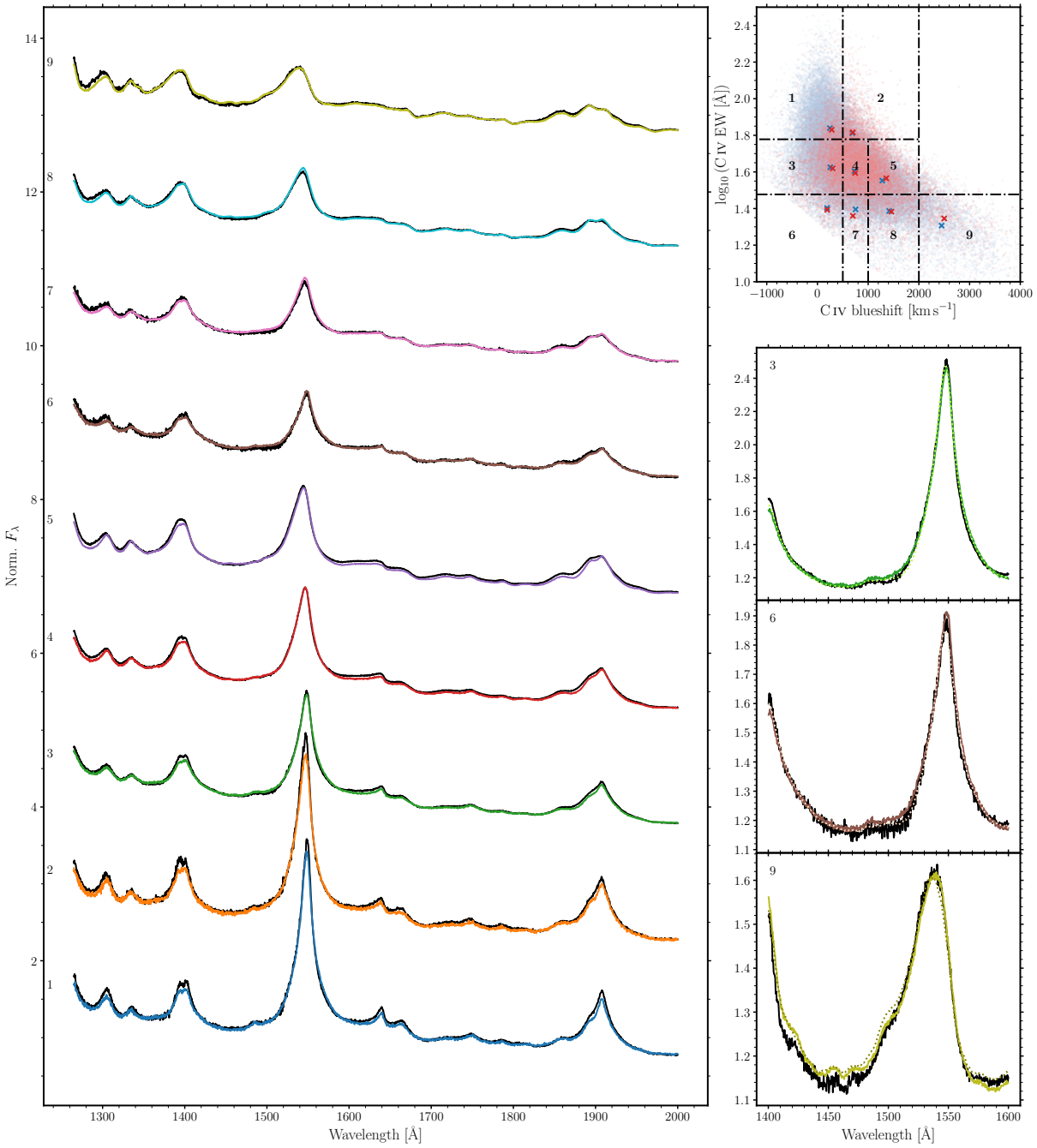

Figure B.1: Composite spectra from the numbered C IV regions in the top right panel. BAL composite spectra are in black and non-BAL quasars in colours. Each composite is numbered according to its location in C IV emission space. For three of the regions we plot the C IV emission in the lower right panels. Composite BAL reconstructions are also plotted here (coloured dotted lines). The C IV parameters measured from the composite spectra (crosses) and from individual quasars (points) are plotted in the C IV emission space with non-BALs in blue and BALs in red.

Appendix C

AI trough width

Figure C.1 contains the distribution of the widths of the troughs in the AI(BI=0) quasar population. The AI(BI>0) population also contains some AI troughs with BI = 0 and these are treated in the same way as the AI troughs in the AI(BI=0) quasar population. The current procedure for selecting NALs that are *in* AI troughs as opposed to *being* AI troughs is based on whether $V_{F\mathrm{depth},450} \leq 3000\,\mathrm{km\,s^{-1}}$ or $> 3000\,\mathrm{km\,s^{-1}}$, respectively. The former sub-sample can easily contain troughs with widths $> 2000\,\mathrm{km\,s^{-1}}$ and still have BI = 0 if the majority of the trough extends below the $3000\,\mathrm{km\,s^{-1}}$-minimum BI trough starting velocity. There is an excess of troughs with widths around the C IV doublet separation and the triplet separation in the $V_{F\mathrm{depth},450} > 3000\,\mathrm{km\,s^{-1}}$ sub-sample. However, there are such troughs in both sub-samples. In the future, it would be sensible to decide which AI troughs are wholly C IV NALs using the width of the troughs instead of splitting by location of the deepest part of the trough.

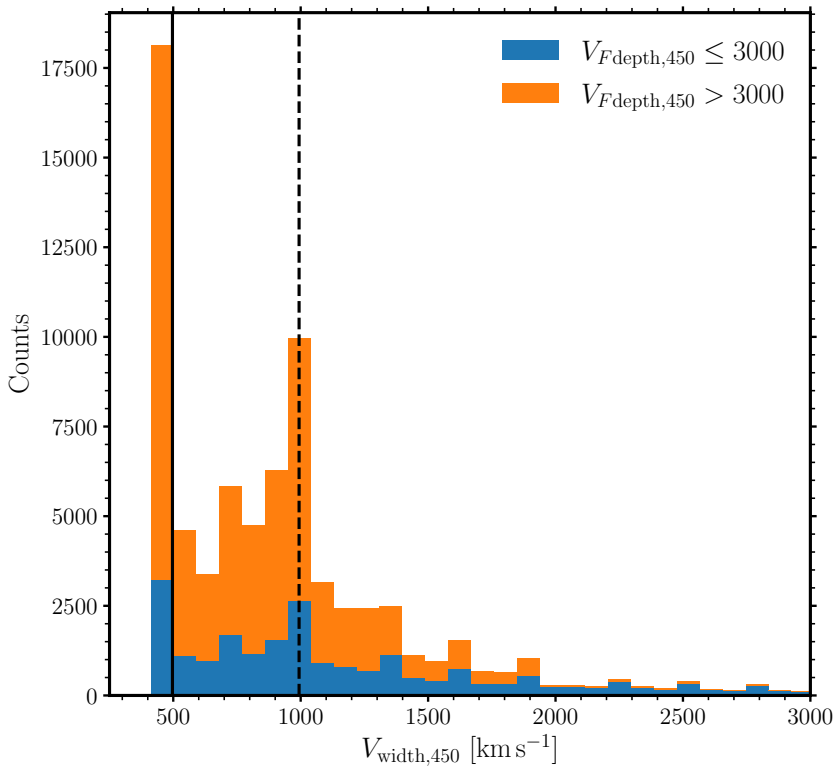

Figure C.1: Width of the AI(BI=0) troughs. The blue histogram contains the troughs with $V_{F\mathrm{depth,450}} \leq 3000\,\mathrm{km\,s^{-1}}$and the orange stacked on top contains those with $V_{F\mathrm{depth,450}} > 3000\,\mathrm{km\,s^{-1}}$. Many troughs in both sub-samples have widths around the C IV doublet separation (∼500 km s^{-1}; solid vertical line) and the triplet separation (∼1000 km s^{-1}; dashed vertical line).

Appendix D

Redshift evolution in C IV emission space

We have split the quasar sample into three redshift bins: [1.5, 2.0], (2.0, 2.5] and (2.5, 3.5], comprising 4421, 3391 and 2313 quasars, respectively, to investigate the redshift distribution in C IV emission space (top panels of Fig. D.1). In the lowest redshift bin, there is full coverage of the C IV emission space such that the detection and radio-loud fractions as functions of C IV blueshift (bottom row of Fig. D.1) are in closest agreement with the full sample and Fig. 5.3. As redshift increases, the highest C IV-EW sources – which are lower luminosity than low-EW sources – are lost from the sample; however, the detection and radio-loud fractions remain in qualitative agreement with the full sample. Also of note and a result of LOFAR's finite resolution is the change from most radio-loud sources having resolved emission in the lowest redshift bin ($\simeq$59 per cent of radio-loud sources) to being mostly unresolved in the highest redshift bin ($\simeq$24 per cent are resolved).

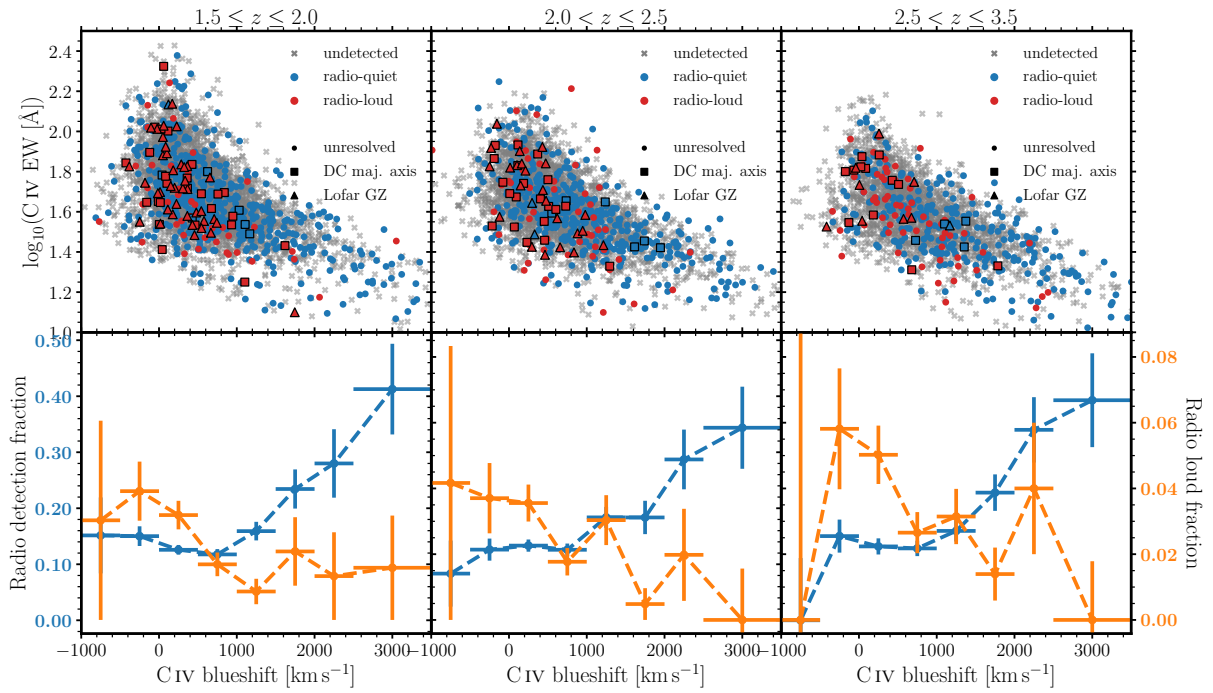

Figure D.1: Top row: the C IV emission space populated by quasars in the three redshift ranges. Red and blue markers indicate whether a source is radio-loud or radio-quiet (see Section 5.3.1). Note that all but four of the undetected quasars (grey crosses) have radio luminosity upper limits that would classify them as radio-quiet. Marker shape denotes whether the largest linear size (see Section 5.3.3) of the radio emission is calculated from the deconvolved major axis (square) or from the LOFAR Galaxy Zoo project (triangle), or if the emission is unresolved (circle). Bottom row: detection (left-hand axes, blue) and radio-loud (right-hand axes, orange) fractions as functions of C IV blueshift for the three redshift ranges. Vertical error bars for bins empty of radio-loud quasars have been calculated assuming the presence of one radio-loud quasar. This is the case for the lowest and highest C IV blueshift bins in the highest redshift subsample, and the highest C IV blueshift bin in the middle redshift subsample.

Appendix E

Effect of target selection on radio fractions

We have limited the sample to the quasars targeted as part of the CORE BOSS sample, reducing the sample from 10 163 to 2195 quasars. The 7968 quasars removed included 14 quasars targeted for their FIRST detections. Figure E.1 contains the radio-detection and radio-loud fractions as a function of blueshift for this limited sample and can be compared directly to Fig. 5.3. Due to the decreased sample size, the error bars are much larger than in Fig. 5.3. Limiting the sample in this way has not changed the qualitative trends illustrated in Fig. 5.3: the detection fraction increases with C IV blueshift whilst the radio-loud fraction decreases with increasing blueshift.

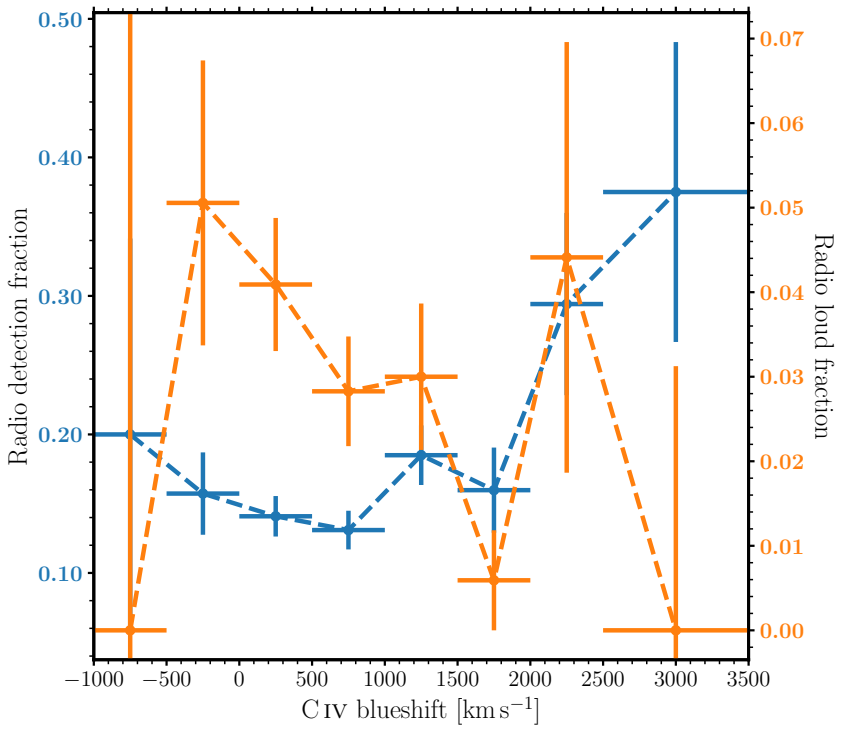

Figure E.1: Same as Fig. 5.3 but having limited the sample to quasars only targeted as part of the CORE BOSS sample. The lowest and highest C IV blueshift bins contain zero radio-loud quasars, thus their vertical error bars are estimated based on one radio-loud quasar populating these bins. An overall increase in detection fraction and decreasing radio-loud fraction as blueshift increases are observed.

Bibliography

Abolfathi, B., Aguado, D. S., Aguilar, G., *et al.* (2018): *The Fourteenth Data Release of the Sloan Digital Sky Survey: First Spectroscopic Data from the Extended Baryon Oscillation Spectroscopic Survey and from the Second Phase of the Apache Point Observatory Galactic Evolution Experiment*
The Astrophysical Journal Supplement Series, Volume 235, Issue 2, Page 42 [DOI] [ADS] [arXiv]

Aird, J., Nandra, K., Laird, E. S., *et al.* (2010): *The evolution of the hard X-ray luminosity function of AGN*
Monthly Notices of the Royal Astronomical Society, Volume 401, Issue 4, Pages 2531–2551 [DOI] [ADS] [arXiv]

Allen, J. T., Hewett, P. C., Maddox, N., *et al.* (2011): *A strong redshift dependence of the broad absorption line quasar fraction*
Monthly Notices of the Royal Astronomical Society, Volume 410, Issue 2, Pages 860–884 [DOI] [ADS] [arXiv]

Allen, J. T., Hewett, P. C., Richardson, C. T., *et al.* (2013): *Classification and analysis of emission-line galaxies using mean field independent component analysis*
Monthly Notices of the Royal Astronomical Society, Volume 430, Issue 4, Pages 3510–3536 [DOI] [ADS] [arXiv]

An, T. & Baan, W. A. (2012): *The Dynamic Evolution of Young Extragalactic Radio Sources*
The Astrophysical Journal, Volume 760, Issue 1, Page 77 [DOI] [ADS] [arXiv]

Antonucci, R. (1993): *Unified models for active galactic nuclei and quasars.*
Annual Review of Astronomy & Astrophysics, Volume 31, Pages 473–521 [DOI] [ADS]

Arav, N., Liu, G., Xu, X., *et al.* (2018): *Evidence that 50% of BALQSO Outflows Are Situated at Least 100 pc from the Central Source*
The Astrophysical Journal, Volume 857, Issue 1, Page 60 [DOI] [ADS] [arXiv]

Arnaud, M., Pratt, G. W., Piffaretti, R., *et al.* (2010): *The universal galaxy cluster pressure profile from a representative sample of nearby systems (REXCESS) and the Y_{SZ} - M_{500} relation*
Astronomy & Astrophysics, Volume 517, Page A92 [DOI] [ADS] [arXiv]

Baldi, R. D., Capetti, A., & Giovannini, G. (2015): *Pilot study of the radio-emitting AGN population: the emerging new class of FR 0 radio-galaxies*
Astronomy & Astrophysics, Volume 576, Page A38 [DOI] [ADS] [arXiv]

Baldi, R. D., Capetti, A., & Massaro, F. (2018): *FR0CAT: a FIRST catalog of FR 0 radio galaxies*
Astronomy & Astrophysics, Volume 609, Page A1 [DOI] [ADS] [arXiv]

Baldwin, J. A. (1977): *Luminosity Indicators in the Spectra of Quasi-Stellar Objects*
The Astrophysical Journal, Volume 214, Pages 679–684 [DOI] [ADS]

Baldwin, J. E. (1982): *Evolutionary tracks of extended radio sources*
In Heeschen, D. S. & Wade, C. M. (eds.): *Extragalactic Radio Sources.* D. Reidel Publishing Co., Dordrecht [ADS]

Baloković, M., Smolčić, V., Ivezić, Ž., *et al.* (2012): *Disclosing the Radio Loudness Distribution Dichotomy in Quasars: An Unbiased Monte Carlo Approach Applied to the SDSS-FIRST Quasar Sample*
The Astrophysical Journal, Volume 759, Issue 1, Page 30 [DOI] [ADS] [arXiv]

Barthel, P., Podigachoski, P., Wilkes, B., *et al.* (2017): *Starburst-driven Superwinds in Quasar Host Galaxies*
The Astrophysical Journal Letters, Volume 843, Issue 1, Page L16 [DOI] [ADS] [arXiv]

Baskin, A., Laor, A., & Hamann, F. (2013): *The average absorption properties of broad absorption line quasars at $800 < \lambda_{rest} < 3000$ Å, and the underlying physical parameters*
Monthly Notices of the Royal Astronomical Society, Volume 432, Issue 2, Pages 1525–1543 [DOI] [ADS] [arXiv]

Baskin, A., Laor, A., & Hamann, F. (2015): *On the origins of C IV absorption profile diversity in broad absorption line quasars*
Monthly Notices of the Royal Astronomical Society, Volume 449, Issue 2, Pages 1593–1604 [DOI] [ADS] [arXiv]

Baum, S. A., Zirbel, E. L., & O'Dea, C. P. (1995): *Toward Understanding the Fanaroff-Riley Dichotomy in Radio Source Morphology and Power*
The Astrophysical Journal, Volume 451, Page 88 [DOI] [ADS]

Becker, J. K., Biermann, P. L., Dreyer, J., *et al.* (2009): *Cosmic Rays VI - Starburst galaxies at multiwavelengths*
arXiv e-prints (0901.1775) [ADS] [arXiv]

Becker, R. H., White, R. L., Gregg, M. D., *et al.* (2000): *Properties of Radio-selected Broad Absorption Line Quasars from the First Bright Quasar Survey*
The Astrophysical Journal, Volume 538, Issue 1, Pages 72–82 [DOI] [ADS] [arXiv]

Becker, R. H., White, R. L., & Helfand, D. J. (**1995**): *The FIRST Survey: Faint Images of the Radio Sky at Twenty Centimeters*
The Astrophysical Journal, Volume 450, Page 559 [DOI] [ADS]

Beckwith, K., Hawley, J. F., & Krolik, J. H. (**2009**): *Transport of Large-Scale Poloidal Flux in Black Hole Accretion*
The Astrophysical Journal, Volume 707, Issue 1, Pages 428–445 [DOI] [ADS] [arXiv]

Best, P. N. (**2009**): *Radio source populations: Results from SDSS*
Astronomische Nachrichten, Volume 330, Issue 2, Pages 184–189 [DOI] [ADS]

Best, P. N. & Heckman, T. M. (**2012**): *On the fundamental dichotomy in the local radio-AGN population: accretion, evolution and host galaxy properties*
Monthly Notices of the Royal Astronomical Society, Volume 421, Issue 2, Pages 1569–1582 [DOI] [ADS] [arXiv]

Bicknell, G. V. (**1995**): *Relativistic Jets and the Fanaroff-Riley Classification of Radio Galaxies*
The Astrophysical Journal Supplement Series, Volume 101, Page 29 [DOI] [ADS] [arXiv]

Blandford, R., Meier, D., & Readhead, A. (**2019**): *Relativistic Jets from Active Galactic Nuclei*
Annual Review of Astronomy & Astrophysics, Volume 57, Pages 467–509 [DOI] [ADS] [arXiv]

Blandford, R. D. & Payne, D. G. (**1982**): *Hydromagnetic flows from accretion disks and the production of radio jets.*
Monthly Notices of the Royal Astronomical Society, Volume 199, Pages 883–903 [DOI] [ADS]

Blandford, R. D. & Znajek, R. L. (**1977**): *Electromagnetic extraction of energy from Kerr black holes.*
Monthly Notices of the Royal Astronomical Society, Volume 179, Pages 433–456 [DOI] [ADS]

Blundell, K. M. & Beasley, A. J. (**1998**): *The central engines of radio-quiet quasars*
Monthly Notices of the Royal Astronomical Society, Volume 299, Issue 1, Pages 165–170 [DOI] [ADS] [arXiv]

Blundell, K. M., Beasley, A. J., & Bicknell, G. V. (**2003**): *A Relativistic Jet in the Radio-quiet Quasar PG 1407+263*
The Astrophysical Journal Letters, Volume 591, Issue 2, Pages L103–L106 [DOI] [ADS] [arXiv]

Blundell, K. M. & Kuncic, Z. (**2007**): *On the Origin of Radio Core Emission in Radio-quiet Quasars*
The Astrophysical Journal Letters, Volume 668, Issue 2, Pages L103–L106 [DOI] [ADS] [arXiv]

Blundell, K. M. & Rawlings, S. (**2000**): *The Spectra and Energies of Classical Double Radio Lobes*
The Astronomical Journal, Volume 119, Issue 3, Pages 1111–1122 [DOI] [ADS] [arXiv]

Blundell, K. M., Rawlings, S., & Willott, C. J. (**1999**): *The Nature and Evolution of Classical Double Radio Sources from Complete Samples*
The Astronomical Journal, Volume 117, Issue 2, Pages 677–706 [DOI] [ADS] [arXiv]

Blundell, K. M., Rawlings, S., & Willott, C. J. (**2000**): *The Evolution of Classical Doubles: Clues from Complete Samples*
In van Haarlem, M. P. (ed.): *Perspectives on Radio Astronomy: Science with Large Antenna Arrays*. ASTRON, Dwingeloo [ADS] [arXiv]

Boroson, T. A. & Green, R. F. (**1992**): *The Emission-Line Properties of Low-Redshift Quasi-stellar Objects*
The Astrophysical Journal Supplement Series, Volume 80, Page 109 [DOI] [ADS]

Bowler, R. A. A., Hewett, P. C., Allen, J. T., *et al.* (**2014**): *Line-driven radiative outflows in luminous quasars*
Monthly Notices of the Royal Astronomical Society, Volume 445, Issue 1, Pages 359–377 [DOI] [ADS] [arXiv]

Broderick, J. W. & Fender, R. P. (**2011**): *Is there really a dichotomy in active galactic nucleus jet power?*
Monthly Notices of the Royal Astronomical Society, Volume 417, Issue 1, Pages 184–197 [DOI] [ADS] [arXiv]

Brotherton, M. S., Tran, H. D., Becker, R. H., *et al.* (**2001**): *Composite Spectra from the FIRST Bright Quasar Survey*
The Astrophysical Journal, Volume 546, Issue 2, Pages 775–781 [DOI] [ADS] [arXiv]

Burbidge, E. M. & Burbidge, G. R. (**1975**): *Empirical evidence concerning absorption lines and radiation pressure in quasi-stellar objects.*
The Astrophysical Journal, Volume 202, Pages 287–295 [DOI] [ADS]

Buttiglione, S., Capetti, A., Celotti, A., *et al.* (**2010**): *An optical spectroscopic survey of the 3CR sample of radio galaxies with $z < 0.3$. II. Spectroscopic classes and accretion modes in radio-loud AGN*
Astronomy & Astrophysics, Volume 509, Page A6 [DOI] [ADS] [arXiv]

Calistro Rivera, G., Williams, W. L., Hardcastle, M. J., *et al.* (**2017**): *The LOFAR window on star-forming galaxies and AGNs - curved radio SEDs and IR-radio correlation at* $0 < z < 2.5$
Monthly Notices of the Royal Astronomical Society, Volume 469, Issue 3, Pages 3468–3488 [DOI] [ADS] [arXiv]

Capellupo, D. M., Hamann, F., Shields, J. C., *et al.* (**2012**): *Variability in quasar broad absorption line outflows - II. Multi-epoch monitoring of Si IV and C IV broad absorption line variability*
Monthly Notices of the Royal Astronomical Society, Volume 422, Issue 4, Pages 3249–3267 [DOI] [ADS] [arXiv]

Capellupo, D. M., Hamann, F., Shields, J. C., *et al.* (**2013**): *Variability in quasar broad absorption line outflows - III. What happens on the shortest time-scales?*
Monthly Notices of the Royal Astronomical Society, Volume 429, Issue 3, Pages 1872–1886 [DOI] [ADS] [arXiv]

Chajet, L. S. & Hall, P. B. (**2013**): *Magnetohydrodynamic disc winds and linewidth distributions*
Monthly Notices of the Royal Astronomical Society, Volume 429, Issue 4, Pages 3214–3229 [DOI] [ADS] [arXiv]

Chartas, G., Brandt, W. N., Gallagher, S. C., *et al.* (**2002**): *CHANDRA Detects Relativistic Broad Absorption Lines from APM 08279+5255*
The Astrophysical Journal, Volume 579, Issue 1, Pages 169–175 [DOI] [ADS] [arXiv]

Chelouche, D. & Netzer, H. (**2003**): *Continuum shielding and flow dynamics in active galactic nuclei*
Monthly Notices of the Royal Astronomical Society, Volume 344, Issue 1, Pages 233–241 [DOI] [ADS] [arXiv]

Chen, C., Hamann, F., & Ma, B. (**2021**): *Extreme High-velocity Outflows from High-redshift BOSS Quasars*
The Astrophysical Journal, Volume 909, Issue 2, Page 208 [DOI] [ADS] [arXiv]

Chen, C., Hamann, F., Ma, B., *et al.* (**2020**): *Absorption-line Environments of High-redshift BOSS Quasars*
The Astrophysical Journal, Volume 902, Issue 1, Page 57 [DOI] [ADS] [arXiv]

Coatman, L., Hewett, P. C., Banerji, M., *et al.* (2016): *C IV emission-line properties and systematic trends in quasar black hole mass estimates*
Monthly Notices of the Royal Astronomical Society, Volume 461, Issue 1, Pages 647–665 [DOI] [ADS] [arXiv]

Coatman, L., Hewett, P. C., Banerji, M., *et al.* (2017): *Correcting C IV-based virial black hole masses*
Monthly Notices of the Royal Astronomical Society, Volume 465, Issue 2, Pages 2120–2142 [DOI] [ADS] [arXiv]

Coatman, L., Hewett, P. C., Banerji, M., *et al.* (2019): *Kinematics of C IV and [O III] emission in luminous high-redshift quasars*
Monthly Notices of the Royal Astronomical Society, Volume 486, Issue 4, Pages 5335–5348 [DOI] [ADS] [arXiv]

Condon, J. J. (1992): *Radio emission from normal galaxies.*
Annual Review of Astronomy & Astrophysics, Volume 30, Pages 575–611 [DOI] [ADS]

Condon, J. J., Kellermann, K. I., Kimball, A. E., *et al.* (2013): *Active Galactic Nucleus and Starburst Radio Emission from Optically Selected Quasi-stellar Objects*
The Astrophysical Journal, Volume 768, Issue 1, Page 37 [DOI] [ADS] [arXiv]

Cooksey, K. L., Kao, M. M., Simcoe, R. A., *et al.* (2013): *Precious Metals in SDSS Quasar Spectra. I. Tracking the Evolution of Strong, 1.5 < z < 4.5 C IV Absorbers with Thousands of Systems*
The Astrophysical Journal, Volume 763, Issue 1, Page 37 [DOI] [ADS] [arXiv]

Croston, J. H., Hardcastle, M. J., Harris, D. E., *et al.* (2005): *An X-Ray Study of Magnetic Field Strengths and Particle Content in the Lobes of FR II Radio Sources*
The Astrophysical Journal, Volume 626, Pages 733–747 [DOI]

Dai, X., Shankar, F., & Sivakoff, G. R. (2008): *2MASS Reveals a Large Intrinsic Fraction of BALQSOs*
The Astrophysical Journal, Volume 672, Issue 1, Pages 108–114 [DOI] [ADS] [arXiv]

Davis, S. W. & Tchekhovskoy, A. (2020): *Magnetohydrodynamics Simulations of Active Galactic Nucleus Disks and Jets*
Annual Review of Astronomy & Astrophysics, Volume 58, Pages 407–439 [DOI] [ADS] [arXiv]

Drouart, G., De Breuck, C., Vernet, J., *et al.* (2014): *Rapidly growing black holes and host galaxies in the distant Universe from the Herschel Radio Galaxy Evolution Project*
Astronomy & Astrophysics, Volume 566, Page A53 [DOI] [ADS] [arXiv]

Duncan, K. J., Sabater, J., Röttgering, H. J. A., *et al.* (2019): *The LOFAR Two-metre Sky Survey. IV. First Data Release: Photometric redshifts and rest-frame magnitudes*
Astronomy & Astrophysics, Volume 622, Page A3 [DOI] [ADS] [arXiv]

Dunn, J. P., Bautista, M., Arav, N., *et al.* (2010): *The Quasar Outflow Contribution to AGN Feedback: VLT Measurements of SDSS J0318-0600*
The Astrophysical Journal, Volume 709, Issue 2, Pages 611–631 [DOI] [ADS] [arXiv]

Elvis, M. (2000): *A Structure for Quasars*
The Astrophysical Journal, Volume 545, Issue 1, Pages 63–76 [DOI] [ADS] [arXiv]

Elvis, M., Risaliti, G., & Zamorani, G. (2002): *Most Supermassive Black Holes Must Be Rapidly Rotating*
The Astrophysical Journal Letters, Volume 565, Issue 2, Pages L75–L77 [DOI] [ADS] [arXiv]

Fabian, A. C. (2012): *Observational Evidence of Active Galactic Nuclei Feedback*
Annual Review of Astronomy & Astrophysics, Volume 50, Pages 455–489 [DOI] [ADS] [arXiv]

Falcke, H., Sherwood, W., & Patnaik, A. R. (1996): *The Nature of Radio-intermediate Quasars: What Is Radio-loud and What Is Radio-quiet?*
The Astrophysical Journal, Volume 471, Page 106 [DOI] [ADS] [arXiv]

Fanaroff, B. L. & Riley, J. M. (1974): *The morphology of extragalactic radio sources of high and low luminosity*
Monthly Notices of the Royal Astronomical Society, Volume 167, Pages 31P–36P [DOI] [ADS]

Fawcett, V. A., Alexander, D. M., Rosario, D. J., *et al.* (2020): *Fundamental differences in the radio properties of red and blue quasars: enhanced compact AGN emission in red quasars*
Monthly Notices of the Royal Astronomical Society, Volume 494, Pages 4802–4818 [DOI]

Fender, R. P., Belloni, T. M., & Gallo, E. (2004): *Towards a unified model for black hole X-ray binary jets*
Monthly Notices of the Royal Astronomical Society, Volume 355, Issue 4, Pages 1105–1118 [DOI] [ADS] [arXiv]

Ferland, G. J., Chatzikos, M., Guzmán, F., *et al.* (2017): *The 2017 Release Cloudy*
Revista Mexicana de Astronomia y Astrofisica, Volume 53, Pages 385–438 [ADS] [arXiv]

Ferrarese, L. & Merritt, D. (2000): *A Fundamental Relation between Supermassive Black Holes and Their Host Galaxies*
The Astrophysical Journal Letters, Volume 539, Issue 1, Pages L9–L12 [DOI] [ADS] [arXiv]

Filiz Ak, N., Brandt, W. N., Hall, P. B., *et al.* (2012): *Broad Absorption Line Disappearance on Multi-year Timescales in a Large Quasar Sample*
The Astrophysical Journal, Volume 757, Issue 2, Page 114 [DOI] [ADS] [arXiv]

Filiz Ak, N., Brandt, W. N., Hall, P. B., *et al.* (2013): *Broad Absorption Line Variability on Multi-year Timescales in a Large Quasar Sample*
The Astrophysical Journal, Volume 777, Issue 2, Page 168 [DOI] [ADS] [arXiv]

Francis, P. J., Hewett, P. C., Foltz, C. B., *et al.* (1992): *An Objective Classification Scheme for QSO Spectra*
The Astrophysical Journal, Volume 398, Page 476 [DOI] [ADS]

Frank, J., King, A., & Raine, D. J. (2002): *Accretion Power in Astrophysics: Third Edition*
Cambridge University Press, Cambridge, UK [ADS]

Gaskell, C. M. (**1982**): *A redshift difference between high and low ionization emission-line regions in QSO's-evidence for radial motions.*
The Astrophysical Journal, Volume 263, Pages 79–86 [DOI] [ADS]

Gebhardt, K., Bender, R., Bower, G., *et al.* (**2000**): *A Relationship between Nuclear Black Hole Mass and Galaxy Velocity Dispersion*
The Astrophysical Journal Letters, Volume 539, Issue 1, Pages L13–L16 [DOI] [ADS] [arXiv]

Gendre, M. A., Best, P. N., Wall, J. V., *et al.* (**2013**): *The relation between morphology, accretion modes and environmental factors in local radio AGN*
Monthly Notices of the Royal Astronomical Society, Volume 430, Issue 4, Pages 3086–3101 [DOI] [ADS] [arXiv]

Gibson, R. R., Brandt, W. N., Gallagher, S. C., *et al.* (**2010**): *The Evolution of Quasar C IV and Si IV Broad Absorption Lines over Multi-year Timescales*
The Astrophysical Journal, Volume 713, Issue 1, Pages 220–231 [DOI] [ADS] [arXiv]

Giustini, M. & Proga, D. (**2019**): *A global view of the inner accretion and ejection flow around super massive black holes. Radiation-driven accretion disk winds in a physical context*
Astronomy & Astrophysics, Volume 630, Page A94 [DOI] [ADS] [arXiv]

Green, R. F., Schmidt, M., & Liebert, J. (**1986**): *The Palomar-Green Catalog of Ultraviolet-Excess Stellar Objects*
The Astrophysical Journal Supplement Series, Volume 61, Page 305 [DOI] [ADS]

Grier, C. J., Shen, Y., Horne, K., *et al.* (**2019**): *The Sloan Digital Sky Survey Reverberation Mapping Project: Initial C IV Lag Results from Four Years of Data*
The Astrophysical Journal, Volume 887, Issue 1, Page 38 [DOI] [ADS] [arXiv]

Gürkan, G., Hardcastle, M. J., Best, P. N., *et al.* (**2019**): *LoTSS/HETDEX: Optical quasars. I. Low-frequency radio properties of optically selected quasars*
Astronomy & Astrophysics, Volume 622, Page A11 [DOI] [ADS] [arXiv]

Gürkan, G., Hardcastle, M. J., Jarvis, M. J., *et al.* (**2015**): *Herschel-ATLAS: the connection between star formation and AGN activity in radio-loud and radio-quiet active galaxies*
Monthly Notices of the Royal Astronomical Society, Volume 452, Issue 4, Pages 3776–3794 [DOI] [ADS] [arXiv]

Gürkan, G., Hardcastle, M. J., Smith, D. J. B., *et al.* (**2018**): *LOFAR/H-ATLAS: the low-frequency radio luminosity-star formation rate relation*
Monthly Notices of the Royal Astronomical Society, Volume 475, Issue 3, Pages 3010–3028 [DOI] [ADS] [arXiv]

Hall, P. B., Anderson, S. F., Strauss, M. A., *et al.* (**2002**): *Unusual Broad Absorption Line Quasars from the Sloan Digital Sky Survey*
The Astrophysical Journal Supplement Series, Volume 141, Issue 2, Pages 267–309 [DOI] [ADS] [arXiv]

Hall, P. B., Brandt, W. N., Petitjean, P., *et al.* (**2013**): *Broad absorption line quasars with redshifted troughs: high-velocity infall or rotationally dominated outflows?*
Monthly Notices of the Royal Astronomical Society, Volume 434, Issue 1, Pages 222–256 [DOI] [ADS] [arXiv]

Hamann, F., Herbst, H., Paris, I., *et al.* (**2019**): *On the structure and energetics of quasar broad absorption-line outflows*
Monthly Notices of the Royal Astronomical Society, Volume 483, Issue 2, Pages 1808–1828 [DOI] [ADS] [arXiv]

Hamann, F., Kanekar, N., Prochaska, J. X., *et al.* (**2011**): *A high-velocity narrow absorption line outflow in the quasar J212329.46 - 005052.9*
Monthly Notices of the Royal Astronomical Society, Volume 410, Issue 3, Pages 1957–1974 [DOI] [ADS] [arXiv]

Hardcastle, M. J. (**2018**): *A simulation-based analytic model of radio galaxies*
Monthly Notices of the Royal Astronomical Society, Volume 475, Issue 2, Pages 2768–2786 [DOI] [ADS] [arXiv]

Hardcastle, M. J. & Croston, J. H. (**2020**): *Radio galaxies and feedback from AGN jets*
New Astronomy Reviews, Volume 88, Page 101539 [DOI] [ADS] [arXiv]

Hardcastle, M. J., Williams, W. L., Best, P. N., *et al.* (**2019**): *Radio-loud AGN in the first LoTSS data release. The lifetimes and environmental impact of jet-driven sources*
Astronomy & Astrophysics, Volume 622, Page A12 [DOI] [ADS] [arXiv]

Harris, K., Farrah, D., Schulz, B., *et al.* (**2016**): *Star formation rates in luminous quasars at $2 < z < 3$*
Monthly Notices of the Royal Astronomical Society, Volume 457, Issue 4, Pages 4179–4194 [DOI] [ADS] [arXiv]

Harwood, J. J., Croston, J. H., Intema, H. T., *et al.* (**2016**): *FR II radio galaxies at low frequencies - I. Morphology, magnetic field strength and energetics*
Monthly Notices of the Royal Astronomical Society, Volume 458, Issue 4, Pages 4443–4455 [DOI] [ADS] [arXiv]

Harwood, J. J., Hardcastle, M. J., Morganti, R., *et al.* (**2017**): *FR II radio galaxies at low frequencies - II. Spectral ageing and source dynamics*
Monthly Notices of the Royal Astronomical Society, Volume 469, Issue 1, Pages 639–655 [DOI] [ADS] [arXiv]

Heckman, T. M. & Best, P. N. (**2014**): *The Coevolution of Galaxies and Supermassive Black Holes: Insights from Surveys of the Contemporary Universe*
Annual Review of Astronomy & Astrophysics, Volume 52, Pages 589–660 [DOI] [ADS] [arXiv]

Helou, G., Soifer, B. T., & Rowan-Robinson, M. (**1985**): *Thermal infrared and nonthermal radio : remarkable correlation in disks of galaxies.*
The Astrophysical Journal Letters, Volume 298, Pages L7–L11 [DOI] [ADS]

Herrera Ruiz, N., Middelberg, E., Norris, R. P., *et al.* (**2016**): *Unveiling the origin of the radio emission in radio-quiet quasars*
Astronomy & Astrophysics, Volume 589, Page L2 [DOI] [ADS] [arXiv]

Hewett, P. C. & Foltz, C. B. (**2003**): *The Frequency and Radio Properties of Broad Absorption Line Quasars*
The Astronomical Journal, Volume 125, Issue 4, Pages 1784–1794 [DOI] [ADS] [arXiv]

Hewett, P. C., Foltz, C. B., & Chaffee, F. H. (**1995**): *The Large Bright Quasar Survey. VI. Quasar Catalog and Survey Parameters*
The Astronomical Journal, Volume 109, Page 1498 [DOI] [ADS]

Hewett, P. C. & Wild, V. (**2010**): *Improved redshifts for SDSS quasar spectra*
Monthly Notices of the Royal Astronomical Society, Volume 405, Issue 4, Pages 2302–2316 [DOI] [ADS] [arXiv]

Higginbottom, N., Knigge, C., Sim, S. A., *et al.* (**2020**): *Thermal and radiation driving can produce observable disc winds in hard-state X-ray binaries*
Monthly Notices of the Royal Astronomical Society, Volume 492, Issue 4, Pages 5271–5279 [DOI] [ADS] [arXiv]

Hill, G. J. & Lilly, S. J. (**1991**): *A Change in the Cluster Environments of Radio Galaxies with Cosmic Epoch*
The Astrophysical Journal, Volume 367, Page 1 [DOI] [ADS]

Højen-Sørensen, P. A., Winther, O., & Hansen, L. K. (**2002**): *Mean-Field Approaches to Independent Component Analysis*
Neural Computation, Volume 14, Issue 4, Pages 889–918 [DOI]

Ivezić, Ž. & et al. (**2019**): *LSST: From Science Drivers to Reference Design and Anticipated Data Products*
The Astrophysical Journal, Volume 873, Issue 2, Page 111 [DOI] [ADS] [arXiv]

Ivezić, Ž., Menou, K., Knapp, G. R., *et al.* (**2002**): *Optical and Radio Properties of Extragalactic Sources Observed by the FIRST Survey and the Sloan Digital Sky Survey*
The Astronomical Journal, Volume 124, Issue 5, Pages 2364–2400 [DOI] [ADS] [arXiv]

Izumi, T., Wada, K., Fukushige, R., *et al.* (**2018**): *Circumnuclear Multiphase Gas in the Circinus Galaxy. II. The Molecular and Atomic Obscuring Structures Revealed with ALMA*
The Astrophysical Journal, Volume 867, Issue 1, Page 48 [DOI] [ADS] [arXiv]

Jarvis, M. E., Harrison, C. M., Thomson, A. P., *et al.* (**2019**): *Prevalence of radio jets associated with galactic outflows and feedback from quasars*
Monthly Notices of the Royal Astronomical Society, Volume 485, Issue 2, Pages 2710–2730 [DOI] [ADS] [arXiv]

Jarvis, M. J. & Rawlings, S. (**2004**): *The accretion history of the universe with the SKA*
New Astronomy Reviews, Volume 48, Issue 11-12, Pages 1173–1185 [DOI] [ADS] [arXiv]

Jiang, L., Fan, X., Ivezić, Ž., *et al.* (**2007**): *The Radio-Loud Fraction of Quasars is a Strong Function of Redshift and Optical Luminosity*
The Astrophysical Journal, Volume 656, Issue 2, Pages 680–690 [DOI] [ADS] [arXiv]

Kaiser, C. R. & Best, P. N. (**2007**): *Luminosity function, sizes and FR dichotomy of radio-loud AGN*
Monthly Notices of the Royal Astronomical Society, Volume 381, Issue 4, Pages 1548–1560 [DOI] [ADS] [arXiv]

Kellermann, K. I., Sramek, R., Schmidt, M., *et al.* (**1989**): *VLA Observations of Objects in the Palomar Bright Quasar Survey*
The Astronomical Journal, Volume 98, Page 1195 [DOI] [ADS]

Kimball, A. E., Kellermann, K. I., Condon, J. J., *et al.* (**2011**): *The Two-component Radio Luminosity Function of Quasi-stellar Objects: Star Formation and Active Galactic Nucleus*
The Astrophysical Journal Letters, Volume 739, Issue 1, Page L29 [DOI] [ADS] [arXiv]

King, A. & Nixon, C. (**2015**): *AGN flickering and chaotic accretion*
Monthly Notices of the Royal Astronomical Society, Volume 453, Issue 1, Pages L46–L47 [DOI] [ADS] [arXiv]

King, A. R. & Pringle, J. E. (**2007**): *Fuelling active galactic nuclei*
Monthly Notices of the Royal Astronomical Society, Volume 377, Issue 1, Pages L25–L28 [DOI] [ADS] [arXiv]

Klindt, L., Alexander, D. M., Rosario, D. J., *et al.* (**2019**): *Fundamental differences in the radio properties of red and blue quasars: evolution strongly favoured over orientation*
Monthly Notices of the Royal Astronomical Society, Volume 488, Issue 3, Pages 3109–3128 [DOI] [ADS] [arXiv]

Knigge, C., Scaringi, S., Goad, M. R., *et al.* (**2008**): *The intrinsic fraction of broad-absorption line quasars*
Monthly Notices of the Royal Astronomical Society, Volume 386, Issue 3, Pages 1426–1435 [DOI] [ADS] [arXiv]

Kollmeier, J. A., Zasowski, G., Rix, H.-W., *et al.* (**2017**): *SDSS-V: Pioneering Panoptic Spectroscopy*
arXiv e-prints (1711.03234) [ADS] [arXiv]

Konar, C., Saikia, D. J., Jamrozy, M., *et al.* (**2006**): *Spectral ageing analysis of the double-double radio galaxy J1453+3308*
Monthly Notices of the Royal Astronomical Society, Volume 372, Issue 2, Pages 693–702 [DOI] [ADS] [arXiv]

Körding, E. G., Jester, S., & Fender, R. (**2006**): *Accretion states and radio loudness in active galactic nuclei: analogies with X-ray binaries*
Monthly Notices of the Royal Astronomical Society, Volume 372, Issue 3, Pages 1366–1378 [DOI] [ADS] [arXiv]

Kormendy, J. & Ho, L. C. (**2013**): *Coevolution (Or Not) of Supermassive Black Holes and Host Galaxies*
Annual Review of Astronomy & Astrophysics, Volume 51, Issue 1, Pages 511–653 [DOI] [ADS] [arXiv]

Kratzer, R. M. & Richards, G. T. (**2015**): *Mean and Extreme Radio Properties of Quasars and the Origin of Radio Emission*
The Astronomical Journal, Volume 149, Issue 2, Page 61 [DOI] [ADS]

Laing, R. A., Jenkins, C. R., Wall, J. V., *et al.* (**1994**): *Spectrophotometry of a Complete Sample of 3CR Radio Sources: Implications for Unified Models*
In Bicknell, G. V., Dopita, M. A., & Quinn, P. J. (eds.): *The Physics of Active Galaxies*. Astron. Soc. Pac., San Francisco [ADS]

LaMassa, S. M., Cales, S., Moran, E. C., *et al.* (**2015**): *The Discovery of the First "Changing Look" Quasar: New Insights Into the Physics and Phenomenology of Active Galactic Nucleus*
The Astrophysical Journal, Volume 800, Issue 2, Page 144 [DOI] [ADS] [arXiv]

Laor, A. & Behar, E. (**2008**): *On the origin of radio emission in radio-quiet quasars*
Monthly Notices of the Royal Astronomical Society, Volume 390, Issue 2, Pages 847–862 [DOI] [ADS] [arXiv]

Ledlow, M. J. & Owen, F. N. (**1996**): *20 CM VLA Survey of Abell Clusters of Galaxies. VI. Radio/Optical Luminosity Functions*
The Astronomical Journal, Volume 112, Page 9 [DOI] [ADS] [arXiv]

Leighly, K. M. (**2004**): *Hubble Space Telescope STIS Ultraviolet Spectral Evidence of Outflow in Extreme Narrow-Line Seyfert 1 Galaxies. II. Modeling and Interpretation*
The Astrophysical Journal, Volume 611, Issue 1, Pages 125–152 [DOI] [ADS] [arXiv]

Li, J., Shen, Y., Horne, K., *et al.* (**2017**): *The Sloan Digital Sky Survey Reverberation Mapping Project: Composite Lags at $z \leq 1$*
The Astrophysical Journal, Volume 846, Issue 1, Page 79 [DOI] [ADS] [arXiv]

Liska, M., Tchekhovskoy, A., & Quataert, E. (**2020**): *Large-scale poloidal magnetic field dynamo leads to powerful jets in GRMHD simulations of black hole accretion with toroidal field*
Monthly Notices of the Royal Astronomical Society, Volume 494, Issue 3, Pages 3656–3662 [DOI] [ADS] [arXiv]

Luo, B., Brandt, W. N., Hall, P. B., *et al.* (**2015**): *X-ray Insights into the Nature of PHL 1811 Analogs and Weak Emission-line Quasars: Unification with a Geometrically Thick Accretion Disk?*
The Astrophysical Journal, Volume 805, Issue 2, Page 122 [DOI] [ADS] [arXiv]

Lyke, B. W., Higley, A. N., McLane, J. N., *et al.* (**2020**): *The Sloan Digital Sky Survey Quasar Catalog: Sixteenth Data Release*
The Astrophysical Journal Supplement Series, Volume 250, Issue 1, Page 8 [DOI] [ADS] [arXiv]

Lynden-Bell, D. (**1969**): *Galactic Nuclei as Collapsed Old Quasars*
Nature, Volume 223, Issue 5207, Pages 690–694 [DOI] [ADS]

Maccagni, F. M., Murgia, M., Serra, P., *et al.* (**2020**): *The flickering nuclear activity of Fornax A*
Astronomy & Astrophysics, Volume 634, Page A9 [DOI] [ADS] [arXiv]

MacLeod, C. L., Ross, N. P., Lawrence, A., *et al.* (**2016**): *A systematic search for changing-look quasars in SDSS*
Monthly Notices of the Royal Astronomical Society, Volume 457, Issue 1, Pages 389–404 [DOI] [ADS] [arXiv]

Maddox, N., Hewett, P. C., Péroux, C., *et al.* (**2012**): *The large area KX quasar catalogue - I. Analysis of the photometric redshift selection and the complete quasar catalogue*
Monthly Notices of the Royal Astronomical Society, Volume 424, Issue 4, Pages 2876–2895 [DOI] [ADS] [arXiv]

Magorrian, J., Tremaine, S., Richstone, D., *et al.* (**1998**): *The Demography of Massive Dark Objects in Galaxy Centers*
The Astronomical Journal, Volume 115, Issue 6, Pages 2285–2305 [DOI] [ADS] [arXiv]

Marconi, A., Risaliti, G., Gilli, R., *et al.* (**2004**): *Local supermassive black holes, relics of active galactic nuclei and the X-ray background*
Monthly Notices of the Royal Astronomical Society, Volume 351, Issue 1, Pages 169–185 [DOI] [ADS] [arXiv]

Margala, D., Kirkby, D., Dawson, K., *et al.* (**2016**): *Improved Spectrophotometric Calibration of the SDSS-III BOSS Quasar Sample*
The Astrophysical Journal, Volume 831, Issue 2, Page 157 [DOI] [ADS] [arXiv]

Marin, F. (**2016**): *Are there reliable methods to estimate the nuclear orientation of Seyfert galaxies?*
Monthly Notices of the Royal Astronomical Society, Volume 460, Issue 4, Pages 3679–3705 [DOI] [ADS] [arXiv]

Marlar, A., Shemmer, O., Anderson, S. F., *et al.* (**2018**): *Steep Hard-X-Ray Spectra Indicate Extremely High Accretion Rates in Weak Emission-line Quasars*
The Astrophysical Journal, Volume 865, Issue 2, Page 92 [DOI] [ADS] [arXiv]

Mas-Ribas, L. & Mauland, R. (**2019**): *The Ubiquitous Imprint of Radiative Acceleration in the Mean Absorption Spectrum of Quasar Outflows*
The Astrophysical Journal, Volume 886, Issue 2, Page 151 [DOI] [ADS] [arXiv]

Matthews, J. H., Knigge, C., Higginbottom, N., *et al.* (**2020**): *Stratified disc wind models for the AGN broad-line region: ultraviolet, optical, and X-ray properties*
Monthly Notices of the Royal Astronomical Society, Volume 492, Issue 4, Pages 5540–5560 [DOI] [ADS] [arXiv]

Matthews, J. H., Knigge, C., & Long, K. S. (**2017**): *Quasar emission lines as probes of orientation: implications for disc wind geometries and unification*
Monthly Notices of the Royal Astronomical Society, Volume 467, Issue 3, Pages 2571–2584 [DOI] [ADS] [arXiv]

Matthews, J. H., Knigge, C., Long, K. S., *et al.* (**2016**): *Testing quasar unification: radiative transfer in clumpy winds*
Monthly Notices of the Royal Astronomical Society, Volume 458, Issue 1, Pages 293–305 [DOI] [ADS] [arXiv]

Mauch, T. & Sadler, E. M. (**2007**): *Radio sources in the 6dFGS: local luminosity functions at 1.4GHz for star-forming galaxies and radio-loud AGN*
Monthly Notices of the Royal Astronomical Society, Volume 375, Issue 3, Pages 931–950 [DOI] [ADS] [arXiv]

Mehdipour, M. & Costantini, E. (**2019**): *Relation between winds and jets in radio-loud AGN*
Astronomy & Astrophysics, Volume 625, Page A25 [DOI] [ADS] [arXiv]

Merloni, A., Predehl, P., Becker, W., *et al.* (**2012**): *eROSITA Science Book: Mapping the Structure of the Energetic Universe*
arXiv e-prints (1209.3114) [ADS] [arXiv]

Miller, B. P., Brandt, W. N., Schneider, D. P., *et al.* (**2011**): *X-ray Emission from Optically Selected Radio-intermediate and Radio-loud Quasars*
The Astrophysical Journal, Volume 726, Issue 1, Page 20 [DOI] [ADS] [arXiv]

Mingo, B., Croston, J. H., Hardcastle, M. J., *et al.* (**2019**): *Revisiting the Fanaroff-Riley dichotomy and radio-galaxy morphology with the LOFAR Two-Metre Sky Survey (LoTSS)*
Monthly Notices of the Royal Astronomical Society, Volume 488, Issue 2, Pages 2701–2721 [DOI] [ADS] [arXiv]

Miraghaei, H. & Best, P. N. (**2017**): *The nuclear properties and extended morphologies of powerful radio galaxies: the roles of host galaxy and environment*
Monthly Notices of the Royal Astronomical Society, Volume 466, Issue 4, Pages 4346–4363 [DOI] [ADS] [arXiv]

Molyneux, S. J., Harrison, C. M., & Jarvis, M. E. (**2019**): *Extreme ionised outflows are more common when the radio emission is compact in AGN host galaxies*
Astronomy & Astrophysics, Volume 631, Page A132 [DOI] [ADS] [arXiv]

Morabito, L. K., Matthews, J. H., Best, P. N., *et al.* (**2019**): *The origin of radio emission in broad absorption line quasars: Results from the LOFAR Two-metre Sky Survey*
Astronomy & Astrophysics, Volume 622, Page A15 [DOI] [ADS] [arXiv]

Muñoz-Darias, T., Jiménez-Ibarra, F., Panizo-Espinar, G., *et al.* (**2019**): *Hard-state Accretion Disk Winds from Black Holes: The Revealing Case of MAXI J1820+070*
The Astrophysical Journal Letters, Volume 879, Issue 1, Page L4 [DOI] [ADS] [arXiv]

Murray, N., Chiang, J., Grossman, S. A., *et al.* (**1995**): *Accretion Disk Winds from Active Galactic Nuclei*
The Astrophysical Journal, Volume 451, Page 498 [DOI] [ADS]

Myers, A. D., Palanque-Delabrouille, N., Prakash, A., *et al.* (**2015**): *The SDSS-IV Extended Baryon Oscillation Spectroscopic Survey: Quasar Target Selection*
The Astrophysical Journal Supplement Series, Volume 221, Issue 2, Page 27 [DOI] [ADS] [arXiv]

Nestor, D., Hamann, F., & Rodriguez Hidalgo, P. (**2008**): *The quasar-frame velocity distribution of narrow CIV absorbers*
Monthly Notices of the Royal Astronomical Society, Volume 386, Issue 4, Pages 2055–2064 [DOI] [ADS] [arXiv]

Newville, M., Stensitzki, T., Allen, D. B., *et al.* (**2014**): *LMFIT: Non-Linear Least-Square Minimization and Curve-Fitting for Python*
Zenodo, accessed August 7, 2019 [DOI] [ADS]

Nims, J., Quataert, E., & Faucher-Giguère, C.-A. (**2015**): *Observational signatures of galactic winds powered by active galactic nuclei*
Monthly Notices of the Royal Astronomical Society, Volume 447, Issue 4, Pages 3612–3622 [DOI] [ADS] [arXiv]

Nipoti, C. & Binney, J. (**2005**): *Time variability of active galactic nuclei and heating of cooling flows*
Monthly Notices of the Royal Astronomical Society, Volume 361, Issue 2, Pages 428–436 [DOI] [ADS] [arXiv]

O'Dea, C. P. (**1998**): *The Compact Steep-Spectrum and Gigahertz Peaked-Spectrum Radio Sources*
Publications of the Astronomical Society of the Pacific, Volume 110, Issue 747, Pages 493–532 [DOI] [ADS]

O'Dea, C. P., Baum, S. A., & Stanghellini, C. (**1991**): *What Are the Gigahertz Peaked-Spectrum Radio Sources?*
The Astrophysical Journal, Volume 380, Page 66 [DOI] [ADS]

O'Dea, C. P. & Saikia, D. J. (**2021**): *Compact steep-spectrum and peaked-spectrum radio sources*
The Astronomy and Astrophysics Review, Volume 29, Issue 1, Page 3 [DOI] [ADS] [arXiv]

Opper, M. & Winther, O. (**2005**): *Expectation Consistent Approximate Inference*
Journal of Machine Learning Research, Volume 6, Pages 2177–2204

Orienti, M. (**2016**): *Radio properties of Compact Steep Spectrum and GHz-Peaked Spectrum radio sources*
Astronomische Nachrichten, Volume 337, Issue 1-2, Page 9 [DOI] [ADS] [arXiv]

Panessa, F., Baldi, R. D., Laor, A., *et al.* (**2019**): *The origin of radio emission from radio-quiet active galactic nuclei*
Nature Astronomy, Volume 3, Pages 387–396 [DOI] [ADS] [arXiv]

Pâris, I., Petitjean, P., Aubourg, É., *et al.* (**2018**): *The Sloan Digital Sky Survey Quasar Catalog: Fourteenth data release*
Astronomy & Astrophysics, Volume 613, Page A51 [DOI] [ADS] [arXiv]

Pâris, I., Petitjean, P., Ross, N. P., *et al.* (**2017**): *The Sloan Digital Sky Survey Quasar Catalog: Twelfth data release*
Astronomy & Astrophysics, Volume 597, Page A79 [DOI] [ADS] [arXiv]

Perrotta, S., D'Odorico, V., Hamann, F., *et al.* (**2018**): *Hunting for metals using XQ-100 Legacy Survey composite spectra*
Monthly Notices of the Royal Astronomical Society, Volume 481, Issue 1, Pages 105–121 [DOI] [ADS] [arXiv]

Peterson, B. M. (**2001**): *Variability of Active Galactic Nuclei*
In Aretxaga, I., Kunth, D., & Mújica, R. (eds.): *Advanced Lectures on the Starburst-AGN*. World Scientific, Singapore [DOI] [ADS] [arXiv]

Pitchford, L. K., Hatziminaoglou, E., Feltre, A., *et al.* (**2016**): *Extreme star formation events in quasar hosts over $0.5 < z < 4$*
Monthly Notices of the Royal Astronomical Society, Volume 462, Issue 4, Pages 4067–4077 [DOI] [ADS] [arXiv]

Polletta, M., Tajer, M., Maraschi, L., *et al.* (**2007**): *Spectral Energy Distributions of Hard X-Ray Selected Active Galactic Nuclei in the XMM-Newton Medium Deep Survey*
The Astrophysical Journal, Volume 663, Issue 1, Pages 81–102 [DOI] [ADS] [arXiv]

Ponti, G., Fender, R. P., Begelman, M. C., *et al.* (**2012**): *Ubiquitous equatorial accretion disc winds in black hole soft states*
Monthly Notices of the Royal Astronomical Society, Volume 422, Issue 1, Pages L11–L15 [DOI] [ADS] [arXiv]

Predehl, P., Andritschke, R., Arefiev, V., *et al.* (**2020**): *The eROSITA X-ray telescope on SRG*
arXiv e-prints (2010.03477) [ADS] [arXiv]

Proga, D. (**2003**): *Numerical Simulations of Mass Outflows Driven from Accretion Disks by Radiation and Magnetic Forces*
The Astrophysical Journal, Volume 585, Issue 1, Pages 406–417 [DOI] [ADS] [arXiv]

Proga, D., Jiang, Y.-F., Davis, S. W., *et al.* (**2014**): *The Effects of Irradiation on Cloud Evolution in Active Galactic Nuclei*
The Astrophysical Journal, Volume 780, Issue 1, Page 51 [DOI] [ADS] [arXiv]

Proga, D., Stone, J. M., & Kallman, T. R. (**2000**): *Dynamics of Line-driven Disk Winds in Active Galactic Nuclei*
The Astrophysical Journal, Volume 543, Issue 2, Pages 686–696 [DOI] [ADS] [arXiv]

Raginski, I. & Laor, A. (**2016**): *AGN coronal emission models - I. The predicted radio emission*
Monthly Notices of the Royal Astronomical Society, Volume 459, Issue 2, Pages 2082–2096 [DOI] [ADS] [arXiv]

Rankine, A. L., Hewett, P. C., Banerji, M., *et al.* (**2020**): *BAL and non-BAL quasars: continuum, emission, and absorption properties establish a common parent sample*
Monthly Notices of the Royal Astronomical Society, Volume 492, Issue 3, Pages 4553–4575 [DOI] [ADS] [arXiv]

Rankine, A. L., Matthews, J. H., Hewett, P. C., *et al.* (**2021**): *Placing LOFAR-detected quasars in C IV emission space: implications for winds, jets and star formation*
Monthly Notices of the Royal Astronomical Society, Volume 502, Issue 3, Pages 4154–4169 [DOI] [ADS] [arXiv]

Read, S. C., Smith, D. J. B., Gürkan, G., *et al.* (**2018**): *The Far-Infrared Radio Correlation at low radio frequency with LOFAR/H-ATLAS*
Monthly Notices of the Royal Astronomical Society, Volume 480, Issue 4, Pages 5625–5644 [DOI] [ADS] [arXiv]

Reichard, T. A., Richards, G. T., Hall, P. B., *et al.* (**2003**): *Continuum and Emission-Line Properties of Broad Absorption Line Quasars*
The Astronomical Journal, Volume 126, Issue 6, Pages 2594–2607 [DOI] [ADS] [arXiv]

Reynolds, C. S. (**2014**): *Measuring Black Hole Spin Using X-Ray Reflection Spectroscopy*
Space Science Reviews, Volume 183, Issue 1-4, Pages 277–294 [DOI] [ADS] [arXiv]

Richards, G. T. (**2006**): *AGN Outflows in Emission and Absorption: The SDSS Perspective*
arXiv e-prints (astro-ph/0603827), Pages astro–ph/0603 827 [ADS] [arXiv]

Richards, G. T. (**2012**): *CIV Emission as a Probe of Accretion Disk Winds*
In Chartas, G., Hamann, F., & Leighly, K. M. (eds.): *AGN Winds in Charleston*. Astron. Soc. Pac., San Francisco [ADS] [arXiv]

Richards, G. T., Fan, X., Newberg, H. J., *et al.* (**2002a**): *Spectroscopic Target Selection in the Sloan Digital Sky Survey: The Quasar Sample*
The Astronomical Journal, Volume 123, Issue 6, Pages 2945–2975 [DOI] [ADS] [arXiv]

Richards, G. T., Kruczek, N. E., Gallagher, S. C., *et al.* (**2011**): *Unification of Luminous Type 1 Quasars through C IV Emission*
The Astronomical Journal, Volume 141, Issue 5, Page 167 [DOI] [ADS] [arXiv]

Richards, G. T., Plotkin, R. M., Hewett, P. C., *et al.* (**2021**): *A Novel Test of Quasar Orientation*
arXiv e-prints (2106.02633) [ADS] [arXiv]

Richards, G. T., Vanden Berk, D. E., Reichard, T. A., *et al.* (**2002b**): *Broad Emission-Line Shifts in Quasars: An Orientation Measure for Radio-Quiet Quasars?*
The Astronomical Journal, Volume 124, Issue 1, Pages 1–17 [DOI] [ADS] [arXiv]

Rogerson, J. (**2019**): *First Release: BALparams*
Zenodo, accessed May 1, 2019 [DOI] [ADS]

Rogerson, J. A., Hall, P. B., Ahmed, N. S., *et al.* (**2018**): *Emergence and Variability of Broad Absorption Line Quasar Outflows*
The Astrophysical Journal, Volume 862, Issue 1, Page 22 [DOI] [ADS] [arXiv]

Rojas Lobos, P. A., Goosmann, R. W., Marin, F., *et al.* (**2018**): *Modeling optical and UV polarization of AGNs. IV. Polarization timing*
Astronomy & Astrophysics, Volume 611, Page A39 [DOI] [ADS]

Rosario, D. J., Fawcett, V. A., Klindt, L., *et al.* (**2020**): *Fundamental differences in the radio properties of red and blue quasars: insight from the LOFAR Two-metre Sky Survey (LoTSS)*
Monthly Notices of the Royal Astronomical Society, Volume 494, Issue 3, Pages 3061–3079 [DOI] [ADS] [arXiv]

Ross, N. P., Myers, A. D., Sheldon, E. S., *et al.* (**2012**): *The SDSS-III Baryon Oscillation Spectroscopic Survey: Quasar Target Selection for Data Release Nine*
The Astrophysical Journal Supplement Series, Volume 199, Issue 1, Page 3 [DOI] [ADS] [arXiv]

Runnoe, J. C., Cales, S., Ruan, J. J., *et al.* (**2016**): *Now you see it, now you don't: the disappearing central engine of the quasar J1011+5442*
Monthly Notices of the Royal Astronomical Society, Volume 455, Issue 2, Pages 1691–1701 [DOI] [ADS] [arXiv]

Rusinek, K., Sikora, M., Kozieł-Wierzbowska, D., *et al.* (**2020**): *On the Diversity of Jet Production Efficiency in Swift/BAT AGNs*
The Astrophysical Journal, Volume 900, Issue 2, Page 125 [DOI] [ADS] [arXiv]

Sadler, E. M., Ekers, R. D., Mahony, E. K., *et al.* (**2014**): *The local radio-galaxy population at 20 GHz*
Monthly Notices of the Royal Astronomical Society, Volume 438, Issue 1, Pages 796–824 [DOI] [ADS] [arXiv]

Sameer, Brandt, W. N., Anderson, S., *et al.* (**2019**): *X-ray and multi-epoch optical/UV investigations of BAL to non-BAL quasar transformations*
Monthly Notices of the Royal Astronomical Society, Volume 482, Issue 1, Pages 1121–1134 [DOI] [ADS] [arXiv]

Sargent, W. L. W. & Boroson, T. A. (**1977**): *A Statistical Assessment of the Evidence for Line-Locking in Quasar Spectra*
The Astrophysical Journal, Volume 212, Pages 383–389 [DOI] [ADS]

Scargle, J. D. (**1973**): *The production of discrete, quantized outflow velocities by radiation pressure in stars, Seyfert nuclei, and quasi-stellar objects.*
The Astrophysical Journal, Volume 179, Page 705 [DOI] [ADS]

Schawinski, K., Koss, M., Berney, S., *et al.* (**2015**): *Active galactic nuclei flicker: an observational estimate of the duration of black hole growth phases of $\sim 10^5$ yr*
Monthly Notices of the Royal Astronomical Society, Volume 451, Issue 3, Pages 2517–2523 [DOI] [ADS] [arXiv]

Scheuer, P. A. G. (**1987**): *Tests of beaming models*
In Zensus, J. A. & Pearson, T. J. (eds.): *Superluminal Radio Sources*. Cambridge University Press, Cambridge

Schmidt, M. (**1963**): *3C 273 : A Star-Like Object with Large Red-Shift*
Nature, Volume 197, Issue 4872, Page 1040 [DOI] [ADS]

Schmidt, M. & Green, R. F. (**1983**): *Quasar evolution derived from the Palomar bright quasar survey and other complete quasar surveys.*
The Astrophysical Journal, Volume 269, Pages 352–374 [DOI] [ADS]

Schneider, D. P., Richards, G. T., Hall, P. B., *et al.* (**2010**): *The Sloan Digital Sky Survey Quasar Catalog. V. Seventh Data Release*
The Astronomical Journal, Volume 139, Issue 6, Page 2360 [DOI] [ADS] [arXiv]

Shabala, S. S., Jurlin, N., Morganti, R., *et al.* (**2020**): *The duty cycle of radio galaxies revealed by LOFAR: remnant and restarted radio source populations in the Lockman Hole*
Monthly Notices of the Royal Astronomical Society, Volume 496, Issue 2, Pages 1706–1717 [DOI] [ADS] [arXiv]

Shakura, N. I. & Sunyaev, R. A. (**1973**): *Reprint of 1973A&A....24..337S. Black holes in binary systems. Observational appearance.*
Astronomy & Astrophysics, Volume 500, Pages 33–51 [ADS]

Shankar, F., Weinberg, D. H., Marsden, C., *et al.* (**2020**): *Probing black hole accretion tracks, scaling relations, and radiative efficiencies from stacked X-ray active galactic nuclei*
Monthly Notices of the Royal Astronomical Society, Volume 493, Issue 1, Pages 1500–1511 [DOI] [ADS] [arXiv]

Shemmer, O., Brandt, W. N., Netzer, H., *et al.* (**2006**): *The Hard X-Ray Spectral Slope as an Accretion Rate Indicator in Radio-quiet Active Galactic Nuclei*
The Astrophysical Journal Letters, Volume 646, Issue 1, Pages L29–L32 [DOI] [ADS] [arXiv]

Shen, Y., Richards, G. T., Strauss, M. A., *et al.* (**2011**): *A Catalog of Quasar Properties from Sloan Digital Sky Survey Data Release 7*
The Astrophysical Journal Supplement Series, Volume 194, Issue 2, Page 45 [DOI] [ADS] [arXiv]

Shimwell, T. W., Röttgering, H. J. A., Best, P. N., *et al.* (**2017**): *The LOFAR Two-metre Sky Survey. I. Survey description and preliminary data release*
Astronomy & Astrophysics, Volume 598, Page A104 [DOI] [ADS] [arXiv]

Shimwell, T. W., Tasse, C., Hardcastle, M. J., *et al.* (**2019**): *The LOFAR Two-metre Sky Survey. II. First data release*
Astronomy & Astrophysics, Volume 622, Page A1 [DOI] [ADS] [arXiv]

Sikora, M. & Begelman, M. C. (**2013**): *Magnetic Flux Paradigm for Radio Loudness of Active Galactic Nuclei*
The Astrophysical Journal Letters, Volume 764, Issue 2, Page L24 [DOI] [ADS] [arXiv]

Sikora, M., Stawarz, Ł., & Lasota, J.-P. (**2007**): *Radio Loudness of Active Galactic Nuclei: Observational Facts and Theoretical Implications*
The Astrophysical Journal, Volume 658, Issue 2, Pages 815–828 [DOI] [ADS] [arXiv]

Simpson, C. (**2017**): *Extragalactic radio surveys in the pre-Square Kilometre Array era*
Royal Society Open Science, Volume 4, Issue 7, Page 170522 [DOI] [ADS] [arXiv]

Smith, K. L., Koss, M., Mushotzky, R., *et al.* (**2020**): *Significant Suppression of Star Formation in Radio-quiet AGN Host Galaxies with Kiloparsec-scale Radio Structures*
The Astrophysical Journal, Volume 904, Issue 2, Page 83 [DOI] [ADS] [arXiv]

Soltan, A. (**1982**): *Masses of quasars.*
Monthly Notices of the Royal Astronomical Society, Volume 200, Pages 115–122 [DOI] [ADS]

Somerville, R. S. & Davé, R. (**2015**): *Physical Models of Galaxy Formation in a Cosmological Framework*
Annual Review of Astronomy & Astrophysics, Volume 53, Pages 51–113 [DOI] [ADS] [arXiv]

Stanley, F., Alexander, D. M., Harrison, C. M., *et al.* (**2017**): *The mean star formation rates of unobscured QSOs: searching for evidence of suppressed or enhanced star formation*
Monthly Notices of the Royal Astronomical Society, Volume 472, Issue 2, Pages 2221–2240 [DOI] [ADS] [arXiv]

Stocke, J. T., Morris, S. L., Weymann, R. J., *et al.* (**1992**): *The Radio Properties of the Broad-Absorption-Line QSOs*
The Astrophysical Journal, Volume 396, Page 487 [DOI] [ADS]

Stone, R. B. & Richards, G. T. (**2019**): *Narrow, intrinsic C IV absorption in quasars as it relates to outflows, orientation, and radio properties*
Monthly Notices of the Royal Astronomical Society, Volume 488, Issue 4, Pages 5916–5934 [DOI] [ADS] [arXiv]

Strittmatter, P. A., Carswell, R. F., Burbidge, E. M., *et al.* (**1973**): *The Absorption Line Spectrum of 1331+170*
The Astrophysical Journal, Volume 183, Pages 767–776 [DOI] [ADS]

Strittmatter, P. A., Hill, P., Pauliny-Toth, I. I. K., *et al.* (**1980**): *Radio observations of optically selected quasars*
Astronomy & Astrophysics, Volume 88, Issue 3, Pages L12–L15 [ADS]

Sulentic, J. W., Zwitter, T., Marziani, P., *et al.* (**2000**): *Eigenvector 1: An Optimal Correlation Space for Active Galactic Nuclei*
The Astrophysical Journal Letters, Volume 536, Issue 1, Pages L5–L9 [DOI] [ADS] [arXiv]

Symeonidis, M. (**2017**): *What produces the far-infrared/submillimetre emission in the most luminous QSOs?*
Monthly Notices of the Royal Astronomical Society, Volume 465, Issue 2, Pages 1401–1408 [DOI] [ADS] [arXiv]

Tadhunter, C. N., Morganti, R., Robinson, A., *et al.* (**1998**): *The nature of the optical-radio correlations for powerful radio galaxies*
Monthly Notices of the Royal Astronomical Society, Volume 298, Issue 4, Pages 1035–1047 [DOI] [ADS] [arXiv]

Tchekhovskoy, A., Narayan, R., & McKinney, J. C. (**2011**): *Efficient generation of jets from magnetically arrested accretion on a rapidly spinning black hole*
Monthly Notices of the Royal Astronomical Society, Volume 418, Issue 1, Pages L79–L83 [DOI] [ADS] [arXiv]

Temple, M. J., Banerji, M., Hewett, P. C., *et al.* (**2019**): *[O III] Emission line properties in a new sample of heavily reddened quasars at z > 2*
Monthly Notices of the Royal Astronomical Society, Volume 487, Issue 2, Pages 2594–2613 [DOI] [ADS] [arXiv]

Temple, M. J., Banerji, M., Hewett, P. C., *et al.* (**2021**): *Exploring the link between C IV outflow kinematics and sublimation-temperature dust in quasars*
Monthly Notices of the Royal Astronomical Society, Volume 501, Issue 2, Pages 3061–3073 [DOI] [ADS] [arXiv]

Thompson, T. A., Quataert, E., Waxman, E., *et al.* (2006): *Magnetic Fields in Starburst Galaxies and the Origin of the FIR-Radio Correlation*
The Astrophysical Journal, Volume 645, Issue 1, Pages 186–198 [DOI] [ADS] [arXiv]

Trump, J. R., Hall, P. B., Reichard, T. A., *et al.* (2006): *A Catalog of Broad Absorption Line Quasars from the Sloan Digital Sky Survey Third Data Release*
The Astrophysical Journal Supplement Series, Volume 165, Issue 1, Pages 1–18 [DOI] [ADS] [arXiv]

Turner, R. J. (2018): *Duty-cycle and energetics of remnant radio-loud AGN*
Monthly Notices of the Royal Astronomical Society, Volume 476, Issue 2, Pages 2522–2529 [DOI] [ADS] [arXiv]

Turnshek, D. A. (1988): *BAL QSOs: Observations, Models and Implications for Narrow Absorption Line Systems*
In Blades, J. C., Turnshek, D. A., & Norman, C. A. (eds.): *QSO Absorption Lines: Probing the Universe*. Cambridge University Press, Cambridge [ADS]

Ulrich, M.-H., Maraschi, L., & Urry, C. M. (1997): *Variability of Active Galactic Nuclei*
Annual Review of Astronomy & Astrophysics, Volume 35, Pages 445–502 [DOI] [ADS]

Urry, C. M. & Padovani, P. (1995): *Unified Schemes for Radio-Loud Active Galactic Nuclei*
Publications of the Astronomical Society of the Pacific, Volume 107, Page 803 [DOI] [ADS] [arXiv]

van Haarlem, M. P. & et al. (2013): *LOFAR: The LOw-Frequency ARray*
Astronomy & Astrophysics, Volume 556, Page A2 [DOI] [ADS] [arXiv]

Veilleux, S., Maiolino, R., Bolatto, A. D., *et al.* (2020): *Cool outflows in galaxies and their implications*
The Astronomy and Astrophysics Review, Volume 28, Issue 1, Page 2 [DOI] [ADS] [arXiv]

Vestergaard, M. (2003): *Occurrence and Global Properties of Narrow C IV λ1549 Å Absorption Lines in Moderate-Redshift Quasars*
The Astrophysical Journal, Volume 599, Issue 1, Pages 116–139 [DOI] [ADS] [arXiv]

Vogelsberger, M., Marinacci, F., Torrey, P., *et al.* (2020): *Cosmological simulations of galaxy formation*
Nature Reviews Physics, Volume 2, Issue 1, Pages 42–66 [DOI] [ADS] [arXiv]

Wada, K. (2012): *Radiation-driven Fountain and Origin of Torus around Active Galactic Nuclei*
The Astrophysical Journal, Volume 758, Issue 1, Page 66 [DOI] [ADS] [arXiv]

Weymann, R. J., Morris, S. L., Foltz, C. B., *et al.* (1991): *Comparisons of the Emission-Line and Continuum Properties of Broad Absorption Line and Normal Quasi-stellar Objects*
The Astrophysical Journal, Volume 373, Page 23 [DOI] [ADS]

Weymann, R. J., Williams, R. E., Peterson, B. M., *et al.* (1979): *Results of a homogeneous survey of absorption lines in QSOs of small and intermediate emission redshift.*
The Astrophysical Journal, Volume 234, Pages 33–46 [DOI] [ADS]

White, R. L., Helfand, D. J., Becker, R. H., *et al.* (2007): *Signals from the Noise: Image Stacking for Quasars in the FIRST Survey*
The Astrophysical Journal, Volume 654, Issue 1, Pages 99–114 [DOI] [ADS] [arXiv]

White, S. V., Jarvis, M. J., Häußler, B., *et al.* (2015): *Radio-quiet quasars in the VIDEO survey: evidence for AGN-powered radio emission at $S_{1.4GHz} < 1$ mJy*
Monthly Notices of the Royal Astronomical Society, Volume 448, Issue 3, Pages 2665–2686 [DOI] [ADS] [arXiv]

White, S. V., Jarvis, M. J., Kalfountzou, E., *et al.* (2017): *Evidence that the AGN dominates the radio emission in $z \sim 1$ radio-quiet quasars*
Monthly Notices of the Royal Astronomical Society, Volume 468, Issue 1, Pages 217–238 [DOI] [ADS] [arXiv]

Wild, V., Kauffmann, G., White, S., *et al.* (2008): *Narrow associated quasi-stellar object absorbers: clustering, outflows and the line-of-sight proximity effect*
Monthly Notices of the Royal Astronomical Society, Volume 388, Issue 1, Pages 227–241 [DOI] [ADS] [arXiv]

Williams, W. L., Hardcastle, M. J., Best, P. N., *et al.* (2019): *The LOFAR Two-metre Sky Survey. III. First data release: Optical/infrared identifications and value-added catalogue*
Astronomy & Astrophysics, Volume 622, Page A2 [DOI] [ADS] [arXiv]

Willott, C. J., Rawlings, S., Blundell, K. M., *et al.* (1999): *The emission line-radio correlation for radio sources using the 7C Redshift Survey*
Monthly Notices of the Royal Astronomical Society, Volume 309, Issue 4, Pages 1017–1033 [DOI] [ADS] [arXiv]

Xu, X., Arav, N., Miller, T., *et al.* (2019): *VLT/X-Shooter Survey of BAL Quasars: Large Distance Scale and AGN Feedback*
The Astrophysical Journal, Volume 876, Issue 2, Page 105 [DOI] [ADS] [arXiv]

Xu, X., Zakamska, N. L., Arav, N., *et al.* (2020): *Evidence that emission and absorption outflows in quasars are related*
Monthly Notices of the Royal Astronomical Society, Volume 495, Issue 1, Pages 305–320 [DOI] [ADS] [arXiv]

Yi, W., Vivek, M., Brandt, W. N., *et al.* (2019): *Broad Absorption Line Disappearance/Emergence in Multiple Ions in a Weak Emission-line Quasar*
The Astrophysical Journal Letters, Volume 870, Issue 2, Page L25 [DOI] [ADS] [arXiv]

Yip, C. W., Connolly, A. J., Szalay, A. S., *et al.* (2004): *Distributions of Galaxy Spectral Types in the Sloan Digital Sky Survey*
The Astronomical Journal, Volume 128, Issue 2, Pages 585–609 [DOI] [ADS] [arXiv]

Yong, S. Y., King, A. L., Webster, R. L., *et al.* (2018): *Using the Properties of Broad Absorption Line Quasars to Illuminate Quasar Structure*
Monthly Notices of the Royal Astronomical Society, Volume 479, Issue 3, Pages 4153–4171 [DOI] [ADS] [arXiv]

Yong, S. Y., Webster, R. L., King, A. L., *et al.* (2017): *The Kinematics of Quasar Broad Emission Line Regions Using a Disk-Wind Model*
Publications of the Astronomical Society of Australia, Volume 34, Page e042 [DOI] [ADS] [arXiv]

York, D. G., Adelman, J., Anderson, J., John E., *et al.* (2000): *The Sloan Digital Sky Survey: Technical Summary*
The Astronomical Journal, Volume 120, Issue 3, Pages 1579–1587 [DOI] [ADS] [arXiv]

Yu, Q. & Tremaine, S. (**2002**): *Observational constraints on growth of massive black holes*
Monthly Notices of the Royal Astronomical Society, Volume 335, Issue 4, Pages 965–976 [DOI] [ADS] [arXiv]

Yun, M. S., Reddy, N. A., & Condon, J. J. (**2001**): *Radio Properties of Infrared-selected Galaxies in the IRAS 2 Jy Sample*
The Astrophysical Journal, Volume 554, Issue 2, Pages 803–822 [DOI] [ADS] [arXiv]

Zakamska, N. L. & Greene, J. E. (**2014**): *Quasar feedback and the origin of radio emission in radio-quiet quasars*
Monthly Notices of the Royal Astronomical Society, Volume 442, Issue 1, Pages 784–804 [DOI] [ADS] [arXiv]

Zarrouk, P., Burtin, E., Gil-Marín, H., *et al.* (**2018**): *The clustering of the SDSS-IV extended Baryon Oscillation Spectroscopic Survey DR14 quasar sample: measurement of the growth rate of structure from the anisotropic correlation function between redshift 0.8 and 2.2*
Monthly Notices of the Royal Astronomical Society, Volume 477, Issue 2, Pages 1639–1663 [DOI] [ADS] [arXiv]